INTEGRATED COMPUTATIONAL MATERIALS ENGINEERING DEVELOPMENT OF CARBON FIBER COMPOSITES FOR LIGHTWEIGHT VEHICLES – FORD MOTOR COMPANY

Xuming Su, Principal Investigator
Ford Research and Advanced Engineering
Ford Research and Innovation Center
2101 Village Road, Dearborn, MI 48124
Phone: 313- 845-5643
E-mail: xsu1@ford.com

David Wagner, Principal Investigator
Ford Research and Advanced Engineering
Ford Research and Innovation Center
2101 Village Road, Dearborn, MI 48124
Phone: 313-845-2547
E-mail: dwagner6@ford.com

John Terneus, Project Manager
National Energy Technology Laboratory
626 Cochrans Mill Road,
P.O. Box 10940
Pittsburgh, PA 15236
Phone: 304-285-4254
E-Mail: John.Terneus@netl.doe.gov

Felix Wu, Program Manager
U.S. Department of Energy
1000 Independence Avenue, SW
Washington, DC 20585
Phone: 202-586-4830
Email: Felix.Wu@ee.doe.gov

Contractor: Ford Motor Company

Contract No.: DE-EE0006867

Contents

1. EXECUTIVE SUMMARY

This project, Integrated Computational Materials Engineering Development of Carbon Fiber Composites for Lightweight Vehicles, develops Integrated Computational Materials Engineering (ICME) techniques for Carbon Fiber Reinforced Polymer (CFRP) composites and uses these ICME tools within a multi-disciplinary optimization scheme to design a carbon-fiber intensive front subframe for a passenger sedan. The subframe is a structural automotive component with stringent requirements for vibration, strength, durability and safety performance. CFRP composites, with a density of 1.55 g/cm^3 and a tensile strength of up to 2,000 MPa in the fiber direction, have a high strength-to-weight ratio, making them one of the most promising candidates to replace the metals currently used for automotive structural components. By increasing the accessibility of CFRP component designs, reducing development-to-deployment lead time of CFRP components, and improving the robustness of initial designs, this project supports weight reduction in light-duty vehicles. These efforts can help mitigate greenhouse gas emissions from passenger vehicles and have the potential to improve national energy independence.

The four-year project concluded in early FY2019 and leveraged a total budget of $8.58 million dollars. The U.S. Department of Energy funded the project under award DE-EE0006867 for $6M and industry partners supplied the remaining $2.58M. Researchers from Ford Motor Company led the project team with colleagues from the Dow Chemical Company, Northwestern University, the University of Maryland and partners from the following software companies: Livermore Software Technology Corporation (LS-DYNA), ESTECO (modeFRONTIER), HBM Prenscia (nCode) and Autodesk, Inc. (Moldflow).

The project focused on three key architectures of epoxy-resin CFRP composites: chopped carbon fiber, unidirectional (UD) carbon fiber and woven carbon fiber. The chopped carbon fiber was investigated in the sheet molding compound (SMC) form. All three architectures, chopped SMC, UD and woven were investigated in the compression molding manufacturing process. The mechanical properties of CFRP are highly direction-dependent as the initial fabric quality, material layout, preforming and molding processes all determine the final local orientation of the fiber. As the local fiber orientation significantly affects the properties and performance of a CFRP-intensive component, achieving the optimal component design requires tools that are capable of predicting both the microstructure and performance of the component based on fiber architecture, molding process, and curing history. Strong consideration should also be made of the uncertainty inherent in each process, and the probabilistic nature of materials and manufacturing processes. The ICME tools developed in this project meet these design challenges.

The new, validated and integrated ICME tools significantly advance the capabilities of the industry and include a novel non-orthogonal material model for preforming analysis, improved compression molding simulations of chopped carbon fiber SMC, industry-first multiscale models of constitutive behavior of chopped SMC, UD and woven continuous fiber composite, refined crash analysis models, and fatigue models. These models are incorporated for the first time into a multi-disciplinary optimization workflow for the design of a CFRP composite component. modeFRONTIER serves as the platform for ICME tool integration and design optimization. Existing capabilities and added scripts enable a seamless integration of manufacturing simulation and component performance analysis.

The project results improve the infrastructure for CFRP composite design for automotive structures. The data from each of the three considered epoxy-resin CFRP composite materials (UD, woven and chopped SMC) add to the publicly available materials characterization database housed at the National

Institute of Standards and Technology (NIST). In total, more than 700 coupon test results provide the data necessary for input and validation of the material models for CFRP, including those currently available and developed in this project. The project contributes improved and novel models for CFRP composites in both manufacturing and performance simulations. Newly defined models generate fiber orientation during the preforming process for continuous and chopped fiber tows. Model improvements in the compression molding simulations add speed and accuracy to manufacturing simulations. These updated manufacturing models pass information to novel local property models for the crash, strength, fatigue, and vibration performance simulations of CFRP components. These local material models embrace a stochastic multiscale framework that leverages quantified measures of uncertainty and its propagation across length scales. modeFRONTIER connects the ICME-based models into a multi-disciplinary optimization workflow that modifies geometry, part thickness, material selection, and composite layup from the manufacturing process through various engineering performance simulations. Finally, the design exercise combines a component weight and variable cost estimate into the ICME-based multi-disciplinary optimization for an industry-first end-to-end design tool for CFRP components and systems.

This ICME-based multi-disciplinary design process is an industry first.

A representative hat section is modeled and compared with physical molded parts to validate the full ICME-based multi-disciplinary optimization. A similar modeFRONTIER workflow produces an initial design for a subframe. The multi-material subframe design meets critical engineering requirements and achieves at least a 25% weight reduction with a cost increase of less than $4.27 per pound of weight saved when compared to the baseline stamped steel subframe.

The final phase of the project produces an initial subframe design that saves 30% weight and costs an additional $4.01 per pound saved compared to a stamped steel baseline subframe. The multi-material design utilizes 79 wt% (percentage by weight) steel with reinforcements of 16 wt% chopped carbon fiber SMC and patches of UD carbon fiber composite 5 wt%. This initial design meets critical stiffness, strength and durability targets, and one key safety metric. For the first time, multiple diverse design variables are concurrently investigated in an automated procedure processed in batch mode on a high-performance computing platform to produce a design that meets multiple engineering performance metrics and variable cost.

The ICME models are all accurate within 15% of experimental values, except in the case of specific dynamic, high loading-rate behaviors that require ongoing investigation to refine predictive capabilities. The inclusion of a variable cost estimate into the multi-disciplinary optimization adds tremendous value for users in the automotive industry by expanding the objectives in the optimization scheme to include cast as well as weight while adding little cost or complexity to the computational procedures. This combination of ICME-based models and tools showcases the advantage of producing an initial design of a complex automotive part with a methodology that concurrently considers materials, performance and costs.

The public benefits from improved CFRP composite materials testing methods and a plethora of novel data, simulation tools applicable to many industries, and a multi-disciplinary optimization scheme that includes performance and variable cost in a holistic component design.

The ICME-based multi-level, multi-disciplinary design optimization developed in this project produces an initial design that meets the selected engineering performance metrics. While a production-ready final design must also address other considerations such as manufacturability, serviceability, corrosion performance and repair, the initial design criteria integrated through ICME methods in this

project are a critical subset of factors to produce a robust initial design. This exercise produces an initial design that could be used as a robust starting point for the more detailed final design. Experience shows that moving from a robust initial design to a final design typically results in small changes in weight and variable cost.

2. SUMMARY OF ACCOMPLISHMENTS VS. GOALS

The project has two main goals, (1) to develop Integrated Computational Materials Engineering (ICME) techniques for carbon fiber composites that reduce development to deployment lead time for lightweight carbon fiber composite components, and (2) to create an initial design for a structural carbon fiber composite subframe to support immediate weight reduction in Light Duty Vehicles. Additionally, the project includes dissemination of results through multiple publications, conference papers and presentations as well as through the infrastructure and methods identified by the National Institute of Standards and Technology (NIST).

This project utilizes an ICME approach to develop, integrate and implement predictive models for Carbon Fiber Reinforced Polymer (CFRP) composites that link the materials design, molding process, local material properties and final performance, with considerations of uncertainties and probabilistic nature of materials, processes and in-service conditions. The developed ICME techniques are used to design, develop and optimize an integrated CFRP composite subframe chassis component with performance, weight and cost compared to a baseline assembly.

The project produces an initial design of a light duty vehicle carbon fiber composite subframe capable of achieving a $\geq$25% weight reduction as well as $\leq$\$4.27 per pound of weight saved when compared to the baseline technology to be replaced. The subframe significantly contributes to the structural performance of the vehicle in driving and crash conditions. The developed carbon fiber composite subframe achieves critical functions and packaging requirements of the baseline subframe to be replaced.

The project achieves both of these two main goals.

The four main project tasks each have goals and accomplishments attained through this project.

Task 1: Material Characterization and ICME Database Model Development

Perform and document coupon testing to address gaps in basic material and process characterization of three thermoset epoxy CFRP composites, UD, woven and chopped SMC. Quantify the impact of process variation on the performance of the resulting composite and define a robust suite of characterization techniques to reliably qualify a composite material for automotive use. Include all the test processes and results in the NIST materials database.

Task 2: ICME Model Development and Validation

Develop and validate ICME modeling tools for three forms of thermoset epoxy carbon fiber composites for compression molding and engineering performance including both fiber architecture and the manufacturing process, with considerations of uncertainties and probabilistic nature of materials, processes, and in-service conditions.

Task 3: ICME Model Integration and Validation

Construct and exercise an ICME-based multi-disciplinary optimization workflow connecting a variety of CAD and CAE tools, optimization algorithms plus results visualization and analysis for the initial design of a CFRP composite component.

Task 4: ICME-Based Design and Optimization

Generate an initial design of a carbon fiber front subframe for a five-passenger sedan using ICME models developed (CAE only, no prototypes or vehicle tests), meet packaging, NVH, safety and durability requirements while achieving $\geq$ 25% weight reduction at a cost penalty $\leq$ \$4.27 / lb. of weight saved.

Table 2-1 highlights these major project goals and lists the accomplishments.

Table 2-1 Task Goals versus Accomplishments for DE-EE0006867

	GOAL			ACCOMPLISHMENT	
	Description	**Target**		**Description**	**Metric**
Task 1	Material testing and NIST database documentation	Test UD, woven and chopped SMC CFRP epoxy composite coupons characterizing mechanical properties of the constituents (fiber and resin) and composite coupons at quasi-static and elevated strain rates, and from ambient to elevated temperatures.	Three or more repeats per test condition	Tested coupons to determine characteristics of constituents (fiber and resin), uncured composite sheets, cured composite laminates, and the interphase region between fiber and matrix in the cured composite at multiple strain rates and temperatures.	Performed over 700 coupon tests and included all methods and results in a NIST repository
Task 2	Constituent material modeling (fiber / interphase / resin / and assembly of such)	Robust, accurate and reliable constitutive models for each constituent material as well as the composite assembly under expected service conditions including high-strain rates utilizing physics based model	≤ 15% accuracy	Model to Test correlation studies on coupons	≤ 15% some dynamic behavior has higher error
	Part Properties During and After Molding	Microstructure morphology, Optimized cycle time, and local thickness, fiber length and orientation of the final part	≤ 15% accuracy	Model correlation to hat section testing	≤ 15% agreement
	Assembly Properties After Joining and Assembly	Load to failure, failure location, and failure mode, stiffness/deflection, dynamic performance, energy absorption/crashworthiness	15% accuracy	Model correlation to hat section testing	≤ 15% some crash modes have higher error
Task 3	ICME-based multi-disciplinary optimization workflow	Construct an ICME-based multi-disciplinary optimization workflow connecting multiple CAD and CAE tools to optimize an initial design of a CFRP composite component	Batch process on Ford High Performance Computing platform	Established an integrated workflow to automate the entire ICME analysis process, composite material processing, microstructure description, material properties, and component performance with optimization and results analysis on the Ford High Performance Computing platform.	Approximately 100 design iteration per day.
				TASK 4 ACCOMPLISHMENTS	
Task 4	CFRP composite front subframe initial design	Develop an initial design of a CFRP composite front subframe that meets all package, stiffness, strength, durability, and safety metrics at the weight and cost targets		**Steel Intensive Design** 79 wt% steel 16 wt% CF-SMC 5 wt% CF-UD	**CF-SMC Intensive Design** 12 wt% steel 83 wt% CF-SMC 5 wt% CF-UD
		Weight save target	≥ 25% weight save	30% Weight Save	41% Weight Save
		Additional Variable cost per pound of weight saved target	≤ $4.27 per pound saved	$4.01 additional cost per pound of weight saved	$8.90 additional cost per pound of weight saved

After a thorough survey of models and methods for analyzing CFRP composite materials and structures and after a review of previous CFRP design and analysis projects, particularly U.S. Department of Energy project DE-EE-0005661, "Validation of Material Models for Automotive Carbon Fiber Composite Structures," the project team developed a list of gaps to address. This list includes material testing and characterization for improved modeling. Additional identified needs include molding simulation, local fiber volume and orientation especially related to local material properties. The project embraces uncertainly analysis in the composite production, preforming and molding.

Beginning from the material performance of the resin and carbon fiber three composite materials multi-scales models characterize the molding, curing and performance. These material models improve the prediction of the CFRP composite performance in the final component by accounting for the effects of

processing, manufacturing including uncertainty in each step. The resulting ICME-based models are linked together in the multi-disciplinary optimization scheme. This scheme produces an initial design of the front subframe that meets the critical engineering performance metrics at the weight savings and additional cost per pound of weight saved targets.

The proposed initial subframe design saves 30% weight ($\geq$ 25% weight save target) and costs an additional $4.01 per pound saved ($\leq$$4.27 per pound weight saved target) compared to a stamped steel baseline subframe. The multi material design utilizes steel, 79 wt% with reinforcements of chopped carbon fiber SMC, 16 wt%, and selected patches of UD carbon fiber non-crimped fabric (NCF) composite, 5 wt%. This initial design meets critical stiffness, strength, durability and one safety metric. Figure 2-1 shows the material distribution in the proposed initial subframe design.

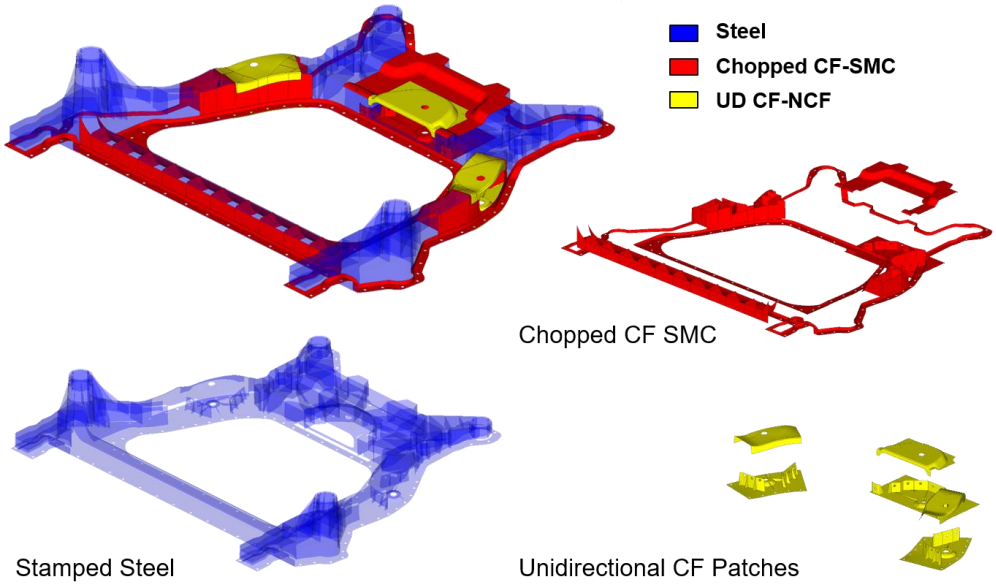

Figure 2-1 Proposed initial subframe design at 30% weight save and additional cost of $4.01 per pound saved material distribution.

Through all the project exercises, certain gaps appear and are captured as areas for future improvements and future research. In the CFRP composite materials testing fatigue characterization has been developed and improved but further efforts and refinements are certainly needed. The modeling efforts can be further enhanced by improvements in the multi-scale modeling protocols.

The modeling efforts identify gaps in nanoscale simulations of highly cross-linked epoxy resins that offer a promising way for the development of new continuum theories and models. The modeling of chopped carbon fiber SMC depends strongly on the processing method to formulate the SMC. In UD and woven CFRP composite the delamination during crushing that often limits ultimate load capacity depends on the processing and formulation. The fatigue modeling future improvements include further understanding of multi-axial fatigue properties of CFRP composites and development of a multi-axial fatigue failure criterion. The modeling task made good progress on these models but further work remains.

One major challenge of implementing the ICME-based multi-disciplinary optimization approach for composite design is that the design space is notably enlarged by including design variables from multiple

domains. Second, the composite design problem is often mixed-variable type, i.e., the design variables are a mixture of continuous (e.g., part thickness and height, fiber volume fraction), discrete (e.g., fiber rotation angle, levels of speed and force in preforming), or categorical variables (e.g., type of materials), posing challenges to the optimization search due to the combinatorial nature. Therefore, future work needs to refine the design variables and/or improve the computational efficiency of all the analytical methods from preforming, through molding to fatigue and safety simulations.

The subframe design optimization task highlights the need for improvements in the geometry and architecture morphing to produce high quality CAE models for manufacturing and engineering performance simulations. The different mesh requirements for the preforming, molding, stiffness, durability, strength and safety simulations presents the most difficult challenge in using these tools in an automated batch process. Particularly the Moldflow requirement for tetrahedral mesh in a continuous closed volume is so different from the shell mesh that is most appropriate for the durability and safety simulations that an automated process to produce both these meshes proved elusive within this project.

3. TASK REPORTS

The research activities of the projects are divided into four interrelated tasks. They are

Task 1: Material Characterization and ICME Database

Task 2: ICME Model Development and Validation

Task 3: ICME Model Integration and Validation

Task 4: ICME-Based Design and Optimization

The accomplishments of each task and lessons learned will be discussed in following sections.

3.1 Task 1: Material Characterization and ICME Database

Task 1 characterizes material CFRP and its constituent at the coupon level. The results are bases of multiscale and other material models of ICME. All tests original planned for the project were completed by FY2017. Additional tests were performed and test method developed to enhance material database for ICME model validation.

The materials chosen for the project were produced by Dow Chemical. Thermoset epoxy resin was chosen to make prepregs with continuous fibers and Sheet Molding Compound (SMC) with chopped fibers. Vacuum assisted compression molding process was used in order to achieve aggressive cycle time and cost requirements. Figure 3.1-1 shows the fiber system and fabric architecture considered in this project:

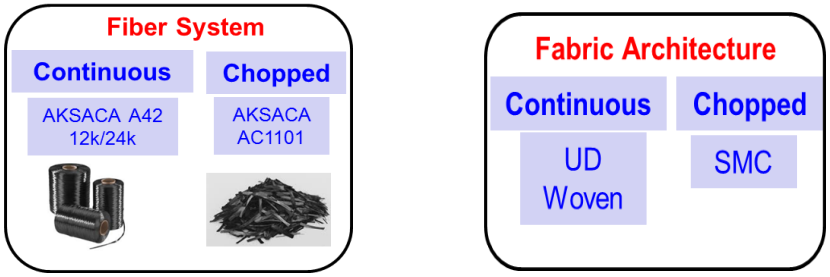

Figure 3.1-1 Material systems studied in the project.

As the weight or volume fraction of carbon fiber in a composite is the key driver of mechanical properties and cost, multiple volume fractions of fiber were considered as well. The mechanical properties of the constituents (fiber and resin) and composite coupons were characterized at quasi-static and elevated strain rates, and from ambient to elevated temperatures. The characterization results were used to inform and correlate ICME models developed in Task 2. In total, more than 700 specimens were tested to acquire the necessary data; furthermore, many of the needed parameters required novel or non-standard test methods as discussed in the following sections. Key results are highlighted in this report, and all results have been made available to the public through a repository hosted by the National Institute of Standards and Technology (NIST).

3.1.1 Resin Characterization

The resin system considered in this study was a Dow proprietary thermoset epoxy resin blend having the following characteristics:

- Room temperature shelf stability (30 days at 25°C);
- Tack free system to allow automated curing, stacking and stitching;
- Shelf stable preforms to allow automated preforming;
- Snap cure (t < 2 min) for automated molding;
- Part glass transition temperature of 160°C;
- Release characteristics enhanced by internal mold release (IMR).

Mechanical characterization of the fully cured, "neat" resin (resin only, with no carbon fiber) was conducted at Northwestern University and the University of Maryland. These tests were conducted at quasi-static (QS) and elevated strain rates (ER) and at ambient and elevated temperatures (ET). A limited number of tests were conducted on the chopped fiber "charges" (uncured sheets of chopped fiber composite) to define key parameters for the compression molding simulation.

1) Uncured chopped fiber SMC charge

Characterization of the uncured chopped fiber composite charges was conducted at Moldex3D. Differential scanning calorimetry was conducted on discs in accordance with ASTM E1269 to generate non-isothermal curves ranging from 30°C to 250°C with ordinate values representing the degree of cure and ranging from 0 (fully uncured) to 1 (fully cured), as shown in Figure 3.1-2.

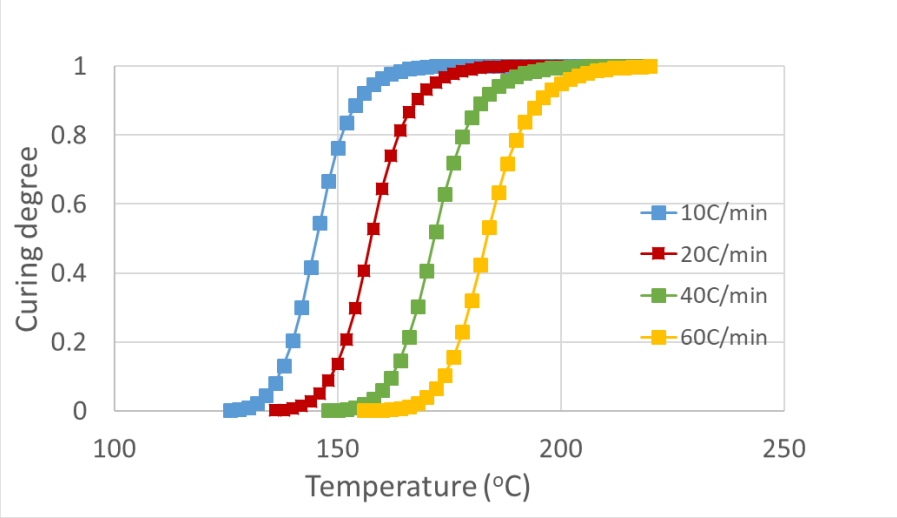

Figure 3.1-2. Iso-rate curves of uncured chopped fiber charges subjected to dynamic heating leading to curing.

Reactive viscosity measurements in the range of 70°C to 250°C were conducted according to ASTM D4440 on discs of material loaded to 5% strain at angular frequencies of 100, 200, 300 and 400 radians per second. Heating rates of 5, 10 and 20°C per minute were applied to generate non-isothermal measurements of viscosity as a function of loading frequency and heating rate.

Pressure-volume-temperature (PVT) measurements, which described the volume change of the chopped fiber charge at different pressures and temperatures, were conducted according to ISO 17744 in a GoTech PVT6000 piston type instrument. The temperature was varied from 40 to 250°C at a rate of 10°C per minute, and the pressure was varied from 200 to 300 and 400 bar. The resulting iso-pressure curves, shown in Figure 3.1-3.

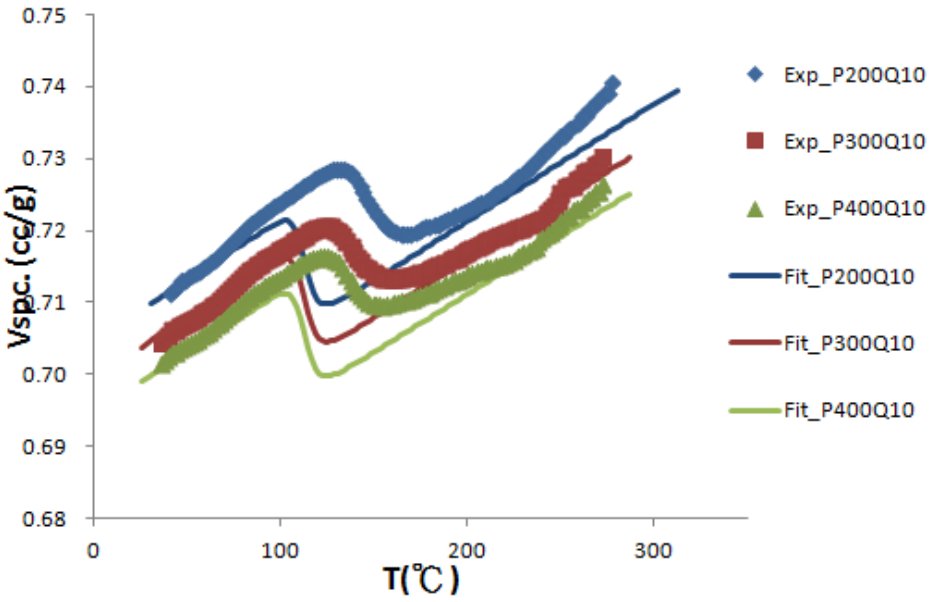

Figure 3.1-3. Iso-pressure curves of uncured chopped fiber charges subjected to dynamic heating leading to volumetric change.

Heat capacity of the chopped fiber charges were determined according to ASTM E1269 by heating the charge to 260°C and cooling at a controlled rate to 30°C. Thermal conductivity was measured at 23°C in a TechMax H5DR hot disk sensor. The measured values were used as input to the compression molding simulation.

2) Cured resin

Samples for mechanical characterization tests of the cured resin were cast at Northwestern University for compression tests and Dow for tensile tests. Uniaxial tensile tests were conducted according to ASTM D638 with a dogbone specimen geometry at quasi-static strain rates of 0.0001 per second to 0.001 per second and elevated strain rates up to 100 per second. Figure 3.1-4 shows the modulus, strength and strain to failure resulting from tensile tests on the neat resin at different strain rates, and illustrates the extent of scatter observed in the testing data. There is little trend apparent in the effect of strain rate on strength or modulus, but strain to failure is observed to decrease with increasing rate. An increased ratio of imperfections (including bubbles, voids, inclusions) were found on the fracture surface at higher rates, indicating that the pure resin material exhibits an increased sensitivity to defects at higher rates of loading. As the energy absorbed by an epoxy-based composite could be impacted by a decrease in strain at failure of the resin constituent, this observation suggests that future research will likely need to consider the impact of manufacturing defects on the performance of epoxy-based composites used in structural automotive applications.

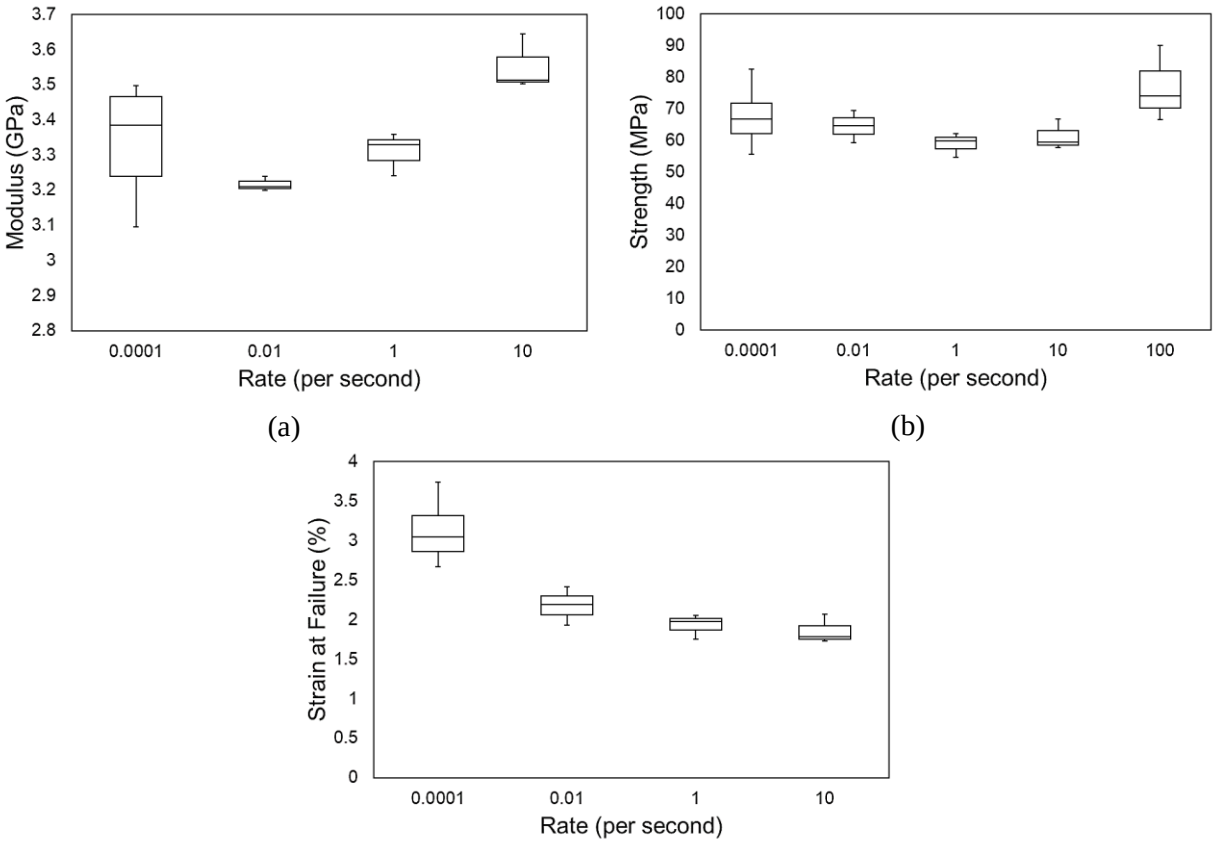

Figure 3.1-4. Tensile test results on cured neat resin from quasi-static to elevated strain rates including (a) elastic modulus, (b) ultimate strength and (c) strain at failure.

Additional tensile tests were conducted at a quasi-static strain rate and temperatures varied from ambient to 60°C, 98°C and 135°C to determine the effect on temperature on the resin constituent under a range of potential automotive use conditions. With increasing temperature, the modulus and strength were observed to decrease significantly, while the strain to failure was found to increase.

Uniaxial compression, thin-walled cylinder in torsion, and notched beam in bending tests were conducted. Tests were conducted under ambient conditions at quasi-static rates on specimens having geometries illustrated in Figure 3.1-5.

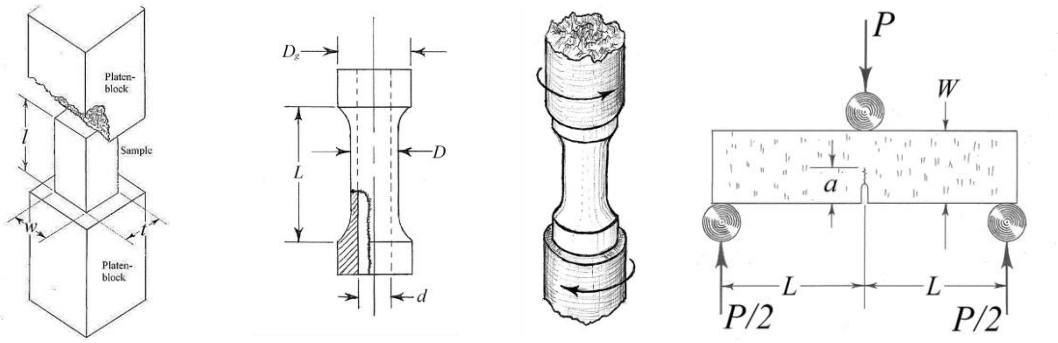

(a) (b) (c)

Figure 3.1-5. Illustration of specimens used cured neat resin tests in (a) compression, (b) thin-walled cylinder in torsion and (c) notched beam in bending.

Finally, to understand better the response of the cured neat resin material to varied strain rate, a limited number of tests were performed in compression at elevated strain rates of 0.01/s and 1/s using the same methodology as applied at the quasi-static strain rate. While the modulus and strength of a material are generally symmetric in tension and compression, the resin material was expected to exhibit less sensitivity to stress concentrations induced by defects under compression loading. The measured strength and modulus properties shown in Figure 3.1-6 confirm that the cured resin material is sensitive to strain rate. Furthermore, since the strength measured in compression increases monotonically with strain rate but remained mostly insensitive in tension, this is further indication of the important role of defects on the ability of the material to absorb energy prior to fracture.

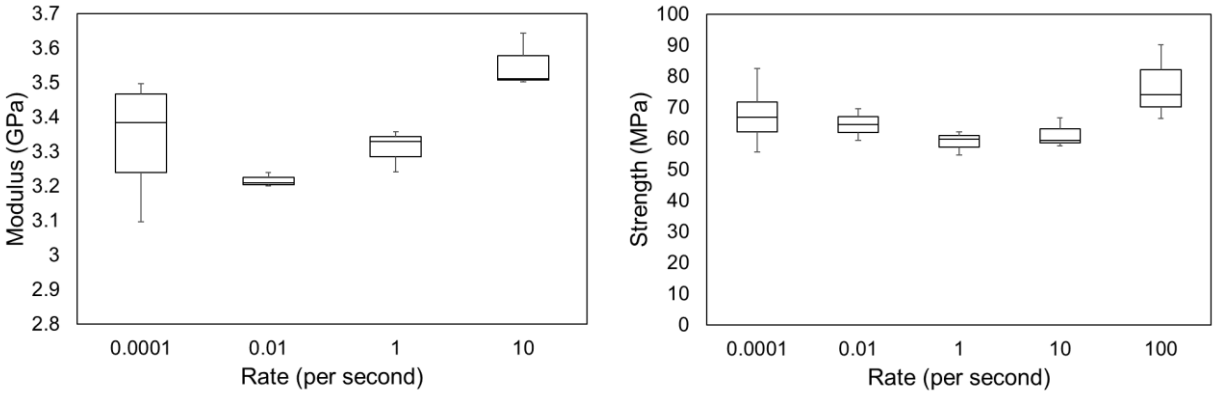

(a) (b)

Figure 3.1-6. Compression test results on cured neat resin from quasi-static to elevated strain rates including (a) elastic modulus and (b) ultimate strength

3.1.2 Carbon Fiber and Fabric Characterization

1) Single fibers

Single fiber tests were conducted at the Michigan State University Composite Materials and Structures Center. Individual fibers were extracted from a tow having a sizing but no resin. A strand was taped to a sheet of paper to enable alignment in the load train, and then was gripped at two ends before the paper

was cut. Multiple measurements were made of the fiber diameter with a laser micrometer prior to the fiber being loaded to failure at a quasi-static displacement rate. Based on measurements, it was observed that the fiber cross-section was not approximately circular as presumed. Microstructural images shown in Figure 3.1-7 reveal that the cross-section is fabiform because of the fiber manufacturing process. The fiber modulus, strength and strain at break, and the distribution of those properties, was measured.

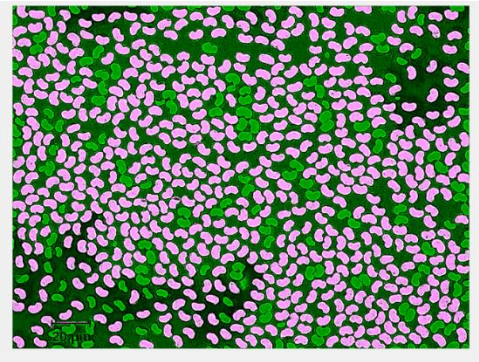

Figure 3.1-7. Optical microscope image depicting the cross-sectional shape of fibers considered in this study. Colored items in the image are fibers.

2) Uncured prepregs

The uncured prepreg was characterized via tensile and bias extension tests conducted. The prepreg considered was a twill weave with 660 grams per square meter (gsm) fabric weight, and a Non-Crimped Fabric (NCF). Individual plies only were considered in these tests. The ends of rectangular specimens were cured to permit secure clamping of the specimen. Planar strain was measured in the cross-section with a digital image correlation (DIC) system while the specimen was loaded under displacement control at a quasi-static rate. As the load increased, the specimen width decreased at the center of the gauge section as illustrated in Figure 3.1-8. For clarity, the red polygons in the images trace an outline drawn directly onto the prepreg prior to the start of testing (in the image at the far left) and its deformation throughout the test.

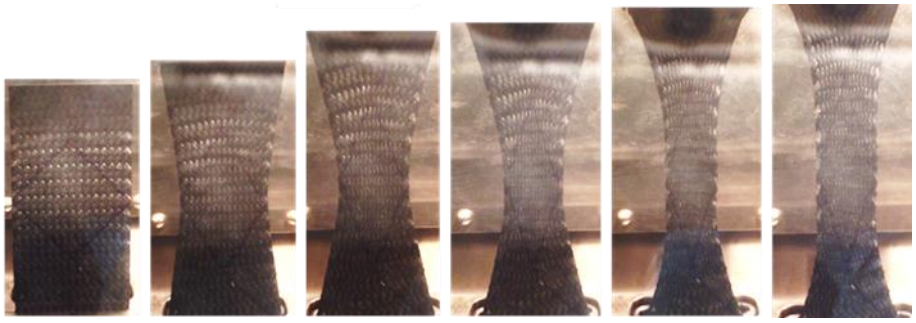

Figure 3.1-8. Progressive loading of the same bias extension specimen from left to right results in a longitudinal stretching and transverse narrowing in the gauge section

At the shear-locking angle, the fibers locked against each other, preventing further narrowing of the specimen. The shear-locking angle from both loading cases was determined from the local load-displacement curves and observation of the physical specimens. The shear-locking angle is indicated on the macroscale (coupon-level) load-displacement curves shown in Figure 3.1-9.

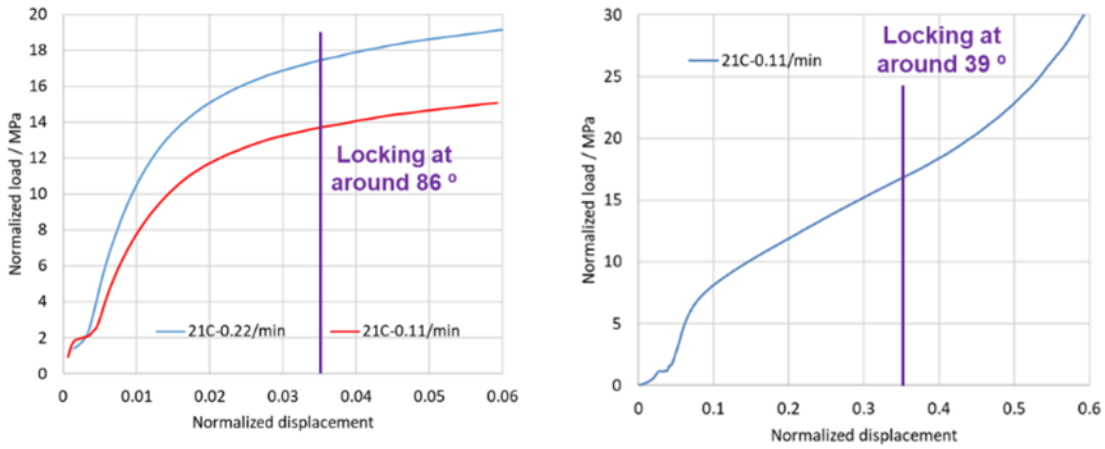

(a) (b)

Figure 3.1-9. Load-displacement curves from bias extension tests of (a) NCF and (b) 660 gsm twill woven fabrics.

3.1.3 Interfacial / Interphase Property Characterization

The interface between the fiber and matrix was identified as a feature of interest at the onset of the project, in conjunction with the characterization of each constituent as described in the preceding sections. At the interface, the sizing, which is chemically bonded to the fiber and is compatible with the intended resin system, intermixes with the resin forming an interphase region of finite thickness around the fiber. The interphase features a gradation of properties due to the intermixing of sizing and resin. The thickness of the interphase region is on the order of 100 nm to 1,000 nm for most carbon and glass fiber composites. While the thickness of the interphase region may be determined from nanoindentation, nanoscratch or thermal capacity jump measurements, the mechanical properties of the region are typically inferred from fiber push-out or pull-out tests, or may be correlated from representative finite element models.

However, due to safety issues when making specimen for pull out test, the fiber pull-out tests were not pursued in this project. Instead, RVE models and molecular dynamics were employed to inverse engineering the interphase properties based on conventional UD tests. The interphase properties were correlated from transverse tensile tests of a UD composite having a 50% fiber volume fraction. Further details of the correlation are described in Section 3.2.

3.1.4 Plaque Molding and Characterization

Several different architectures were considered including unidirectional (UD) fiber with three different fiber contents, twill woven fabrics in two different mass area, a plain woven fabric, a Non-Crimped Fabric (NCF) and a random chopped fiber. These tests were conducted in multiple plaque directions, including 0°, 10°, 45° and 90° to the fiber or warp direction (or in a consistent orientation to the plaque tool, in the case of chopped fiber plaques), at quasi-static (QS) and elevated strain rates (ER), and at ambient and elevated temperatures (ET). The tests conducted on the composite plaques, and the properties obtained, are listed in Table 3.1-1:

Table 3.1-1. List of mechanical characterization tests performed on the considered composite plaques and corresponding properties obtained.

	Test	Properties
Long UD (50%)	1. Tension 0° (QS, ER, ET) 2. Tension 90° (QS, ER) 3. Tension 10° (QS) 4. Compression 0° (QS, ER) 5. Compression 90° (QS, ER) 6. Coupon in torsion (QS) 7. Short sandwich beam (QS) 8. Double cantilevered tapered (QS) 9. Edge notched flexure (QS)	1. E_1, ν_{12}, F_{1t} , ε_{1t}^u 2. E_2, F_{2t}, ε_{2t}^u 3. G_{12}, F_{12}, γ_{12}^u 4. E_1, F_{1c}, ε_{1c}^u 5. E_2, F_{2c}, ε_{2c}^u 6. G_{13}, G_{23} 7. F_{23} 8. G_{Ic} 9. G_{IIc}
Long UD (45%)	10. Tension 0° (QS, ER) 11. Tension 90° (QS, ER) 12. Tension 10° (QS)	10. E_1, ν_{12}, F_{1t} 11. E_2, F_{2t} 12. G_{12}, F_{12}, γ_{12}^u
Long UD (55%)	13. Tension 0° (QS, ER) 14. Tension 90° (QS, ER, ET) 15. Tension 10° (QS)	13. E_1, ν_{12}, F_{1t} 14. E_2, F_{2t} 15. G_{12}, F_{12}, γ_{12}^u
Twill 660gsm	16. Tension 0° (QS, ER) 17. Tension 45° (QS) 18. Compression 0° (QS) 19. Coupon in torsion (QS) 20. Short beam in bending (QS) 21. Double cantilevered tapered (QS)	16. E_1, ν_{12}, F_{1t} , ε_{1t}^u 17. G_{12}, F_{12}, γ_{12}^u 18. E_1, F_{1c} 19. G_{13}, G_{23} 20. F_{13} 21. G_{Ic}
Twill 400 gsm	22. Tension 0° (QS) 23. Tension 45° (QS) 24. Tension 90° (QS) 25. Compression 0° (QS) 26. Compression 90° (QS)	22. E_1, ν_{12}, F_{1t} , ε_{1t}^u 23. G_{12}, F_{12}, γ_{12}^u 24. E_2, ν_{21}, F_{2t} , ε_{2t}^u 25. E_1, F_{1c}, ε_{1c}^u 26. E_2, F_{2c}, ε_{2c}^u
Plain 660gsm	27. Tension 0° (QS) 28. Tension 45° (QS) 29. Tension 90° (QS) 30. Compression 0° (QS) 31. Compression 90° (QS)	27. E_1, ν_{12}, F_{1t} , ε_{1t}^u 28. G_{12}, F_{12}, γ_{12}^u 29. E_2, ν_{21}, F_{2t} , ε_{2t}^u 30. E_1, F_{1c}, ε_{1c}^u 31. E_2, F_{2c}, ε_{2c}^u
NCF	32. Tension 0° (QS) 33. Tension 45° (QS) 34. Coupon in torsion (QS)	32. E_y, ν_{yx}, F_{yt} 33. G_{xy}, F_{xy} 34. G_{xz}, G_{yz}
Chopped (50%)	35. Tension 0° (QS) 36. Tension 90° (QS) 37. Compression 0° (QS) 38. Compression 90° (QS) 39. Iosipescu shear (QS)	35. E_1, ν_{12}, F_{1t} , ε_{1t}^u 36. E_2, ν_{21}, F_{2t} , ε_{2t}^u 37. E_1, F_{1c}, ε_{1c}^u 38. E_2, F_{2c}, ε_{2c}^u 39. G_{12}

Key results are highlighted here, but all testing data with interpretation can be found in the NIST repository described in Section 3.1.5.

1) Unidirectional composite with various fiber contents

Tests were conducted primarily in the fiber direction (0°) and transverse to it (90°), though additional tests were conducted in other directions to obtain properties or strength.

Plaques were molded in three nominal thicknesses: 1.2 mm, 2.4 mm and 4.8 mm. The majority of tests were conducted on plaques with a thickness of 2.4 mm, while thicker plaques were used to support certain tests described in this section, as well as fatigue tests described in Task 2. Thinner plaques were used to refine the molding tools and processes and only limited characterization was performed on these. Tests at quasi-static rates were conducted according to the applicable standard or practice. Testing methods for elevated rates and temperatures had not yet been established through standards and so non-standard methods were developed. Three different fiber volume fractions were considered: a large array of tests were conducted on a UD material having 50% fiber volume fraction, while a limited slate of tests were additionally conducted on materials having 45% and 55% fiber volume fraction.

Tensile tests in the 0°, 10° and 90° directions were conducted on rectangular coupons according to ASTM D3039 at ambient temperature and a quasi-static strain rate. From theory, it was expected that the 45% fiber volume content would produce the lowest values of strength and modulus, while the 55% material would produce the highest. However, the results shown in Figure 3.1-10 show almost no correlation between the fiber volume content and the strength or modulus measured at any of the considered orientations.

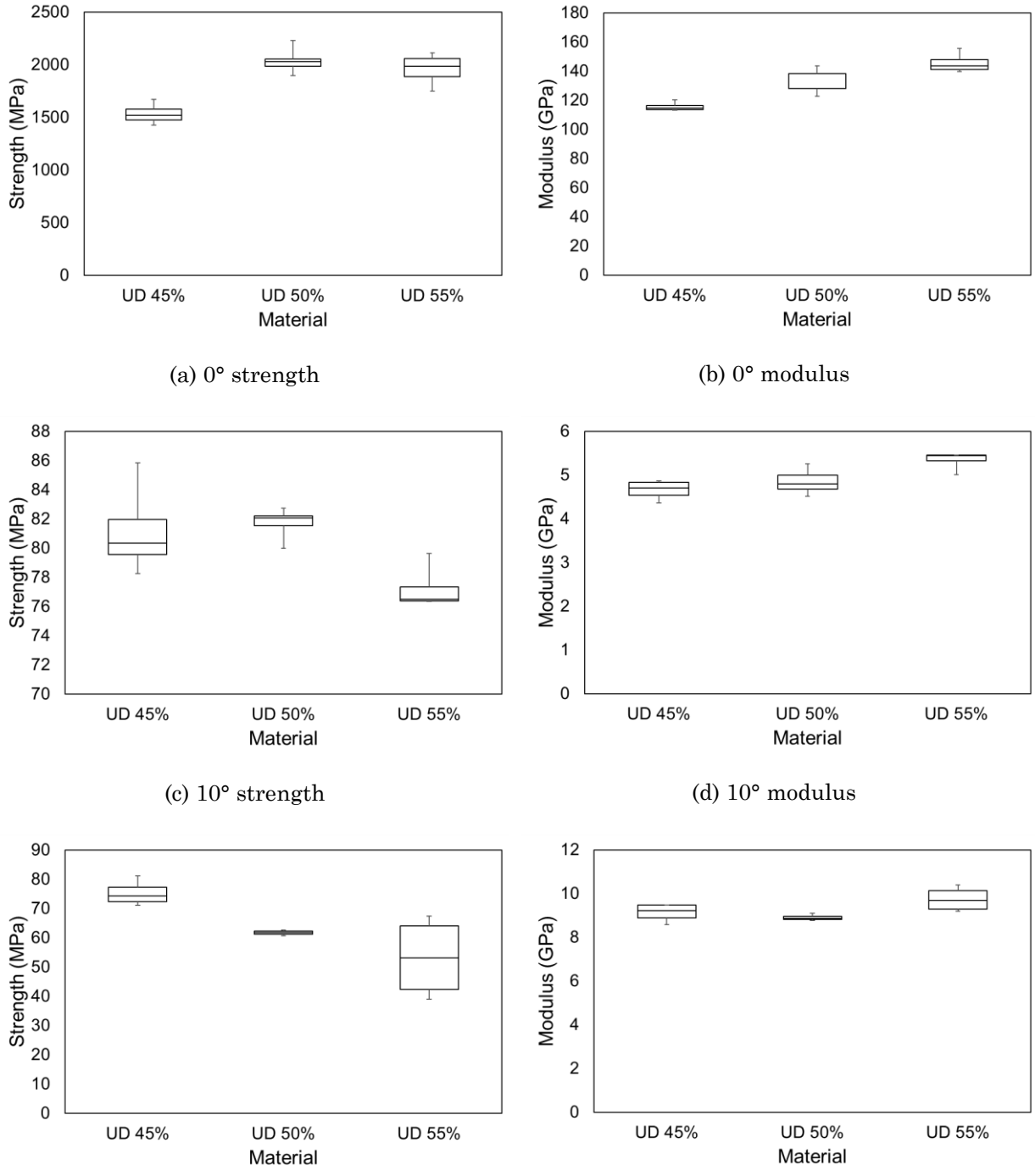

(a) 0° strength

(b) 0° modulus

(c) 10° strength

(d) 10° modulus

(e) 90° strength

(f) 90° modulus

Figure 3.1-10. Tensile strength and modulus measured in UD composite with 45, 50 and 55% fiber volume fraction

Because of the departure of experimental values from those predicted by theory, an investigation was held to determine the molding history and microstructure of the three plaque materials. The 45% and 55% materials were molded at a later date than the 50% material, and large inclusions were present on the

surface of the 45% and 55% plaques that were not observed on the 50% plaques but which may act as stress concentrators and lead to premature failure of the 45% and 55% fiber volume fraction materials. The fiber content determined from burn-off and Archimedes-type buoyancy tests on specimens of the three materials was found to be approximately nominal. Optical micrographs illustrate that all three materials exhibit a stratified appearance in the thickness direction, but no significant microstructural differences that would account for the lack of correlation between properties and fiber content. Other factors that may contribute to the deviation of measured properties from the expected values, but are difficult to quantify, include experimental error (though systematic error is unlikely as the 50% material values were confirmed with new tests at the time the 45% and 55% materials were tested), differences in fiber manufacturing, differences introduced in the prepreg process, age of prepreg, or differences in the manufacturing process not observable from post-examination. It is critical that future research consider all steps of the manufacturing process to identify those having the greatest impact on the properties of the final, cured composite to enable use of carbon fiber composites at automotive scales. For the remainder of the properties on UD composite, only the 50% fiber volume fraction material, having exhibited performance closest to the theoretical values, was considered.

As compression tests at elevated strain rates in the neat resin enabled observation of bulk material trends with decreased sensitivity to defects, similar tests were conducted on UD composite with a 50% fiber volume fraction at strain rates of 0.0025, 0.0025, 0.025 and 0.25 per second, as well as at high strain rates via Kolsky bar. The strain rates under Kolsky bar tests are not strictly controlled, but can be measured. Observed strain rates were in the range of 1,000/s, ranging from 295/s to 3,600/s. The resulting strengths are shown in Figure 3.1-11 for measurements conducted at 0° and 90° to the fiber direction. In the 0° (Figure 3.1-11 (a)), there is little impact of strain rate on strength given that tests were conducted over six orders of magnitude different in rate. This is consistent with expectation that properties in the fiber direction should be insensitive to strain rate. At 90° to the fiber direction, increasing the strain rate from 0.25/s to 2300/s significantly increases the measured strength, while at strain rates below 0.25 per second, shown at larger scale in the red box in Figure 3.1-11 (b), no relationship between is discernible between strain rate and strength. It should be noted that all strengths are higher than measured from the cured neat resin (see Figure 3.1-4). This indicates that the strength of the UD composite, even transverse to the fiber direction, is improved by the presence of the fibers.

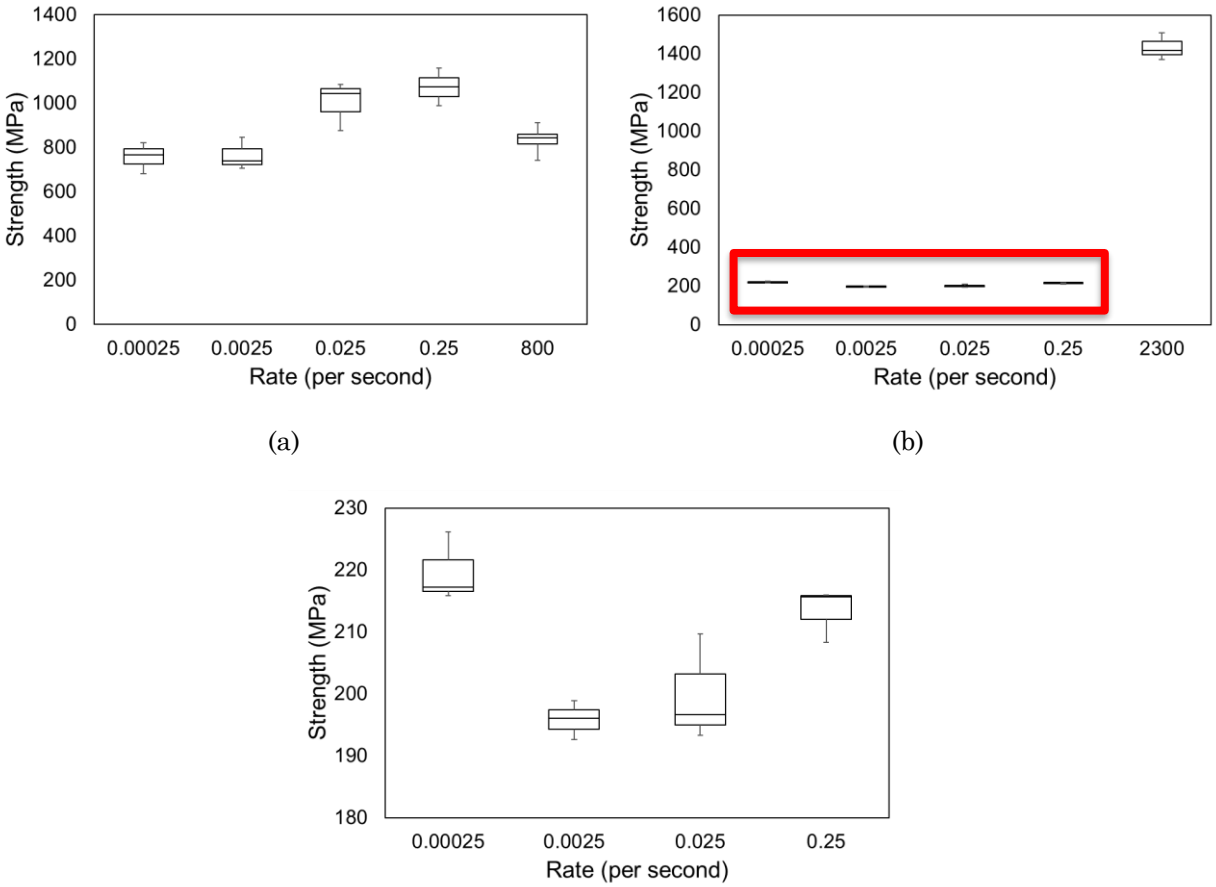

Figure 3.1-11. Strengths of a UD composite with 50% fiber volume fraction in compression at elevated strain rates at (a) 0° and (b) 90° to the fiber direction with boxed-in data (≤0.25 per second) shown in more detail in (c).

Fracture toughness tests were conducted on the UD material having a 50% fiber volume fraction in Mode I and Mode II by the width-taper double cantilever beam and end-notched flexure tests, respectively, to obtain the properties listed in Table 3.1-1, Items 8 and 9. Cracks were initiated at the midplane of the specimen by razor blade tapping, and then grown to a consistent size through cyclic loading. Once the crack achieved a designated length, the specimen was loaded monotonically to failure. Figure 3.1-12 shows the Mode I and Mode II fracture toughness results of the UD composite, as well as the Mode I fracture toughness obtained from notched beam in bending tests of the cured neat resin. For both modes, the results obtained from the UD composite are higher than that obtained from the resin. Fiber bridging was observed between beams in the specimen under Mode I loading, which suggests that even in a UD composite, fiber waviness in the through-thickness direction may affect energy absorption. Mode II loading yielding significantly higher results than Mode I. This may be due to friction or interface pressure applied at the crack tip. Future investigation should consider alternate methods of testing Mode II fracture toughness that minimize loading in the through-thickness direction.

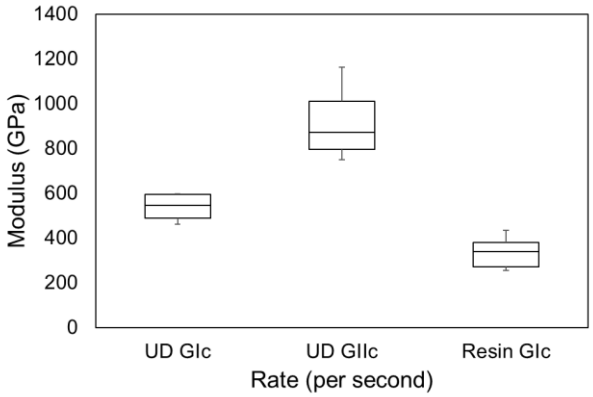

Figure 3.1-12. Comparison of fracture toughness values obtained in Mode I and Mode II loading for a UD composite with 50% fiber volume fraction with the cured neat resin in Mode I.

2) Woven composite with various architecture and fabric mass weights

Two architectures of woven fabric, a 2x2 twill weave and a 1x1 plain weave, were used to create composite plaques with nominal thicknesses of 2.4 mm and 4.8 mm. The two architectures are illustrated in Figure 3.1-13. Two different fabric mass weights, measured in grams per square meter (gsm), were considered for the twill weave: 660 gsm and 440 gsm. The plain weave was only considered with a weight of 660 gsm.

(a) (b)

Figure 3.1-13. Illustration of (a) 1x1 plain weave and (b) 2x2 twill weave.

Tensile tests were performed at 0° and 45° to the warp direction on the three woven composite materials to obtain the properties listed in Table 3.1-1, Items 16-17, 22-23 and 27-28. Tensile tests were conducted in accordance with ASTM D3039 on rectangular specimens having a minimum width of 20 mm. The largest unit cell size in the considered materials was approximately 6 mm, which ensured that at least three unit cells were present across the gauge section. Figure 3.1-14 summarizes the resulting strength and modulus properties for both testing directions. The strength and modulus of the two composites with a 660 gsm fabric weight were similar in both the 0° and 45° directions, while the 400 gsm fabric consistently demonstrated a higher strength. The modulus of the lower weight fabric is slightly lower than that of the heavier fabrics. As fabric weight is an indicator of fiber content, the expected finding is that the modulus and strength of the lower weight composite would be lower. However, as the strength of the 400 gsm twill exceeds that of the 660 gsm twill, this indicates that the local geometry of

the fiber, which can be influenced by the fabric and composite manufacturing processes, in addition to the macroscopic qualities of the fabric, may play an important role in the macroscale properties.

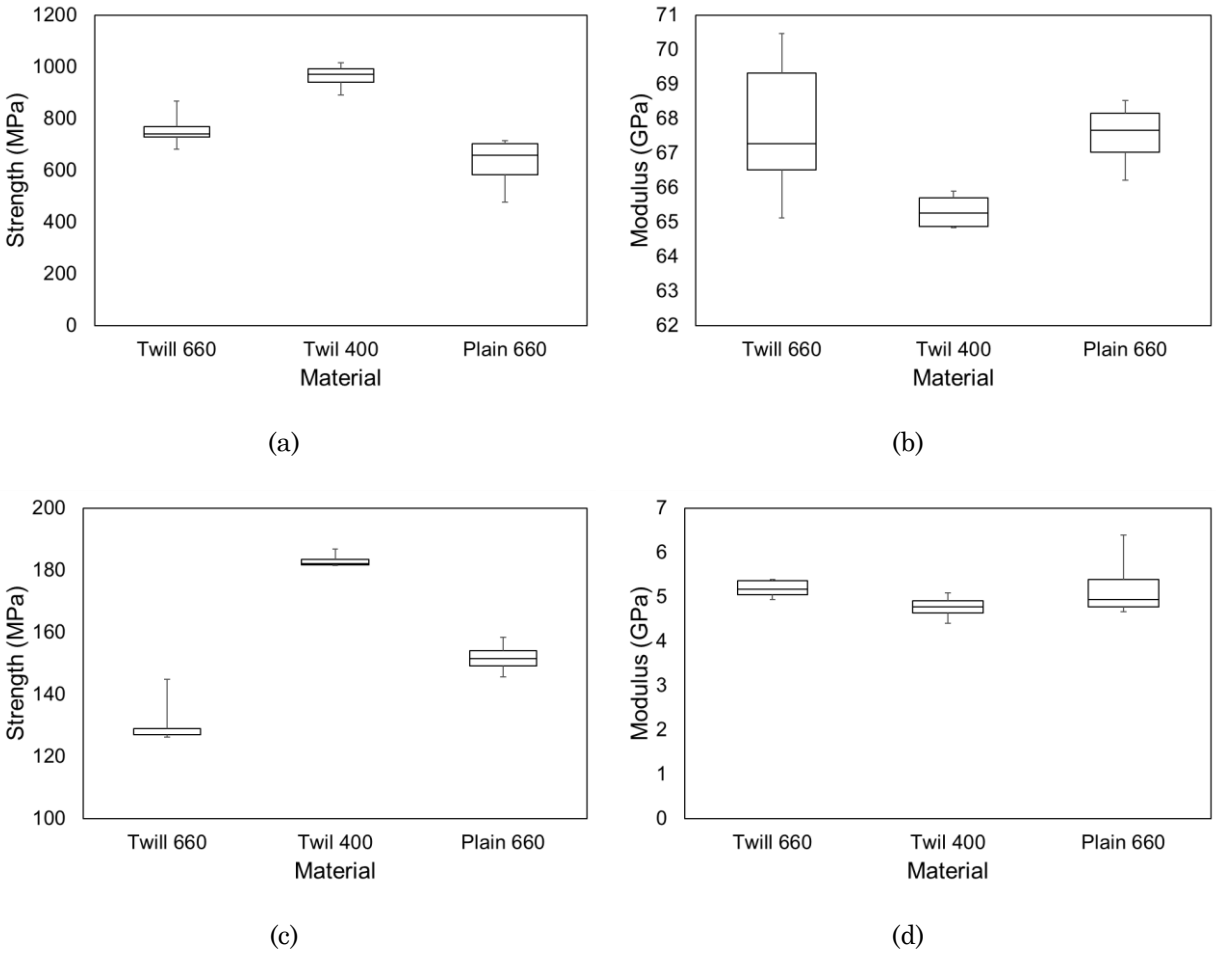

Figure 3.1-14. Tensile properties obtained from 660 and 400 gsm twill and 660 gsm plain composites: (a) strength at 0°, (b) modulus at 0°, (c) strength at 45° and (d) modulus at 45°.

Additional tensile tests were conducted to probe the local deformation characteristics of the twill 660 gsm composite under tensile loading. A digital image correlation (DIC) system was used to measure planar strain on the wide face of the specimen as monotonic loading was applied at a quasi-static rate in the warp direction. Data are also stored in NIST repository described in Section 3.1.5.

3) Non-crimped fabric

A small number of composite plaques were created with a non-crimped fabric (NCF) material consisting of UD layer (plies) stacked in [0/90]s layup. Figure 3.1-15 depicts the typical appearance of an NCF fabric with black carbon fibers and white stitches. Four layers having this stacking sequence were stitched together, and then multiple layers were stacked and compression molded to create plaques having nominal thicknesses of 2.4mm and 4.8mm.

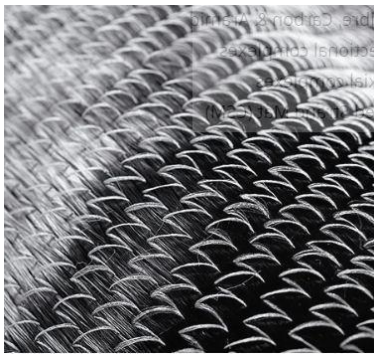

Figure 3.1-15. Close-up photograph of a NCF composite consistently of alternating layers of UD material stitched together with white threads.

Tensile tests were conducted at 0° and 45° to the fiber direction (the 0° direction being arbitrary due to the symmetric lay-up), as well as coupon-in-torsion tests, at Northwestern University at quasi-static rates. Testing was conducted as described in previous sections to obtain the properties listed in Table 3.1-1, Items 32 to 34.

4) Chopped fiber

Chopped, or short fiber composites were produced at Ford using the same DowAksa carbon fiber and Dow resin system as the long fiber composites. Long fibers were chopped into sections approximately 25 mm in length and having an appearance shown in Figure 3.1-16 (a), which were then distributed onto a resin film to create a charge. Charges were stacked to achieve the appropriate nominal thickness and were then compression molded. The resulting typical microstructure is shown in Figure 3.1-16 (b). The light and dark areas, as well as the swirl pattern evident in Figure 3.1-16 (b), indicate the presence and varied orientation of the fiber chips.

(a) (b)

Figure 3.1-16. A typical random chopped fiber material (a) raw fiber material prepared into chips and (b) compression molded microstructure.

Chopped fiber composites (also known as sheet molded compounds or SMC) were prepared with different processing conditions to inform and validate the Moldflow simulations conducted in Task 2. The initial charges were cut and preheated in an oven to 60ºC and then placed in the center of the molding tool, which had planar dimensions of 300 mm by 457 mm. The charges were compressed at 150ºC for 3

minutes using different press speeds and force profiles. The molded plaques were characterized under quasi-static loading for the monotonic tensile, compressive and shear properties listed in Table 3.1-1, Items 35 to 39.

Quasi-static tensile tests were conducted in two orientations to the plaque-molding tool, named as 0°and 90°, to determine the degree of isotropy in the plaques. It is important to note that these names do not correspond to a relationship with fiber direction in the chopped fiber case as fiber chips are randomly distributed. Five locations labeled as A-E in Figure 3.1-17 were considered. With these base coordinates, samples could be cut in different orientations in different plaques such that all 0° samples were cut from one plaque and 90° samples from a second.

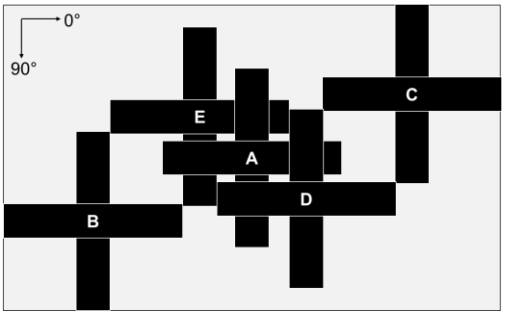

Figure 3.1-17. Schematic of sample location for chopped fiber tensile tests. The large grey rectangle demarcates the edges of a plaque, while the black rectangles indicate the location of specimens. Orientation is annotated in the upper left corner of the image.

Figure 3.1-18.illustrates typical tensile properties obtained from the plaques. There is no significant different between the tests conducted in two orientations, which indicates a fairly low degree of anisotropy in the flat plaques, and illustrates the possibility of plaque-to-plaque consistency; however, the degree of scatter in both strength and modulus is large, with a coefficient of variation exceeding 20% in the modulus and 40% in the strength. Initial work was conducted to determine the mechanism by which cracks initiate and propagate under monotonic and cyclic loading in random chopped fiber material having chips as the predominant microstructural feature. The key observation was that cracks tend to form where resin-rich areas are present. Thus, if the specimen gauge volume were insufficient relative to the chip size, it may be that the presence of randomly-distributed resin-rich zones having lower elastic and failure properties is disproportionally represented in some samples, leading to a higher degree of scatter. Future work should consider explicitly the effect of sample size and should make an effort to relate chip size to a representative gauge volume.

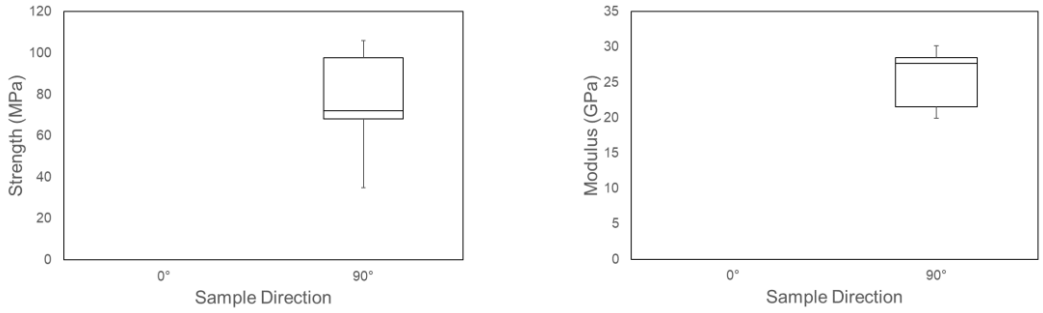

(a) (b)

Figure 3.1-18. Tensile (a) strength and (b) modulus measured from random chopped fiber samples produced at 0° and 90° to the plaque molding tool.

Quasi-static compression and shear tests were similarly conducted according to ASTM D6641 and ASTM D7078, respectively, at 0° and 90° to the plaque-molding tool. The resulting strength and modulus, shown in Figure 3.1-19 for compression tests and Figure 3.1-20 for shear tests, show no significant different in properties between the two directions tested, but display scatter similar in magnitude to that observed from tensile tests.

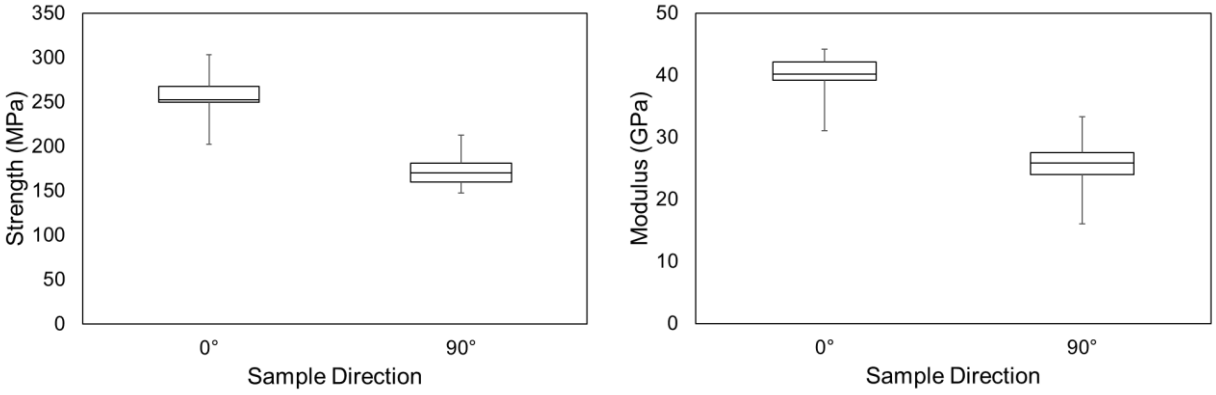

(a) (b)

Figure 3.1-19. Compression (a) strength and (b) modulus measured from random chopped fiber samples produced at 0° and 90° to the plaque molding tool.

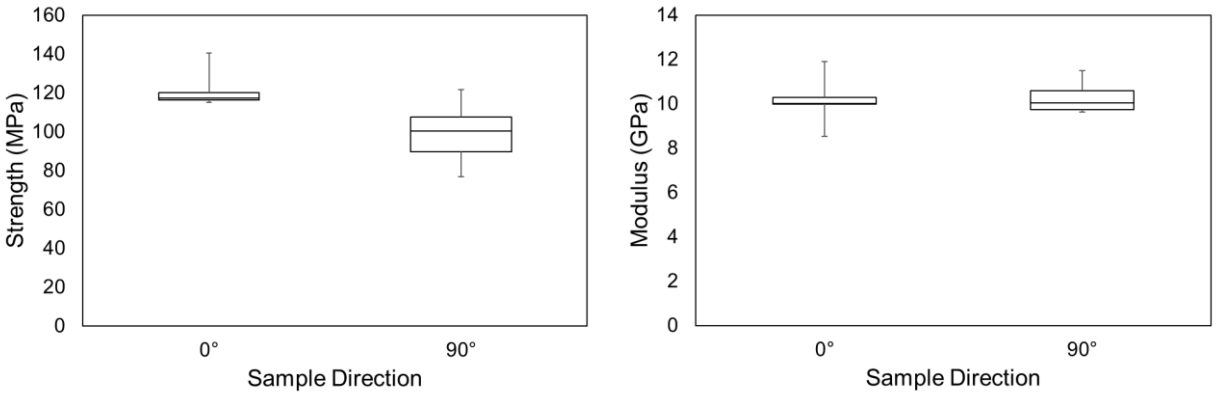

(a) (b)

Figure 3.1-20. Shear (a) strength and (b) modulus measured from random chopped fiber samples produced at 0° and 90° to the plaque molding tool.

3.1.5 ICME Database

A public database of testing data was established in the Materials Data Repository (DSpace) hosted by NIST. The data community "ICME of Carbon Fiber Composites for Lightweight Vehicles" houses all the testing data produced in the course of this project in consistently formatted templates. Testing information including addressed applicable ISO and ASTM standards for reporting results. Photos of the test set-up and tested specimen are included, as are detailed drawings of the specimens. Data sets (e.g., load-displacement and stress-strain curves) are provided for all tested specimens with minimal processing to enable future users to conduct their own analyses, though an interpretation of the results is provided as it was conducted in the course of this project. The information and data provided are sufficient to serve as a standalone reference for use by engineers and researchers with interest in the materials considered in this project.

References

[1] Cech, V., Palesch, E., Lukes, J., (2013), The glass fiber–polymer matrix interface/interphase characterized by nanoscale imaging techniques, Compos. Sci. Tech. 83:22-26

3.2 Task 2: ICME Model Development and Validation

Task 2 consists of key modules in the ICME framework. The research activities of this task are divided into seven subtasks. They are:

Task 2.1: Development of atomistically informed resin infusion models, which has the finest scale, on the order of a nanometer, to link the fundamental chemical condition to larger-scale mechanical and thermal properties.

Task 2.2: Development of preforming and compression molding manufacturing process models. This subtask addresses the critical link that this project focus on, i.e., link structure properties with manufacturing processes.

Task 2.3: Development of mechanistic RVE models to obtain the mechanical properties of the composites.

Task 2.4 & Task 2.5: Addressing key modeling of crashworthiness and fatigue life of CFRP.

Task 2.6: Development of the multiscale approach material property uncertainty quantification and propagation analysis.

Task 2.7: Conducting experiments at the part level for ICME model validations

3.2.1 Atomistically Informed Resin Infusion Model

Resin properties are very much dependent on molecular weight and structure, especially the degree of crosslink. Nanoscale simulations of epoxy resins offer a promising way to characterize their properties and their relation to molecular-level factors. Atomistic molecular dynamics (MD) simulations on epoxy resins have been successfully applied to predict various material properties in this project. MD simulations have been carried out to predict the glass transition temperature (Tg) and provided valuable insights into the effects of strain rate, temperature, and crosslink degree on Young's modulus and yielding behavior. In addition, the elastic behavior of the interphase region that exists between fibers and resin matrices has been modeled and incorporated into a modified Representative Volume Element (RVE) model, in which the three phases, fiber, matrix, and the interphase, were included. This modified RVE model was shown to improve significantly in predictions of the modulus and failure strength of the composites.

1) MDA model development for epoxy resin

Two representative epoxy systems are chosen as our model system: (1) an epoxy resin commercially known as Epon 825, consisting of diglycidyl ether of Bisphenol A (DGEBA) with curing agent 3,3-diaminodiphenyl sulfone (33DDS); and (2) an epoxy commercially denominated as 3501-6, mainly composed by tetraglycidyl methylenedianiline (TGMDA) with curing agent 4,4- diaminodiphenyl sulfone (44DDS). The chemical structures of the two representative epoxy resins as well as a representative atomistic model used in MD simulations are shown in Figure 3.2-1

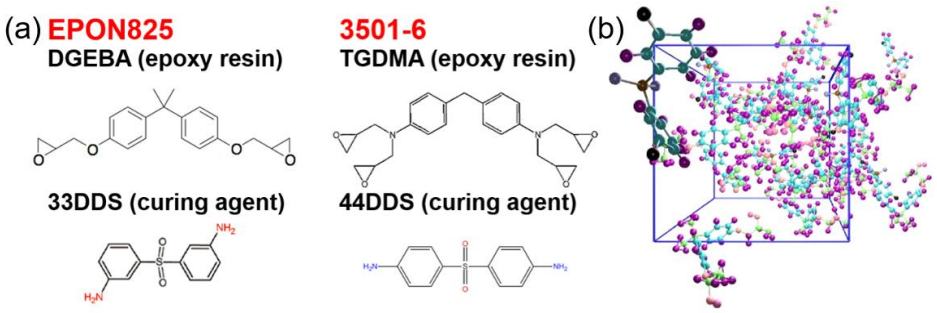

Figure 3.2-1. (a) Chemical structures of Epon 825 and 3501-6. (b) Atomistic model to be used in MD simulations.

A polymatic algorithm developed by Abbott et al. [1] was integrated with the LAMMPS Molecular Dynamics Simulator to simulate the crosslinking process. Basically, covalent crosslink bonds were added between eligible atoms based on pair-wise separation distance. Also, for every several crosslink bonds formed, energy minimization and equilibration simulations were conducted with MD to alleviate the stress generated. This workflow was able to generate atomistic structures of epoxy resins with different crosslink degrees from different initial chemistries and component ratios.

To obtain the yield surface of typical epoxy resins, the stress-strain responses of the Epon 825 model system were first calculated from the MD simulations at different temperatures and at a strain rate of $5 \times 10^8\ /s^{-1}$. The high strain rate is inherent in MD simulations given the small time-step used. During these simulations, proper thermostatting is applied to maintain the systems at specified temperatures. The results for uniaxial tensile and compressive loading cases are plotted in Figure 3.2-2. As can be seen in the figures, the entire stress-strain response for both loads is temperature dependent, affecting the yield stresses and the elastic moduli. This behavior is well-known in MD simulations of glassy polymers.

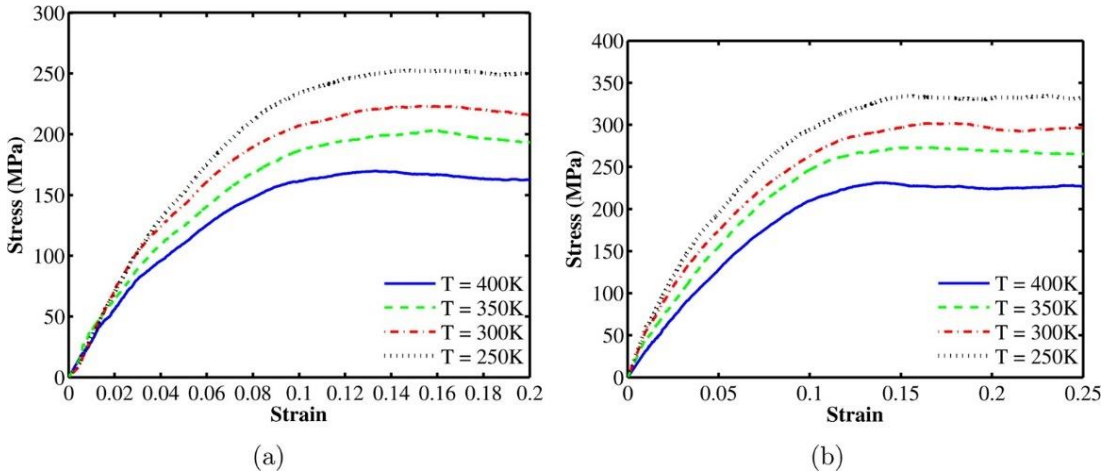

Figure 3.2-2. Uniaxially tensile (a) and compressive (b) stress-strain curves for Epon 825 deformed at a strain rate of $5 \times 10^8\ s^{-1}$ for different temperatures.

The subsequently obtained yield surfaces for the model system at different temperatures is shown in Figure 3.2-3. There is a good agreement between the MD results with the paraboloidal yield surface proposed by Tschoegl et al. [2]. This yield criterion is determined uniquely by two material parameters, the compressive and tensile yield stresses:

$$f\left(\sigma, \sigma_{Y_c}, \sigma_{Y_T}\right) = 6J_2 + 2(\sigma_c - \sigma_T)I_1 - 2\sigma_c\sigma_T \qquad (3.2\text{-}1)$$

where J_2 is the second invariant of the deviatoric stress tensor, and I_1 is the first invariant of the stress tensor. σ_T and σ_c denote the tensile and compressive yielding stress, respectively.

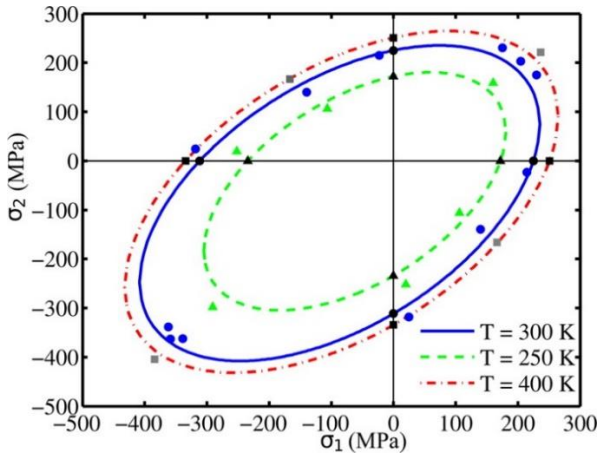

Figure 3.2-3. Yield surfaces obtained for different temperatures where the points are simulation results and the lines are theoretical prediction using Equation (3.2-1).

The framework for developing crosslinked epoxy resin structures as well as yield surface characterizations is generally applicable to other epoxy resin systems with different chemistries.

2) Dependence of thermomechanical properties on molecular chemistry

The large-deformation behavior of epoxy resins was studied and their failure response was characterized at the atomistic level. During large deformation, there are inevitable bond breaking events happening in the network structures of epoxy resins. In this work, a reactive force field [3] was adopted to capture the realistic bond breaking phenomena, which has been validated to preserve the elastic and plastic responses of the epoxy resins studied here. Stress-strain curves of 3501-6 epoxy systems with different crosslink degrees and component ratios are plotted in Figure 3.2-4. Consistent "elastic - yielding – hardening - failure" behavior is observed for all the cases. With increasing crosslink degree, both yield and maximum stresses increase, which is associated with decreasing failure strain or deformability. Varying the component ratio has a subtler change in the stress-strain curves, but the stoichiometric one has the highest yield stress and maximum stress while the lowest deformability. Thus, from atomistic level tensile simulations, we showed that the molecular-chemistries of resins strongly influence their mechanical properties and failure responses.

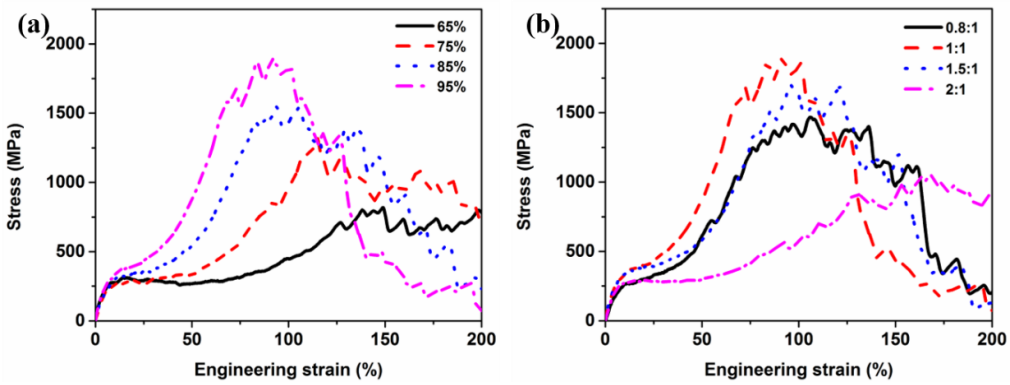

Figure 3.2-4. Effect of crosslink degree and component ratio on the stress-strain behavior by using epoxy 3501-6 as a model system.

Building upon the stress-strain curves from tensile simulations and the parameters quantifying the structural changes such as chain reorientation and void formation, we have linked this atomistic level failure response of resins to their macroscopic fracture properties on the basis of a continuum fracture mechanics model. This work provided physical insights into the molecular mechanisms that govern the fracture characteristics of epoxy resins and demonstrated the success of utilizing atomistic simulations toward predicting macroscopic fracture energies.

3) Interphase property characterization

Due to the surface roughness of carbon fibers, the surface treatments during fiber manufacturing process, and matrix affected regions, there exists a submicron-thick interphase region around carbon fibers. The thickness of the interphase region has been evaluated to be about 200 nm with an analysis from transmission electron microscopy (TEM) [4]. Here, the interphase region is further simplified as a cylindrical shell adjacent to the fiber, with the inner radius r_f being the same as the fiber radius and outer radius $r_i = r_f + 200\ nm$, as shown in Figure 3.2-5. In the following text, sub-indices f, i and m denote fiber, interphase region and matrix, respectively.

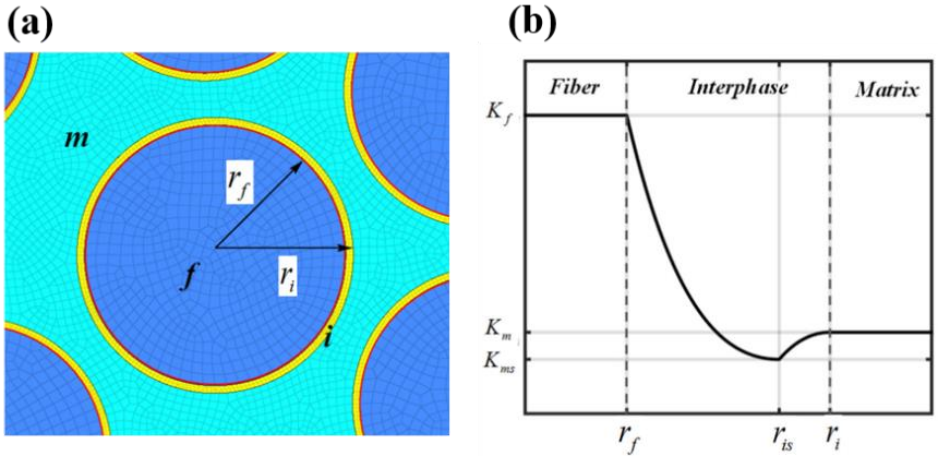

Figure 3.2-5. Interphase property characterization. (a) Schematic of the cross-section including the interphase region (yellow). (b) Variation of Young's modulus or strength inside the interphase region.

To characterize the average properties of the interphase region, we adopted an analytical gradient model to describe the modulus and strength profile inside the interphase. As shown in Figure 3.2-5 (b),

the proposed gradient model includes two parts. In the first part, Young's modulus and strength decrease from the fiber values to a lowest value. In the second part, the value gradually increases from the lowest to the value of the matrix. The increasing trend is because of the intrinsic epoxy resin stiffening through sufficient crosslinking.

The position of the lowest values (r_{is}) is assumed to be at three quarters of the interphase width away from the fiber surface ($r_{is} - r_f = 0.75(r_i - r_f)$). The position is chosen near the matrix side, since the fiber sizing forms the middle part of the interphase and the incompatibility between sizing and matrix resin mainly induces the insufficient crosslinking. The variations of the properties of interphase region are assumed to follow the exponential functions as following:

For the first part of the interphase region:

$$E_i = E_{ms} + \left(E_f - E_{ms}\right)R(r) \tag{3.2-2a}$$

$$\sigma_i = \sigma_{ms} + \left(\sigma_f - \sigma_{ms}\right)R(r) \tag{3.2-2b}$$

For the second part of the interphase region:

$$E_i = E_m + (E_{ms} - E_m)Q(r) \tag{3.2-2c}$$

$$\sigma_i = \sigma_m + (\sigma_{ms} - \sigma_m)Q(r) \tag{3.2-2d}$$

where functions $R(r)$ and $Q(r)$ in Equation (3.2a-d) are constructed to match the boundary conditions:

$$R(r) = \frac{1 - (r/r_{is})\exp(1 - r/r_{is})}{1 - (r_f/r_{is})\exp(1 - r_f/r_{is})}$$

$$Q(r) = \frac{1 - (r/r_i)\exp(1 - r/r_i)}{1 - (r_{is}/r_i)\exp(1 - r_{is}/r_i)} \tag{3.2-3}$$

E_i and σ_i are predicted modulus and strength within the interphase, E_f , E_m , E_{ms} are moduli of the fiber, matrix and the lowest value inside the interphase region, σ_f , σ_m , σ_{ms} are the strengths of the fiber, matrix and the lowest value inside the interphase region, respectively. There values are defined through integration of the MDA results, which will be explained in detain below.

The modulus at the left bound of the interphase region is taken as the average moduli of the fiber: $E_f(r = r_f) = \frac{E_{f11} + E_{f22} + E_{f33}}{3} = 95\ GPa$. The modulus at the right bound of the interphase region is taken the modulus of the matrix: $E_m(r = r_i) = E_m = 3.8\ GPa$. The strength at left bound is assumed to be the same as the carbon fibers $\sigma_f = 3\ GPa$, while the strength at the right bound is the same as the matrix, $\sigma_m = 68\ MPa$. Thus, the boundary values for both Young's modulus and strength of the interphase region are obtained.

MD analysis are integrated to obtain E_{ms} and σ_{ms} in the interphase region. The MDA analysis results in Figure 3.2-4 show increase of Young's modulus and strength increasing with curing degree, which

indicates that insufficient crosslinking process leads to deleterious mechanical properties. The difference in the Young's modulus between under-cured epoxy (~70% curing degree) and fully cured epoxy (95% curing degree) is around 20%, and the difference in the strengths between them could be up to 50%. Thus, the results provide reasonable lower bounds as: $E_{ms}/E_m = 0.8,\ \sigma_{ms}/\sigma_m = 0.5$.

The average modulus and strength in the interphase region can be obtained by as:

$$\bar{E}_i = \int_{r_f}^{r_i} E_i(r)dr\ /(r_i - r_f) \tag{3.2-4a}$$

$$\bar{\sigma}_i = \int_{r_f}^{r_i} \sigma_i(r)dr\ /(r_i - r_f \tag{3.2-4b}$$

Substituting the parameters of both modulus and strength values into the above Equation (3.2-3.4), we finally have:

$$\bar{E}_i = 22.5\ GPa$$
$$\bar{\sigma}_i = 670\ MPa \tag{3.2-5}$$

With matrix modulus ($E_m = 3.8\ GPa$) and tensile strength($\sigma_{ft} = 68\ MPa$), the average Young's modulus and strength of the interphase region are increased by around 5 and 9 times, respectively. As a result, the interphase region shows an obvious stiffened response compared to the bulk matrix, although a portion of the interphase region is weaker due to insufficient crosslinking.

Reference

[1] L.J. Abbott, K.E. Hart, C.M. Colina, Polymatic: a generalized simulated polymerization algorithm for amorphous polymers, Theoretical Chemistry Accounts 132(3) (2013) 1-19.

[2] N. Tschoegl, Failure surfaces in principal stress space, Journal of polymer science Part C: Polymer symposia, Wiley Online Library, 1971, pp. 239-267.

[3] T.R. Mattsson, J.M.D. Lane, K.R. Cochrane, M.P. Desjarlais, A.P. Thompson, F. Pierce, *et al.*, First-principles and classical molecular dynamics simulation of shocked polymers, Phys Rev B 81(5) (2010) 054103.

[4] Q. Wu, M. Li, Y. Gu, Y. Li, Z. Zhang, Nano-analysis on the structure and chemical composition of the interphase region in carbon fiber composite, Composites Part A: Applied Science and Manufacturing 56 (2014) 143-149.

3.2.2 Preform and Compression Molding Modeling

One of the key elements in the ICME modeling framework is to consider the variation of material microstructure due to the manufacturing process. Predicted microstructure information from manufacturing simulation models provides essential input for the quantification of local material properties of the CFRP during the performance prediction of formed composites parts. In this section, the model development of the compression molding process for both continuous and chopped CFRP composites are discussed in detail.

3.2.2.1 Preforming model development for continuous fiber composites

Compression molding process is one of the major manufacturing processes to produce high strength structure components for continuous carbon fiber composite parts. As illustrated in Figure 3.2-6, compression molding of continuous CFRP includes both preforming and curing processes. The first step is to stack layers of uncured thermoset carbon fiber prepregs in an optimized fiber orientation combination. Then, these prepregs are heated to soften the resin and subsequently formed to desired 3D shapes on a press machine during the preforming step. Finally, the parts are cured to achieve the design geometry. Most of the fiber re-orientation is introduced in the preforming step. Since mechanical stiffness and strength of the composites are mostly affected by the fiber orientation, the selection of the preforming parameters such as process temperature and initial prepreg layout is critical to the final part performance.

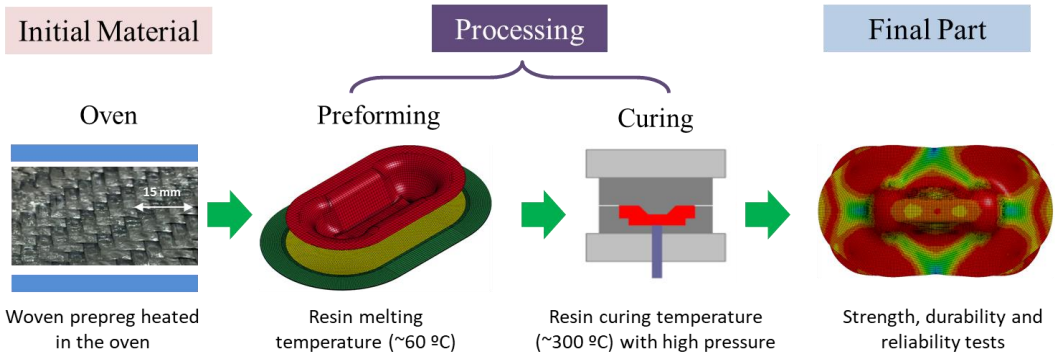

Figure 3.2-6. Schematic for the continuous fiber composite compression molding process.

The major technical target for the preforming modeling in this project is to develop a computational simulation method that can capture the deformation of carbon fiber prepregs, including part geometry, fiber orientation, and forming force during preforming process, with high accuracy and less than 15% error. With this simulation method, the material cost and development period for design and optimization of carbon fiber composite can be reduced significantly compared to the conventional manufacturing process design methods, which rely heavily on trial-and error experiments.

For the potential of commercialization and user-friendly operation, a non-orthogonal material model for the CFRP preforming simulation was developed by Northwestern University and was implemented into a commercial FEM code ABAQUS® as a user-defined material subroutine [1]. Although the intention of coupling the tensile and shear behavior in the new constitutive law was applaudable for having the most general form, it encountered inaccuracy especially when woven CFRP is subject to large shear deformation. As an advancement, an improved non-orthogonal model for the woven CFRP preforming process is invented in this project. It has been validated by benchmark tests and has been incorporated into the LS-DYNA® as MAT_COMPRF (MAT_293) through the joint effort of this academic and industry team [2].

For the success of development, experimental material characterization techniques are designed and performed systematically, first to provide correct input to simulation models. Then models at both mesoscale and macroscale are to be established and validated. The goal of mesoscopic modeling is to perform virtual material characterization to replace the unsatisfactory direct experimental characterization. The goal of macroscopic modeling, on the other hand, is to form a platform for part-scale preforming simulation when measured material properties are input. Finally, these modeling tools are to be combined with proper calibration techniques to form a high accuracy and high fidelity hierarchical multiscale modeling method for the prepreg preforming process.

Work related to preforming process modeling in this project can be divided into four portions:

1) Hydro-lubricant uncured prepreg surface interaction model
2) Macroscopic non-orthogonal material model for uncured prepreg
3) Mesoscopic RVE model for uncured prepreg
4) Multiscale uncured prepreg preforming model with Bayesian calibration

1) Hydro-lubricant uncured prepreg surface interaction model

A 2x2 twill woven composite as shown in Figure 3.2-7 is studied in this project. The characteristic sizes of woven structure, i.e., yarn width, yarn gap, and yarn thickness, listed in Table 3.2-1, were measured by microscopes from the cross-section of the material. The average thickness of the prepreg is obtained via a caliper.

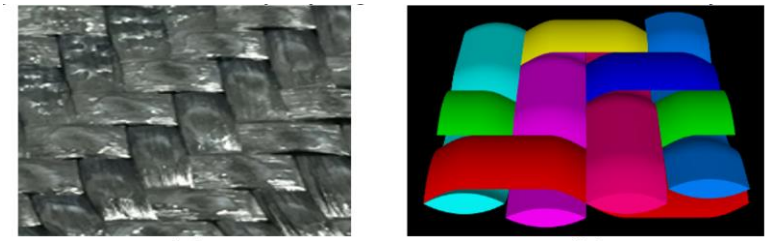

Figure 3.2-7. Illustration of the prepreg structure via (a) real product photo and (b) model generated by the open source software TexGen.[3]

Table 3.2-1. Parameters for the displacement normalization method in the bias-extension tests.

Yarn width	Yarn gap	Yarn thickness	Prepreg thickness
2.430±0.112 mm	0.004±0.004 mm	0.503±0.012 mm	0.85±0.15

Textures affect the interaction of the textured surfaces. A hydrodynamic model was developed and applied to simulate and study the prepreg surface interaction. In this model, the top and bottom woven fabrics were aligned to the same direction with 0/90/0/90 fiber orientation for 2D simplification. These fabrics were treated as rigid because 1) they were firmly stretched in the fiber matrix, so that the vertical deformation was minimal; and 2) the normal load was low. Relative movement of the interface can be considered by the general lubrication system illustrated in Figure 3.2-8. This system is formed with two solids separated by a continuous fluid film. In the simulation, the solid geometry was determined based on the cross-section of the 2x2 twill woven prepreg. The single warp yarn cross-section was idealized as an elliptical shape, while the cross-section of the weft yarn on top of the two warp yarns was modeled as a plane tangent to two half elliptical shapes. It was assumed that, in the simulation, the upper layer would move with respect to the lower one. To describe the dynamic of viscous resin, one-dimensional transient Reynolds equation for incompressible Newtonian fluid flow is utilized.

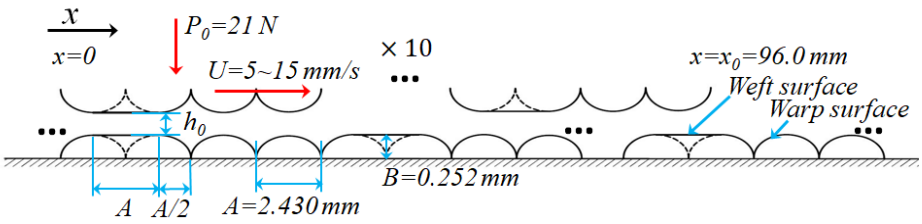

Figure 3.2-8. Geometry and forces of the simulated two 2x2 twill fabric interface.

With this hydro-lubricant model, surface interaction at various temperatures is simulated at a relative motion speed set of 10 mm/s. The comparison of numerical and experimental results is shown in Figure 3.2-9, where the average, maximum, and minimum values of the interaction factor are plotted. At 50 ºC, the numerically calculated interaction factor is significantly larger than the experimental one because the continuity assumption is not valid. In the simulation, the resin layer behaves like a continuous fluid with high viscosity, while in the experiment, the resin may only partially melt, so there is still an interface where friction takes place between the top and bottom prepregs. It should be noted that, at this interface which breaks the continuity assumption in the simulation, the friction should be lower. Moreover, in the numerical calculation, the prepreg fiber is assumed to be rigid for simplification. In the experiment, on the other hand, the highly viscous resin at this temperature leads to large fluid shear stress, deforming the prepreg fiber, changing the surface profile and in return reducing the interaction. At 60 ºC, the numerical results agree very well with the experimental ones because the viscosity falls in a reasonable range, and the continuity assumption is valid since the resin fully melts. At the 70 ºC condition, the numerical predictions are slightly smaller than the experimental result. A larger interaction factor in the experiment is due to the direct contact between two woven fabrics. It was found that at this condition, the minimum film thickness would reach 0.06 mm during the calculation because the viscosity of the resin becomes very small. The minimum film thickness is in the same order of the 0.012 mm half-yarn thickness variation; thus, in the real tests, two woven fabric surfaces may contact each other at some positions, resulting in a boundary-mixed-hydrodynamic lubrication cycling.

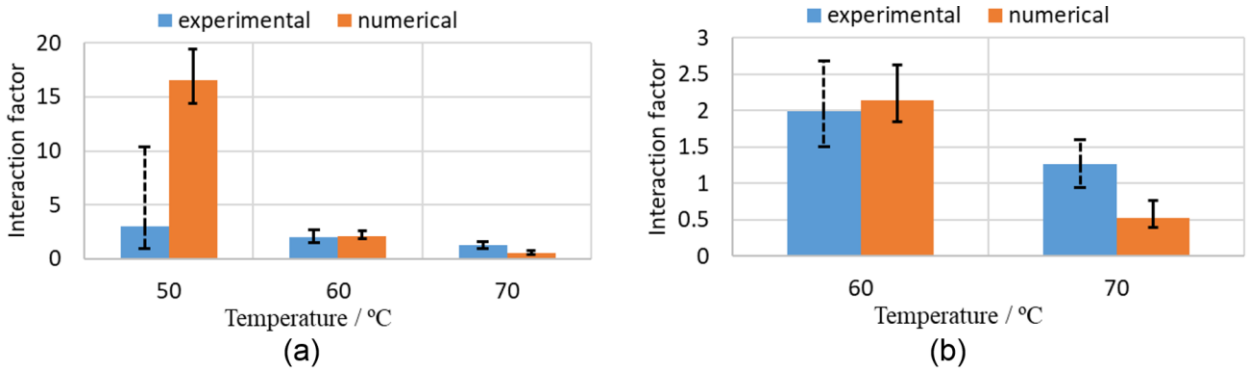

Figure 3.2-9. (a) Experimental and numerical interaction factor comparison at various temperatures and 10 mm/s. (b) A zoom-in to 60 ºc and 70 ºc for clear illustration.

For the interaction at 60 ºC, the numerical calculations with various relative motion speeds were then performed. The experimental and numerical results for the average, maximum, and minimum interaction factors are plotted in Figure 3.2-10. The interaction model results agree well with the experimental ones in general. However, the speed effect is slightly more significant than that found in the experiments because of the hydrodynamics assumption between rigid surfaces in the model, which is sensitive to

sliding speed. However, in the real experiment, other factors can also contribute to the speed effect. At low speed, there is sufficient time for the resin to mix and inter-diffuse, so that the resin is tackier and tends to stick the two surfaces together, thus increasing fluid resistance to motion. At high speed, the interaction force increases because of the viscous friction, so elastic deformation of the fiber increases correspondingly, which in return flattens the surface and reduces the interaction in the real materials.

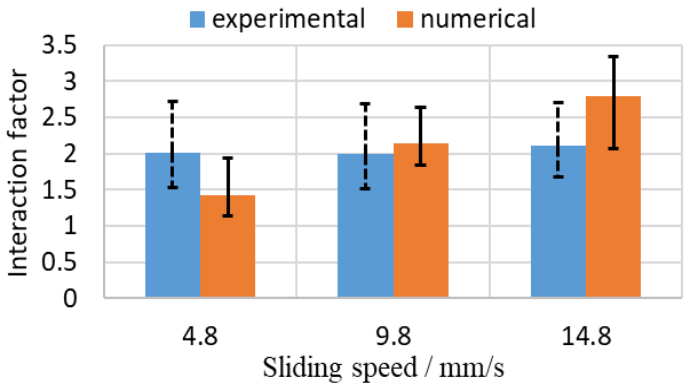

Figure 3.2-10. Experimental and numerical interaction factor comparison at various speeds and 60 ºC temperature. The points are moved away with the input speeds artificially to better differentiate between the data.

Finally, with this hydro-lubricant model, the periodic interaction factor variation was investigated. The Fast Fourier Transformation (FFT) was applied to both experimental and numerical results. Results at 60 ºC and 10 mm/s are plotted in Figure 3.2-11, showing that all the experimental and numerical curves have the 1st order length frequency of about 0.1/mm, which means that the interaction factor changes in the period of about 10 mm. This phenomenon is dominated by the size of the prepreg unit cell, which has a 2x2 twill element of 9.74 mm side length. However, for higher order frequencies, numerical results agree less with experimental ones, especially in terms of amplitude. This might be explained by the fact that viscoelasticity of the real material can absorb high frequency vibration energy during sliding.

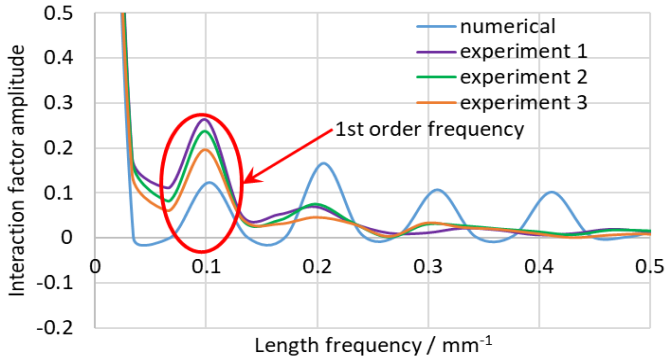

Figure 3.2-11. Fast Fourier transformation (FFT) results of the numerical and experimental data.

Experiment validation demonstrates that under certain preforming conditions, i.e., 60 ºC temperature and 5-15 mm/s sliding speed for the supplied woven prepreg, interaction between two prepreg surfaces can be explained by the hydro-lubricant mechanism and predicted via the numerical method developed in this project. The elastic deformation of the fabric and the resin mixing with inter-diffusion at various deformation rates and temperatures should be considered in the future work in order to model the prepreg-prepreg interaction more accurately and predict the interaction behavior subjected to wider conditions.

2) Macroscopic non-orthogonal material model for uncured prepreg

A non-orthogonal material model for the CFRP preforming simulation was developed, aiming to accurately predict the deformation of the uncured prepreg during preforming especially under large shear. This material model was developed in the form of ABAQUS explicit user-defined material subroutine (ABAQUS VUMAT) and LS-DYNA user-define material subroutine (LS-DYNA UMAT). Because of its ease of use and high prediction accuracy for part shape and fiber orientation, this model was implemented in the LS-DYNA as MAT_293 (MAT_COMPRF). The fundamentals of this model can be found following this section.

Woven prepregs have highly anisotropic mechanical properties, with large tensile modulus (10 GPa level) along warp and weft yarns because of the stiff carbon fibers reinforcement, but small intra-ply shear modulus (0.1 MPa level). During preforming, the most dominant deformation mode is the intra-ply shear. To capture this fiber-orientation-dominant anisotropy, the material model needs to simulate tension along the yarns and shear separately.

Stress analysis for the woven uncured prepreg with the non-orthogonal model developed in this project is shown in Figure 3.2-12. σ_{f1}, and σ_{f2} are the stress components caused by yarn stretch, and they are along the warp and weft yarn directions, respectively. σ_{m1} and σ_{m2} are the stress components caused by the yarn rotation. These stress components will be transformed into the local corotational coordinate, summed up as σ_{XX}, σ_{XY}, and σ_{YY}, and will then be output from the material model to FEM software. In this model, deformation gradient tensor F is utilized to trace yarn directions and stretch ratios during preforming via g=F•G, where g and G are the final and initial orientations of the local fibers respectively. It can be used to calculate α, which indicates the relative rotation between the local warp direction and the X-direction in the local corotational coordinate, and yarn angle β, which indicates the amount of shear deformation in the material. Calculation procedure of this non-orthogonal model is shown from Equations (3.2-6) to (3.2-14).

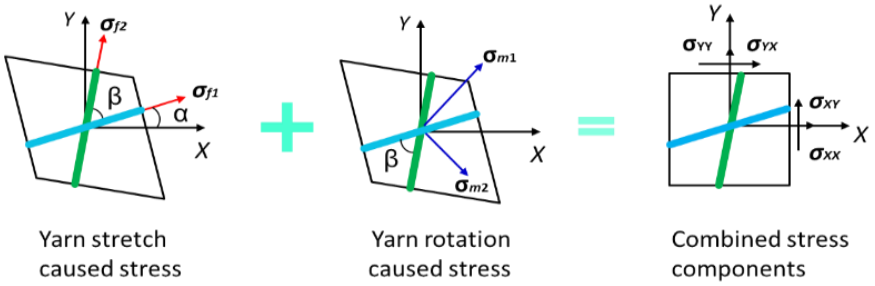

Figure 3.2-12. Stress analysis in the non-orthogonal material model.

$$\sigma_{XX}^{f} = \sigma_{f1} \cdot \cos^2 \alpha + \sigma_{f2} \cdot \cos^2(\alpha + \beta) \quad (3.2\text{-}6)$$

$$\sigma_{XX}^{f} = \sigma_{f1} \cdot \cos^2 \alpha + \sigma_{f2} \cdot \cos^2(\alpha + \beta) \quad (3.2\text{-}7)$$

$$\sigma_{YY}^{f} = \sigma_{f1} \cdot sin^2 \alpha + \sigma_{f2} \cdot sin^2(\alpha + \beta) \quad (3.2\text{-}8)$$

$$\sigma_{XX}^{m} = \frac{\sigma_{m1}+\sigma_{m2}}{2} + \frac{\sigma_{m1}-\sigma_{m2}}{2} \cos(2\alpha + \beta) \quad (3.2\text{-}9)$$

$$\sigma_{XY}^{m} = \sigma_{YX}^{m} = \frac{\sigma_{m1}-\sigma_{m2}}{2}\sin(2\alpha+\beta) \quad (3.2\text{-}10)$$

$$\sigma_{YY}^{m} = \frac{\sigma_{m1}+\sigma_{m2}}{2} - \frac{\sigma_{m1}-\sigma_{m2}}{2}\cos(2\alpha+\beta) \quad (3.2\text{-}11)$$

$$\sigma_{XX} = \sigma_{XX}^{f} + \sigma_{XX}^{m} \quad (3.2\text{-}12)$$

$$\sigma_{XY} = \sigma_{YX} = \sigma_{XY}^{f} + \sigma_{XY}^{m} \quad (3.2\text{-}13)$$

$$\sigma_{YY} = \sigma_{YY}^{f} + \sigma_{YY}^{m} \quad (3.2\text{-}14)$$

This non-orthogonal material model was implemented into both ABAQUS and LS-DYNA. This model enables users to directly input experimental data to define the stress-strain curves, as well as the shear locking angle, which indicates whether the shear deformation reaches to the extent that the rotation resistance between warp and weft yarns is no longer small compared to the tensile modulus of the material. Figure 3.2-13 shows the calculation flowchart of this model in FEM software. From this flowchart it can be seen that warp and weft directions for each element are calculated from deformation gradient tensor. If the angle between warp and weft yarns are smaller than the shear locking angle, small shear modulus condition will hold, and total stress in the element will be updated via Equations (3.2-6) to (3.2-14). If the angle between warp and weft yarns reaches the shear locking one, resistance for further shear deformation will greatly increase because contacted fiber yarns stiffen the woven structure. In this situation, the "Yarn stretch caused stress" will still be calculated via Equations (3.2-6) to (3.2-8), while the shear components of the "Yarn rotation caused stress" will be derived with the Equation (3.2-15) in incremental form as:

$$d\sigma_{XY}^{m} = d\sigma_{YX}^{m} = E \cdot d\varepsilon_{XY} \quad (3.2\text{-}15)$$

where E is the stable transverse compression modulus of the yarns, and $d\varepsilon_{XY}$ is the shear strain increment after shear locking.

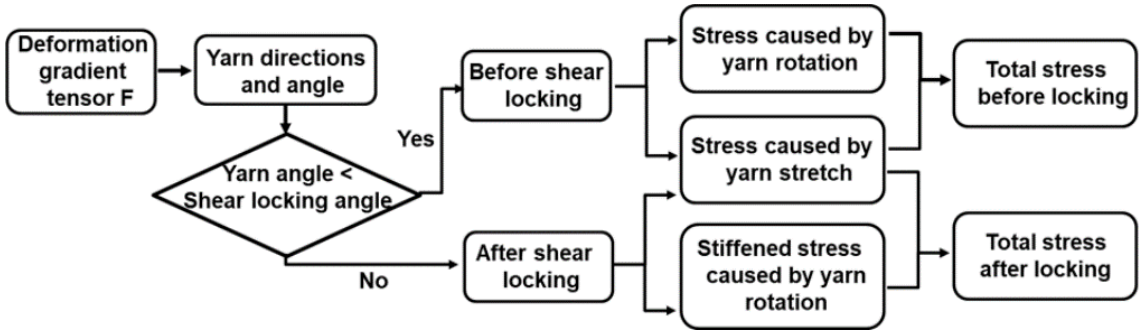

Figure 3.2-13. Calculation flowchart of the LS-DYNA MAT_293.

Material characterization is essential for FEM models. The calibration can be performed directly by the uniaxial tension and bias-extension experiments. The out-of-plane behaviors of the uncured prepreg, are characterized by the single layer bending and double layer interaction tests.

When the material model and the experimental input are prepared, double-dome benchmark tests are conducted and simulated to validate the capability of the material model for a 3D shape forming,

considering different yarn orientations and stacking sequences. These validation results indicate that this non-orthogonal model can partly reach the 15% error target for fiber orientation prediction. Details of this part-level validation will be elaborated in Section 3.2.7.

3) Mesoscopic RVE model for uncured prepreg

Mesoscopic RVE modeling and virtual material characterization requires building of an RVE finite element model, calibration of mesoscopic yarn properties, and generating a prepreg constitutive law as a function of strain. To build the mesh of a prepreg RVE with a fine balance between speed and accuracy, a novel 2-step geometrical modeling method was developed in this project. In this method, the rough composite structure without yarn-to-yarn penetration is first generated by TexGen in Step 1 with the specified woven pattern and key characteristic sizes, such as weaving pattern, yarn width, yarn gap, and yarn thickness, Figure 3.2-14 (a), Gaps, between yarns as demonstrated in Figure 3.2-14 (b), would be introduced in the meshes so generated. As a solution to close these gaps, the compression method is introduced in Step 2. To this end, two rigid plates are employed to compress the prepreg RVE in the thickness direction to reduce the thickness to the average value of the real material, as illustrated in Figure 3.2-14(c). The deformed mesh of step 2 will be used in RVE modeling.

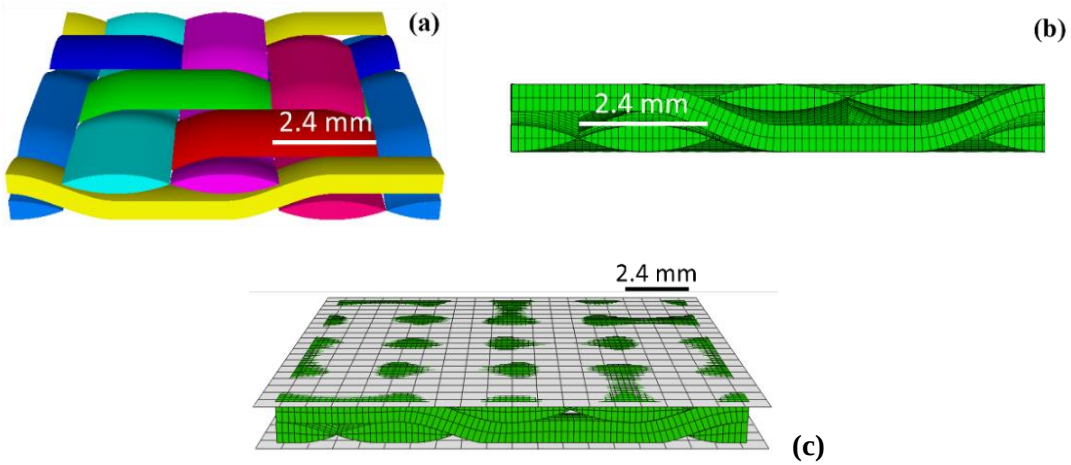

Figure 3.2-14. RVE mesh generation (prepregs with the thickness of 1.2 mm): (a) The structure, and (b) the cross-section of the corresponding mesh after step 1. (c) Adjust mesh thickness by FEA analysis of compression of the mesh using two rigid plates.

In addition to the RVE structure, the yarn material model should also be correctly established. Because preforming is a one-step loading process and material recovery after the deformation should be included, yarns within RVE models are assumed purely elastic. Prepreg yarns that consist of quasi-unidirectional fibers and uncured resin exhibit a transverse isotropy. Direct implementation of such material behavior, however, leads to numerical errors. One kind of error happens when compression load is applied along the width direction to a single yarn. This loading condition is common for prepregs in shear deformation where, as illustrated in Figure 3.2-15 (a), fibers rearrange as resin flows in real yarns. Consequently, the yarn deforms (i.e., its dimensions change) while preserving the basic elliptical shape. In finite element simulation, yarns are treated as continuum with relatively flat cross-section geometry. If the transversely isotropic material model is utilized, numerical errors such as artificial bending and excessive element distortion will appear especially on the edges, as illustrated in Figure 3.2-15 (b). To address this issue, the transverse shear and normal behaviors in the yarn material model are decoupled to control bending and

distortion of yarns while maintaining their compression property. With this approach, deformation similar to the real material can be achieved, as shown in Figure 3.2-15 (c).

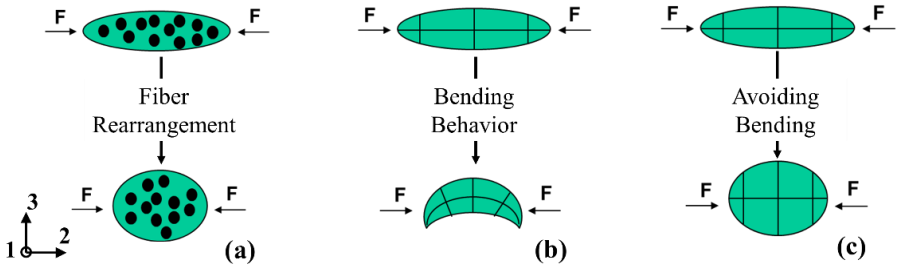

Figure 3.2-15. Illustration of the yarn cross-section deformation upon compression along the width direction: (a) Real material deformation mode, (b) FE deformation mode with transversely isotropic material model, and (c) FE deformation mode with decoupled material model in FE.

Based on the decoupling approach, the yarn is modeled using an anisotropic elastic constitutive law with distinct Young's and shear moduli in different directions. This constitutive law is defined in the co-rotational frame which is updated with the deformation gradient tensor to accurately trace the local fiber orientation upon large yarn deformation and rotation under the RVE deformation. In the prepreg yarns, the very stiff carbon fibers are aligned in the longitudinal direction along which the applied load is predominantly present. Meanwhile, the soft uncured resin governs the transverse deformation. Therefore, it is straightforward to decouple the yarn deformation in the longitudinal and transverse directions.

Once the structure and the material model of the RVE are generated, they are input into the finite element simulation given normal true strain along yarns, shear angle, and yarn properties. After simulation, the stress of each element is extracted and averaged to obtain the stress response of the RVE. Mechanical properties of mesoscopic yarns including elastic moduli, Poisson's ratios, and friction coefficient are difficult to directly characterize because of small sizes, single yarn specimen preparation, and soft resin. As a result, the unknown material properties are manually adjusted at this stage and the stress prediction from the RVE is compared to the experimental data. One of the best example comparisons is illustrated in Figure 3.2-16. The RVE result agrees very well with the experimental one when the shear angle is less than 0.6 radian, validating the 2-step approach developed. When the shear angle further increases, the discrepancy between the simulation and the experiment becomes large, indicating the necessities for calibration.

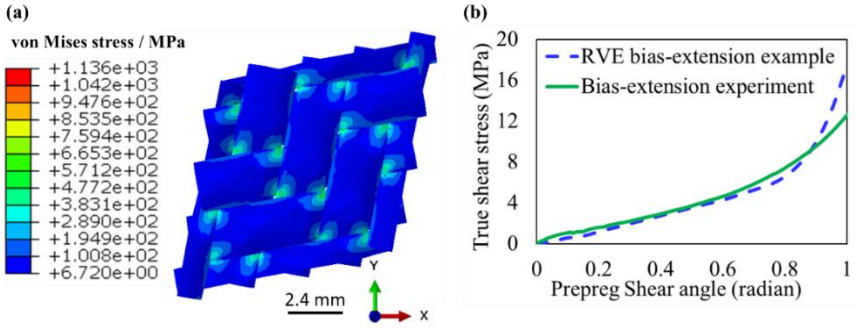

Figure 3.2-16. One bias-extension RVE simulation example: (a) Illustration of the von Mises stress contour on the RVE; (b) Comparison of the simulation and experimental true shear stress.

4) Multiscale uncured prepreg preforming model with Bayesian calibration

Using RVE directly in the preforming simulation is computationally expensive. RVE is used to obtain the material parameters, the prepreg yarn properties, for non-orthogonal model. Bayesian calibration is applied in the process. Uniaxial tension and bias-extension data is employed to: (1) estimate calibration parameters of the RVE model; (2) determine whether the RVE simulator is biased; and (3) build a cheap-to-evaluate emulator to replace the expensive RVE simulation in macroscale analyses. To this end, a modularized version of the Bayesian calibration framework of Kennedy and O'Hagan (KOH) [4] is adopted. The goal of Bayesian calibration is to combine three data sources (experiments, simulations, and prior knowledge from experience in the field) to estimate the unknowns. As illustrated in Figure 3.2-17, where x represents strain and θ represents yarn properties, this process starts by replacing expensive mesoscopic RVE simulation with a GP emulator (metamodel) η(x, θ) in Module 1. Then, uniaxial tension experimental data and prior knowledge on mesoscopic yarn properties p(θ) are used to fit the GP emulator δ(x) to the bias function in Module 2. Our reason for introducing δ(x) is that even if true calibration parameters were known (which they are not) and used in simulation, the stress predictions from the RVE model might not match with the experiments. In Module 3, joint posterior distribution of the mesoscopic yarn properties p(θ|d) are obtained given d, i.e., collection of the results from experiments and simulation. Finally, in Module 4, the updated emulator is compared against the bias-extension experimental data for validation. Once validated, the updated emulator, as virtually characterized constitutive law, is utilized to predict the stress response of the RVE under any strain state.

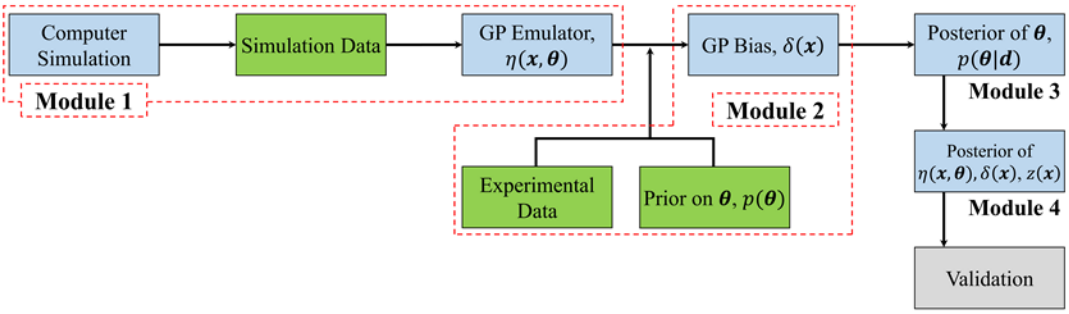

Figure 3.2-17. Modular Bayesian calibration: The approach has four stages and enables estimating the potential simulator bias as well as the joint posterior distribution of the calibration parameters.

Figure 3.2-18 illustrates the predictions of the orthogonal stress components by the updated emulator under various deformation states. Normal stress σ_{11} is plotted against normal true strain along warp and weft yarns, ε'_{11} and ε'_{22}, for two different values of γ'_{12} in Figure 3.2-18 (a). Similarly, shear stress σ_{12} is plotted in Figure 3.2-18 (b) where its symmetry with respect to ε'_{11} and ε'_{22} is evident. Compared to σ_{12}, σ_{11} is less sensitive to γ'_{12}. It can also be observed that σ_{12} monotonically increases as any of the strain components increase. This monotonic behavior is also observed in Figure 3.2-18 (a) but is slightly compromised when there is no shear strain (i.e., in the red surface). This small inconsistency may be due to (1) dynamic explicit numerical issues such as the artificially high strain rate to reduce the run-time in the RVE simulation, and (2) lack of simulation data with very small γ'_{12}, resulting in extrapolation during the Bayesian calibration. In Figure 3.2-18 (c), uniaxial tension experimental and predicted results are plotted. Since this test was used for calibration, the predictions are expected to match the experiments. In Figure 3.2-18 (d) bias extension experimental and predicted results are plotted. Since this data are not used in calibration, this figure illustrates that the calibration has been effective in learning the stress-strain behavior. The posterior of the resulting GP model can now be used as the constitutive law of integration points in the macroscopic preforming simulations.

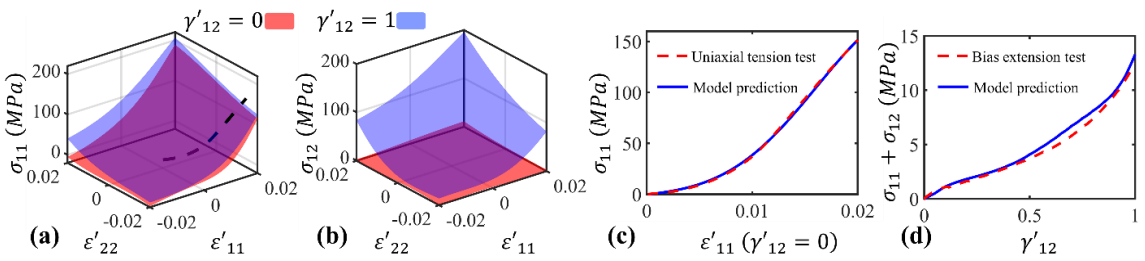

Figure 3.2-18. Posterior mean of the responses: (a) Normal stress as a function of normal true strain along the yarns for two different shear angles. (b) Shear stress as a function of normal true strain along the yarns for two different fabric shear angles. (c) Uniaxial tension test used in calibration vs. our predictions. (d) Bias extension test which is not used in calibration vs. our predictions.

The mesoscopic stress emulator is implemented into the developed non-orthogonal material model to form a multiscale simulation approach. This emulator is learned at mesoscale and acts as the non-orthogonal material constitutive law by replacing the expensive mesoscale RVE finite element simulation at each integration point in macroscale preforming analysis. For the macroscopic constitutive law in this multiscale approach, deformation input consists of normal true strain ε'_{11} and ε'_{22} along warp and weft yarn directions, and shear angle γ'_{12}. These inputs are all calculated using the non-orthogonal coordinate algorithm. The predicted stress components are obtained in orthogonal material coordinate directly. Hence, the constitutive law does not require coordinate transformation of stress. It should be noted that the prepreg stress emulator is learned over the range of $\varepsilon'_{11} \in [-2, 2]$ %, $\varepsilon'_{22} \in [-2,2]$ %, and $\gamma'_{12} \in [0, 1]$ radian. For the deformation states outside these ranges, the prepreg will transfer into shear locking state, and the finite element simulation employs the shear locking state algorithm in the non-orthogonal model.

When the multiscale preforming simulation method is established, double-dome benchmark tests are conducted and modeled to validate the capability of the multiscale method for 3D shape forming considering different yarn orientations and stacking sequences. This validation result reveals that this multiscale method leads to a slight improvement regarding the prediction of part geometry and fiber angle distribution, with an average of 4.0% error for fiber orientation prediction, which achieves the proposal target. Moreover, the forming force prediction accuracy of this multiscale method sees a significant increase of over 26% compared to the experiment-based non-orthogonal model and it agrees very well with the experimental results.

The flowchart of the approach discussed above is illustrated in Figure 3.2-19.

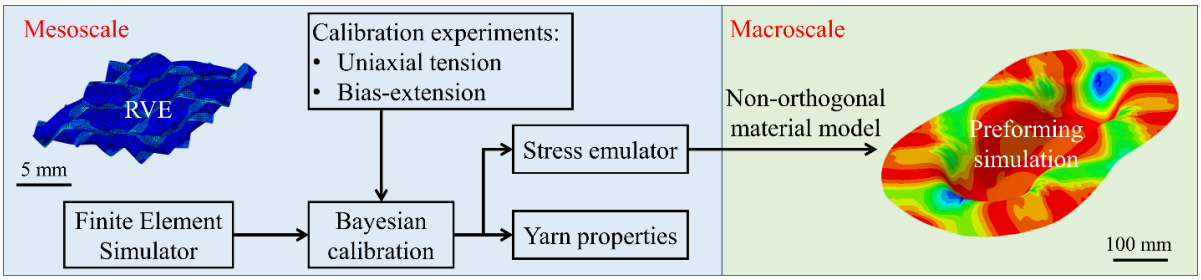

Figure 3.2-19. Flowchart of the developed multiscale preforming simulation method: The Bayesian calibration utilizes the RVE and experiments to obtain the yarn properties and the mesoscale stress

emulator. The stress emulator is then implemented into the non-orthogonal material model for macroscopic preformation simulation.

3.2.2.2 Compression molding simulation for chopped SMC CFRP

While polymer reinforced continuous carbon fiber composite shows great performance as has been reported widely, significant material cost and limited formability hesitate their application in automobile industry. Alternatively, chopped carbon fiber composites produced via SMC compression molding approach present a more balanced solution with lower cost and better formability and thus have gained increasing interest in recent years. However, due to the random fiber distribution in the SMC chopped carbon fiber composites, remarkable inhomogeneity and anisotropy are commonly observed which pose challenges to the design of parts using such type of material. Moreover, these material behaviors are closely related to the processing conditions during compression molding process and thus are also sensitive to variations during molding, which amplifies the difficulty in predicting the material properties in the molded parts. Traditional trial-and-error practices during part design are therefore inevitably accompanied with large testing matrix to consider all the factors that can lead to the various part performance, which is obviously cost inefficient. ICME approaches, aiming at replacing unnecessary tests with simulations to reach an optimal design, are therefore favored during the development of the SMC chopped carbon fiber composites.

The role of this subtask in the ICME workflow is shown in Figure 3.2-20. As one of the key enablers in the ICME workflow, compression molding simulation for SMC CFRP parts provides essential microstructure information to be fed into the downstream modeling workflow. With the tools developed in this subtask, the impact of the manufacturing process to the distribution of local material properties can be considered.

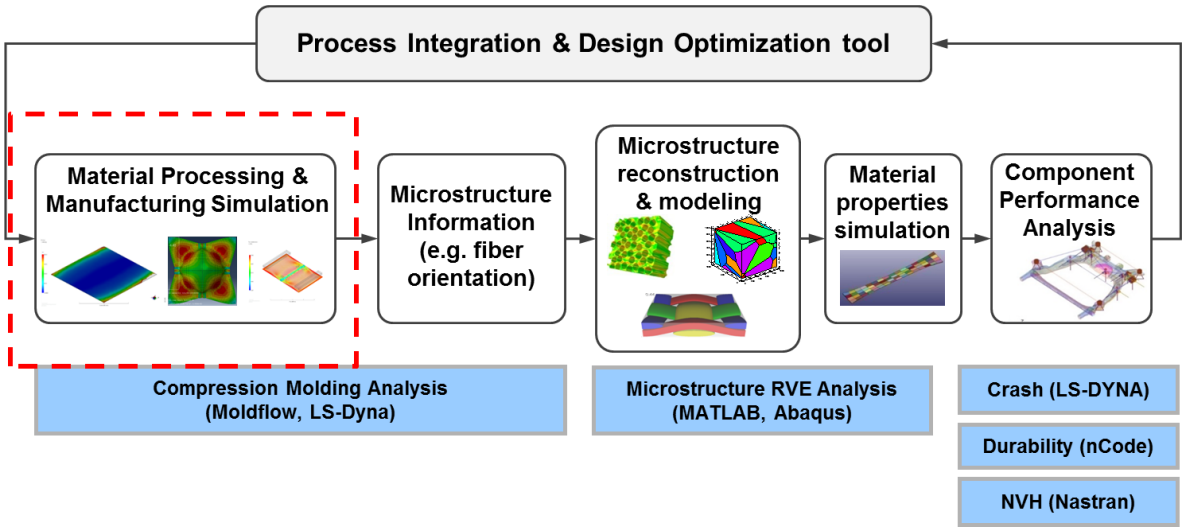

Figure 3.2-20. The role of the SMC compression molding simulation modeling in the ICME workflow.

Hereafter the procedure of setting up SMC compression molding simulation in Moldflow is introduced. Several improvements to the default modeling procedure based on the findings in the experiments are then discussed. The testing results to validate the compression molding simulation models are shown in Section 3.2.7.2. It is also found that some special steps are required when configuring the simulation in Moldflow for SMC parts with complex geometry. These steps are discussed with the SMC subframe as the demonstrative example.

1) SMC compression molding process in Moldflow

The schematic of SMC compression molding process is depicted in Figure 3.2-21. The carbon fiber chips are chopped from continuous tows and mixed with resin to fabricate the initial charge. Before the molding, the initial charges are trimmed and heated. As the charge become paste-like solid, it is placed in the designed locations in the heated mold. The paste-like charge is squeezed to fill the cavity after contacts with the hydraulic press. Crosslink of the resin happens as under the pressure and temperature and finally the part is solidified. The fiber orientation of the chips is usually random in the initial charge. The material flow during the compression molding then changes the fiber orientation, which leads to heterogeneous and anisotropic mechanical properties of the molded part.

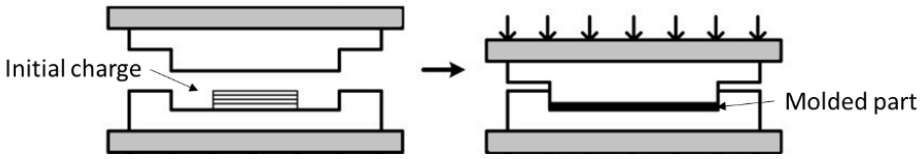

Figure 3.2-21. Schematic of SMC compression molding process.

Reactive compression molding modulus in Autodesk Moldflow was developed to simulate the compression molding process for SMC. The input to the compression molding simulation includes:

1. CAD geometry of the part and initial charge
2. Characterization data of the initial charge, e.g., reactive viscosity, curing kinetics, thermal properties and parameters for fiber orientation model.
3. Manufacturing processing conditions, e.g., mold temperature, press force/speed profile etc.

With the provided input, the manufacturing process can be simulated. The fiber orientation tensor, as a key output to the downstream ICME models is also obtained.

2) Improved modeling procedure

While this modeling module was well developed in commercial software, the application of this modeling on CF SMC composites is not fully validated. While performing the simulation following the conventional procedure, several issues are identified:

Excessive element distortion is observed on tested double-dome model meshed using the default meshing algorithm in Moldflow, as shown in Figure 3.2-22 (a) and 3.2-22 (b). The issue is reported to Moldflow team and an improved meshing algorithm is developed to generate mesh with better quality. As shown in Figure 3.2-22 (c), the nodes along thickness direction is better aligned and uniformly distributed along thickness direction. The predicted filling pattern of the double-dome model (Figure 3.2-22 (d)) shows reasonable results.

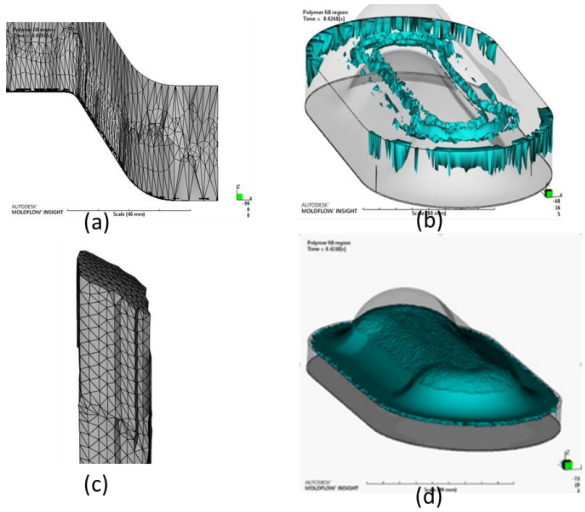

Figure 3.2-22. Mesh and results using old meshing algorithm in Moldflow are shown in (a) and (b). Better quality mesh (c) is obtained with the improved meshing algorithm in Moldflow, which leads to reasonable simulated filling pattern (d).

It is also found that characterized material data from material supplier shows unphysical filling pattern if directly used in Moldflow simulation. As depicted in Figure 3.2-23, plaque is fully filled under a given processing condition in molding trials. However, by using the default parameters from the material supplier, Moldflow predicts obvious short fill. In addition, the characterized viscosity from different sources on the same initial charge sample shows large deviation. Therefore, a calibration is performed to obtain a new set of viscosity parameters based on the characterization data from the material supplier. As shown in Figure 3.2-23 (c), the filling pattern is correctly predicted. Additional validation on the press force prediction to verify the calibration is shown in Section 3.2.7. However, it is noted that to date the characterization of reactive viscosity for SMC CFRP with high fiber content is still challenging. The standardized tesing procedure is not suitable as the diameter of disk in rheometer is close to the dimension of the fiber chips in the initial charge, which may lead to questionable testing results. The issue of viscosity characterization for SMC CFRP should be studied in depth in the future work.

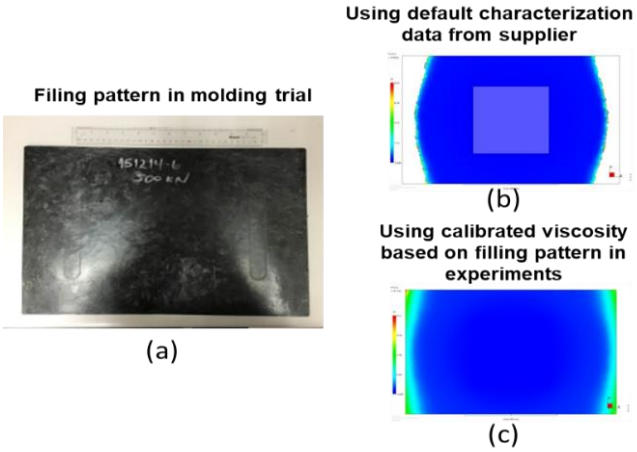

Figure 3.2-23. The fully filled plaque is shown in (a). Following the same processing condition, the predicted filling pattern in Moldflow is shown in (b) and (c), using default and calibrated viscosity, respectively.

Another improvement is the fiber orientation model for SMC CFRP. In old version of Moldflow, the default Folgar-Tucker model predicts obvious skin-core distribution for the fiber orientation tensor along thickness for SMC, which contradicts with experiments. To reflect the slowed flow dynamics for SMC, the reduced strain closure (RSC) model is recommended by Moldflow team. Following a series of trial-and-error procedure, the Ci parameter from RSC is determined as 0.08 for the SMC material in this project, which provides reasonably well prediction for the in-plane fiber orientation tensor component. However, it is further found that due to the isotropic diffusion term in RSC, the out-of-plane fiber orientation tensor component is always over-predicted. Since the part thickness is usually much smaller than the length of fiber chips in SMC, the out-of-plane component should be negligible. This issue is fixed by using a latest fiber orientation model, i.e., Moldflow rotational diffusion (MRD) model. It is found that with the default D1, D2 and D3 values in MRD model and the calibrated Ci parameter, the out-of-plane fiber orientation tensor component is constrained to a reasonable value while in-plane component is close to the measured data. It is further suggested a procedure should be developed to standardize the calibration of Ci for SMC material which is within our scope of future work.

The modeling practice is also improved for definition of initial value of fiber orientation tensor data. Prior version of Moldflow cannot consider the rotation of fiber orientation due to the initial deformation of initial charge. This has to be manually fixed by the user. The issue is brought to Moldflow team and an improvement is implemented in the latest release of Moldflow, in which the solver can handle such rotation before the flow solver takes over.

3) Compression molding simulation of the subframe part

The developed modeling procedure for flat plaques can be mostly followed when simulating a complex part. However, some minor modifications are required, especially for geometry and meshing, since modeling this complex part geometry with many ribs and steep wall features is found to be challenging in Moldflow in terms of mesh qualities. To solve this problem, the meshing procedure is improved by integrating the HyperMesh and Moldflow to ensure the part is meshed correctly. The CAD file containing the 2D surfaces enclosing the volume of the SMC subframe part is imported into Hypermesh. Minor modifications on the CAD will be applied in case there are any errors on the features in the CAD. The 2D automeshing function in HyperMesh is then applied to generate the triangular

elements with acceptable quality for these surfaces. The mesh is exported from using a Nastran mesh file which is also readable in Moldflow. Once the mesh is imported into Moldlfow, automesher is utilized to generate layered tetra elements that are refined enough for the SMC compression molding simulation. Creation of the initial charge elements is also achieved in the similar manner. The part and initial charge elements are finally combined in Moldflow and other parameters of the model, including processing conditions, material properties and fiber orientation model, can then be assigned. This modeling process combines the advantages of HyperMesh on 2D meshing and Moldflow on 3D layered tetra meshing and proves to be effective when dealing with such complex part geometry. Following this procedure, Moldflow models of the upper and the lower half component in the subframe part are generated. The model and fiber orientation prediction of the compression molding simulation of subframe upper half is shown in Figure 3.2-24 (a) and 3.2-24 (b), respectively. As the initial charge covers most area of the part, the flow length is limited and thus the fiber orientation is close to 2D isotropic random distribution in most of the part. There are some small regions with slightly aligned fiber orientation, for example, the positions marked in Figure 3.2-24 (b), where the preferential fiber orientation is along X axis. While the modeling procedure is functioning well, it is found that considerable computational cost is generated for the complex model with around 6.5 million tetra elements. This results in tremendous computational cost.

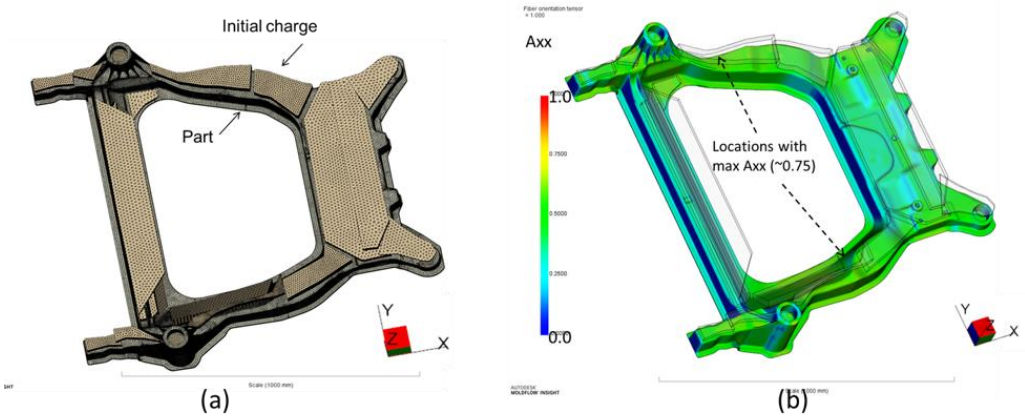

Figure 3.2-24. (a)The Moldflow model of SMC subframe upper shell and (b) fiber orientation prediction.

References

[1] P. Xue, X. Peng, J. Cao, 'A non-orthogonal constitutive model for characterizing woven composites. Composites Part A', Applied Science and Manufacturing, 2003. 34(2): p. 183-193.

[2] W. Zhang, H. Ren, B. Liang, D. Zeng, X. Su, J. Dahl, M. Mirdamadi, Q. Zhao, J. Cao, 'A non-orthogonal material model of woven composites in the preforming process', CIRP Annals, 2017. 66(1): p. 257-260.

[3] Open source software: TexGen, http://texgen.sourceforge.net/index.php/Main_Page

[4] M. Kennedy and A. O'Hagan, 'Bayesian calibration of computer models', J.R. Statist., Soc. B , 63, Part 3, pp. 425-464, 2001.

3.2.3 Mechanistic Continuum Models for CFRP

CFRP composites, including UD, woven and chopped fiber SMC, have orientation dependent material properties. To study the mechanical behavior of CFRP materials, it is necessary to model their actual microstructure for analyzing the performance of the cured CFRP. The focus of this subtask is to generate

mechanistic constitutive models with results from manufacturing process simulations as the input. The multiscale RVE approach will be used. RVE models will be developed to generate the stress-strain responses for a number of stress states from which it is possible to develop a yield surface and a failure envelope for the composites. Numerical tests were conducted to validate the predicted material properties. In addition, a concurrent multiscale modeling method based on a reduced order modeling approach on RVE model has been established to obtain efficient part-level performance prediction.

3.2.3.1 Multiscale RVE model development

The present goal of RVE modeling is to develop a complete modeling workflow that allows users to reconstruct UD, woven and chopped fiber SMC microstructures, generate finite element mesh and predict material properties. The microstructure information, such as UD fiber volume fraction, woven yarn angle, etc. can be assigned by the users. The finite element mesh can be used to perform traction free loadings in three normal directions and three shear directions. The effective stress and strain results from all six loadings will be used to compute the material engineering constants. The present process provides direct numerical homogenization of CFRP's material properties.

In the ICME process, a bottom-up multiscale modeling approach is adopted. As shown in Figure 3.2-25, it is convenient to use a three-scale model to describe a cured CFRP part: UD in microscale, woven and SMC in mesoscale, and part in macroscale. The RVE models for UD, woven and SMC are built in order to evaluate their mechanical properties, such as stiffness tensors. The information obtained at lower scales can then be used in higher scales. For example, fiber tow in the woven and SMC RVE can be treated as having the same properties of UD RVE. Therefore, the UD RVE can also be used to compute fiber tow properties that are used in evaluating woven and SMC RVE's mechanical properties. Therefore, UD RVE modeling is introduced first.

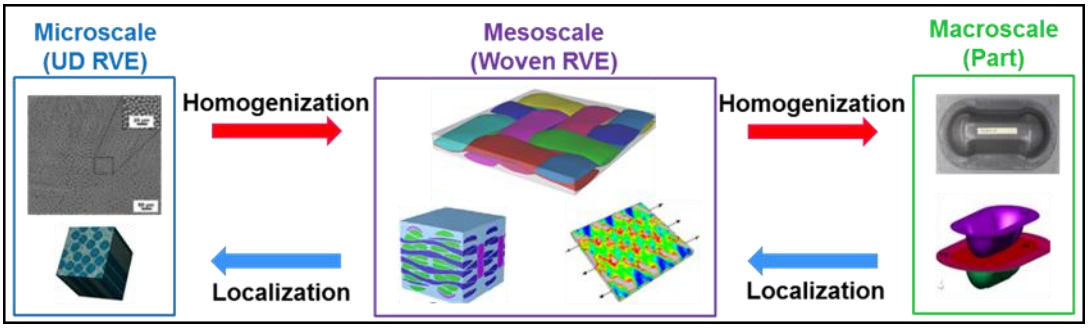

Figure 3.2-25. Schematic of Different Scales in CFRP.

Moreover, the UD RVE can be applied into a recently proposed Reduced Order Modeling (ROM) method, namely Self-consistent Clustering Analysis (SCA). SCA allows one to compress UD RVE from many voxel elements into a ROM database made with several clusters. The ROM of the UD can be solved using the SCA method, hereafter called "UDSCA", to compute elasto-plastic responses of UD in an efficient manner. UDSCA not only provides an efficient way to compute mechanical responses (elastic and plastic) of UD, but also links UD microstructure to UD part performance. A concurrent multiscale modeling framework is established for UD material for the first time and it can be used for structural property prediction.

The RVE modeling of CFRP materials is split into three parts: 1) UD CFRP modeling; 2) Woven CFRP modeling and 3) SMC CFRP modeling

3.2.3.2 RVE modeling for UD CFRP

The properties of CFRP composites is anisotropic and microstructure dependent. Therefore, accurate capture of CFRP's mechanical properties, such as stiffness tensor, requires 1) reconstruction of the microstructure; and 2) accurate numerical modeling. For UD CFRP, its stiffness can be simplified as the volumetric average by the rule of mixture. It is possible to estimate the UD stiffness by using either Voigt average or Reuss average, but the accuracy is questionable since Voigt average gives the upper limit while Reuss average gives the lower limit. In addition, it is also proposed the modeling of UD CFRP by assuming a well-structured and periodic packing pattern of fibers, such as hexagonal packing, and model UD CFRP by Representative Unit Cells (RUC). RUC provides easy modeling of UD CFRP since it only models the minimum repeating unit in UD CFRP and it allows different packing patterns and fiber volume fractions. RUC can be easily modeled in finite element mesh and allows one to compute effective UD elastic properties without dealing with algebra, compared to the analytical homogenization approach. Unfortunately, in real UD CFRP product, carbon fibers are of a random distribution. Therefore, the RUC model might not provide accurate information about the UD's properties. In order to include realistic microstructure, a better modeling technique is identified and implemented in this project.

1) RVE mesh generation

The UD RVE model developed in this project captures the random distribution of fibers in the matrix material. Building a UD RVE allows one to consider arbitrary fiber distribution and fiber shapes.

By adopting an algorithm proposed by Melro et al. [1], we generate the cross-section microstructure of RVE model with cylindrical fibers randomly distributed in the matrix. In addition to the fiber and matrix phase, the RVE model also includes a finite thickness (~200 nm) interphase region adjacent to the fibers. This interphase region is used to capture the unique properties of the transition zone between the carbon fiber and resin matrix. The interphase properties are characterized from MDA analysis in Section 3.2.1. A zero-thickness interface between fiber and interphase region is also considered to capture the realistic failure strength and debonding failure mechanism by inserting cohesive elements, as shown in Figure 3.2-26. The fiber volume fraction within the RVE is about 51%, which is the same as the experimental sample tested in this project.

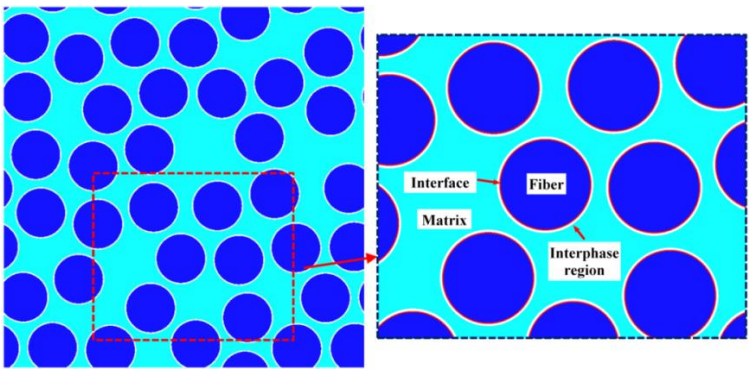

Figure 3.2-26. Schematic cross-section view of the microstructure of UD CFRP composites used in the RVE model.

In this study, we limit our RVE size to include around 50 fibers, and this size was reported to be sufficient to capture the essential micro-scale features with minimal computational cost. Apart from the selection of the RVE size, the applied boundary conditions play a key role on the assessment of homogenized properties. One should notice that RVE size and boundary conditions are actually closely related, the invariance to the boundary condition is considered as the indicator for the sufficiency of the RVE size. There are four common types of boundary conditions that have been widely used in study: (1) homogeneous displacement boundary conditions (KUBC) or isostrain (Hill-Reuss): the displacement is imposed at point belonging to the boundary (SUBC) or isostress (Hill-Voigt); (2) homogeneous traction boundary conditions: the traction vector is prescribed at the boundary; (3) mixed uniform boundary conditions (MUBC) or uniform displacement-traction boundary conditions; (4) periodic boundary condition (PBC). The classical approach to introduce PBC in a RVE is by means of the definition of constraint equations (*EQUATION in ABAQUS) between periodic nodes, hence imposing constrains to their allowed displacements. In its essence, this method requires the mesh to be periodic, in such a way that every node on each RVE boundary has its homologous node on the respective opposite boundary. The traditional PBC approach is well appropriate for standard and implicit integration numerical schemes, but exhibits several drawbacks when explicit dynamic time integration is used. It is observed that the relationships between master and slave displacement is translated into equations that introduce intense high-frequency oscillations in the system that compromise the numerical solution. Moreover, the method with traditional PBC is computationally expensive.

2) Constitutive and damage model of constituents

In the RVE model, carbon fibers are assumed to be transversally isotropic linearly elastic. The values of the five independent material constants that characterize the DOW AKSACA carbon fibers are listed in Table 3.2-2 from the material sheet. The UD composite studied in this project has a fiber volume fraction of 51% with an average fiber diameter of 7 μm.

Table 3.2-2 Carbon fiber material properties.

E11 (GPa)	E22=E33(GPa)	G12=G13(GPa)	G23(GPa)	v12
245.0	19.8	29.2	5.9	0.28

The epoxy is modeled with an isotropic elasto-plastic solid with an isotropic damage law proposed by Melro et al. [1]. Since such material exhibits a yield behavior that is sensitive to hydrostatic stress, the paraboloidal yield criterion [2] is more suitable for polymeric matrix, which considers the non-isotropic tensile-compressive yield behaviors with a non-associative flow rule:

$$f\left(\sigma,\sigma_{Y_C},\sigma_{Y_T}\right)=6J_2+2\left(\sigma_{C}-\sigma_{T}\right)I_1-2\sigma_{C}\sigma_{T} \tag{3.2-16}$$

where J_2 is the second invariant of deviatoric stress tensor, I_1 is the first invariant of the stress tensor. σ_T and σ_c denote the tensile and compressive yielding stress, respectively.

The non-associative flow rule is introduced to correct the volumetric deformation in plasticity:

$$g=\sigma_{vm}^2+\alpha p^2 \tag{3.2-17}$$

where $\sigma_{vm}=\sqrt{3J_2}$ is the von Mises equivalent stress, $P=1/3\ I_1$ is the hydrostatic pressure, and α is the material parameter to correct the volumetric component of the plastic flow:

$$\alpha=\frac{9}{2}\frac{1-2\nu_p}{1+\nu_p} \tag{3.2-18}$$

In order to mitigate the mesh dependency due to material softening, the damage evolution law is implemented with a characteristic element length derived from Bažant crack band theory. A thermodynamically consistent isotropic damage model is adopted, in which the damage activation function is similar to the paraboloidal yield criterion but with the yield strengths replaced by the failure strengths:

$$\frac{3\tilde{J}_2}{\sigma_{ft}\sigma_{fc}}+\frac{\tilde{I}_1\left(\sigma_{fc}-\sigma_{ft}\right)}{\sigma_{ft}\sigma_{fc}}-1=0 \tag{3.2-19}$$

where σ_{fc} and σ_{ft} represent the compressive and tensile strengths of the matrix, while the invariants $\tilde{J}_2$ and $\tilde{I}_1$ are determined using the undamaged stiffness tensor.

The exponential damage evolution law is given in the Equation (3.2-20):

$$d_m=1-\frac{e^{A_m\left(3-\sqrt{7+2r_m^2}\right)}}{\sqrt{7+2r_m^2}-2} \tag{3.2-20}$$

where A_m is the parameter responsible for energy release rate, correlated with the characteristic element size, and r_m is the damage internal variable.

3) Matrix constitutive behavior validation

The matrix adopted in this study is developed by Dow Chemical. Table 3.2-3 summarizes the basic epoxy properties obtained through experimental characterization; E_m and v_m are Young's modulus and

Poisson's ratio, v_p is the plastic Poisson's ratio. G_{IC} is the Mode I fracture toughness. These properties serve as the basic parameters for the elasto-plastic damage model, and an ABAQUS user subroutine (VUMAT) has been developed to implement the matrix model.

Table 3.2-3 Material properties of epoxy.

Linear	E_m		v_m	v_p
elasticity	3.73±0.30 GPa		0.38±0.01	0.3
Damage	σ_{ft}	σ_{fc}	G_{IC}	
model	61.6±4.6 MPa	300±30.6 MPa	334.1±73 J/m^2	

The epoxy properties have been calibrated and validated by computational analysis compared with experimental characterization under different loading modes: tension, compression and torsion, as shown in Figure 3.2-27. For the tension case, using single element is sufficient to calibrate the tensile parameters, as shown in Figure 3.2-27 (a). The elastic modulus and strength match very well between computation and experiments as they are the basic input for the computational model. For the compression case, a symmetrical one-quarter model of the specimen size is adopted to simulate the compressive behavior of epoxy since the single element cannot capture the microscopic behavior, as shown in Figure 3.2-27 (b). The results show that not only the elastic property and strength are perfectly captured, also the general elastic-yielding-strain hardening shape is well preserved using the matrix model. Furthermore, the current matrix model validates the shear modulus and post-elastic behavior of epoxy resin compared with the torsion experiment (Figure 3.2-27 (c)), although the basic parameters in our matrix model are from tension and compression tests, as illustrated in Table 3.2-3. In the torsion simulation, the CAE result agrees well with the experiment, meaning the calibration from the tension and compression is reliable. Thus, the matrix model proposed here is sufficient to describe the matrix constitutive behavior under different loading conditions. The calibrated and validated matrix model is then introduced to the composite RVE model to predict the material failure mechanism at UD CFRP composites level.

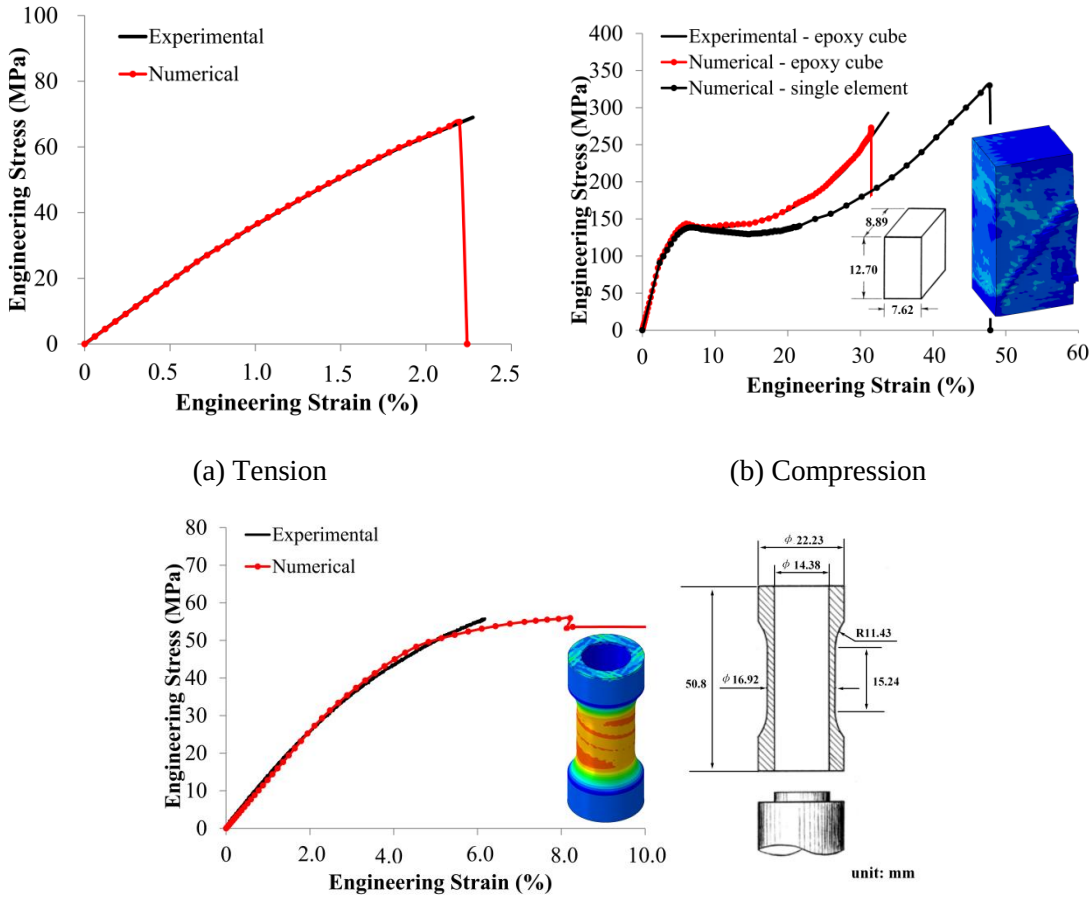

Figure 3.2-27. Comparison of epoxy stress-strain curves between CAE and experiments.

4) Cohesive elements for interface between the fiber and matrix/interphase region

Interfacial debonding is considered in the simulation by using cohesive elements at the interface, with the constitutive response defined by a bilinear mixed-mode softening law. Damage onset is predicted by means of a quadratic interaction criterion that is a function of the interface strength for each of the damage modes. Once debonding is initiated, the cohesive tractions transferred through the interface decrease linearly to zero. This is based on the energy-based Benzeggath-Kenane (BK) damage propagation criterion that accounts for the dependence of the fracture energy dissipation on mixed-mode fracture. The interfacial fracture strength and energy have been calibrated based on a reverse engineering method according to experimental tests [3]. The calibrated and validated cohesive parameters are also listed in Table 3.2-4.

Table 3.2-4 Interface properties.

Interface Properties		Value
Interfacial maximum strengths	τ_1	70 (MPa)
	$\tau_2=\tau_3$	80 (MPa)
Interfacial fracture energy	G_{IC}	0.002 (N/mm)
	$G_{IIC}= G_{IIIC}$	0.032(N/mm)

5) Results and discussions

i) Prediction in elastic properties

In order to obtain the whole elastic property of UD CFRP composites, 6 different loading cases are simulated, as shown in Figure 3.2-28, which includes 3 tension modes and 3 shear modes. In the tension loading modes, a displacement is added to the loading surfaces and the other faces are fixed rather than free. Since the current problem is only about elastic property, a relative small strain (here is 0.0004) is applied. A comparison between experiment as well as RVE simulation results and rule of mixtures shows a good accuracy of current method, as shown in Figure 3.2-29 and Table 3.2-5. The results predicted by rule of mixture shows good agreement with experiment data in fiber direction, but underpredict the properties in the transverse direction.

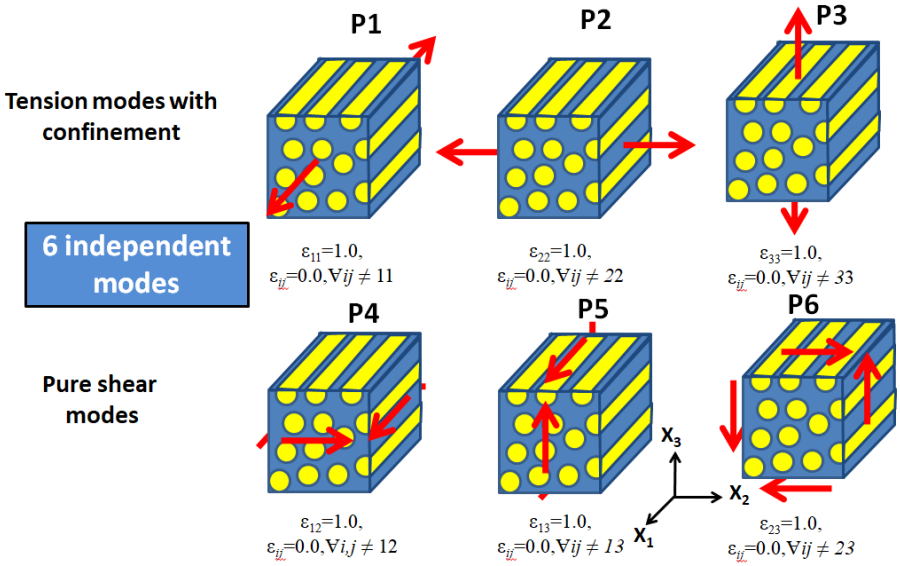

Figure 3.2-28. Six loading modes for UD RVE elastic property calculation.

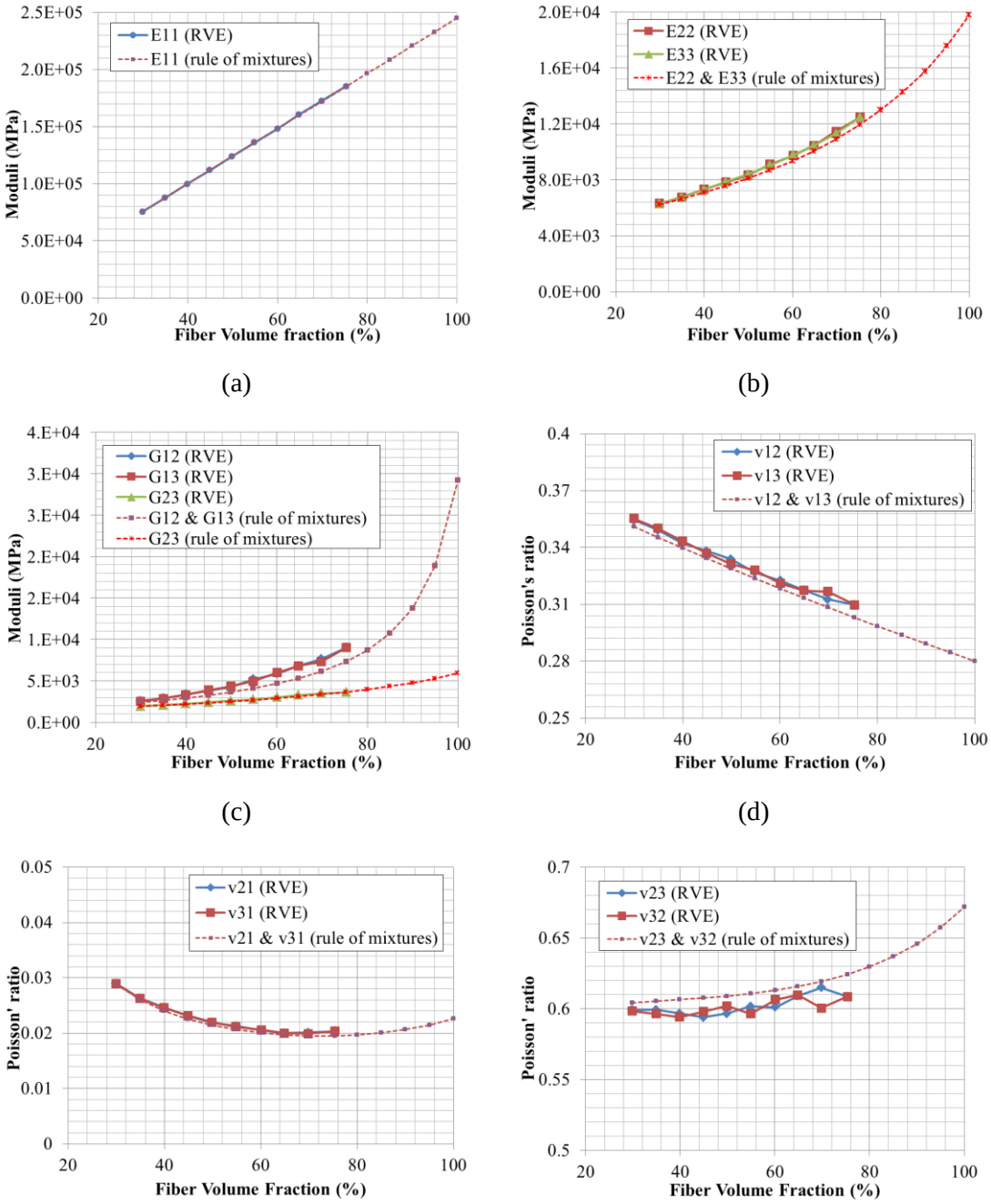

Figure 3.2-29. Comparison between rule of mixtures and RVE predictions.

Table 3.2-5. Comparison among experiment results, RVE predictions and rule of mixtures.

	E11(GPa)	E22 (GPa)	E33(GPa)	G12 (GPa)	G13 (GPa)	G23 (GPa)
Experiment	125.26	8.89	8.89	4.85	4.85	
RVE	127.81	8.57	8.58	4.58	4.54	2.66
Rule of mixtures	127.79	8.26	8.26	3.78	3.78	2.57

	v12	v21	v13	v31	v23	V32
Experiment	0.33	0.02	0.33	0.02		
RVE	0.33	0.02	0.33	0.02	0.60	0.60
Rule of mixtures	0.33	0.02	0.33	0.02	0.61	0.61

ii) Failure analysis under various loading conditions: Transverse tension

The computational model has the advantage of clearly revealing the damage initiation and evolution process of UD CFRP composites. Under the transverse tension, interfacial debonding first occurs at the poles of the closely neighboring fibers where the stress concentration in fiber/interphase region are higher, which can be seen more clearly by a partial enlarged drawing of cohesive element, as shown in Figure 3.2-30 (a). After that, bands of interfacial cracks develop perpendicular to the loading direction. Within these bands of interfacial cracks, the matrix and interphase region are subject to plastic deformation, which further results in the coalescence of neighboring interfacial cracks, as shown in Figure 3.2-30 (b) and (c). Finally, interfacial cracks and interphase region failure at different locations are connected by matrix cracks through the entire RVE, causing the ultimate fracture of the RVE perpendicular to the loading axis, as illustrated in Figure 3.2-30 (d).

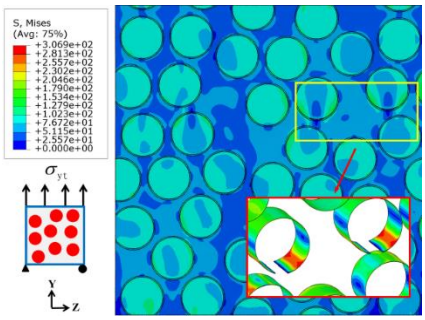

(a) Initial interface debonding ε=0.83%.

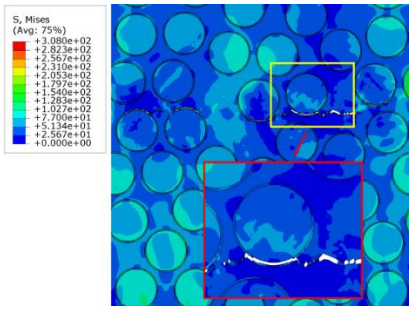

(b) Plastic damage of Interphase region and matrix happen at the vicinity of the interfacial cracks, ε=0.86%

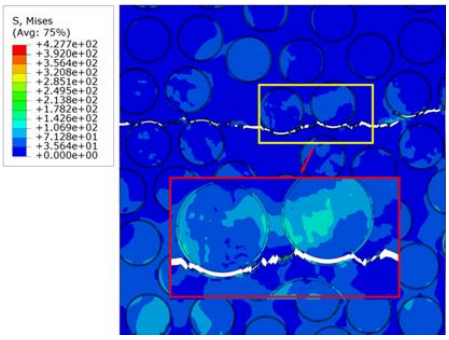

(c) Interfacial debonding and interphase matrix damage at different locations are connected by matrix cracks throughout the RVE, ε=0.90%.

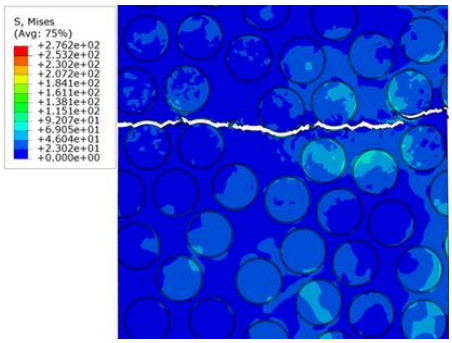

(d) The ultimate failure perpendicular to the loading axis, ε=0.92%.

Figure 3.2-30. Damage initiation and evolution under transverse tension loading.

iii) Failure analysis under various loading conditions: longitudinal compression

Failure analysis in fiber longitudinal direction needs to consider local fiber waviness, which is characterized in an interval between $x_1 \leq x \leq x_2$ in the longitudinal direction located in the middle of the 3D RVE model, as shown in Figure 3.2-31 (a). The total length of the 3D RVE model is $L_T = 700\ um$. We use half of the wavelength of a cosine wave to represent the fiber waviness, and the wavelength (L=1000 *um*) is estimated by evaluating the experimental sample, which is assumed to be constant for all the fibers in the computational micromechanics RVE model. Different maximum waviness angles (θ_{max}) can be achieved by changing the wave amplitudes (A). Figure 3.2-31 (a) shows the imperfection area and the parameters for the local fiber waviness.

The waviness function of the bottom boundary is given by:

$$y = \begin{cases} 0 & 0 \leq x < x_1 \\ A\cos(2\pi x/L) & x_1 \leq x \leq x_2 \\ A & x_2 < x \leq L_T \end{cases} \qquad (3.2\text{-}21)$$

The initial misalignment is geometrically introduced according to the derivation of y(x),

$$tan\theta(x) = -\frac{2\pi A}{L}\sin(2\pi x/L) \qquad (3.2\text{-}22)$$

The computational micromechanics model is able to capture the formation of the kink-band as well as some relevant post peak-load features. As shown in Figure 3.2-31 (b), the fiber rotation angle (α) and band width (W) can be identified in the model. The predicted values α≈21.5°and W≈187.2 um are in good agreement with experimental results. A parametric study relating the material properties and θmax is conducted using our computational model. Figure 3.2-31 (c) shows the comparison between the experimental results and the predictions on the stress-strain curves as a function of θmax. In the same figure, we also show the compressive test results of multiple specimens which exhibit variant Young's modulus and strength values. The waviness at θmax=5.38° causes approximately 15% reduction in Young's modulus (Ec1) compared with that of a UD CRFP composite with straightly-aligned fibers (E1). Compressive strength is even more sensitive to fiber waviness than the Young's modulus. For θmax=5.38°, the compressive strength decreases by approximately 70%. Our computational results corroborate the variations observed in experimental test results. They also suggest that the fiber waviness in specimens is below the waviness scale in θmax=1.80°, as the Young's modulus and strength obtained from θmax=1.80° case is below all the experimental test results. Table 3.2-6 summarized the simulate results for different θmax.

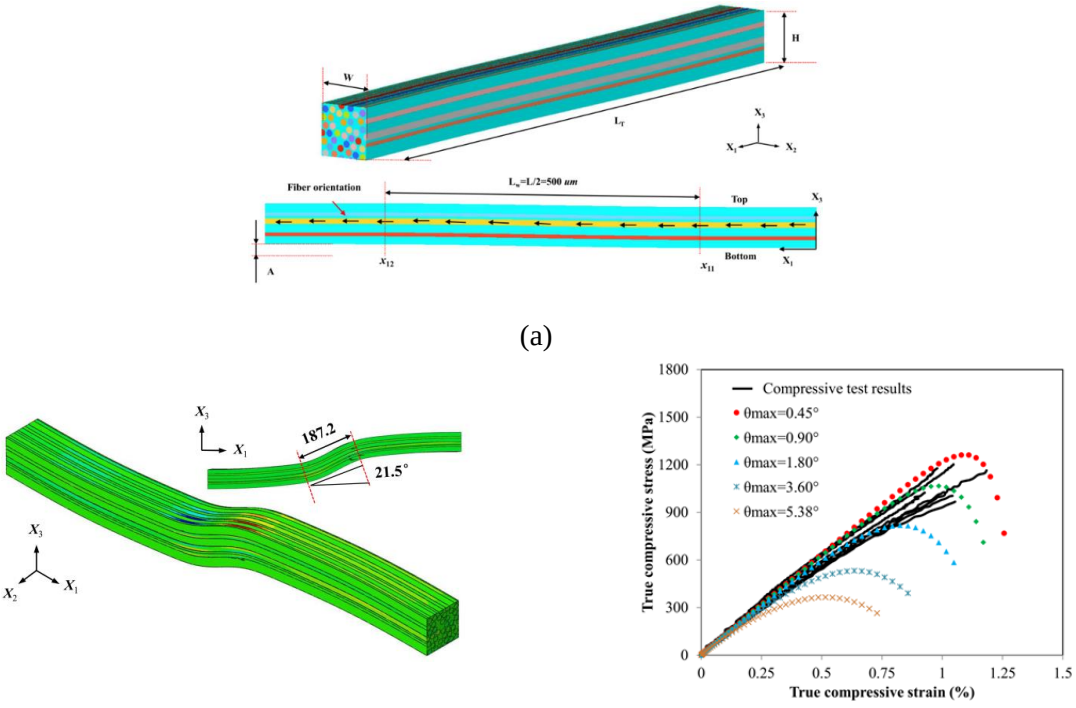

(a)

(b)

(c)

Figure 3.2-31. (a) The local fiber waviness applied in the computational model (L_W=L/2=500 *um*, L_T=700 *um*). (b) The simulation result of king-band of UD CFRP composite under uniaxial compressive loading. (c) Comparison between the predictions of computational results (discrete points) and the experiments (solid lines) on the stress-strain curves.

Table 3.2-6. Summary the simulate results for different θ_{max}.

θ_{max}	E_{C1}	E_{C1}/E_1	Strength (*MPa*)	*W*(*um*)	α (°)
0°	127.90	1.0000			
0.45°	127.28	0.9952	1261.45	191.2	21.3
0.90°	126.93	0.9924	1066.26	187.2	21.5
1.80°	125.13	0.9783	818.81	193.7	20.8
3.60°	118.75	0.9284	531.98	187.7	20.9
5.38°	108.49	0.8482	365.58	190.2	21.3

3.2.3.3. RVE modeling for woven CFRP

For woven composites, the RVE model allows one to capture a larger region with multiple fiber tows in warp and weft directions, and an accurate prediction of woven mechanical performance can be made. In addition, woven RVE enables to quantitatively study the composite architecture variations such as fiber volume fraction, fiber misalignment in fiber tow effect on the material properties.

The woven RVE generation utilized TexGen, an open source software that allows one to build a textile structure at any given pattern and fiber tow (or yarn) geometry. The woven CFRP studied in this project is made of twill pattern. The minimum repeating unit of the twill woven consists of four warp and four weft fiber yarns. The woven RVE generated is shown in Figure 3.2-32, where the woven RVE is discretized by voxel elements with a resolution of 210 by 210 by 20. warp yarn is in the 2 direction and weft yarn is in the 1 direction.

Once the mesh of woven RVE is generated, it can be used in FE software to perform numerical homogenization to obtain its elastic material constants. Here, the matrix material has the same material properties as in UD composites. Fiber yarn property is obtained from UD RVE with 65% fiber volume fraction.

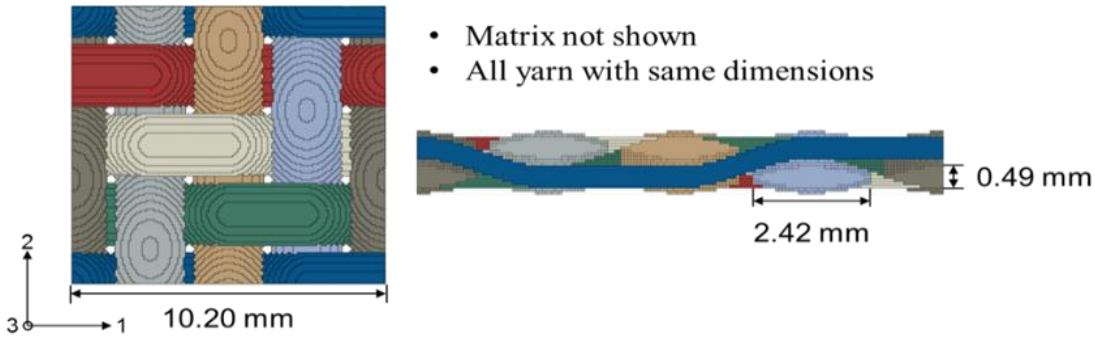

Figure 3.2-32. Woven RVE Geometry.

The computed effective elastic properties of woven RVE are listed in Table 3.2-7 below. All predictions met with the proposed 10% difference compared with the experimental data.

Table 3.2-7. Woven elastic moduli from woven RVE and experimental data.

	E11	**G12**	**G23**
Woven RVE	59.96 GPa	5.68 GPa	3.60 GPa
Experimental Data	65.95 GPa	5.18 GPa	3.49 GPa
Difference, %	9.08	9.65	3.15

The advantage of using a woven RVE numerical model is that various microstructures can be addressed in the RVE model and quantitative analyses can be done to understand the effect of those variations. The woven RVE model are used to examine the effect of three woven microstructure variations as shown in Figure 3.2-33: 1) yarn angle; 2) yarn fiber volume fraction; 3) yarn local fiber misalignment.

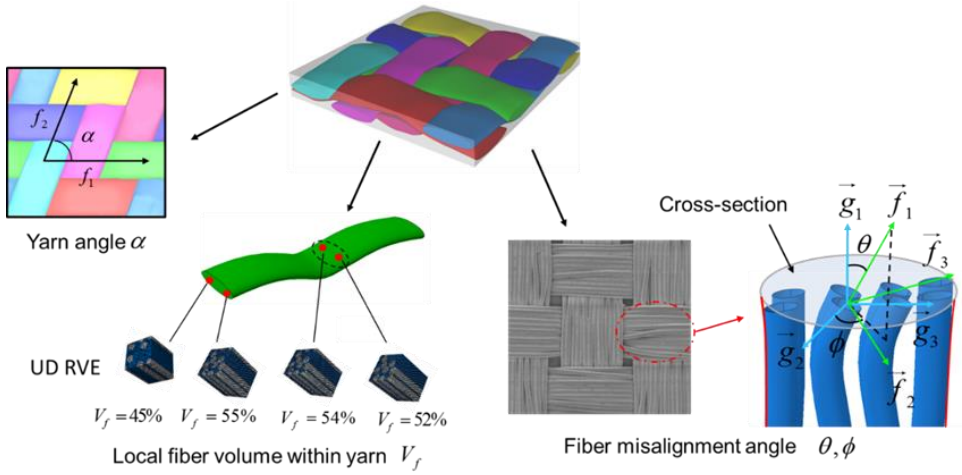

Figure 3.2-33. Illustration of yarn angle, yarn fiber volume fraction, and fiber misalignment in yarn.

The effect of yarn angle is studied by constructing woven RVEs with various yarn angle α shown in Figure 3.2-34. The stiffness matrices of each woven RVE realization are computed and all components are plotted in Figure 3.2-34. The results show that the yarn angle has the most significant effects on C_{11}, C_{22}, C_{44}, and C_{24}. As the yarn angle decreases, warp yarns will gradually lean to 1 direction and C_{22} direction reduces significantly. However, C_{11} remains constant until the yarn angle is less than 60˚. This means that the interaction between warp and weft yarns is not significant when the yarn angle is larger than 60˚. C_{44} tends to increase as yarn angle decreases, this means the woven in-plane stiffness at a smaller yarn angle will be stronger than that at a larger yarn angle. The concave shape of C_{24} reveals the shear-tension coupling effect, where the in-plane shear strain will contribute to stress in 22 direction when yarn angle is not 90°. All those observations reaffirm the importance of woven yarn angle for an accurate capture of the mechanical properties of woven RVE.

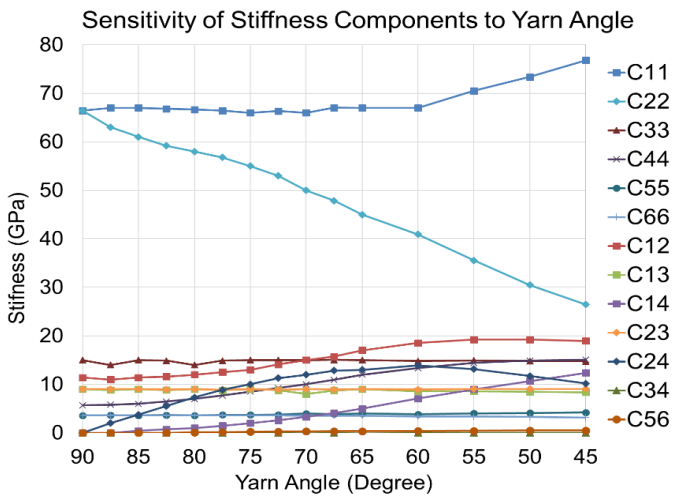

Figure 3.2-34. Effect of yarn angle on components of woven stiffness matrix.

Besides yarn angle, yarn fiber volume fraction, denoted as V_f, and yarn fiber misalignment effects are also investigated. The results obtained in Table 3.2-7 does not consider uncertainty, meaning the yarn material is homogenous, which is usually not the case for real material manufactured due to manufacturing process variations. As shown in Figure 3.2-33, each yarn in the woven RVE is made with multiple voxel elements, where each voxel element contains one integration point, representing one UD RVE. Therefore, by varying fiber volume fraction at each voxel element, inhomogeneity can be added to the yarn. By assuming fiber volume fraction on each yarn is following a Gaussian distribution, it is possible to assign different UD properties in different voxel elements to simulation different V_f in the yarn. The effect of V_f is summarized in Table 3.2-8, where V_f is following a Gaussian distribution with mean $\bar{V}_f$ = 65% and variance $\boldsymbol{\sigma^2_{V_f}}$ = 0.09%. It can be concluded that the effect of $\boldsymbol{\sigma^2_{V_f}}$ = 0.09% does not affect woven property significantly, primarily depending on its mean value.

Table 3.2-8. Effect of yarn fiber volume fraction on homogenized material properties.

	E_{11} (GPa)	**E_{22} (GPa)**	**E_{33} (GPa)**	**G_{12} (GPa)**	**G_{13} (GPa)**	**G_{23} (GPa)**
V_f = 65%	59.96	59.96	12.57	5.68	3.60	3.60
$\bar{V}_f$ = 65%, $\sigma^2_{V_f}$ = 0.09%	59.96	59.94	12.60	5.66	3.58	3.58
Percentage Difference (%)	0.0011	0.0218	0.2128	0.4066	0.4436	0.4425

Moreover, each voxel element contains a local material orientation that aligns with the yarn center line for homogeneous material. Fiber misalignment is considered as the deviation from perfect alignment direction. Shown in Figure 3.2-33, vector $\vec{g}_1$ represents the irection of perfect fiber direction, which is essentially the tangent line of yarn center line. Plane $\vec{g}_2\vec{g}_3$ is the yarn cross-section and $\vec{g}_1$ is orthogonal to the plane.

Angle θ ($0^o \le \theta \le 90^o$) and Φ ($-180^o \le \Phi \le 180^o$) are used to establish misaligned fiber direction, $\vec{f}_1$. $\vec{f}_1$, $\vec{f}_2$, and $\vec{f}_3$ represent transverse isotropic material frame accounting for fiber misalignment. Equations for calculating $\vec{f}_1$, $\vec{f}_2$, and $\vec{f}_3$ given as below:

$$\vec{f}_1 = \frac{\vec{g}_2}{\|\vec{g}_2\|}\sin\theta\cos\Phi + \frac{\vec{g}_3}{\|\vec{g}_3\|}\sin\theta\sin\Phi + \frac{\vec{g}_1}{\|\vec{g}_1\|}\cos\theta$$
$$\vec{f}_2 = \frac{\vec{g}_2}{\|\vec{g}_2\|}\cos\theta\cos\Phi + \frac{\vec{g}_3}{\|\vec{g}_3\|}\cos\theta\sin\Phi - \frac{\vec{g}_1}{\|\vec{g}_1\|}\sin\theta \qquad (3.2\text{-}23)$$
$$\vec{f}_3 = \vec{f}_1 \times \vec{f}_2$$

For fiber misalignment, θ and Φ follow Gaussian distribution by letting mean $\bar{\theta} = 10°$, variance $\sigma_\theta^2 = 2$, mean $\bar{\Phi} = 0°$, and variance $\sigma_\Phi^2 = 2500°^2$ (to make sure for all element within the yarn, its Φ will fall between -180º and 180º following three sigma rule). The effect of fiber misalignment is summarized in Table 3.2-9, where a significant impact of yarn misalignment on woven properties is observed.

Table 3.2-9. Effect of Fiber Misalignment on homogenized material properties.

	E_{11} (GPa)	E_{22} (GPa)	E_{33} (GPa)	G_{12} (GPa)	G_{13} (GPa)	G_{23} (GPa)
No-Misalignment	59.96	59.96	12.57	5.68	3.60	3.60
$\bar{\theta} = 10°$, $\sigma_\theta^2 = 2$ $\bar{\Phi} = 0°$,$\sigma_\Phi^2 = 2500$	48.01	47.14	12.42	6.15	3.67	3.68
Percentage Difference (%)	24.89	27.19	1.17	7.69	1.88	2.15

3.2.3.4 RVE modeling for SMC CFRP

As shown in Figure 3.2-35, compression molded CF SMC composites have complex microstructure. Observing from the in-plane direction, fiber chips of different sizes are stochastically distributed in the resin matrix. Observing from the through-thickness direction, a layered structure is formed by stacks of fiber chips. The material flow during the compression molding process results in a spatially variant chip orientation distribution in the molded structure. The chip orientation distribution is the most important statistical characteristic of the microstructure, which has a strong influence on both elastic properties and failure strengths. Thus, the proposed framework (Figure 3.2-36) is based on the 3D SMC meso RVE model. It has two new features. First, a conforming mesh-based chip packing algorithm is proposed to reconstruct densely-packed SMC microstructure of prescribed chip orientation distribution. The reconstructed microstructure is converted into a conforming mesh to provide the geometry information for failure analysis. Second, a new material model of fiber chip is proposed and implemented together with the material models of matrix and interface to provide the material property information for failure analysis. The inputs of the framework include the morphology of the fiber chip, fiber chip volume fraction, chip orientation tensor, and the properties of each constituent (fiber chip, matrix and interface) depicted by different material models. Via the multiscale material modeling using finite element RVE

models, the stress-strain curves and the failure process of the SMC can be predicted. The predicted failure modes and failure strength are validated by the experimental data, including microscopic images and the stress-strain curves from the uniaxial tensile tests. Following are the details about this development.

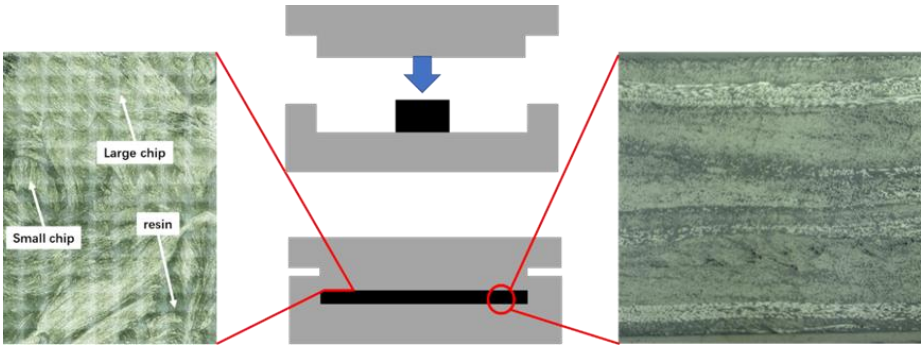

Figure 3.2-35. Microscopic images of chopped carbon fiber SMC mesostructure. Left: in-plane direction; Right: through-thickness direction.

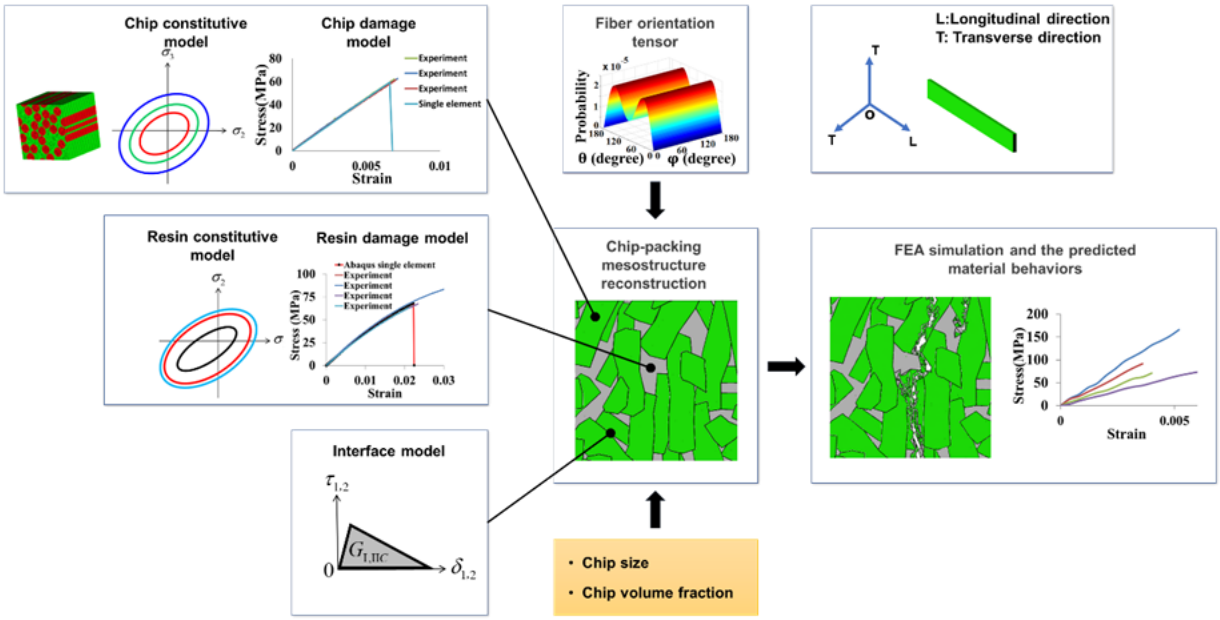

Figure 3.2-36. Computational framework for the failure analysis of chopped CF SMC composites.

1) Conforming mesh-based chip packing reconstruction method

A conforming mesh-based chip packing reconstruction algorithm is proposed in this study. The orientation tensor definition proposed by Advani and Tucker [4] is followed to seamlessly connect with the output of compression molding simulation in Autodesk Moldflow. The probability distribution function (PDF) $\psi(\mathbf{p})$ of the fiber chip orientation is recovered from the input chip orientation tensor:

$$\psi(\mathbf{p}) = \frac{1}{4\pi} + \frac{15}{8\pi} b_{ij} f_{ij}(\mathbf{p}) + \frac{315}{32\pi} b_{ijkl} f_{ijkl}(\mathbf{p}) + \dots \tag{3.2-24}$$

where $\mathbf{p}$ is the unit vector, which describes the direction of a fiber chip; b_{ij},b_{ijkl} are the deviatoric chip orientation tensors, and f_{ij}, f_{ijkl} are tensor basis functions of $\mathbf{p}$:

$$b_{ij} = A_{ij} - \frac{1}{3}\delta_{ij} \tag{3.2-25}$$

$$\delta_{ij} = \begin{cases} 0, & i \neq j \\ 1, & i = j \end{cases} \tag{3.2-26}$$

$$\begin{aligned} b_{ijkl} = A_{ijkl} &- \frac{1}{7}(\delta_{ij}A_{kl} + \delta_{ik}A_{jl} + \delta_{il}A_{jk} + \delta_{jk}A_{il} + \delta_{jl}A_{ik} + \delta_{kl}A_{ij}) \\ &+ \frac{1}{35}(\delta_{ij}\delta_{kl} + \delta_{ik}\delta_{jl} + \delta_{il}\delta_{jk}) \end{aligned} \tag{3.2-27}$$

$$f_{ij}(\mathbf{p}) = p_i p_j - \frac{1}{3}\delta_{ij} \tag{3.2-28}$$

$$\begin{aligned} f_{ijkl}(\mathbf{p}) = p_i p_j p_k p_l &- \frac{1}{7}(\delta_{ij}p_k p_l + \delta_{ik}p_j p_l + \delta_{il}p_j p_k + \delta_{jk}p_i p_l + \delta_{jl}p_i p_k + \delta_{kl}p_i p_j) \\ &+ \frac{1}{35}(\delta_{ij}\delta_{kl} + \delta_{ik}\delta_{jl} + \delta_{il}\delta_{jk}) \end{aligned} \tag{3.2-29}$$

where p_i are the components of the unit vector $\mathbf{p}$; A_{ij} and A_{ijkl} are the second-order and fourth-order chip orientation tensors defined by:

$$A_{ij} = \oint p_i p_j \psi(\mathbf{p}) d\mathbf{p} \tag{3.2-30}$$

$$A_{ijkl} = \oint p_i p_j p_k p_l \psi(\mathbf{p}) d\mathbf{p} \tag{3.2-31}$$

The orientation of each chip is generated by sampling the recovered chip orientation PDF. For the compressed chopped fiber SMC, the fiber chips are usually in-plane orientated and thus the out-of-plane component of the fiber chip's orientation is negligible. Therefore, the chip orientation distribution of the SMC component can be described by a 2D chip orientation tensor for simplification. The relation between the principal and non-principal orientation matrix is expressed as:

$$a_{kl} = R_{ki}R_{lj}A_{ij} \tag{3.2-32}$$

where R_{ki} are the entries of the rotation matrix, a_{kl} are the entries of the principal orientation tensor matrix, and A_{ij} are the entries of the non-principal orientation tensor. According to the definition of A_{ij} and a_{11}:

$$A_{11} + A_{22} = a_{11} + a_{22} = 1 \tag{3.2-33}$$

Therefore, a 2D chip orientation tensor A_{ij} can be fully represented by a single parameter a_{11}.

Given the geometry and orientation information, the fiber chips are placed into the 3D space one-by-one, layer-by-layer using a modified chip packing algorithm (Figure 3.2-37). The orientation distribution of each layer is set as the PDF recovered from the target 2D orientation tensor. This algorithm consists of two steps. First, large chips are packed one-by-one into one layer of the RVE space until the fiber chip volume fraction is close to the target (5% lower than the target fiber volume fraction). During the packing process, a space finding algorithm is applied to find feasible packing locations, which allow no overlap or overlap between at most two chips. For the overlapped chips, the overhanging parts of the upper chip sink to the lower layer. The "overlap-and-sink" process creates bended geometries of the chips. Second, the small chips are randomly placed into the residue space in each layer. Adding chip fragments into RVE is a fine-tuning process, which guarantees the final reconstruction matching the target chip orientation tensor and the target volume fraction precisely. Finally, the reconstructed microstructure is converted into a conforming mesh for FEA. The in-plane view and cross-section view of RVE reconstructions of different chip orientation tensors (a_{11} =0.2, 0.3, 0.4, 0.5, 0.6) are plotted in Figure 3.2-38. When $a_{11} = 0.5$, the distribution of chip orientation is uniformly random in the 2D plane; when a_{11} is close to 0 or 1, the fiber chips are highly aligned to one direction.

The proposed conforming mesh-based reconstruction method has several advantages over the voxel-based algorithm. First, there is no artificial stress concentration at voxel corners/edges. Second, the fiber volume fraction and the chip orientation tensor of each layer match the target values precisely. Our previous voxel-based algorithm can only guarantee that the average fiber volume fraction and the average orientation distribution of all layers match the target values. A large variation is observed from layer to layer.

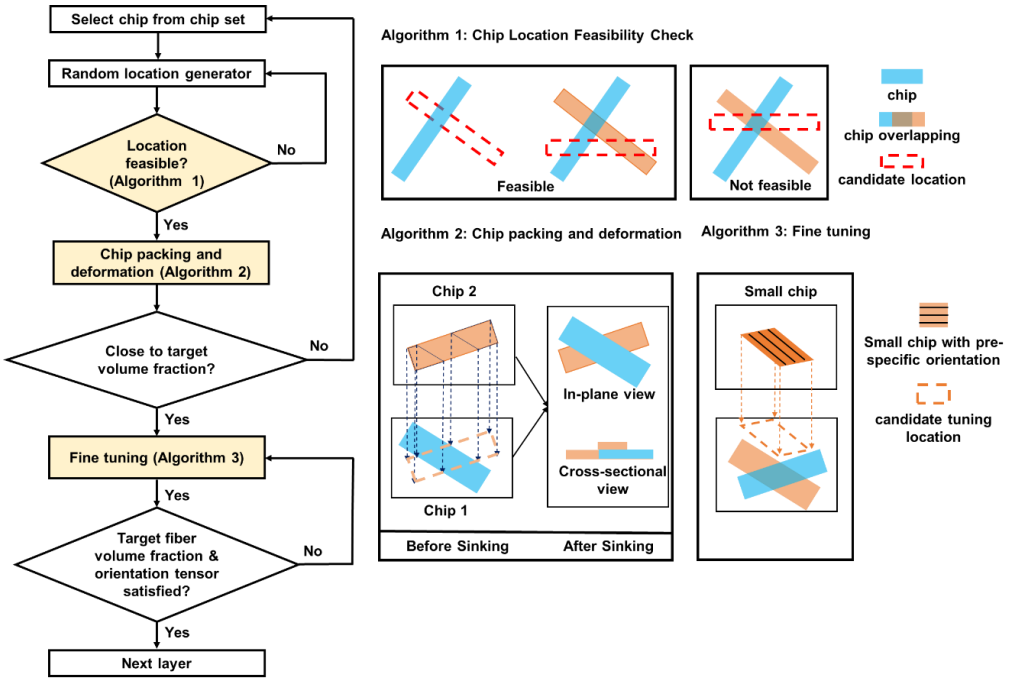

Figure 3.2-37. Flowchart of the modified chip packing algorithm

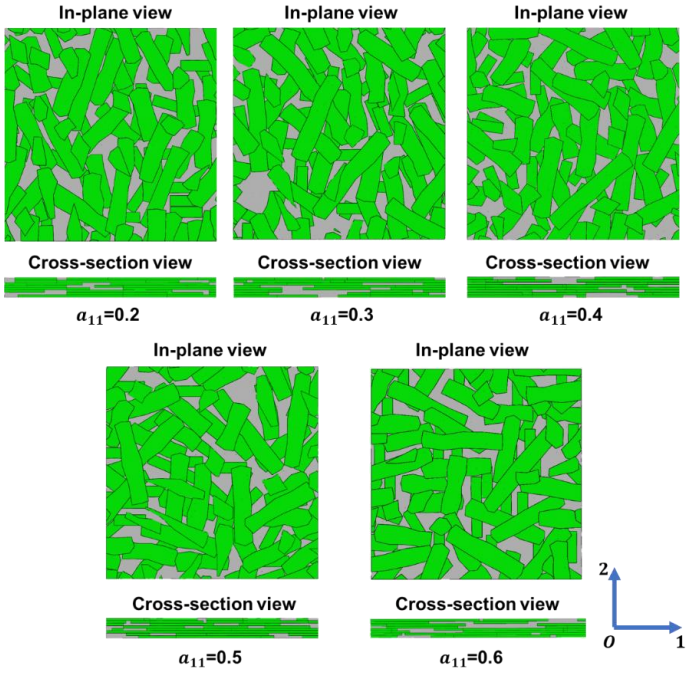

Figure 3.2-38. RVE reconstructions of different chip orientation tensor.

2) Material model development for fiber chip, matrix, and interface

In addition to the reconstructed SMC microstructure, material models of each constituent are required for FEA. The matrix constitutive model is established using the paraboloidal yield criterion and the isotropic damage model, which is the model applied in UD RVE. The material parameters of the epoxy

matrix are listed in Table 3.2-3. These parameters serve as the inputs of the elasto-plastic damage model, which is implemented as a VUMAT subroutine in ABAQUS.

For the carbon fiber chip, a new material model is proposed by combining the Liu-Huang-Stout yield criterion [5] and the Tsai-Wu failure criterion [6]. The interface between matrix and chip is modeled using cohesive element with a bilinear mixed-mode softening law.

i) Carbon fiber chip: elasto-plastic damage model

The fiber chip consists of epoxy and aligned fibers. In this study it is assumed that the fiber chips have similar mechanical behaviors as the unidirectional (UD) carbon fiber composites, or fiber yarns in woven composites. The material model of fiber chips should be able to describe the nonlinear behavior, as it is critical for the further prediction of the failure strength of SMC. However, the existing material models are not suitable for describing the nonlinear behaviors of the fiber chip under complex stress state. In this work, a new material model is proposed by combing the Liu-Huang-Stout yield criterion and the Tsai-Wu failure criterion.

The elasto-plastic behaviors of the fiber chip are described by the Liu-Huang-Stout yield criterion, which was developed to characterize the plastically orthotropic solids. The yield criterion is defined as follows:

$$\Phi_C^Y = \sqrt{F(\sigma_{22}-\sigma_{33})^2 + G(\sigma_{33}-\sigma_{11})^2 + H(\sigma_{11}-\sigma_{22})^2 + 2L\sigma_{23}^2 + 2M\sigma_{13}^2 + 2N\sigma_{12}^2} + I\sigma_{11} + J\sigma_{22} + K\sigma_{33} - 1 \tag{3.2-34}$$

where F, G, …, K are parameters characteristic of the current state of anisotropy. The subscript C denotes matrix. F, G, …, K are defined as follows:

$$F = \frac{1}{2}\left[2\left(\frac{\sigma_{C,Tc}+\sigma_{C,Tt}}{2\sigma_{C,Tc}\sigma_{C,Tt}}\right)^2 - \left(\frac{\sigma_{C,Lc}+\sigma_{C,Lt}}{2\sigma_{C,Lc}\sigma_{C,Lt}}\right)^2\right]; \quad G = H = \frac{1}{2}\left(\frac{\sigma_{C,Lc}+\sigma_{C,Lt}}{2\sigma_{C,Lc}\sigma_{C,Lt}}\right)^2;$$

$$I = \frac{\sigma_{C,Lc}-\sigma_{C,Lt}}{2\sigma_{C,Lc}\sigma_{C,Lt}};\ J = K = \frac{\sigma_{C,Tc}-\sigma_{C,Tt}}{2\sigma_{C,Tc}\sigma_{C,Tt}};\ L = \frac{1}{2\sigma_{C,s}^2};\ M = N = \frac{1}{2(\bar{\sigma}_{C,s})^2} \tag{3.2-35}$$

where $\sigma_{C,Lt}$ and $\sigma_{C,Lc}$ are the longitudinal tensile and compressive yield stresses; $\sigma_{C,Tt}$ and $\sigma_{C,Tc}$ are the transverse tensile and compressive yield stresses; $\bar{\sigma}_{C,s}$ is the in-plane shear yield stress; $\sigma_{C,s}$ is the out-of-plane shear yield stress.

An associative flow rule is adopted to describe the volumetric deformation of fiber chip in plasticity:

$$\dot{\varepsilon} = \dot{\gamma}\frac{\partial \Phi_C^Y}{\partial \sigma} \tag{3.2-36}$$

where $\dot{\gamma}$ represents the time derivative of the plastic multiplier. The Tsai-Wu failure criterion is used to model the damage of the fiber chip:

$$\Phi_C^d = F_{11}\sigma_{11}^2 + F_{22}(\sigma_{22}^2 + \sigma_{33}^2) + 2F_{12}\sigma_{11}(\sigma_{22} + \sigma_{33}) + 2F_{23}\sigma_{22}\sigma_{33} + \\ + F_1\sigma_{11} + F_2(\sigma_{22} + \sigma_{33}) + F_{44}\tau_{23}^2 + F_{66}(\tau_{13}^2 + \tau_{12}^2) - 1 \quad (3.2\text{-}37)$$

$$F_{11} = \frac{1}{\sigma_{C,fLt}\sigma_{C,fLc}}, F_{22} = \frac{1}{\sigma_{C,fTt}\sigma_{C,fTc}}, F_1 = \frac{1}{\sigma_{C,fLt}} - \frac{1}{\sigma_{C,fLc}}, F_2 = \frac{1}{\sigma_{C,fTt}} - \frac{1}{\sigma_{C,fTc}}$$
$$F_{44} = \frac{1}{(\sigma_{C,fs})^2}, \quad F_{66} = \frac{1}{(\bar{\sigma}_{C,fs})^2}, \quad F_{12} = -0.5\sqrt{F_{11}F_{22}}, \quad F_{23} = -0.5F_{22} \quad (3.2\text{-}38)$$

where $\sigma_{C,fLt}$ and $\sigma_{C,fLc}$ are the ultimate tensile and compressive strengths of fiber chip along the fiber direction; $\sigma_{C,fTt}$ and $\sigma_{C,fTc}$ are the ultimate tensile and compressive strengths of fiber chip along the transverse direction; $\bar{\sigma}_{C,fs}$ and $\sigma_{C,fs}$ are the in-plane and out-of-plane shear strengths of fiber chip. The values of these parameters are determined by testing UD composite samples of 51% fiber volume fraction (Table 3.2-10). $E_{C,L}$ is the Young's modulus along the fiber direction, $E_{C,T}$ is the Young's modulus transverse to the fiber direction, $G_{C,LT}$ is the in-plane shear modulus, $v_{C,LT}$ and $v_{C,TT}$ are the Poisson's ratios. The proposed material model is implemented as a VUMAT user subroutine in ABAQUS.

Table 3.2-10. The properties of the fiber chip.

Linear elasticity				Damage model			
$E_{C,L}$ (GPa)	125.9	$E_{C,T}$(GPa)	8.6	$\sigma_{C,fLt}$ (MPa)	2020	$\sigma_{C,fLc}$ (MPa)	1000
$G_{C,LT}$(GPa)	4.87	$v_{C,LT}$	0.32	$\sigma_{C,fTt}$ (MPa)	63.5	$\sigma_{C,fTc}$ (MPa)	175
$v_{C,TT}$	0.60			$\sigma_{C,fs}$ (MPa)	60	$\bar{\sigma}_{C,fs}$ (MPa)	82

In the SMC chopped fiber composites, a fiber chip is constrained by adjacent chips in the upper and lower layers. Therefore, the in-situ effect between chips also need to be considered in the model. The in-situ effect was firstly observed and studied in the multi-ply, laminated composites. If the plies in a 3-layer laminate have different chip orientations, the middle ply has a higher transverse tensile strength and a higher in-plain shear strength than an unconstrained ply. The in-situ transverse tensile and in-plane shear strength of the middle ply in a 0/90/0 laminate are given by [7]:

$$\sigma_{C,isTt} = \sqrt{\frac{8G_{IC}}{\pi t \Lambda_b^o}} \tag{3.2-39}$$

$$\bar{\sigma}_{C,fs} = \sqrt{\frac{8G_{C,LT}G_{IIC}}{\pi t}} \tag{3.2-40}$$

where G_{IC}, G_{IIC} are the fracture toughness (Table 2.3-14); t is the thickness of the fiber chip; Λ_b^o is defined as:

$$\Lambda_b^o = 2\left(\frac{1}{E_{C,T}} - \frac{v_{C,LT}^2}{E_{C,L}}\right) \tag{3.2-41}$$

For the middle ply in a 0/0/0 laminate, there is no in-situ effect. Due to the randomness in chip orientation, the in-situ effect is approximated by the average of the 0/90/0 in-situ strength and the original strengths (unconstraint chip, no in-situ effect).

ii) The constitutive model of interface

The chip-matrix interface and the chip-chip interface are modeled by cohesive elements of zero mesh thickness. The constitutive relation of the cohesive element is defined by a bilinear mixed-mode softening law, which includes damage initiation and damage propagation. Damage initiation is modeled by a quadratic interaction criterion [8]. Once the debond is initiated, the cohesive tractions decrease to zero linearly. Damage propagation is defined by the energy-based Benzeggath-Kenane (BK) criterion, which accounts for the dependence of the fracture energy dissipation on the mixed-mode fracture [9]. The interface properties are listed in Table 3.2-11. K represents the interfacial stiffness. G_{IC}, G_{IIC} and G_{IIIC} are the fracture toughness. τ_1, τ_2, τ_3 are the interfacial strengths of three different fracture modes.

Table 3.2-11. The interface properties

Interfacial properties			
K (N/mm^3)	5 x 10^4	τ_1 (MPa)	85
τ_2 (MPa)	150	τ_3 (MPa)	150
G_{IC} (N/mm)	0.536	G_{IIC} (N/mm)	0.913
G_{IIIC} (N/mm)	0.913		

3) Results and discussions

i) Predictions of elastic modulus

Virtual uniaxial tensile tests are conducted on the reconstructed RVE by FEA. The size of the RVE model is 50 mm × 50 mm × 0.8 mm. RVEs of different chip orientation tensors (a_{11}=0.2, 0.3, 0.4, 0.5, 0.6) are reconstructed to study the influence of chip orientation distribution on the stress-strain relation. For each orientation tensor, three RVE samples are reconstructed and simulated. Regarding the elastic modulus, a good agreement can be observed between the predictions and the reference data reported in our previous work. The reference data are generated from voxel RVE models, which are validated by

experiments as shown in Figure 3.2-39 (a). The average error over all the fiber orientations is less than 6% comparing to the mean modulus of experiment data.

The predicted stress-strain curves of five RVE models of different chip orientation tensors are plotted in Figure 3.2-39 (b). The predicted stress-strain relation is linear until failure occurs. It is consistent with the experimental observation.

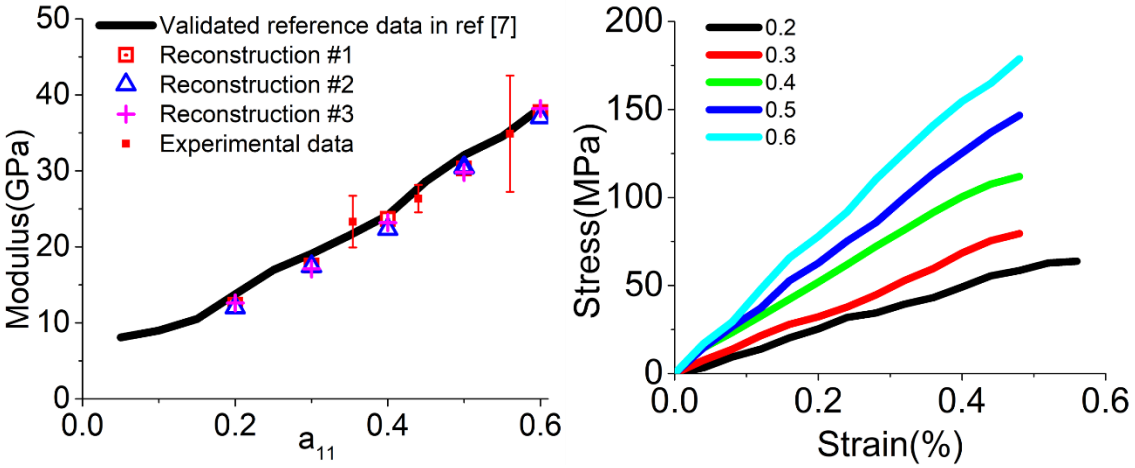

(a) (b)

Figure 3.2-39: Prediction of elastic moduli and stress-strain curves: (a) comparison between the RVE predictions and the reference data; (b) The predicted stress-strain curves of RVEs of different chip orientation tensors.

ii) Failure modes and UTS: predictions and validations

The failure modes and the failure strength of the CF SMC composites are predicted using the proposed framework and then validated by experimental data.

Failure modes and damage evolution

RVE realizations of the same chip orientation tensor demonstrate similar failure modes in simulation. One sample model from each orientation tensor is shown in Figure 3.2-40. Chip splitting failure and matrix failure are highlighted in the zoom-in views A and B, respectively. For all the tested chip orientation tensors, the proposed RVE models successfully reproduce all failure modes (matrix cracking, chip splitting, chip-chip interface failure and chip-matrix) that are observed in experiments. The step-by-step failure processes of the case a_{11}=0.2 is shown in Figure 3.2-41. It is observed that cracks are initiated at the stress concentration locations, such as chip ends and interface. As the load increases, the cracks start to propagate in the matrix. When a crack reaches another chip, it begins to propagate along the interfaces. Chip splitting and chip breakage also occur during crack propagation. Finally, the entire sample breaks.

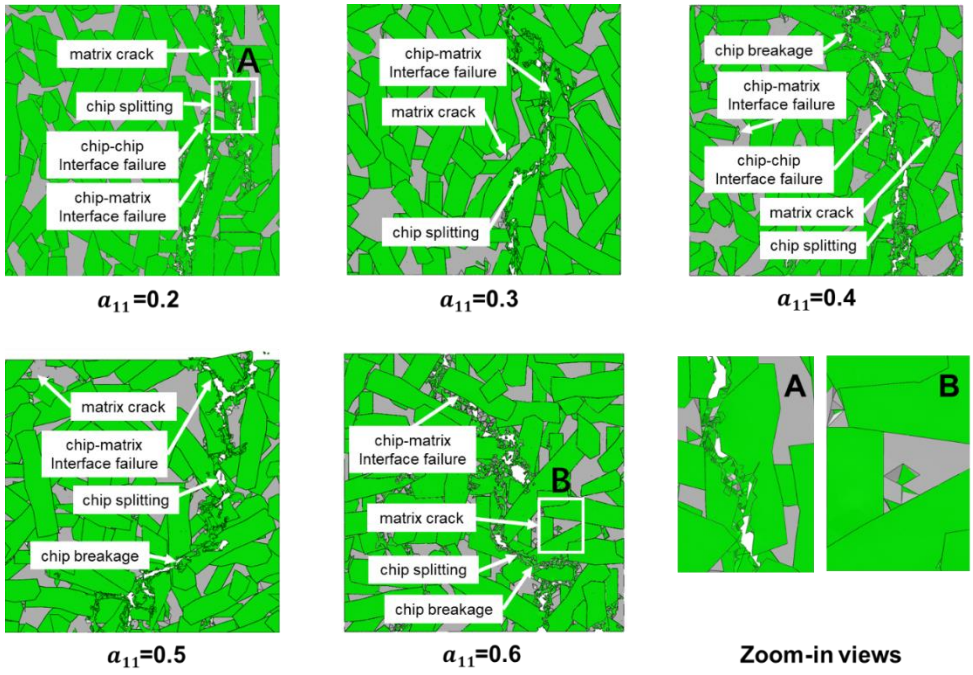

Figure 3.2-40. Failure Modes observed in the RVE models of different chip orientation tensors.

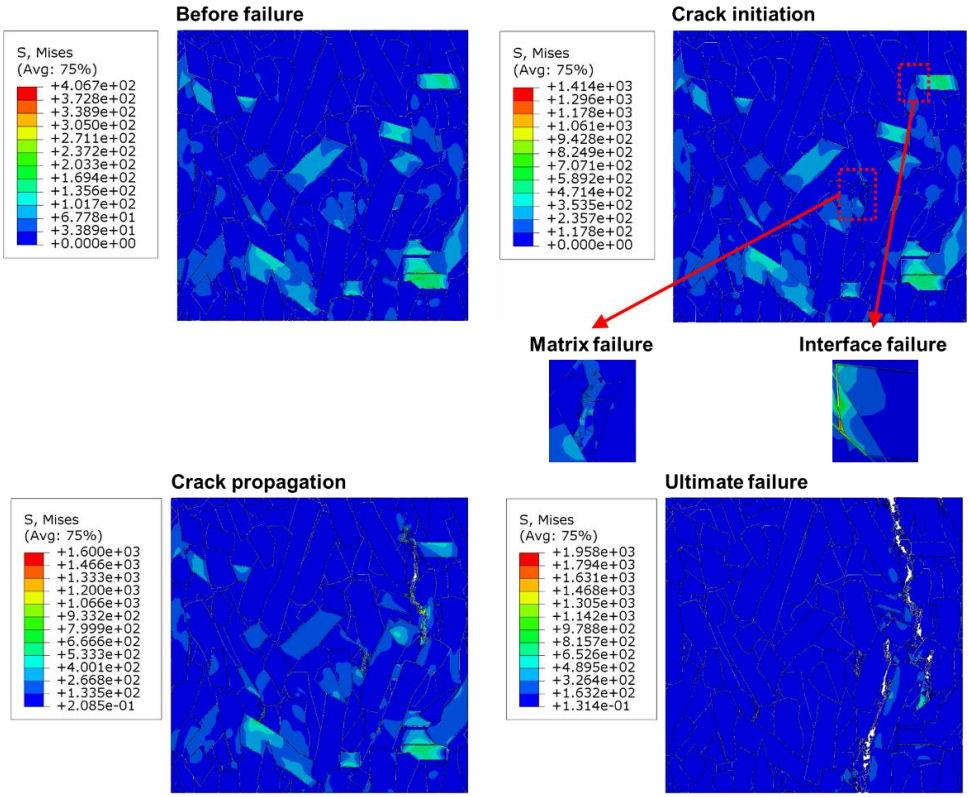

Figure 3.2-41. The failure processes of RVE models for a_{11}=0.2

Ideally, the relation between chip orientation tensor and UTS needs to be obtained from experiments for model validation. The chip orientation tensor of a SMC sample can be obtained by an auto-polishing and imaging characterization process; the UTS is measured by tensile test. Both auto-polishing and UTS testing are destructive, so the chip orientation tensor and UTS cannot be obtained simultaneously on the same SMC sample.

Chip orientation tensor a_{11} has a monotonic increasing relation with the elastic modulus. Also, both tensile modules and UTS can be obtained from the same SMC sample. Therefore, it is proposed to validate the RVE simulations by comparing the predicted tensile modulus-UTS relations with the experimental testing results. In Figure 3.2-42, the tensile modulus-UTS data points of all simulations are plotted together with the experimental data. A good match can be observed between the prediction and the experiments. The maximum deviation is less than 12% compared to tensile test data at different fiber orientation. We can also observe the uncertainties (variations) in the simulated tensile modulus and UTS of each chip orientation tensor. Such uncertainties are induced by the geometrical randomness in the statistically equivalent microstructure reconstructions.

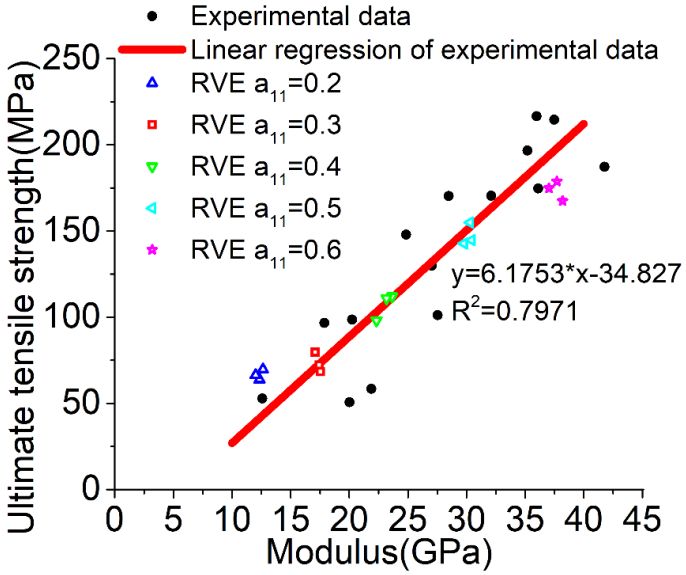

Figure 3.2-42. The tensile modulus-UTS relation: comparing the RVE predictions with the experiment results.

3.2.3.5 Concurrent Simulation

For continuous fiber composites like UD CFRP, an efficient reduced order modeling approach, namely self-consistent clustering analysis (SCA), is applied to reduce the computational cost of RVE computation. This allows one to compute the RVE responses on-the-fly and enables the simulation of the macroscale structure performance, while looking into the microstructure deformation and damage evolution concurrently. Test cases of UD CFRP structure will be presented with experimental validation. It has a broad potential in the evaluation of CFRP structure performance through numerical models and can be used for future CFRP structure design.

1) Reduced order modeling of UD CFRP

The UD RVE model allows the user to analyze the mechanical responses of UD CFRP. However, the high computational cost associated with the fine voxel mesh requires certain Reduced Order Model

(ROM) techniques to achieve 1) faster RVE responses computation; 2) linking UD RVE to large-scale part-level model.

A recently proposed reduced order modeling method, namely Self-Consistent Clustering Analysis (SCA), is a promising method for building ROM for arbitrary voxel mesh, including UD RVE. It is based on the FFT homogenization scheme. In FFT homogenization scheme, strain tensor at each voxel is treated as a combination of overall imposed strain $\boldsymbol{\varepsilon}^{\mathbf{Macro}}$ and a polarization strain $\tilde{\boldsymbol{\varepsilon}}$, shown in Equation (3.2-42) below

$$\boldsymbol{\varepsilon}(\mathbf{X}) = \tilde{\boldsymbol{\varepsilon}} + \boldsymbol{\varepsilon}^{\mathrm{Macro}} \tag{3.2-42}$$

Above equation, also known as Lipmman-Schwinger equation as in Equation (3.2-43), allows one to solve local strain responses $\boldsymbol{\varepsilon}(\mathbf{X})$ when $\boldsymbol{\varepsilon}^{\mathbf{Macro}}$ is fixed. This is the basic of FFT homogenization method, which is time consuming since the evaluation happens for all voxel elements.

$$\boldsymbol{\varepsilon}^{\mathrm{Macro}} - \boldsymbol{\varepsilon}(\mathbf{X}) - \int_{\Omega} \boldsymbol{\Gamma}^{\mathbf{0}}(\mathbf{X}, \mathbf{X}') : [\boldsymbol{\sigma}(\mathbf{X}') - \mathbf{C}^{0} : \boldsymbol{\varepsilon}(\mathbf{X}')] \mathrm{d}\mathbf{X}' = 0 \,, \mathbf{X} \in \Omega \tag{3.2-43}$$

In this project, a reduced order modeling approach is proposed through re-discretizing the voxel mesh into several clusters. Assuming the original voxel mesh contains N elements, the mesh can be compressed into K clusters, where N >> K. Equation (3.2-43)) is reformulated as Equation (3.2-44) as shown below.

$$\boldsymbol{\varepsilon}^{\mathrm{Macro}} - \boldsymbol{\varepsilon}^{\mathrm{I}} - \sum_{J=1}^{\boldsymbol{K}} \boldsymbol{D}^{IJ} : [\boldsymbol{\sigma}^{J} - \mathbf{C}^{0} : \boldsymbol{\varepsilon}^{J}] = \mathbf{0} \tag{3.2-44}$$

Equation (3.2-44) can be easily solved using Newton's method.

To apply SCA to UD RVE, the first step is to build the UD RVE database. This involves two steps:

1) Compressed original RVE from voxel mesh into clusters.
2) Compute interaction tensor $\boldsymbol{D}^{IJ}$ between all cluster pairs.

Once the RVE is compressed, each voxel will be labeled with a cluster. This is illustrated in Figure 3.2-43 below, where the RVE is decomposed into 10 clusters: 2 in the fiber phase and 8 in the matrix phase.

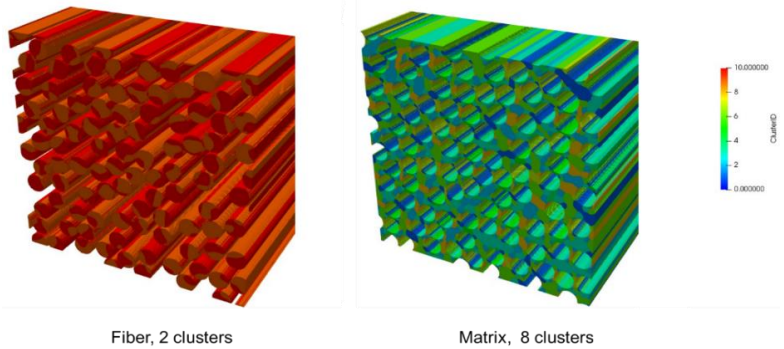

Figure 3.2-43. Illustration of clusters in the fiber phase and the matrix phase.

Once the UD database is built, Equation (3.2-44) is solved to compute stress and strain responses in each cluster when an external loading is given. This ROM, hereinafter referred as UDSCA, can be used to

compute elasto-plastic responses of UD RVE in a timely fashion. A numerical verification of UDSCA is performed as shown in Figure 3.2-44, where transverse tensile loading is considered. In this verification case, two different ROM resolutions are used: one with 16 clusters in the matrix phase and the other with 8 clusters in the matrix phase. The number of clusters in the fiber phase is kept as two. The result showed that using 8 clusters in the matrix phase and 2 clusters in the fiber phase provides good accuracy comparing to DNS solution. Hence, this ROM is used for all UD concurrent modeling cases.

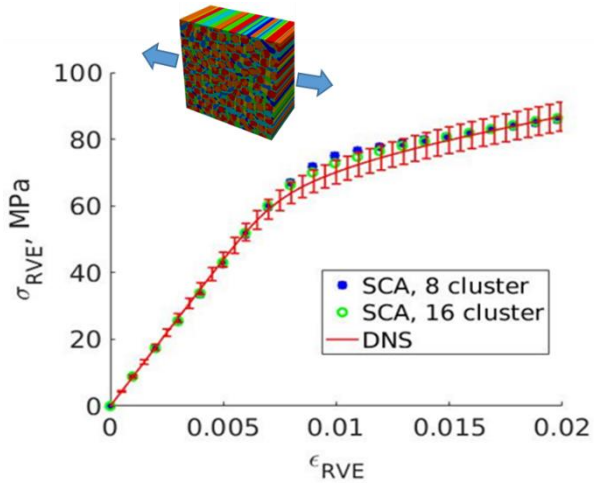

Figure 3.2-44. Transverse Stress and Strain Plots.

For UD 2-scale concurrent modeling, it follows the schematic shown in Figure 3.2-45 below. The macroscale part is discretized as finite element mesh. The ROM of UD RVE intakes strain at the integration point and then passes back stress response to the integration point.

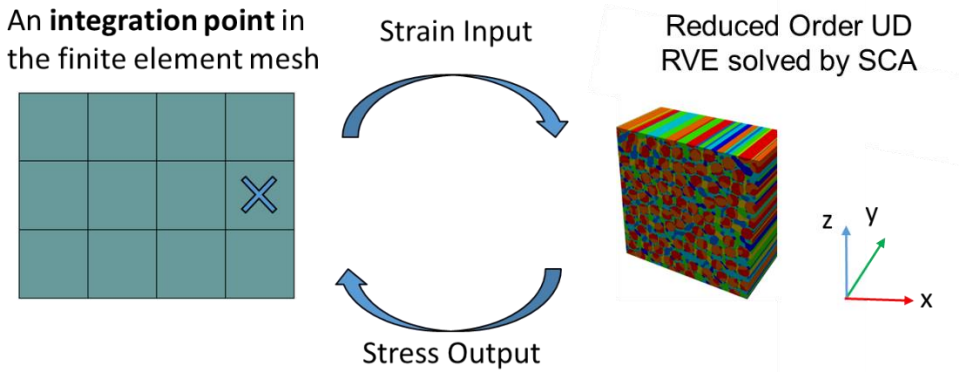

Figure 3.2-45. Schematic of UD Concurrent Multiscale Modeling.

2) UD Off-axial Coupon Tensile Concurrent Modeling

The UDSCA is applied to a coupon off-axial test model to perform concurrent multiscale modeling. For a realistic representation of the epoxy matrix, a paraboloid yielding surface is applied, where the tension and compression curves are extracted from Figure 3.2-46.

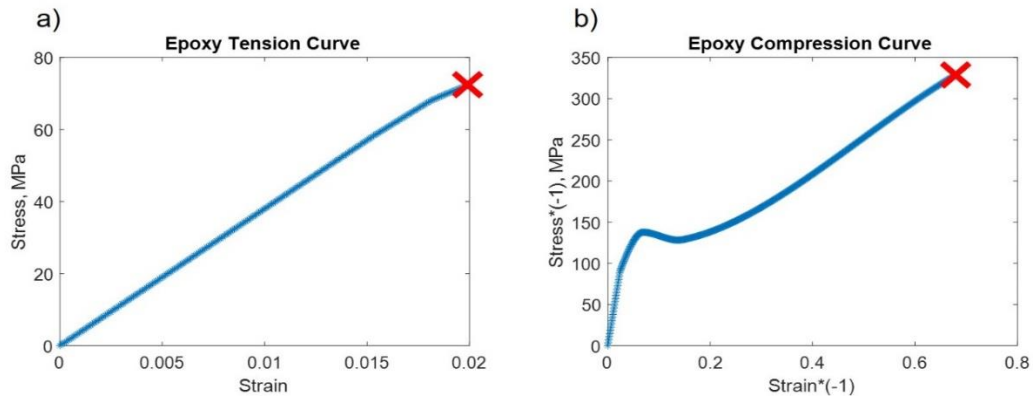

Figure 3.2-46 Tension and Compression Stress and Strain Curve for Epoxy Resin

Through the coupon test cases, two important problems are addressed:

1) Computing material microstructure evolution on-the-fly by realistic RVE.

2) Prediction of CFRP part performance using the multiscale method.

For the coupon model, exact geometry from NIST is used, as shown in Figure 3.2-47. The coupon model is built in commercial finite element software LS-DYNA. Note the teal region is the UD laminate made with 12 UD laminae. It is impossible to model every single fiber in the coupon explicitly since at least 409,422 carbon fibers need to be modeled. If a finite element mesh shown before is coupled to individual integration point of each finite element in the coupon mode, the computational cost is still huge, and the estimated solution time is beyond the capability of existing HPC. However, using UDSCA, UD RVE responses at each integration point can be computed in an efficient manner.

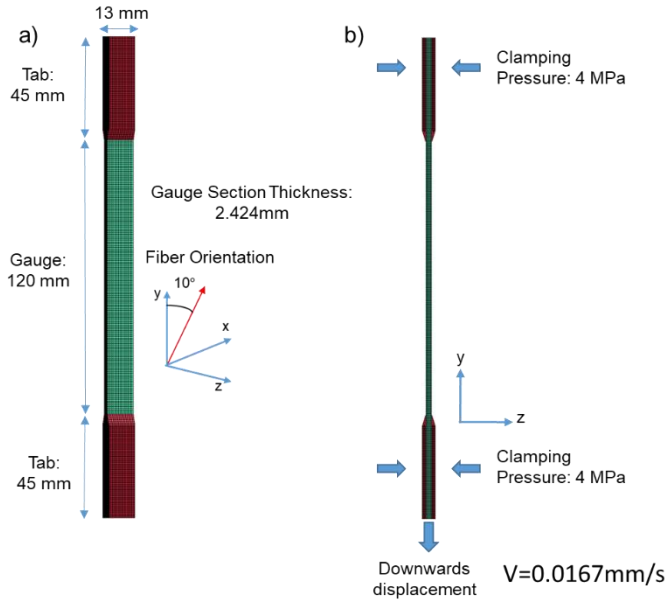

Figure 3.2-47. (a) UD Coupon Modeling Geometry and (b) Boundary Condition.

The simulation took 2560 CPUs hrs to complete. The stress vs. strain curve in the y-direction is computed and compared with the experimental result, as shown in Figure 3.2-48. A summary of the

coupon test is given in Table 3.2-12, where the concurrent model is able to predict ultimate stress and strain reasonably well.

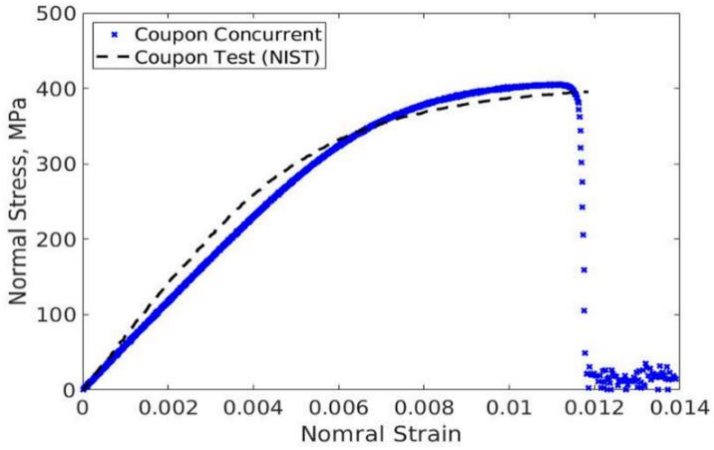

Figure 3.2-48. Normal Stress and Strain Curve of UD off-axial Coupon Test.

Table 3.2-12. Comparison of Ultimate Normal Stress and Normal Strain.

	Prediction	Experiment	Difference
Ultimate Normal Stress	404.81 MPa	395.64 MPa	2.3%
Ultimate Normal Strain	0.011	0.0118	6.7%

In addition, Figure 3.2-49 shows the von Mises stress of local RVEs and the coupon before crack initiation and after crack formation. In Figure 3.2-49, RVEs that represent four different integration points are visualized. In RVEs representing integration points on the crack, stress becomes zero as the integration point is deleted from the coupon model. In RVEs representing integration points that are not deleted, stress is still nonzero due to stress wave propagation. The concurrent capture of macroscale and microscale stress evolution is made possible by the concurrent multiscale modeling scheme.

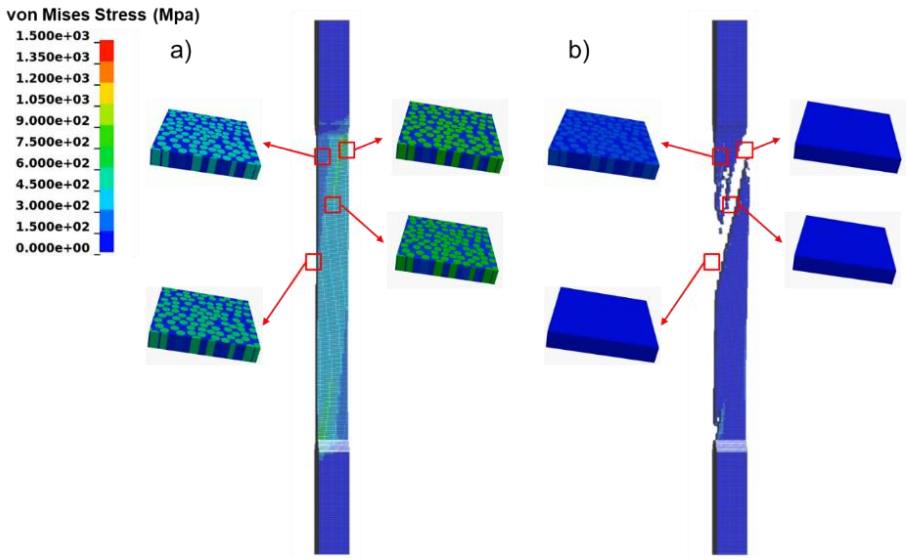

Figure 3.2-49. Von Mises stress contour of the coupon model and local RVEs a) Before crack initiation b) After crack formation.

References

[1] Melro A, Camanho P, Pinho S. Generation of random distribution of fibers in long-fiber reinforced composites. Composites Science and Technology. 2008;68(9):2092-102.

[2] Melro A, Camanho P, Pires FA, Pinho S. Micromechanical analysis of polymer composites reinforced by unidirectional fibers: Part I–Constitutive modelling. International Journal of Solids and Structures. 2013;50(11-12):1897-905.

[3] Vu-Bac N, Bessa M, Rabczuk T, Liu WK. A multiscale model for the quasi-static thermo-plastic behavior of highly cross-linked glassy polymers. Macromolecules. 2015;48(18):6713-23.

[4] Advani SG, Tucker III CL. The use of tensors to describe and predict fiber orientation in short fiber composites. Journal of Rheology. 1987;31:751-84.

[5] Liu C, Huang Y, Stout MG. On the asymmetric yield surface of plastically orthotropic materials: a phenomenological study. Acta materialia 1997; 45(6): 2397-2406.

[6] Tsai SW, Wu EM. A general theory of strength for anisotropic materials. Journal of composite materials 1971; 5(1): 58-80.

[7] Pinho ST. Modelling failure of laminated composites using physically-based failure models. Department of Aeronautics, Imperial College London 2005.

[8] Flaggs DL, Kural MH. Experimental determination of the in situ transverse lamina strength in graphite/epoxy laminates. Journal of composite materials 1982; 16(2): 103-116.

[9] Song K, Dávila CG, Rose CA. Guidelines and parameter selection for the simulation of progressive delamination. ABAQUS User's Conference 2008; 41: 43-44.

3.2.4 Fracture and Energy Absorption Models

In addition to high specific stiffness and specific strength values, CFRP show excellent property of specific energy absorption (SEA) with proper design when compared on a weight basis. For the metallic materials, the main energy absorption mechanism is plastic deformation. Different from the metallic

materials, CFRP with high SEA value is usually related to the material's characteristic to continuously absorb energy by fragmentation and destruction. The material fails through successive facture mechanisms propagating along the compacting direction. This requires that the CFRP structure doesn't fail by instabilities other than progressive failure.

Taking vehicle collision for example, there are five necessary conditions for the basis of crash certification tests: 1) maintaining sufficient occupant space, 2) providing adequate occupant restraint, 3) limiting acceleration and loads experienced by the occupants, 4) providing protection from the release of items of mass, 5) allowing for a safe post-crash egress from the vehicle.

When evaluating the crash performance of a structure, the load-displacement curve from the crash experiment is important to analyze. Figure 3.2-50 shows a typical curve for axial crush experiments. Usually there is an initial force peak, following by stable crashing where force is kept at an almost constant level. A transition zone exists between the peak force and the stable crash zone which depends on how the fracture is triggered. From the load-displacement curve, certain key parameters can be determined: 1) peak load, the maximum point on the load-displacement curve, 2) average crash load (sustained crash force), 3) energy absorption.

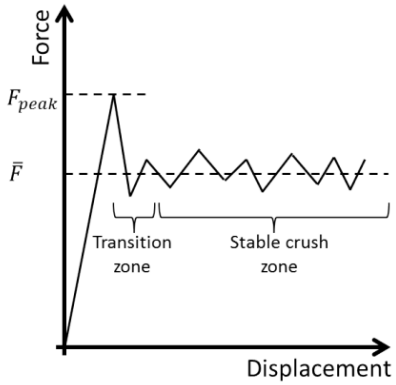

Figure 3.2-50. Typical load-displacement curve for a structure subject to crushing.

The target in this project is to develop a modelling method to capture the crash behavior of CFRP at different loading conditions, i.e. dynamic three point bending and axial crash. The method includes an automatic generation of multi-layer of thick shell element, cohesive element model, and material property predictions from RVE model. With the developed work, the simulation accuracy of CFRP component crash is significantly improved.

1) Meso-scale modelling approach

A new modelling method combined with RVE prediction is proposed, as shown in Figure 3.2-51, which includes three major parts, i.e., the automatic generation of FE model, RVE prediction for material properties and cohesive modeling for interface failure.

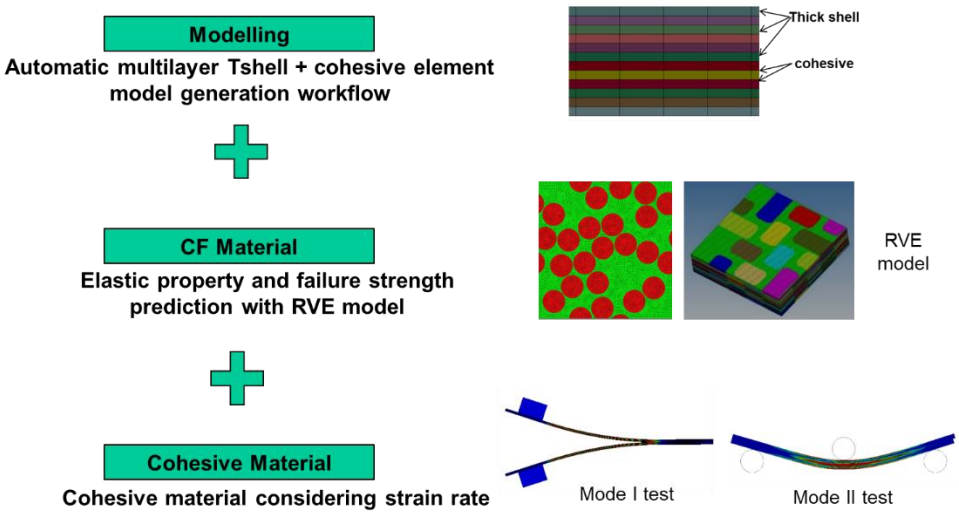

Fig. 3.2-51. Proposed method for CFRP crushing modelling.

2) Crash simulation on UD CFRP

In this section, examples of both axial and dynamic 3-point bending crash simulation on UD CFRP are conducted to illustrate the detailed procedure for the proposed meso-scale modeling approach. The results are compared to testing data to validate the effectiveness of the development.

Figure 3.2-52 show the model setup for the axial crash and dynamic 3-point bending test in LS-DYNA with 12 layer of thick shell elements. The thick shell element is an 8-noded element with kinematics of shell theory but with added strain component through the thickness. Each layer of thick shell element represents one ply, and cohesive element is adopted between two layers.

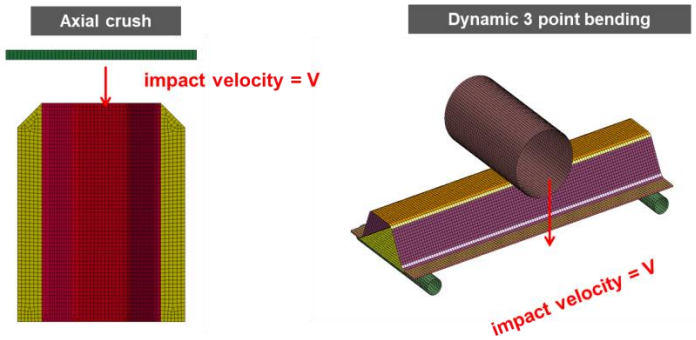

Axial crash model (b) Dynamic 3-point bending model

Figure 3.2-52 Simulation model setup

It is a time consuming to manually build the multilayer thick shell model. An automatic work flow is developed in this work, as shown in Figure 3.2-53. A command file (TCL file) is generated with Matlab based the input information and initial thin shell model, then the TCL file is performed in HyperMesh to generate the FE model. Figure 3.2-54 shows thick shell element model automatically generated by the developed program. The in-plane mesh size is 4 mm. The thickness of each thick shell element is 0.2 mm, and the thickness of the cohesive layer is 0.01 mm.

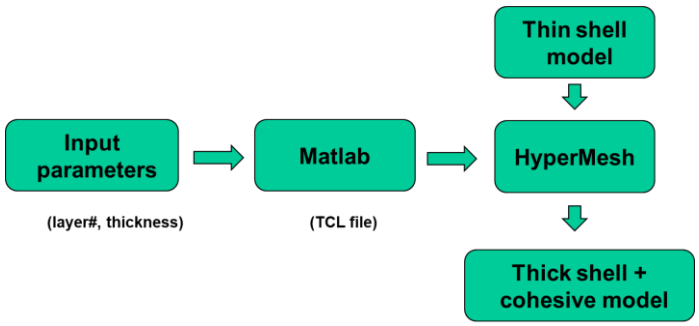

Figure 3.2-53. Work flow for thick shell model establishment.

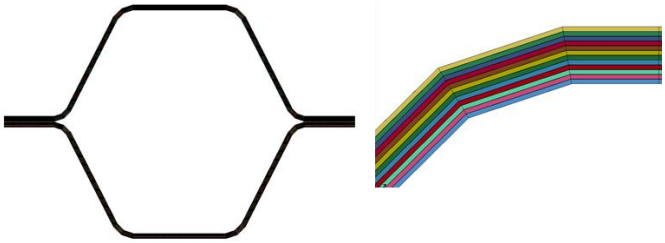

Figure 3.2-54. Thick shell mesh for axial crash model.

MAT_54 in LS-DYNA is used for material modeling. The input material parameters including elastic properties and strength are predicted from UD RVE model developed in Section 3.2.3. Table 3.2-13 lists all the predicted material input parameters from UD RVE model for UD CFRP with 50% volume fraction of carbon fibers.

Table 3.2-13. Material parameters for UD CFRP predicted from RVE model.

Parameter	Value	Parameter	Value
E11	127806(MPa)	E22/33	8567(MPa)
v21=v31	0.0217	v32	0.6004
G12=G13	4576(MPa)	G23	2658(MPa)
Xc	1000(MPa)	Xt	2020(MPa)
Yc	220(MPa)	Yt	220(MPa)
Sc	171(MPa)		

A cohesive material model considering strain rate effect, i.e. MAT_240, in LS-DYNA is adopted to simulate the delamination. A tri-linear traction-separation law with a quadratic yield and damage initiation criterion in mixed-mode is included (Figure 3.2-55). The damage evolution is governed by a power-law formulation. All the input parameters are calibrated from Mode I and Mode II fracture toughness test models, as listed in Table 3.2-14.

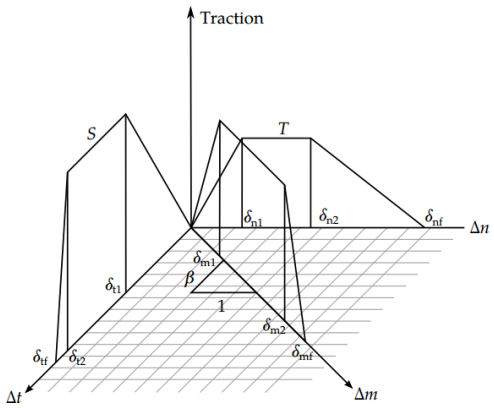

Figure 3.2-55. Trilinear mixed mode traction-separation law.

Table 3.2-14 Material parameters for MAT_240.

Parameter	Value	Parameter	Value
Emod	3850	Gmode	1460
G1C0	0.4	G1C_inf	10
edot_g1	0.5	t0	20
G2C0	0.4	G2C_inf	10
edot_g2	0.5	s0	45

Figure 3.2-56 presents the simulation results of UD with /0/+60/-60 layup of axial crash (v=4.4m/s) and dynamic 3-point bending (v= 4.66710m/s). Figure 3.2-57 compares the energy absorption and force. It can be seen that the current method can capture the results well in both axial crushing and dynamic three-point bending. The validation of the modeling approach through UD and woven CFRP with various layups in axial and dynamic 3-point bending tests are summarized in Section 3.2.7.

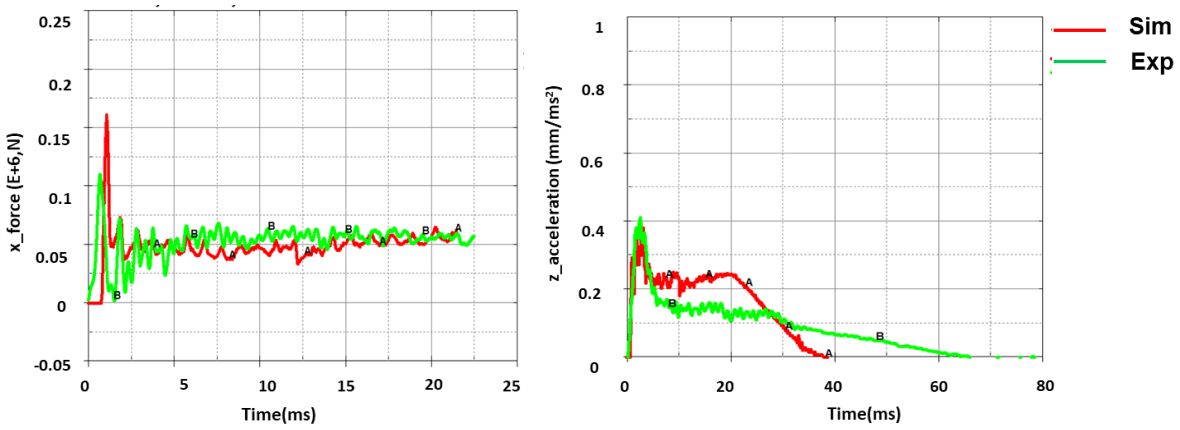

(a) Axial crush, v=4.4m/s (b) Dynamic 3-point bending, v= 4.66710m/s

Figure 3.2-56. Comparison of the simulation results with testing data

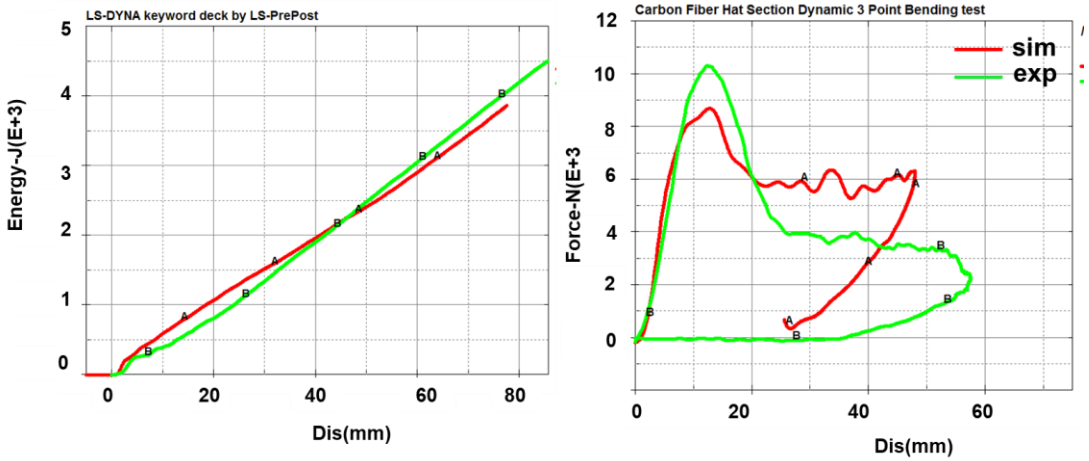

(a) Energy absorption in axial crash (b) Force-displacement in dynamic 3-point bending

Figure 3.2-57. Comparison of the simulation results with testing data

3.2.5 Fatigue and Durability Models

Fatigue failure is an important consideration for CFRP design as components periodically undergo complex loading histories during their service lifetime. The most common and useful approach to represent the fatigue properties of the carbon fiber composites is to construct a Constant Fatigue Life diagram (CFL). The current work aims at establishing proper methodologies for fatigue testing and generating valid CFL diagrams for UD, woven and SMC composites to be used for fatigue life prediction. Also, a fatigue failure prediction methodology is developed based on the linear damage summation approach to capture the fatigue failure behavior and predict fatigue life. The criterion was validated using variable stress amplitude loadings showing good agreement with the experimental data. All the developments are implemented in commercial fatigue software (nCode) for component level fatigue life prediction.

3.2.5.1 Constant fatigue life diagrams construction for CFRP

In this work, we investigate the damage initiation and evolution in UD, woven and SMC CFRP under cyclic loading. While we note that "material separation" fatigue failure criterion may work well for UD and SMC composites, it inaccurately represents the fatigue properties of woven composites due to large delamination observed in woven composites much earlier to final failure. Instead, for woven composites, we propose the use of the "5% stiffness drop" fatigue failure criterion for accurate representation of the CFL diagram. As a validation to our revised approach, we show that the linear damage summation works well in fatigue life prediction for a number of loading cases in woven composites.

Another area of focus in this work is to improve the fatigue testing methodologies. We note that ASTM standards have guidelines to obtain the static mechanical properties of carbon fiber composites, but no standards are dedicated for fatigue tests for CFRP. During a fatigue test, especially for compression-dominated fatigue, the shear force induced due to gripping generates a non-uniform stress field through the thickness of the specimen causing early delamination of the outer layers of the composite. In this respect, the fatigue lives obtained from tests may not be the true fatigue lives of the sample. In the current project, we modified the gripping method during fatigue test by introducing a pre-compressive load. This way, a uniform stress distribution was obtained in the gauge section of the sample, and the theoretical strength of the composite was obtained.

A large number of experiments were conducted to establish the fundamental properties such as the elastic moduli, tensile and compressive strengths, failure strains etc., which depend on the fiber orientations and the fiber volume fractions. We constructed constant fatigue life diagrams for UD, woven and SMCs for different orientations, which were later used in commercial fatigue software (nCode) for component level fatigue life prediction. The results are summarized below.

1) UD/NCF CFRP Results

The fatigue tests at various *R* ratios were conducted for 0° and 90° UD laminates. To achieve valid tests, different geometries of samples were designed for different fiber orientations. The S-N curves at various stress ratios for 0° and 90° UD laminates have been obtained to characterize the fatigue behavior of UD laminated composites.

In order to investigate the size effect on the fatigue lives of UD laminates, fatigue tests for samples with different gauge lengths have been carried out for 0° and 90° UD laminates. We found that the size effect cannot be ignored for tensile dominated fatigue failure for 90° UD laminates, and longer samples generated a shorter fatigue life. To include the size effect into our fatigue characterization, a fatigue model accounting for the size of the sample was proposed based on Weibull distribution.

Constant fatigue life diagrams (CFLD) for 0°, 90° and 10° UD laminates were established based on the fatigue tests by using four different methods: Piecewise model, Kawai's three-segment model and four-segment model [1,2], and Harris's Bell-shape model [3]. The comparison between prediction results and experimental data shows that Kawai's four-segment model is able to provide the most accurate prediction of fatigue life at various stress ratios for 0° and 90° UD laminates. The CFLD for the 0°, 90° and 10° UD composites based on Kawai's four segment model are provided in Figure 3.2-58 (a), (b) and (c), respectively.

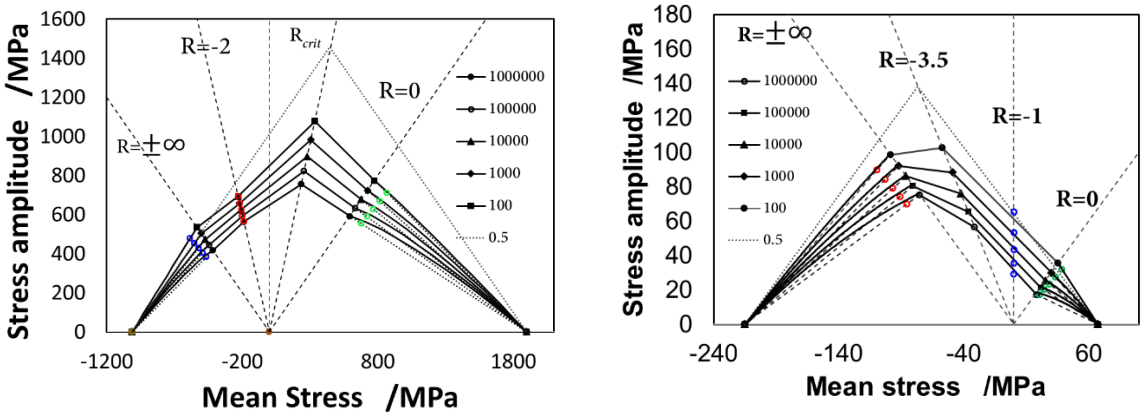

(a) (b)

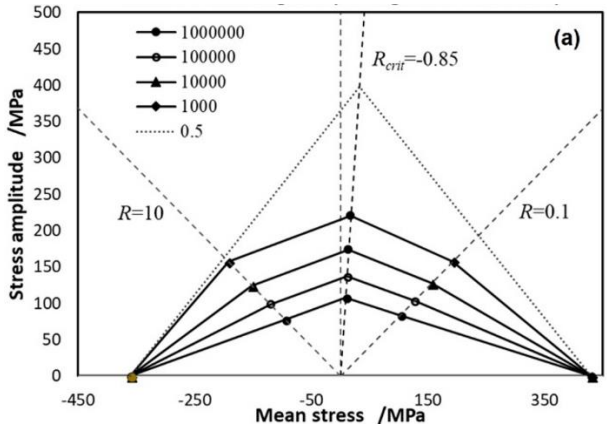

(c)

Figure 3.2-58. Constant fatigue life diagrams (CFLDs) for (a) 0° , (b) 90° and (c) 10° UD laminates based on Kawai's four segment model.

2) Woven CFRP Results

In our studies on tension-tension (T-T) fatigue tests (R=0.1) in woven composites, severe delamination was observed in the first 10 cycles when the maximum stress of T-T cycle was above the "knee" region of the stress strain curve (Figure 3.2-59). Nonetheless, the samples sustained lives beyond 1.0E6 cycles. Although the samples have high degree of damage in the first few cycles, the fiber sustains majority of the loads in tension, and hence the fatigue lives were higher. Utilizing such S-N curves for T-T fatigue which completely ignores damage due to delamination is unsafe for design purposes. For this reason, the fatigue failure criteria of "material separation" was revised to "5 % stiffness degradation", and the CFL diagrams are shown in Figure 3.2-60.

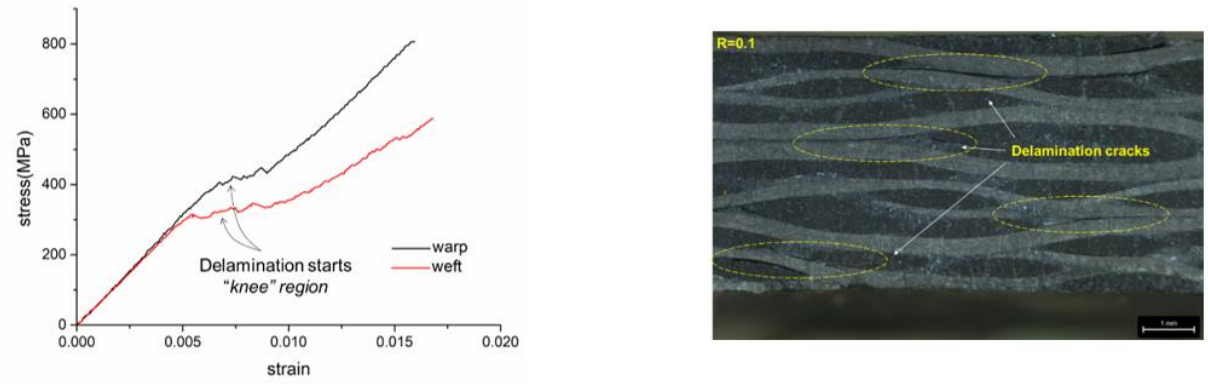

(a) (b)

Figure 3.2-59 (a) Stress-strain response of woven composites in warp and weft directions (b) Delamination in the first 10 cycles in a woven sample (weft direction) subjected to R=0.1 cycling at a stress amplitude of 222 MPa.

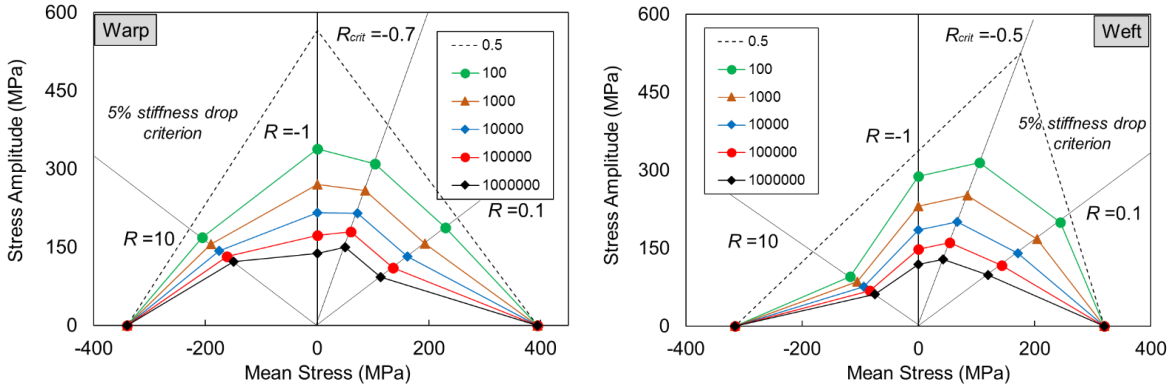

(a) Warp direction (b) Weft direction

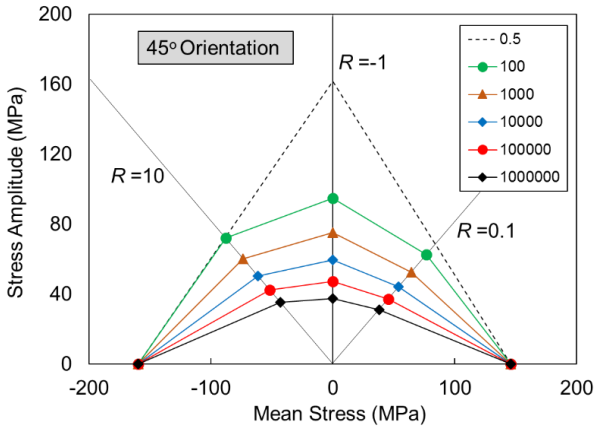

(c) 45° direction

Figure 3.2-60. Constant fatigue Life (CFL) diagram using "5% stiffness drop" fatigue failure criteria.

3) Chopped SMC CFRP results

The fatigue tests of SMC composites were conducted under stress ratio of 0.1, 10 and -1. Prior to the cyclic loading, all specimens had been loaded to approximately 100MPa, so that the strain distribution can be measured using DIC systems to obtain local modulus and distribution of fiber orientation. An analytical approach was developed to correlate the fatigue performance of SMC with its local elastic modulus, which was determined by the fiber orientation distribution. Then a new form of CFL diagram was obtained with the fiber orientation tensor to link its local properties to the fatigue performance. Figure 3.2-61 represents the CFL diagrams obtained in the current study for different principal fiber orientations. It should be mentioned that since there is competition among different local areas, and specimens always fail in the area with lower a11, the fatigue performance with higher a11, i.e., a11 larger than 0.5 was not obtained in experiments.

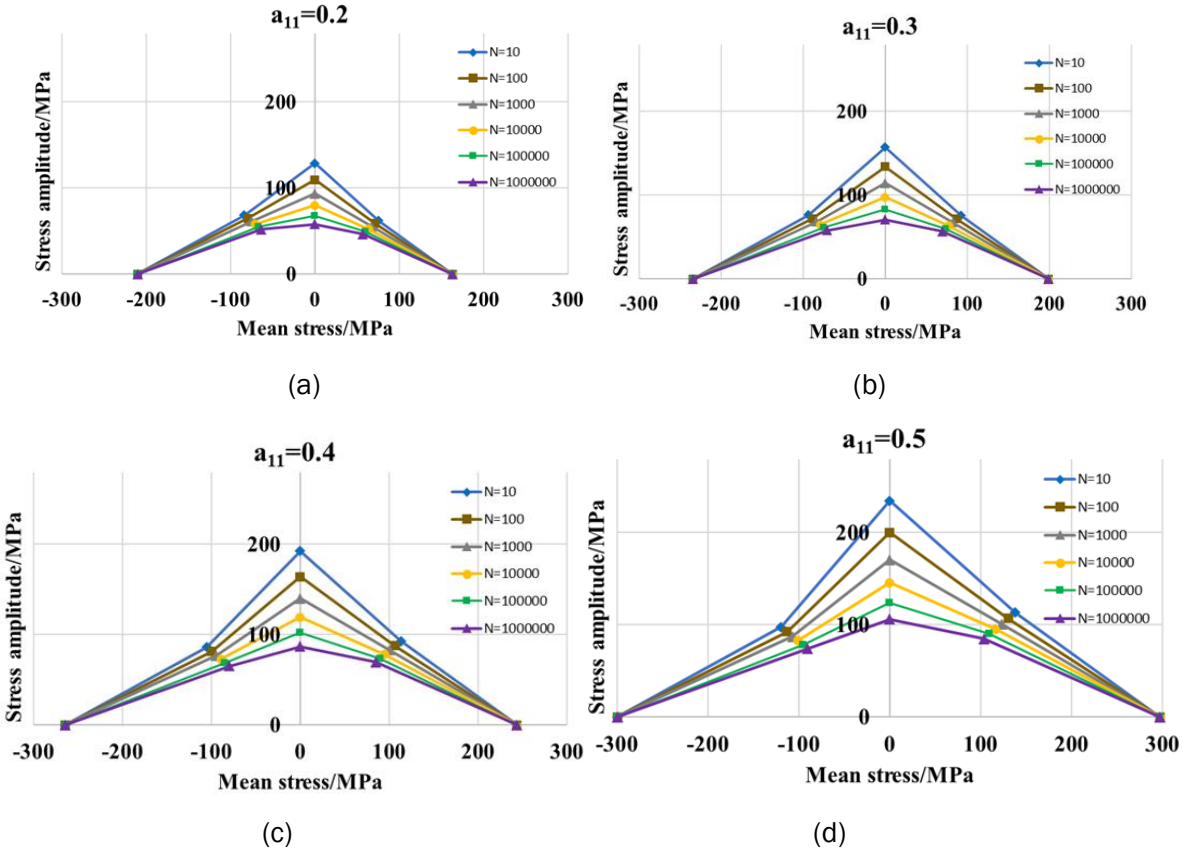

Figure 3.2-61. CFL diagrams of SMC composite with different fiber orientation tensors: (a) $a_{11\text{-}failure}$ = 0.2, (b) $a_{11\text{-}failure}$ = 0.3, (c) $a_{11\text{-}failure}$ = 0.4, and (d) $a_{11\text{-}failure}$ = 0.5.

3.2.5.2 Fatigue failure criterion development using linear damage summation approach

In real service conditions, the loading cases are rather complex with varying stress amplitudes and R-ratios. The CFL diagrams obtained at different R-ratios can be used in conjunction with the linear damage summation approach to predict the fatigue lives of composites. Palmgren-Miner rule [4] is one of the most simplified and widely used methods to estimate the fatigue damage. The rule incorporates the damage accumulated in a material as the fraction of the life spent at a particular stress level (see Equation (3.2-45)). The rule, however, does not incorporate load interaction and load sequence effects. To assess the validity of fatigue life prediction using the CFL diagram obtained using linear damage approach, we

conducted variable stress amplitude fatigue tests. The simplest linear damage summation rule proposed by Palmgren-Miner can be written as follows:

$$D = \sum_{k=1}^{n} \frac{n_k}{N_{fk}} \qquad (3.2\text{-}45)$$

In Equation (3.2-45), n_k and N_{fk} are the corresponding number of load cycles and the cycles to failure at stress level S_k. Fatigue failure occurs when damage term, *D*, is equal to 1. Equation (3.2-45) is used to validate our fatigue life prediction approach due to its mathematical simplicity as it ignores load interaction and load sequence effects. As an example, we conducted two-level variable stress amplitude tests at *R*=-1 for woven composites in weft direction. The results showed that Miner's rule is applicable to woven CFRPs within 5% agreement using CFL diagram obtained in the current study.

2-level block loading at R=-1

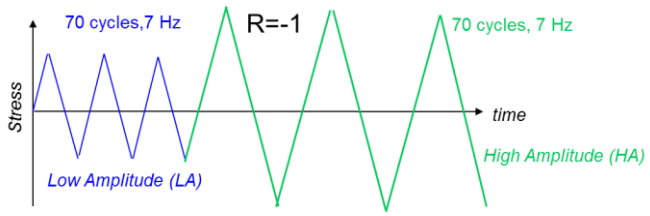

Figure 3.2-62. Schematic of 2-level block loading.

We performed 2-level block loading fatigue tests to validate the linear damage summation rule (Miners rule). As shown in Figure 3.2-62, each block consisted of 70 low amplitude cycles (referred to as "LA" cycles) and 70 high amplitude (HA) cycles at R=-1. The amplitude of LA was 126.4 MPa and that of HA was 158 MPa. The tests were performed at 7 Hz. The experimental number of blocks endured by the specimen prior to failure for this loading case is 576 (average of 2 tests).

We apply the Miners rule to predict the total number of blocks to failure for this case using the CFL diagram presented in Figure 3.2-60. The predicted value of 657 blocks using Miners rule is in good agreement with the experimental value of 576 (within 14%).

3.2.5.3 nCode composite module implementation

The composite module referred to as "Composite Analysis Engine" in nCode requires stresses to be available from finite element model. It incorporates the linear damage summation approach as described earlier to calculate the total life of component under variable stress amplitude loadings. The engine assembles the stress tensor histories, as a function of time or data points, with the load provider (cyclic loads) to calculate the fatigue lives. An example of a typical flow model in nCode utilizing composite module is shown in Figure 3.2-63. The composite analysis engine uses its own material definition, which can be found in the MXD material database. The material definition contains the static properties and the constant fatigue life diagrams which are utilized by the engine to predict lives.

There are numerous failure theories in the literature and no general consensus has yet been found that establishes a unique and universal version. Therefore, several failure criteria have been implemented in

the composite analysis engine, some of which are Maximum Stress and Strain Criteria, Norris, Hoffman, Tsai-Hill, Tsai-Wu, Franklin-Marin, Hashim-Rotem, Christensen, Norris McKinnon, Hasin-Sun, and Modified NU criteria. The engine also allows the user for a user-defined composite failure criteria. The user can select any of these single criteria or perform fatigue calculations using all the available failure criteria and choose the most conservative one for fatigue analysis.

The time taken to run a fatigue analysis depends on the number of entities (nodes and elements), load cases (for superposition events), the type of analysis (S-N versus E-N) and the number of data points in the time series. One of the methods of reducing the time taken to run an analysis is to reduce the number of data points to be processed. In the module, one can choose to use only peak-data valley from a time-series load or use a gate value to discard cycles causing minimal damage. This way, the module allows "time-history compression's option to reduce the computational time by more than 50%.

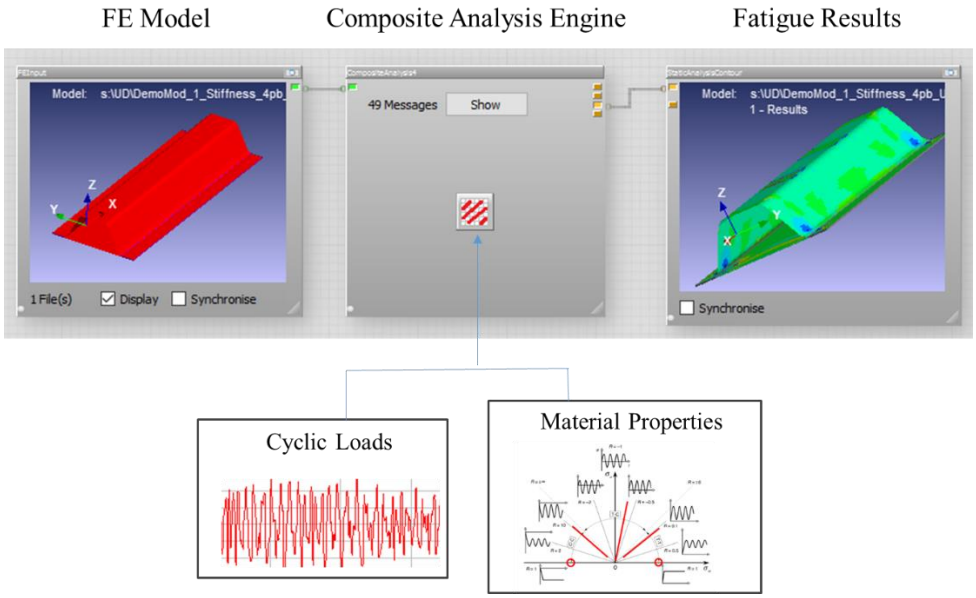

Figure 3.2-63. A typical flow for continuous composite analysis in nCode.

nCode Implementation in SMC subframe

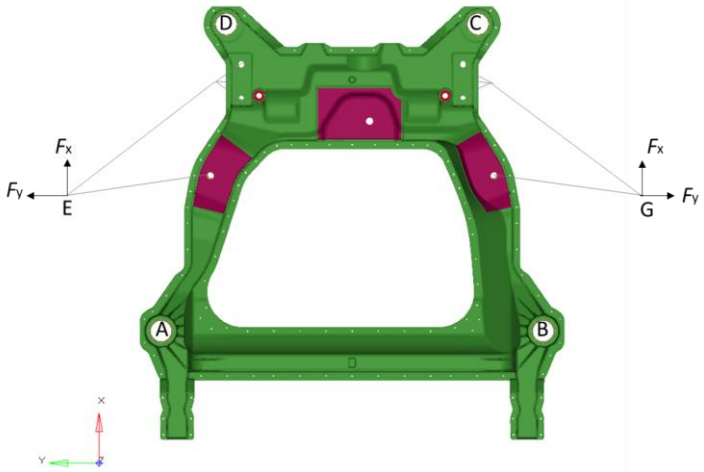

Figure 3.2-64. SMC intensive design of a subframe.

Consider a subframe in Figure 3.2-64 as an example. The green region represents the SMC part while the red regions are the UD patches. The subframe is fixed at body mounts A-D, while unit loads (of 1 N) are applied along X and Y directions at locations E and G to obtain the stress distribution results (.op2 file) from Nastran simulations. The op2 file generated is an input to nCode simulations along with the material properties and the loading history.

Consider that the subframe experiences cyclic load waveforms provided in Figure 3.2-65(a) at the loading locations E and G. The cyclic loads are provided in .rsp file in nCode. The stress distribution in the subframe generated in Nastran due to unit loads are then scaled further with the actual loads of the duty cycle (or the .rsp file). The nCode then calculates the actual distribution of the stresses in the elements and uses the S-N curve for the material to output the lives. The S-N parameters such as fatigue strength and fatigue strength coefficient are provided as an mxd file in nCode as shown in Figure 3.2-65(b). The mxd file also contains information about the volume fraction of the composites, the local fiber orientation and the static mechanical properties. It is important to note that in Figure 3.2-65 (a), the loading history consists of variable stress amplitude loading cycles in repeating units. In this case, the damage is first calculated for each repeating cycle and the linear damage summation rule is applied to calculate the total damage for entire loading cycles. Figure 3.2-66 shows the fatigue results for the subframe. The red regions have higher stress concentrations and hence lower lives, while the lives in the blue region exceed one million cycles.

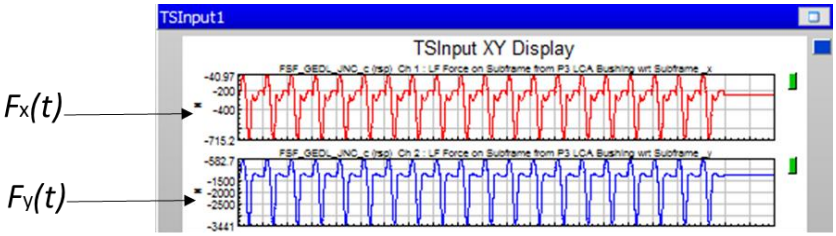

(a)

Properties | Graph

	Dummy::Fibre share = 0.025	Description
MaterialType	1000	Material Type
RR	-1	R-ratio of Test
VolFraction	0.3	Volume Fraction
Nfc	1E10	Fatigue CutOff
SE	0	Standard Error of Log(N)
f	0.025	Fibre share
Phi	90	Orientation of loading direction to dominant fibre direction
UTS	58	Ultimate Tensile Strength (MPa)
UCS		Ultimate Compressive Strength (MPa)
SRI1	160	Stress Range Intercept (MPa)
b1	-0.06525	First Fatigue Strength Exponent
Nc1	1E6	Fatigue Transition Point (cycles)
b2	-0.06525	Second Fatigue Strength Exponent
T	23	Test temperature (deg C)
RH	50	Relative humidity (%)

(b)

Figure 3.2-65. (a) Loading cycle waveforms (b) material database (.mxd) setup for SMC

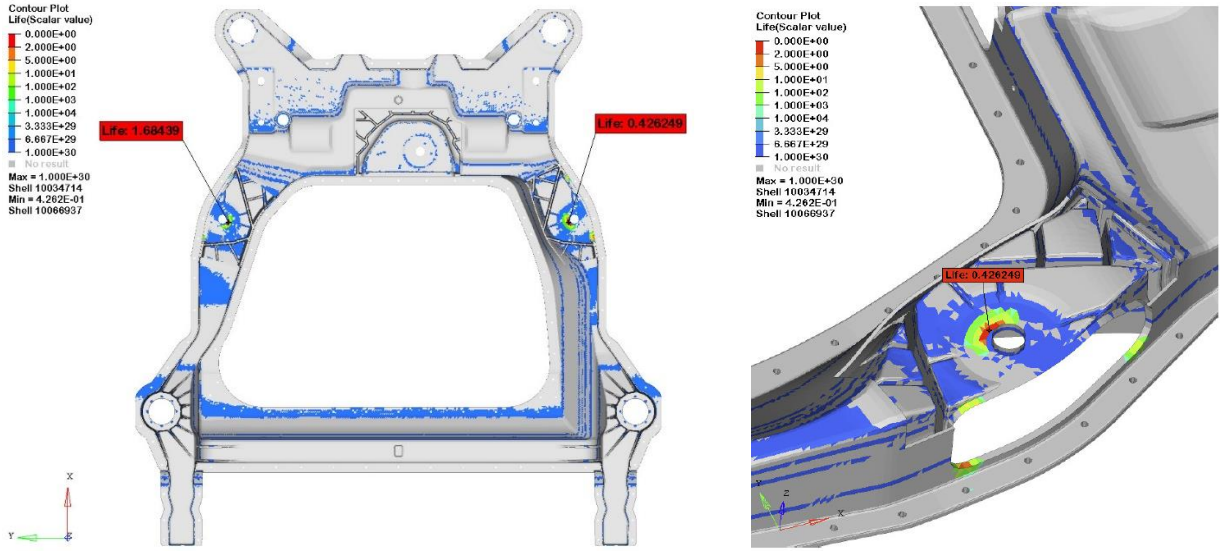

Figure 3.2-66. Subframe showing failure locations (in red) and locations with lives exceeding 1 million cycles (in blue).

In the current project, we investigated the durability of the subframe with different combinations of materials (UD, SMC, woven, Steel and Aluminum) using similar approach as described above. Finally, we obtained an optimized design that meets both the weight and cost target in addition to strength, stiffness and durability requirements. The subframe shown in Figure 3.2-67 consists of SMC and steel materials which meets the weight and the cost target of the current ICME project, and is the best design. The total weight of the subframe is 18.8kg with a cost penalty of $4.01 per pound saved. As shown in Figure 3.2-67, the lives of all the elements in SMC (shown in blue) exceed 1 million cycles (beyond cutoff), and hence meets the durability requirements. The gray region is the steel material, the lives of which also exceed 1 million cycles (not shown here).

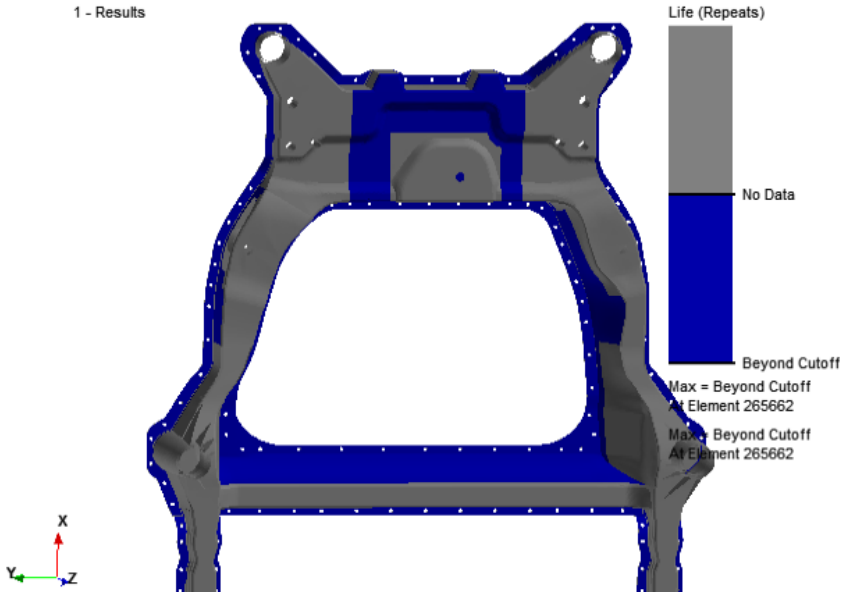

Figure 3.2-67. Subframe (SMC+Steel) design that meets the ICME design requirements.

References

[1] M. Kawai, and M. Koizumi. "NONLINEAR constant fatigue life diagrams for carbon/epoxy laminates at room temperature." Composites Part A: Applied Science and Manufacturing 38, no. 11 (2007): 2342-2353.

[2] M. Kawai, and N. Itoh. "A failure-mode based anisomorphic constant life diagram for a unidirectional carbon/epoxy laminate under off-axis fatigue loading at room temperature." Journal of composite materials 48, no. 5 (2014): 571-592.

[3] B. Harris, N. Gathercole, J. A. Lee, H. Reiter, and T. Adam. 'Life–prediction for constant–stress fatigue in carbon–fiber composites', Philosophical Transactions of the Royal Society of London A: Mathematical, Physical and Engineering Sciences 355, no. 1727 (1997): 1259-1294.

[4] M.A. Miner, 'Cumulative damage in fatigue', ASME J Appl Mech 1945; 12: A159–A164.

3.2.6 Stochastic Multi-Scale Characterization

The effect of microstructural correlations and uncertainties at three scales: micro, meso, and macro-scale were investigated. Major sources of uncertainty at each length scale of the material system of interest were identified. At each particular scale, the spatial correlations among the quantities or parameters of interest are modeled as a function of the spatial coordinates at the next higher scale via a random field. Sensitivity analyses were carried out to make sure that dominant sources of uncertainty at

the mesoscale and macroscale are identified. Uncertainty Quantification (UQ) and Uncertainty Propagation (UP) of both UD and woven composites were studied in this project. The developed methods are summarized in the following sections.

3.2.6.1 Image-based microstructural uncertainty quantification for UD composites

The UQ work for UD composites aims at statistical modeling and reconstruction of the material microstructural features, including (1) non-uniform fiber spatial distribution and (2) fiber waviness. Several machine-learning- and applied-statistics-based approaches are developed for image characterization, information retrieval and generative model building. For the spatial fiber distribution, which exhibits both non-stationarity and non-homogeneity, we first model the data (image) via a tree-regression algorithm then a hierarchical nonparametric sampling approach is developed. The approach is completely data-driven, in the sense that no probability models are assumed and a part of a new sample is generated by resampling from the data.

Fiber waviness is the local orientation of the fiber bundles relative to the global direction of the fibers. Perfectly straight fibers have zero waviness everywhere, however, the transverse images taken from unidirectional fiber composite samples show that waviness does exist. On the other hand, due to the limitation in image quality, only partial fibers are observed in terms of disconnected fragments therefore traditional computer vision algorithms for edge or object detection are not applicable in this project. To conquer this challenge, we developed a segmented regression algorithm that can estimate the local waviness angle via a linear-regression-like-, optimization-based approach. Then the angle distribution along the fiber longitudinal direction are modeled with a time series statistical model, from which we can sample realizations from.

1) Fiber Distribution Modeling

By visually inspecting the distribution of fibers, which is represented by distribution of local volume fraction of fibers (Figure 3.2-68(a)), the spatial correlation between the local fiber volume fractions exhibits two characteristics. The first one is non-homogeneity, which is reflected by the layered structure along the vertical direction. The second one is non-stationarity, which refers to the local curvature of the volume fraction patterns along the horizontal direction. Modeling both features with traditional parametric statistical models will involve estimation of lots of parameters representing these features. Therefore, we use an alternative approach: along the vertical direction, the non-homogeneity, i.e. the shape of some wave-like functions, is sampled from its empirical distribution through resampling from the image dataset (with replacement); along the horizontal direction, the non-stationarity is modeled by looking for a representative statistic of this feature and attempting to find the distribution of the statistics.

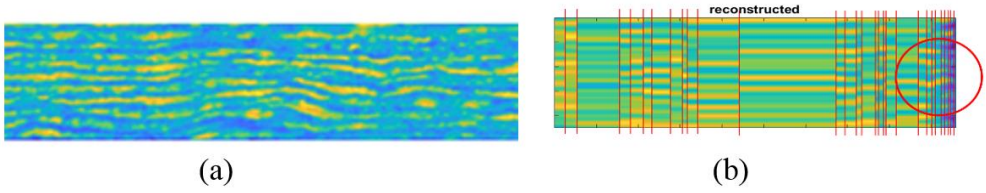

Figure 3.2-68. (a) A typical fiber volume fraction (vf) contour, yellow color represents high vf (~0.6), and blue color represents low vf (~0.4). (b) the use of the location of splitting lines to represent the non-stationarity.

The first step to find such a statistic is to reduce the dimension of each sample image from approximately 450,000 pixels to a manageable size. To compress the data in a sample, we used a

regression tree algorithm, i.e. a sample is represented by a tree-structured field. The locations of the splitting lines (nodes of the tree) are found by minimizing the integrated relative error (IRE), and between the separation lines the data are interpolated linearly. By setting the regression goal to IRE < 5%, we normally obtain 200-300 nodes. Since the splitting lines separate the most distinct areas, the locations of them contain the information of non-stationarity: the denser the lines are, the more local curvatures the area include (Figure 3.2-68 (b)). Note that a dense collection of the lines means smaller inter-line distances. It follows that we can use the distribution of the inter-line distances to characterize the non-stationarity.

The distribution, in terms of probability density estimates, of the inter-line distances are generated with all the samples. The first three plots of Figure 3.2-69 show three of them. It can be observed that each sample has different levels of non-stationarity, which might account for the difference in the material performance. The distributions in the last three plots are estimated by grouping inter-line distance data of 10 randomly selected samples together. The similarity in shape of the probability densities suggests the convergence of the distribution, i.e., the common distribution behind all samples.

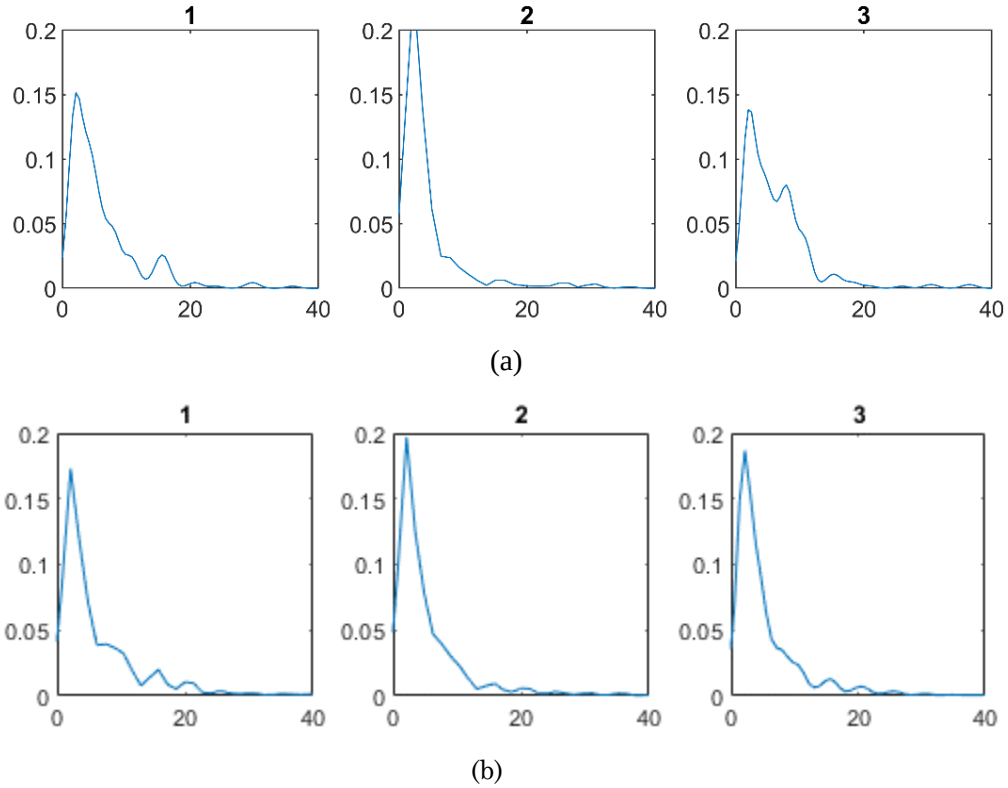

Figure 3.2-69. (a) Probability density estimate of the inter-line distances of 3 of the samples. (b) Probability density estimates of 3 batches of the samples (each batch contains 10 samples).

This observation provides a way of generating random samples with similar levels of non-stationarity, which is sampling the locations of the splitting lines from the common distribution in Figure 3.2-69 (b). The volume fractions along the vertical splitting lines are sampled directly from the empirical distribution estimated from the data. Therefore, a sampling algorithm for the fiber distribution/volume fraction can be constructed by (a) generating random splitting locations from the common distribution of inter-line distances, then (b) resampling the volume fractions along the splitting lines from the dataset, and (c) the areas between the lines are filled by interpolating the neighboring lines. Two example reconstructions are

demonstrated below (Figure 3.2-70), which shows both randomness and high level of similarity compared to the original samples (for example, in Figure 3.2.68(a)).

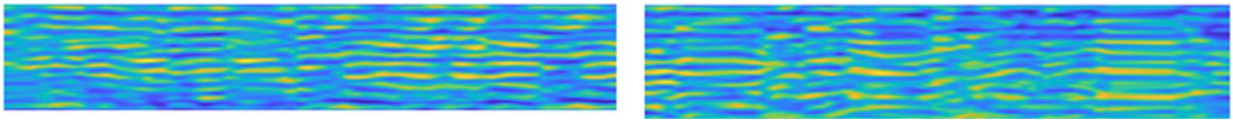

Figure 3.2-70. Two examples of reconstructions.

2) Fiber Waviness Characterization

Characterization of fiber waviness from the transverse images is not as straightforward as fiber distribution characterization, since the local curvature in the image, in terms of local slopes or angles, cannot be calculated directly from the pixel information (e.g. binary or grayscale values). Normally the characterization process would involve detecting each of the fibers on the image and calculate the angles accordingly. However, this approach fails in this project because the fibers in the images are not fully shown, i.e. only partial fibers are observed, and some of the parts appear in just dots or small pieces, the orientation of which are not measurable individually (see, for example, the binary image segment in Figure 3.2-71). It is possible to design filters to remove them as noises, but the fact that they still have a general trend as a group indicates that statistical characterization is helpful in preserving the information. Also note that linear regression is an ideal tool to estimate slopes, therefore we developed a segmented linear regression approach to characterize the local curvature in the images.

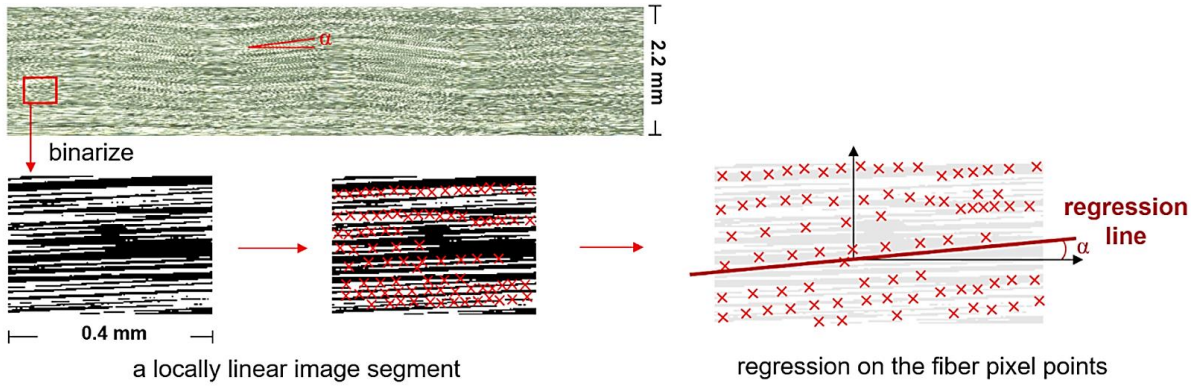

Figure 3.2-71. The segmented linear regression process.

The idea behind this method is: the relationship between the local angle and local slope is given by $\beta = \tan(\alpha)$, where β is the slope and α is the angle, and the local slope is estimated by the slope of the regression line with the points on a locally binarized segment of the original image. The challenging part is to build a valid linear model for the regression: the classic simple linear model assumes the error is normally distributed and the well-known least squares method is derived based on this assumption, which is not valid in our problem. We proposed our own regression algorithm customized for this case: under the assumption that the fiber pixel point and fiber locations are uniformly distributed, assume the origin of the coordinates is put in the center of the image segment, and a regression-through-the-origin mean prediction is given by the function $y = \beta x$, the estimate of the slope β is given by:

$$\hat{\beta} = \underset{\beta}{\operatorname{argmax}} f(e;\beta) \tag{3.2-46}$$

where e is the set of residuals with the regression line $y = \beta x$, $f : \mathbb{R}^n \to \mathbb{R}$ (assume there are n points in total) is the mapping between the residuals and the number of modes in the probability density estimation of the residuals. With this estimation, the trend of the fibers in the transverse direction are correctly captured (see Figures 3.2-72 and 3.2-73 for illustration).

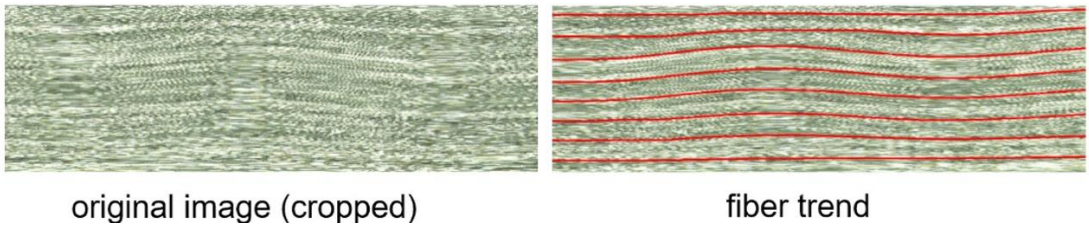

Figure 3.2-72. Illustration of the local waviness found by the proposed method.

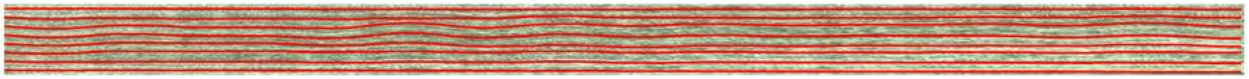

Figure 3.2-73. Fiber waviness characterization of a large image.

3) Fiber waviness modeling

The challenge associated with this task is the very limited number of images. Therefore, assumptions are made to validate our approach to build the statistical model and sampling algorithm: (1) the waviness contained in this image is representative of the waviness distribution, (2) the waviness distribution is stationary, and (3) the impact of the waviness change along the thickness/vertical direction is trivial, therefore only the fiber angle distribution along the horizontal direction is modeled. Based on (3), we can average the waviness angles along the thickness direction and obtain a 1D signal (Figure 3.2-74).

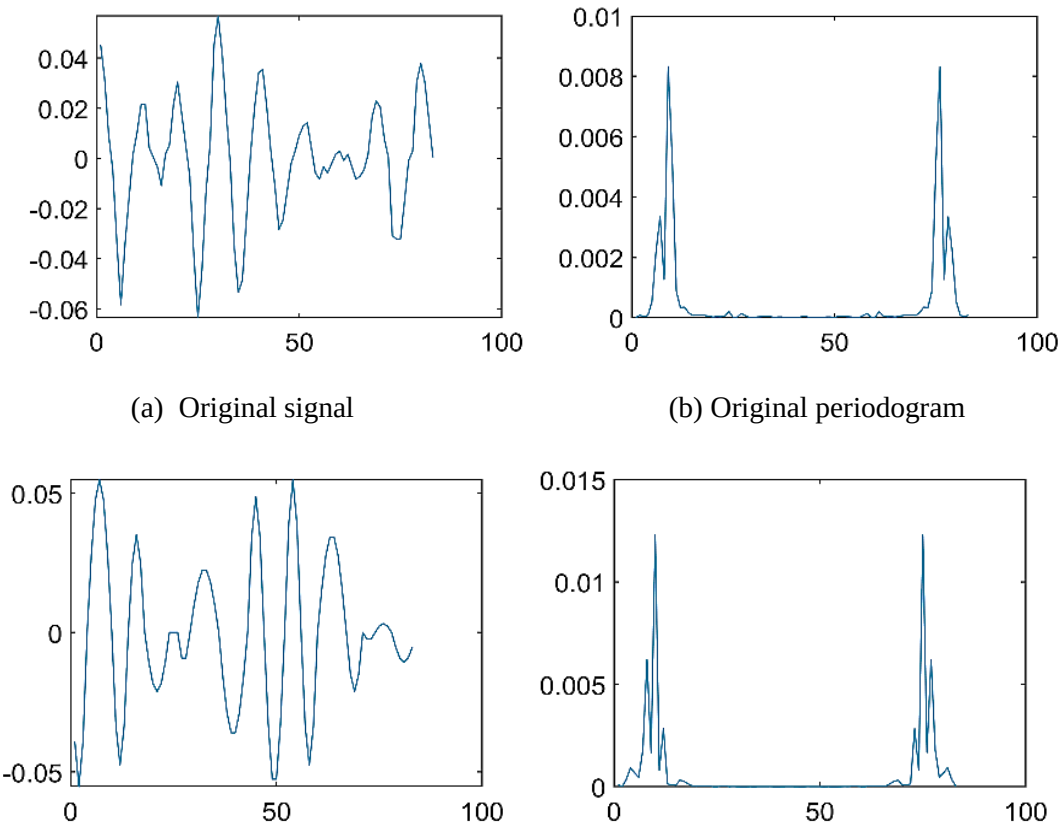

(a) Original signal (b) Original periodogram

(c) Reconstructed signal (d) Reconstructed periodogram

Figure 3.2-74. Fiber waviness reconstruction and the corresponding periodogram.

The resulting signal has a wave shape with varying amplitudes and frequencies. A natural characterization of such signal is the periodogram. A periodogram is the estimate of the spectral density of a signal, which can be obtained by discrete Fourier transform of a time or spatial series. Under assumption (2), it can be shown that the periodogram of a series converges in distribution to a sequence of independently and exponentially distributed random variables as the length of the series increases. The sampling algorithm is then constructed by (i) obtaining the periodogram of the signal, (ii) generating a random periodogram by sampling from independent exponential distributions with parameters given by (i), and (iii) using inverse Fourier transform to obtain the new waviness sample from (ii). Figure 3.2-74 shows the comparison between the original sample and the reconstruction in both spatial and frequency domain.

3.2.6.2 Multiscale uncertainty quantification and propagation analysis for woven composites

Woven composites possess, as illustrated in Figure 3.2-75, a hierarchical structure that spans multiple length-scales from nanoscale to macroscale. Within each of these length-scales, many correlated and spatially varying uncertainty sources are introduced. However, it has not been placed on rigorously modeling the uncertainty sources and statistically propagating their effects across multiple scales. For instance, modeling spatial variations via Random Fields (RFs), connecting them across different spatial scales, and investigating stochastic simulations are often neglected. RFs which are collections of random variables indexed in either time or space was employed in this study. We introduce the Top-down sampling method that builds nested RFs by treating the hyperparameters of one RF as the responses of

another RF. This nested structure allows us to model non-stationary and C^0 (i.e., continuous but not differentiable) RFs at fine length-scales (i.e., mesoscale and microscale) with a stationary and differentiable RF at the macroscale. We motivate the use of multi-response Gaussian processes (MRGPs) to parsimoniously quantify the RFs and conduct sensitivity analyses for dimensionality reduction. The resulting approach is non-intrusive (in that the computational models need not be adapted to account for the uncertainties) and can leverage statistical techniques (such as metamodeling and dimensionality reduction) to address the considerable computational costs of multiscale simulations.

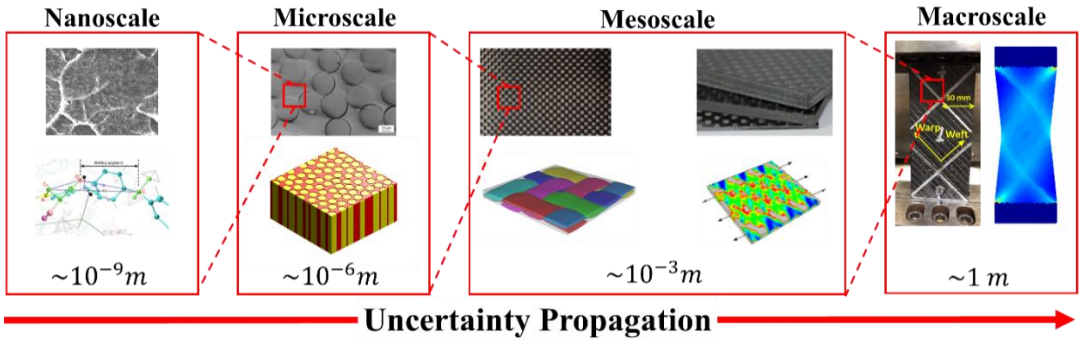

Figure 3.2-75. Multiscale structure: Schematic view of a four-scale woven fiber composite with polymer matrix. In computational modeling of this structure, each integration point at any scale is a realization of a structure at the next finer scale.

Our approach for multiscale Uncertainty Quantification (UQ) and Uncertainty Propagation (UP) has two main stages: Intra-scale UQ and inter-scale UP. We start by identifying the uncertainty sources at each scale and modeling them via RFs where one RF is associated with each structure realization. We employ RFs with sensible (i.e., physically interpretable) parameters for three main reasons: (i) To couple uncertainty sources across length-scales and enable their propagation from lower to higher scales, (ii) To connect the most important parameters of the RFs to the features of the material system and hence identify the dominant uncertainty sources in a physically meaningful way, and (iii) To allow for a non-intrusive UQ procedure by directly using the RFs' outputs in the multiscale FE simulations (instead of adapting the FE formulations for UQ and UP). Due to these reasons, we use the best linear unbiased predictor (BLUP) representation of multi-response Gaussian processes. MRGPs enable sensible characterization of uncertainty sources, are flexible and computationally efficient, and can be easily trained via available data.

At this point, the dimensionality in the UQ and UP tasks has been reduced from the number of degrees of freedom in the multiscale simulation to the few hyperparameters of the MRGP at the coarsest scale. However, depending on the material system and quantities of interest, generally not all the hyperparameters need to be considered in the UP process. Hence, further dimensionality reduction can be achieved by identifying the dominant uncertainty sources and, equivalently, the corresponding RF parameters through, e.g., sensitivity analysis.

The second stage of our approach starts by replacing the nested simulations at fine scales via inexpensive but accurate metamodels (aka surrogates or emulators) to decrease the computational costs of a single multiscale simulation from hours (or even days) to minutes. The choice of the metamodel, its inputs, and its outputs depend on the nature of the FE simulation. Finally, the uncertainty at the highest scale is quantified by propagating the uncertainty from all the finer scales in the UP process. During UP, various multiscale simulations are conducted where for each simulation one realization of the spatially

varying quantities are used in the multiscale material. To generate each of these realizations, we introduce the Top-down sampling approach where realizations are assigned to the spatially varying parameters from the coarsest scale to the finest scale in the material system. This sampling strategy enables modeling (i) non-stationary and C^0 (i.e., continuous but not differentiable) spatial variations at the fine scales, and (ii) partial correlations between the various uncertainty sources within and across scales. Although the top-down sampling method can be integrated with any analytical RF, we have chosen MRGPs since they are sufficiently flexible and possess a few hyperparameters which are all physically interpretable. Additionally, other RFs can sometimes be converted into GPs upon appropriate transformations. Our approach is demonstrated for a composite with two length-scales in Figure 3.2-76.

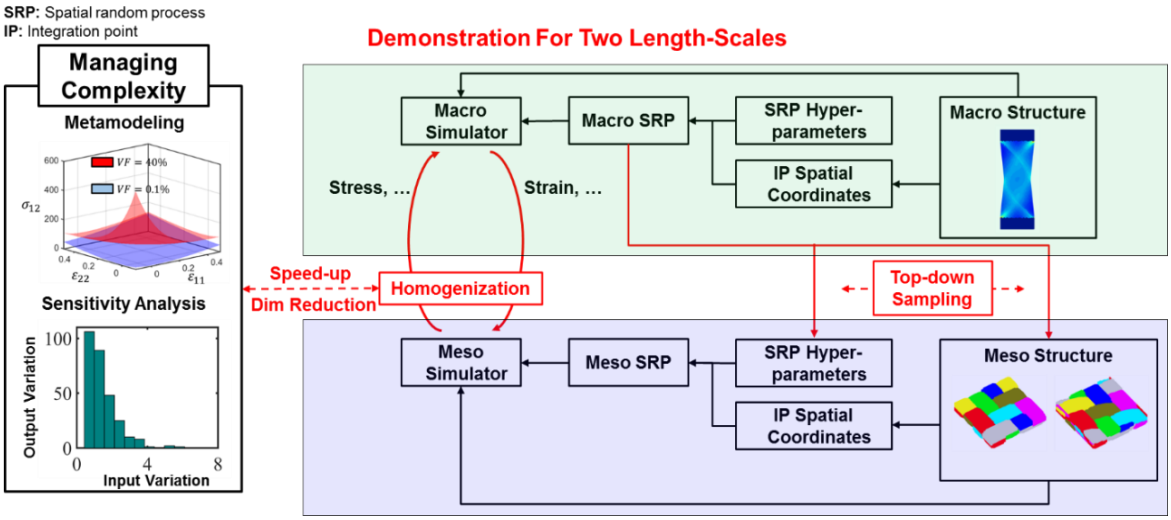

Figure 3.2-76. Demonstration of our approach for two-scale structure: Spatial random processes (SRPs) are employed for generating spatial variations which are connected through the top-down sampling procedure.

1) Multi-response Gaussian processes for uncertainty quantification

MRGPs are widely popular in RF and surrogate modeling and have been used in a wide range of applications including uncertainty quantification, machine learning, sensitivity analyses of complex computer models, Bayesian optimization, and tractable Bayesian calibration, etc. For an RF with q outputs $\boldsymbol{y} = [y_1, \dots, y_q]^T$ and the field (e.g., spatial or temporal) inputs $\boldsymbol{x} = [x_1, \dots, x_d]^T$, the BLUP representation of an MRGP with constant prior means reads as:

$$\boldsymbol{y} \sim \mathbb{N}_q(\boldsymbol{\beta}, c(\boldsymbol{x}, \boldsymbol{x}')) \tag{3.2-47}$$

where $\mathbb{N}_q$ represents a $q-$dimensional Gaussian process, $\boldsymbol{\beta} = [\beta_1, \dots, \beta_q]^T$ is the vector of responses' means, and $c(\boldsymbol{x}, \boldsymbol{x}')$ is a parametric function that measures the covariance between the responses at $\boldsymbol{x}$ and $\boldsymbol{x}'$. One common choice for $c(\boldsymbol{x}, \boldsymbol{x}')$ is:

$$c(\boldsymbol{x}, \boldsymbol{x}') = \boldsymbol{\Sigma} \otimes \exp\left\{\sum_{i=1}^{d} -10^{\omega_i}(x_i - x_i')^2\right\} = \boldsymbol{\Sigma} \otimes r(\boldsymbol{x}, \boldsymbol{x}') \tag{3.2-48}$$

where $\boldsymbol{\Sigma}$ is a $q \times q$ symmetric positive definite matrix that captures the marginal variances and the covariances between the outputs, d is the dimensionality of the field, $\boldsymbol{\omega} = [\omega_1, \dots, \omega_d]^T$ are the so-called

roughness or scale parameters that control the smoothness of the RF, and $\otimes$ is the kronecker product. Note that the dimension of $\boldsymbol{\beta}$ and $\boldsymbol{\Sigma}$ depends on q, while that of $\boldsymbol{\omega}$ depends on d. The parameters $\boldsymbol{\beta}$, $\boldsymbol{\Sigma}$, and $\boldsymbol{\omega}$ are called the hyperparameters of an MRGP model and, collectively, enable it to model a wide range of random processes:

- The mean values of the responses over the entire input space are governed by $\boldsymbol{\beta}$.
- The general correlation between the responses (i.e., y_i and y_j, $i \neq j$) over the input space is captured by the off-diagonal elements of $\boldsymbol{\Sigma}$.
- The variations around the mean for each of the responses are controlled by the diagonal elements of $\boldsymbol{\Sigma}$.
- The smooth/rapid changes of the responses across the input space are controlled by $\boldsymbol{\omega}$.

In case some experimental data are available, all the hyperparameters of an MRGP model can be estimated via, e.g., the maximum likelihood method. Otherwise, as in this work, expert or prior knowledge can be used to adjust these parameters and model a spatially varying quantity. Once these hyperparameters are determined, generating realizations from an MRGP model is achieved through a closed-form formula.

2) Top-down sampling for uncertainty propagation

To carry out one multiscale simulation, material properties must be assigned to all the IPs at all scales where the IP properties at any scale depend on an RVE at the next finer scale (this RVE itself has many IPs). Since these properties depend on the uncertainty sources (or, equivalently, on the RFs), the latter must be coupled across the scales. Recall that, due to the multiscale nature of the structure, the number of RFs significantly increases at the fine scales because we associate an RF to each structure realization.

Having used RFs whose parameters are physically sensible and can be directly linked to the uncertainty sources, this cross-scale coupling is straightforward and can be achieved with top-down sampling where the outputs of the MRGP at each IP of a particular scale serve as the hyperparameters of the MRGP of the RVE associated with that IP. This process constitutes nested RFs. To assign values to the IP parameters in the entire multiscale structure, this approach starts from the coarsest or top scale and hence the name top-down sampling.

While the Top-down sampling method works with any parametric RF representation (e.g., PCE or KL expansion), we highly recommend employing compact representations that include a few hyperparameters. This is mainly because the number of hyperparameters at the coarse scales increases rapidly as the number of spatially varying quantities increases at the fine scales. For instance, assuming three (two) quantities change spatially in a $3D$ microstructure, an MRGP with 12 (8) hyperparameters is required. To model the spatial variations of these 12 (8) hyperparameters at the mesoscale, an MRGP with 93 (47) hyperparameters is required.

3) Case study on cured woven composites

We now follow the steps of our approach to quantify the macroscale uncertainty in the elastic response of a cured woven composite as a function of spatial variations in seven uncertainty sources: fiber volume fraction and misalignment, matrix and fiber modulus, and yarns' geometry parameters (i.e., yarn angle, height, and spacing). The structure is composed of four identical woven plies that are stacked in the same orientation and constitute a total thickness of $2.4\ mm$.

The geometry of these woven plies is obtained via the bias-extension simulation of woven prepregs using the non-orthogonal constitutive preforming model. While the bottom of the sample is clamped, the other end is pulled by 1 mm to generate the bias tension deformation (as shown in Figure 3.2-77). In the macroscale simulations, $3D$ solid continuum elements are employed to discretize the structure. As our focus is on UQ and UP, at this point we have assumed that only elastic deformation occurs.

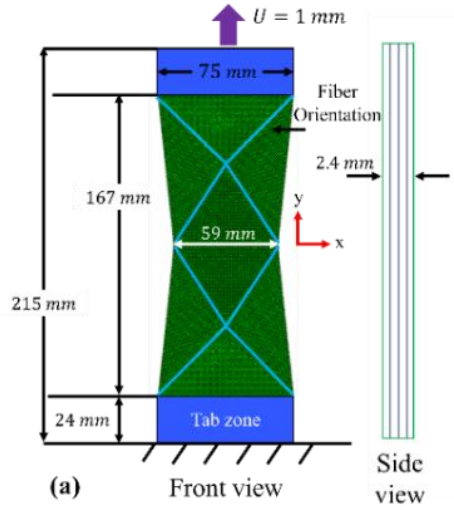

Figure 3.2-77. The macroscopic cured woven laminate structure studied in our work: The deformed structure. The light blue lines indicate the fiber orientation. The dimensions are scaled for a clearer representation.

i) Uncertainty sources

Longitudinal fiber and matrix moduli, E_f and E_m, are the first two uncertainty sources. Given the moduli, the yarn material properties primarily depend on two parameters: fiber volume fraction (in yarn), v, and fiber misalignment. While in most previous works v is postulated to be spatially constant, in practice, it varies along the yarn path particularly where yarns have compact contact [1]. Consequently, our next uncertainty source arises from the spatial variations of v which starts from the microscale and propagates to mesoscale and macroscale. In this work, we have assumed that $45\% \leq v \leq 65\%$ based on our material system.

During the manufacturing process, the fibers in the yarn deviate from the ideal orientation and render the cross-section of the yarn heterogeneous and anisotropic. These deviations result in fiber misalignment which is different from the concept of fiber waviness in that a fiber can be perfectly waved without misalignment. As illustrated in Figure 3.2-78, this misalignment can be characterized by the two angles φ and θ which measure the deviation of the fiber direction, f_1, with respect to the local orthogonal frame on the yarn cross-section, g_k. Based on the available experimental data in the literature [1], in this work we have assumed $-\pi \leq \varphi \leq \pi$ and $0° \leq \theta \leq 90°$.

In modeling the mesoscale woven composites, the yarn architecture is often presumed to be perfect where the yarn angle, α, is set to 90° and the yarn height, h, and spacing, s, are fixed to their nominal values. These assumptions do not hold in practice due to the large in-plane shear deformation during preforming process and manufacturing imperfections. Hence, we also investigate the effect of the spatial variations of the woven RVE architecture (α, h, and s) on the macroscopic properties.

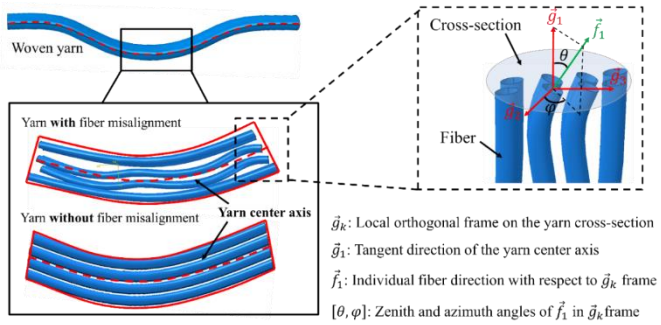

Figure 3.2-78. Fiber misalignment angles: The zenith and azimuth angles characterize the fiber misalignment angle with respect to the local orthogonal frame on the yarn cross-section.

Lastly, we note that in our example the deterministic spatial variation of α in a perfectly manufactured composite is, as opposed to the other parameters (i.e., $[v, \varphi, \theta, h, s]$), available from the preforming process simulation [2]. This deterministic variation is used as the prior mean ($\boldsymbol{\beta}$ in Equation (2.6-2)) of spatial distribution of α while for the other six parameters the nominal values are employed as the (spatially constant) prior mean. In all seven parameters, the posterior spatial variations are stochastic.

ii) Multiscale finite element simulations

We employ the computational homogenization technique for modeling the multiscale woven sample where the material property at any length-scale is calculated through the homogenization of an RVE at the lower scale. At the microscale, the RVEs consist of $300 \times 300 \times 60$ voxels ($42\ \mu m \times 42\ \mu m \times 8.4\ \mu m$) and the fibers have a diameter of $7\ \mu m$. The simulations are elastic where periodic boundary conditions (PBCs) are employed. It is assumed that the fibers and the matrix are well bonded and there are no voids. To obtain the stiffness matrix, $\boldsymbol{C}$, of the UD RVE, six stress-free loading states are applied (i.e., only one of the ε_{xx}, ε_{yy}, ε_{zz}, ε_{xy}, ε_{xz}, and ε_{yz} strain components are applied in each case). Since the simulations are elastic, $\boldsymbol{C}$ mainly depends on the volume fraction.

At the mesoscale, the open source software TexGen is used to create the geometry and mesh for the 2×2 twill woven RVE with 8 yarns. The space between the yarns is filled with matrix and voxel meshes are used to discretize the RVE where each voxel is designated to either a yarn or the matrix. To balance cost and accuracy, we have used a voxel mesh with 625000 elements. To reduce the computation costs, PBCs are employed throughout.

The nominal properties of carbon fibers and epoxy resin were taken from manufacturer's data (see Table 3.2-15). The resin is isotropic, and its material properties are taken from pure epoxy. Yarns with well-aligned fibers are treated as transversely isotropic. With fiber misalignment, however, yarns are not transversely isotropic since the material frame across the IPs on their cross-section is non-uniformly distributed. In this case, the micro-plane triad model proposed by Kedar et al. [3] is employed to account for fiber misalignment by defining an orthotropic micro-triad, $\vec{f}_k$, for each IP of the yarn. This triad is related to the local frame, $\vec{g}_k$ (see Figure 3.2-78), via the misalignment angles:

$$\vec{f}_1 = \cos(\theta)\frac{\vec{g}_1}{|\vec{g}_1|} + \sin(\theta)\cos(\varphi)\frac{\vec{g}_2}{|\vec{g}_2|} + \sin(\theta)\,sin(\varphi)\frac{\vec{g}_3}{|\vec{g}_3|} \qquad (3.2\text{-}49)$$

$$\vec{f}_2 = -\sin(\theta)\frac{\vec{g}_1}{|\vec{g}_1|} + \cos(\theta)\cos(\varphi)\frac{\vec{g}_2}{|\vec{g}_2|} + \cos(\theta)\,sin(\varphi)\frac{\vec{g}_3}{|\vec{g}_3|} \qquad (3.2\text{-}50)$$

$$\vec{f}_3 = \vec{f}_1 \hat{} \vec{f}_2 \tag{3.2-51}$$

where $|\cdot|$ and ^ denote, respectively, the norm of a vector and the cross product. As for the local frame $\vec{g}_k$, it is automatically generated by TexGen for each IP (each voxel at the mesoscale) once the woven RVE is discretized. We note that, the stiffness matrix at each yarn material point is obtained via the UD-RVE homogenization.

To link the mesoscale and macroscale, the stress-strain relations for effective elastic material properties of woven RVE are required. This relation can be written in terms of the symmetric mesoscale stiffness matrix as:

$$\begin{bmatrix} \boldsymbol{\sigma_{11}} \\ \boldsymbol{\sigma_{22}} \\ \boldsymbol{\sigma_{33}} \\ \boldsymbol{\sigma_{12}} \\ \boldsymbol{\sigma_{13}} \\ \boldsymbol{\sigma_{23}} \end{bmatrix} = \begin{bmatrix} \boldsymbol{C_{11}} & \boldsymbol{C_{12}} & \boldsymbol{C_{13}} & \boldsymbol{C_{14}} & \boldsymbol{0} & \boldsymbol{0} \\ & \boldsymbol{C_{22}} & \boldsymbol{C_{23}} & \boldsymbol{C_{24}} & \boldsymbol{0} & \boldsymbol{0} \\ & & \boldsymbol{C_{33}} & \boldsymbol{C_{34}} & \boldsymbol{0} & \boldsymbol{0} \\ & & & \boldsymbol{C_{44}} & \boldsymbol{0} & \boldsymbol{0} \\ & \boldsymbol{Sym.} & & & \boldsymbol{C_{55}} & \boldsymbol{C_{56}} \\ & & & & & \boldsymbol{C_{66}} \end{bmatrix} \begin{bmatrix} \boldsymbol{\varepsilon_{11}} \\ \boldsymbol{\varepsilon_{22}} \\ \boldsymbol{\varepsilon_{33}} \\ \boldsymbol{2\varepsilon_{12}} \\ \boldsymbol{2\varepsilon_{13}} \\ \boldsymbol{2\varepsilon_{23}} \end{bmatrix} \tag{3.2-52}$$

Table 3.2-15. Fiber and matrix properties: The moduli (i.e., E and G) are all in GPa. Poisson's ratios along different directions are also provided.

	E_{zz}	$E_{xx} = E_{yy}$	$\nu_{zx} = \nu_{zy}$	ν_{xy}	$G_{xz} = G_{yz}$	G_{xy}
Carbon fiber	275	19.8	0.28	0.32	29.2	5.92
Epoxy resin	3.25	3.79	0.39	0.39	1.36	1.36

To reduce the multiscale UQ and UP costs, we employ metamodels to replace the micro and mesoscale FE simulations corresponding to each macroscale IP. In particular, the metamodel captures the macroscale spatial variations of the stiffness matrix (see Equation (3.2-52)) of the woven RVEs associated with the macroscale IP's as a function of yarn angle (α^2), average volume fraction ($\bar{v}^2$), yarn height (h) and spacing (s), average misalignment angle ($\bar{\theta}^2$), and fiber and matrix moduli (E_f and E_m). In machine learning parlance, the inputs and outputs of the metamodel are, respectively, $[\alpha^2, \bar{v}^2, s^2, h^2, \bar{\theta}^2, E_f, E_m]$ and the stiffness matrix $\boldsymbol{C}$ of a woven RVE. To fit the metamodel, we generated six training datasets of sizes $60, 70, \dots, 110$ with Sobol sequence [90, 91] for $\alpha^2 \in [45°, 90°]$, $s^2 \in [2.2, 2.5]\ mm$, $h^2 \in [0.3, 0.34]\ mm$, $\bar{v}^2 \in [40\%, 70\%]$, $E_f^2 \in [150, 400]\ GPa$, $E_m^2 \in [1.5, 5]\ GPa$, and $\bar{\theta}^2 \in [0°, 6°]$. Afterwards, we fitted an MRGP metamodel to each dataset. The accuracy of each model was then evaluated against a validation dataset with 30 samples via:

$$e = 100\sqrt{\frac{1}{30}\sum_{i=1}^{30}\left(1 - \frac{\hat{y}_i}{y_i}\right)^2}\ \% \tag{3.2-53}$$

where $\hat{\boldsymbol{y}} = [\hat{y}_1, \dots, \hat{y}_{30}]$ and $\boldsymbol{y} = [y_1, \dots, y_{30}]$ are obtained from, resepectively, the metamodel and FE simulations. The prediction error of each model is illustrated in Figure 3.2-79 where it is evident that with roughly 100 samples all the elements of $\boldsymbol{C}$ can be predicted with less than 6% error.

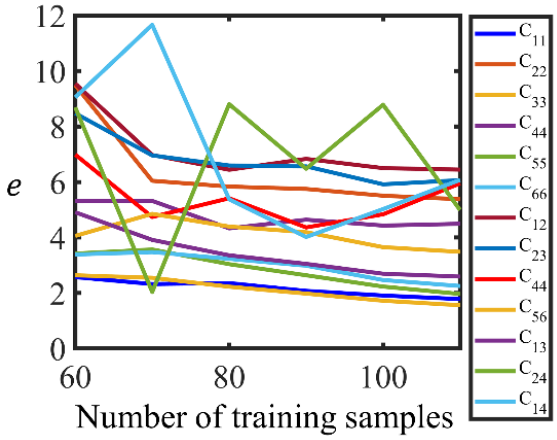

Figure 3.2-79. Prediction error as a function of the number of training samples: As the number of training samples increases, the accuracy of the MRGP metamodel in predicting the elements of the stiffness matrix of the mesoscale woven RVE increases.

As metamodeling is a broadly applicable tool (also outside the field of stochastic multiscale modeling), two user-friendly Graphical Interfaces have been developed: Optimal Latin Hypercube Sampling (OLHS), and Gaussian Process modeling. The ideology behind these tools is to be functional and complete, while being intuitive enough for novice users. Furthermore, the graphical interfaces have been developed using Matlab Guide and can be run on any 64bit computer under the windows operating environment.

As shown in Figure 3.2-80 (a), OLHS Generation and visualization package allows for the automatic generation of training data inputs that span the desired metamodel space as optimal and uniform as possible. Any number of input variables and number of samples can be specified. As shown in Figure 3.2-80 (b), our package for GRP is applicable to multi-dimensional and multi-response datasets and can automatically handle noisy observations once enough training data is provided. Additionally, the interface includes features that allow the user to evaluate metamodel accuracy, perform prediction on unobserved inputs, and visualization that allows the user to conveniently investigate input-output relations regardless of problem dimensionality.

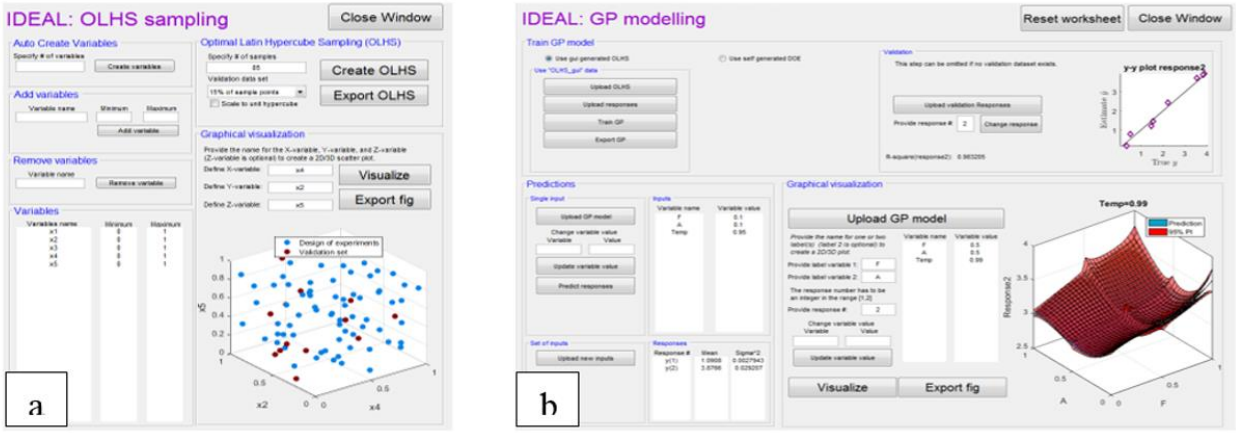

Figure 3.2-80. Screenshots of graphical user interfaces: (a) optimal Latin hypercube sampling user interface. (b) Gaussian process modeling user interface.

iii) Top-down sampling, coupling, and random field modeling of uncertainty sources

To help clarify the descriptions, we first introduce some notation. We denote the three scales with numbers: $1 \rightarrow Macro$, $2 \rightarrow Meso$, $3 \rightarrow Micro$.Superscript and subscripts denote, respectively, scales and IPs. Variables with a bar represent averaged quantities over all the IPs at a particular scale. For instance, v_i^1 denotes the fiber volume fraction assigned to the i^{th} IP at the macroscale. $\bar{\theta}^2 = \frac{1}{N}\sum_{i=1}^{N}\theta_i^2$ represents the average misalignment (zenith) angle at the mesoscale for a woven RVE.

The uncertainty sources in our composite are summarized in Table 3.2-16. While some sources are only defined among different structures (under spatial variations across realizations), others possess an extra degree of variation in that they also change within structures.

Table 3.2-16. Uncertainty sources for one macro structure realization: The sources are fiber misalignment angles (θ and φ), yarn spacing and height (s and h), fiber and matrix moduli (E_f and E_m), fiber volume fraction (v), and yarn angle (α).

Scale	Uncertainty Sources	
Micro	$\bar{v}^3, E_f, E_m$	None
Meso	$\theta_i^2, \varphi_i^2, v_i^2, E_f, E_m, \alpha^2, s^2, h^2$	$\theta_i^2, \varphi_i^2, v_i^2$
Macro	NA	$\theta_i^1, \varphi_i^1, v_i^1, {E_f}_i^1, {E_m}_i^1, \alpha_i^1, s_i^1, h_i^1$

Assuming the eight tows in a woven RVE are statistically independent and the spatial variations within them originate from the same underlying random process, a total of 12 hyperparameters are required to completely characterize the spatial variations of $\left[\theta_i^2, \varphi_i^2, v_i^2\right]$ by an MRGP (see $Eq.17$): three mean values ($\boldsymbol{\beta} = \left[\beta_v, \beta_\varphi, \beta_\theta\right]^T$), six variance/covariance values for $\boldsymbol{\Sigma}$ ($\left[\sigma_{vv}^2, \sigma_{\varphi\varphi}^2, \sigma_{\theta\theta}^2, \sigma_{v\varphi}^2, \sigma_{v\theta}^2, \sigma_{\varphi\theta}^2\right]$), and three roughness parameters ($\boldsymbol{\omega} = \left[\omega_x, \omega_y, \omega_z\right]^T$ where xyz denotes the cartesian coordinate system at the mesoscale). Once these parameters are specified, the spatial coordinates of the IPs in a woven RVE can be used to assign realizations of v, φ, and θ to them. For each IP at the macroscale, however, these 12 hyperparameters serve as some of the responses of the macroscale MRGP whose other responses

correspond to $\left[E_{f_i}^2, E_{m_i}^2, \alpha_i^2, s_i^2, h_i^1\right]$. Therefore, the macroscale MRGP has a total of 173 hyperparameters (17 mean values for $\boldsymbol{\beta}$, 153 unique covariance/variance values for $\boldsymbol{\Sigma}$, and 3 values for $\boldsymbol{\omega} = \left[\omega_\eta, \omega_\xi, \omega_\zeta\right]^T$ where $\eta\xi\zeta$ denotes the cartesian coordinate system at the macroscale). In the top-down sampling approach, first the 173 hyperparameters of the macroscopic MRGP are prescribed. Then, this MRGP is sampled to assign 17 values to each macroscopic IP where 12 of them serve as the hyperparameters of the mesoscopic MRGPs, 3 of them are employed to construct the woven RVE, and 2 of them to determine the fiber and matrix moduli. This process is illustrated in Figure 3.2-81 where, for clarity, only two (out of the 17) hyperparameters at the mesoscale are presented.

iv) Dimension reduction at the mesoscale via sensitivity analysis

By modeling the spatial variations via RFs, the dimensionality of the UQ and UP problem has decreased to the number of RF hyperparameters. Although this is a significant reduction, the considerable cost of multiscale simulations (even in the linear analysis) renders the UQ and UP process computationally demanding. To address this issue, we note that depending on the property of interest a subset of uncertainty sources are generally the dominant ones in physical systems. Since our composite undergoes an elastic deformation, we expect a small subset of the uncertainty sources (i.e., RF hyperparameters) to be important.

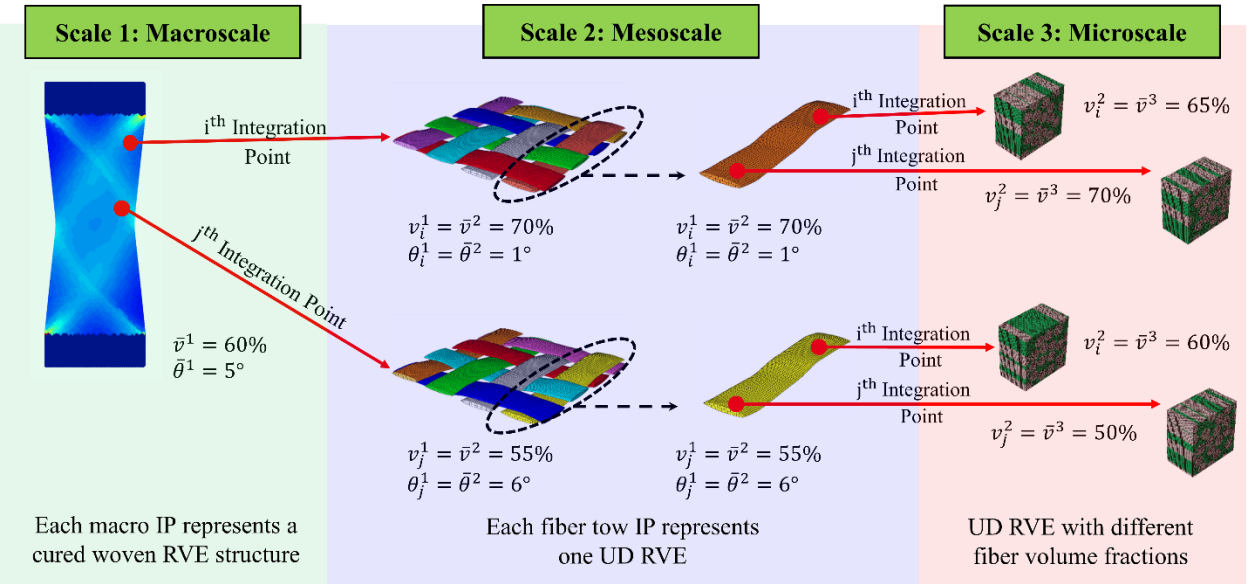

Figure 3.2-81. Coupling the uncertainty sources across the scales: The spatial variations of v and θ at the macroscale are connected to those at the finer scales. For brevity, the coupling is illustrated only for the average values for the two quantities (i.e., the mean of the RFs: $\boldsymbol{\beta} = [\beta_v, \beta_\theta] = [\bar{v}^2, \bar{\theta}^2]$).

We conducted multiscale sensitivity analyses to determine which of the 12 hyperparameters of an MRGP model are the most important ones (and must be considered in UP) based on their impact on mesoscale material response. Our studies (see Table 3.2-17) consisted of changing one of the hyperparameters (while keeping the rest of them fixed) and conducting 20 simulations to account for the randomness. Then, if the variations in the homogenized response (effective moduli) were negligible, the hyperparameter was deemed as insignificant and set to a constant thereafter. All the simulations in this section were conducted on a woven RVE with $\alpha = 90°$.

Table 3.2-17. Case studies to determine the effect of fiber misalignment and its spatial variations: The triplets in the description fields correspond to $\left(\bar{\theta}^2, var(\theta^2), var(\varphi^2)\right)$.

Case ID	Description	Case ID	Description
1	$(1°, 1, 20^2)$	10	$(1°, 1, 50^2)$
2	$(1°, 5, 20^2)$	11	$(1°, 5, 50^2)$
3	$(1°, 10, 20^2)$	12	$(1°, 10, 50^2)$
4	$(3°, 1, 20^2)$	13	$(3°, 1, 50^2)$
5	$(3°, 5, 20^2)$	14	$(3°, 5, 50^2)$
6	$(3°, 10, 20^2)$	15	$(3°, 10, 50^2)$
7	$(5°, 1, 20^2)$	16	$(5°, 1, 50^2)$
8	$(5°, 7, 20^2)$	17	$(5°, 7, 50^2)$
9	$(5°, 10, 20^2)$	18	$(5°, 10, 50^2)$

We found that the homogenized moduli are affected by neither the six covariance/variance values (i.e., $[\sigma^2_{vv}, \sigma^2_{\varphi\varphi}, \sigma^2_{\theta\theta}, \sigma^2_{v\varphi}, \sigma^2_{v\theta}, \sigma^2_{\varphi\theta}]$) nor the three roughness parameters $\boldsymbol{\omega} = [\omega_x, \omega_y, \omega_z]^T$. In case of average values (i.e., $\boldsymbol{\beta}$), the average fiber volume fraction ($\bar{v}$) and zenith angle ($\bar{\theta}$), as opposed to that of the azimuth angle, were found to considerably affect the homogenized response of a woven RVE at the mesoscale. The effect of average values on the effective moduli are summarized in Figure 3.2-82. As illustrated in Figure 3.2-82 (a), the moduli increase linearly as a function of average fiber volume fraction. Comparing the first nine Cases in Figure 3.2-82 (b) with the last nine Cases, it can be concluded that $var(\varphi^2)$ insignificantly affects the moduli and poison ratios. Figure 3.2-82 (b) also indicates that the deviations from the reference solution increase as $\bar{\theta}^2$ increases ($\bar{\theta}^2$ increases between the jumps, see Table 3.2-17).

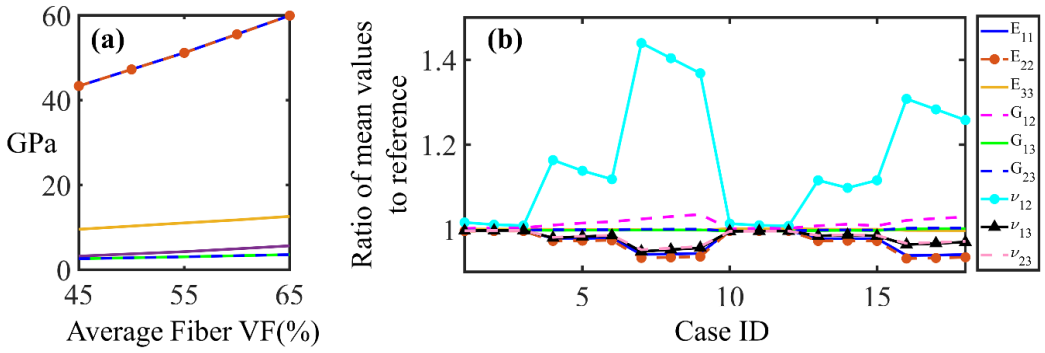

Figure 3.2-82. Effect of average values on the effective moduli of a woven RVE: (a) Effect of fiber volume fraction and, (b) Effect of misalignment. Each point on these figures indicates the average

value over 20 simulations. The Case IDs in (b) are defined in Table 3.2-18. The reference solution refers to a case where there is no misalignment.

It must be noted that since we are interested in the elastic response of the multiscale composite in Figure 3.2-82, the variations of effective moduli were only considered in our sensitivity studies. As opposed to the effective behavior, the local behavior (i.e., stress field) of the woven RVE is quite sensitive to the spatial variations of both v and θ (but not φ) and must be considered in nonlinear analysis.

v) Results on macroscale uncertainty

Multiple macro simulations are conducted where $\theta_i^1, v_i^1, {E_f}_i^1, {E_m}_i^1, \alpha_i^1, s_i^1$, and h_i^1 change spatially across the macroscale IPs. To quantify the importance of these variables' spatial variations on the macroscopic behavior, eight cases are considered. As detailed in Table 3.2-18, the spatial variations are changed with an MRGP at the macroscale in a controlled manner from one case to the next. Except for the last case, 20 independent macroscale simulations are conducted for each case to account for the randomness. In summary, a total of 161 macroscale simulations are conducted. The last case study serves as the reference where there is no misalignment, α_i^1 is determined via the processing simulation over the structure as illustrated in Figure 3.2-83 (b), and all other parameters are set to their nominal values, i.e., $v_i^1 = 55\%, {E_f}_i^1 = 275\ GPa, {E_m}_i^1 = 3.25\ GPa, s_i^1 = 2.35\ mm$, and $h_i^1 = 0.32\ mm$. In cases 1 through 7, the effect of spatial variations is considered for one parameter at a time where the amount of variations with respect to the prior mean is controlled by the variance of the macroscale MRGP. In these cases, we set the variance associated with the spatially varying parameter to, respectively, $9, 25, 1, 0.05^2, 0.01^2, 40^2$, and 1. These variances are large enough to capture realistic spatial variations while small enough to ensure that the realized values are not outside the ranges where the mesoscale MRGP metamodel is fitted. Sample spatial variations for case 1 and 3 are demonstrated in Figure 3.2-83 (b) through 3.2-83 (e).

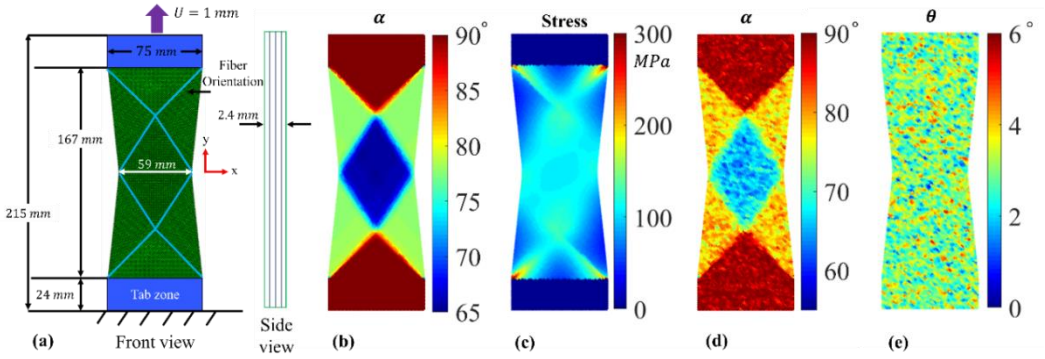

Figure 3.2-83. The macroscopic cured woven laminate structure studied in our work: (a) The deformed structure. The light blue lines indicate the fiber orientation. The dimensions are scaled for a clearer representation. (b) The deterministic spatial variations of yarn angle obtained from simulating a perfectly manufactured composite. (c) Von Mises stress field corresponding to Case 9 (Table 3.2-18). (d) The random spatial variations of yarn angle corresponding to one of the realizations of Case 1 (Table 3.2-18). (e) The random spatial variations of $\bar{\theta}^1$ corresponding to one of the realizations of Case 3 in Table 3.2-18).

Since in reality the uncertainty sources coexist, in case 8 we consider the effect of all the uncertainty sources and their correlation. Here, the individual variances (diagonals of macroscale MRGP, Σ) are the

same as in cases 1 through 7 while the covariances are chosen to reflect the negative correlation between the fiber volume fraction and both yarn and fiber misalignment. To this end, we choose $[\sigma_{\alpha v}, \sigma_{\alpha\theta}, \sigma_{v\theta}] = [-9, 3, -3]$ and set the rest of the off-diagonals of $\mathbf{\Sigma}$ to zero. We note that $\sigma_{\alpha v}$ is negative to model the increase in fiber volume fraction as the yarns get closer after preforming. $\sigma_{v\theta}$ is also negative to consider the decrease in misalignment angle in rich fiber regions.

Table 3.2-18. Description of the simulation settings: Nine simulation cases are considered to quantify the macroscale uncertainties and the relative importance of spatial variations. MRGPs are employed to generate random realizations in all cases. Except for case 9 (reference simulation), all cases consist of 20 simulations to account for randomness where only one uncertainty source exists.

	Description
Case 1	Spatial variations in α with its prior spatial distribution determined by processing simulation
Case 2	Spatial variations in fiber volume fraction with a constant prior of 55% over the structure
Case 3	Spatial variations in fiber misalignment with a constant prior of 3° over the structure
Case 4	Spatial variations in yarn spacing with a constant prior of 2.35 mm over the structure
Case 5	Spatial variations in yarn height with a constant prior of 0.32 mm over the structure
Case 6	Spatial variations in fiber modulus with a constant prior of 275 GPa over the structure
Case 7	Spatial variations in matrix modulus with a constant prior of 3.25 GPa over the structure
Case 8	Spatial variations in all parameters
Case 9	All parameters set to nominal values (α from processing simulation) and no misalignment

Figure 3.2-84 (a) compares the exerted force on the cross-section of the sample for the nine cases where, for cases 1 through 8, the force-displacement line is averaged over the 20 multiscale simulations. The results suggest that in the presence of fiber misalignment, the structure weakens and hence the reaction force decreases. This weakening is exacerbated in the presence of other uncertainty sources. In particular, while in the reference case the maximum reaction force (magnitude) is 15.4 kN, in cases 3 and 8 it is 14 kN and 13.5 kN, respectively. These results indicate that: (i) Fiber misalignment must be accounted for in the simulation of composites even if one is primarily interested in the global response in linear analyses. (ii) The interaction among various uncertainty sources should be considered: once all the uncertainty sources are accounted for, the structure is more noticeably weakened with a 12.3% reduction in reaction force. (iii) The insensitivity to the spatial variations of some parameters can be explained by the fact that in linear analyses the global response is mainly affected by the averaged properties. Since we only introduce spatial variations (we do not change the parameter averages over the structure except for fiber misalignment), the results intuitively make sense.

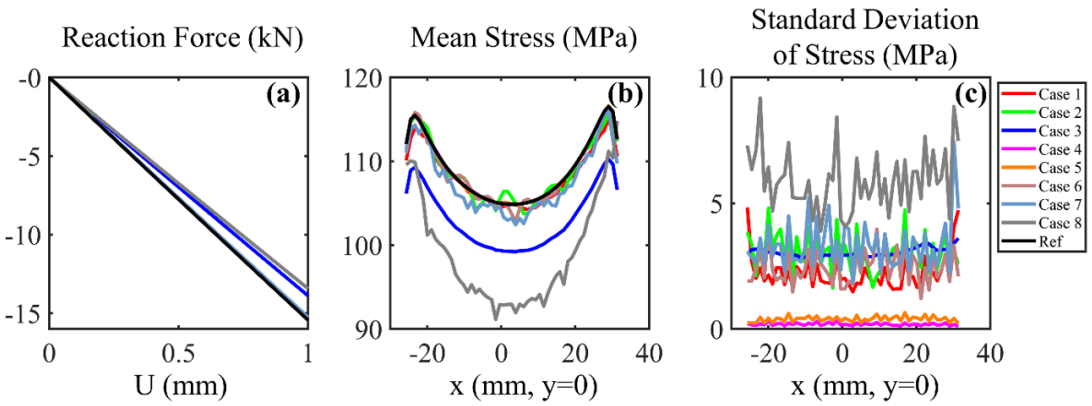

Figure 3.2-84. Global and local response of the macrostructure to the spatial variations: (a) Reaction force, (b) Mean stress at the mid-section, and (c) Standard deviation of the stress field at the mid-section. For cases 1 through 8 in (b) and (c), the curves are based on 20 independent simulations. See Table 3.2-18 for the definition of the cases.

To illustrate the effect of spatial variations on local behavior, we compare the average and standard deviation of the von-Mises stress field over the mid-section of the structure in Figure 3.2-84 (b) and Figure 3.2-84 (c), respectively. We choose the mid-section over the entire structure for analyzing the strain field since an explicit solver is employed in our multiscale FE simulations where artificial stress concentrations might occur at the boundaries of the structure. The curves in these two figures are obtained by analyzing the 20 simulations corresponding to each case. Similar to Figure 3.2-84 (a), Figure 3.2-84 (b) demonstrates that the structure weakens in the presence of fiber misalignment as the mean stress over the mid-section is lower than that of the reference structure (case 9). It is evident that the most realistic case where all the uncertainty sources are present results in the weakest structure. More interestingly, this weakening is not uniform over the mid-section and is the largest at the middle where the reduction is roughly 12.3%.

The highest variations among the simulations of a specific case are observed in case 8, where all the parameters change spatially and relatively, Figure 3.2-84 (c). Cases 2, 3, and 7 are next in line with cases 2 and 7 having more fluctuations among the IPs (note that each point along the x-axis corresponds to an IP in the mid-section). Finally, cases 4 and 5, which correspond to the simulations where the yarn spacing and height change, have the least amount of variations. This is expected since the stiffness matrix of a woven RVE (obtained via the mesoscale MRGP metamodel) is also insignificantly sensitive to these parameters. We highlight, however, that we have considered a relatively small range of variations for these two parameters. Their effect will be more prominent if these ranges are increased.

References

[1] Requena G, Fiedler G, Seiser B, Degischer P, Michiel M.D, Buslaps T. 3D-Quantification of the distribution of continuous fibers in unidirectionally reinforced composites. Composites Part a-Applied Science and Manufacturing, 2009. 40(2): p. 152-163.

[2] Zhang W, Ren H, Liang B, Zeng D, Su X, Dahl J, Mirdamadi M, Zhao Q, Cao J. A non-orthogonal material model of woven composites in the preforming process. CIRP Annals, 2017. 66(1): p. 257-260.

[3] Kirane K, Salviato M, Bažant Z P. Microplane triad model for simple and accurate prediction of orthotropic elastic constants of woven fabric composites. Journal of Composite Materials, 2016. 50(9): p. 1247-1260.

3.2.7 Part-Level Molding and Model Validation

Focus of this subtask is on providing part-level experimental results to validate the models developed in Task 2. Following are the validations conducted:

1) Double-dome preforming with woven composites
2) SMC plaque compression molding
3) Hat section crash simulation
4) UD laminate fatigue life prediction

3.2.7.1 Double-dome preforming with woven prepregs

Part-scale preforming experimental validation in this section measures the prediction accuracy of the non-orthogonal prepreg material model and the multiscale preforming simulation method developed in Section 3.2.2. It also provides guidance about the limitations of current simulation methods and possible solutions in the future. Finally, selection of various process parameters in preforming validation experiments leads to different part qualities. Observation and summary of the relation between process parameters and parts' quality can serve as an empirical rule to produce high-quality parts either for research or for real production application.

Double-dome shape is used to validate the non-orthogonal material model and the multiscale preforming simulation method at part-scale. Double-dome geometry applied in this project has 3D shape and complex double curvature features at the size of common automobile parts. It is an ideal benchmark to quantitatively measure prediction accuracy of the preforming models for real part production. In validation, not only the final part shape, but also the yarn angle at different locations, and forming force, are compared. Different process parameter combinations are tested in order to ensure that the models can work at various production conditions. Comparison between the non-orthogonal model and conventional orthotropic material models is also performed to show the improvement we achieved for preforming simulation.

1) <u>Molding of double-dome parts</u>

Preforming is a temperature varying process because of the utilization of hot prepreg sheets and cold/warm tools in the process. In the double-dome preforming validation experiments performed for this project, supplied prepregs were first heated in an oven to around 70 ºC and then placed in a press for preforming. The geometry of the double-dome punch and the binder are demonstrated in Figure 3.2-85, while the experimental setup is illustrated in Figure 3.2-86. For fast production rate, the press was kept at 23 ºC by the coolant running within it, therefore the temperature of the prepregs dropped from the initial value during preforming. In a single layer preforming setup, temperature history at the top surface center, bottom surface center, and one side point on the top surface of one prepreg are measured by thermocouples and plotted in Figure 3.2-86 (b). The plot indicates that the prepreg reached a temperature of around 70 ºC in the oven. Then, it was cooled down gradually to around 45 ºC by air during the transportation from the oven to the press. When placed in the press, the cooling rate increased greatly due to heat conduction between the hot prepreg and cold metal. Specifically, the temperature dropped 20 ºC within the first 2 seconds. Meanwhile, it took the press 10 seconds to contact the punch and the prepreg and another 6 seconds to finish preforming. Therefore, the actual temperature of the prepreg during this preforming process was very close to 23 ºC, i.e., the press temperature. As a result, although the preforming models are capable of taking temperature-dependence into account, in the current validation experimental setup, it is reasonable to characterize the mechanical properties of prepregs and simulate the preforming process at a fixed temperature of 23 ºC.

Figure 3.2-85. Geometry of the double-dome punch and the binder.

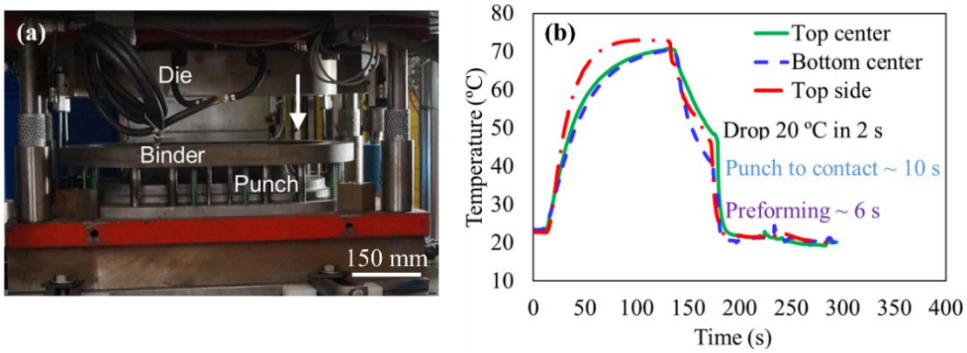

Figure 3.2-86. Double-dome preforming test setup: (a) The press for the preforming, and (b) the prepreg temperature history plot. The plot indicates that the prepreg temperature drops rapidly from the initial 70 ºC to around 23 ºC when it is placed under the press.

Preforming simulation models, utilizing either experiment-based non-orthogonal material model or multiscale method, were established in LS-DYNA using the dynamic explicit integration method. The simulation setup is illustrated Figure 3.2-87: layers of prepregs are preformed in this process where punch displacement is 90 mm, and binder force increases linearly from 4000 N to 8200 N from experimental measurements. Thickness of the prepregs is orders of magnitude smaller compared to its length and width, so the prepregs are discretized by reduced integrated shell element S4R to reduce the computational cost. Each element is about 4 mm × 4 mm with five through-thickness integration points. Tools are simulated as rigid bodies because of their high stiffness compared to the soft prepregs with uncured resin, hence, their element type will not affect simulation results. S3 elements are selected to discretize the tools because of their excellent auto-mesh capability for complex geometries. Friction coefficient between tools and prepregs is set to 0.3 according to the experimental measurement. The friction coefficient is the constant dynamic one in LS-DYNA and the static friction is neglected because the preforming process leads to large prepreg deformation which, in turn, results in large sliding between the tools and prepregs.

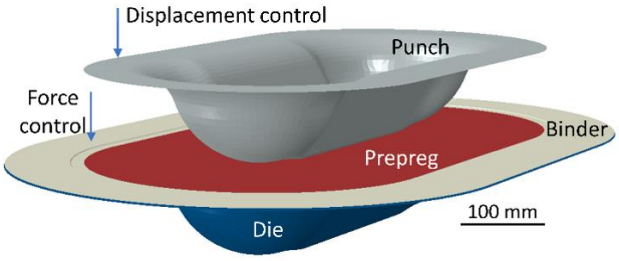

Figure 3.2-87. Double-dome preforming simulation setup.

2) Preforming model validation

For the first set of validation, only one layer of prepreg with ±45º initial fiber orientation was preformed. The results from the experiment, simulation with experiment-based non-orthogonal material model, and simulation with conventional orthotropic material model, are compared. In simulation models, material properties were calibrated using uniaxial tension, bias extension and bending tests at 23ºC, while the initial angle between the yarn direction and the global coordinates was defined as a material input property to identify the fiber layup. The simulation results in the upper-right quarter of Figure 3.2-88 shows that the non-orthogonal material model established is capable of accurately predicting the physical experiments regarding the yarn angle distribution and blank draw-ins. For instance, the deviation of the maximum draw-in distance is about 9 mm, as listed in Table 3.2-19. For comparison, an orthotropic material model (MAT_002) is utilized in another simulation whose result is shown in the upper-left quarter of Figure 3.2-88. Since the orthotropic model cannot track material property changes during the rotation of yarns, the corresponding simulation has a maximum draw-in deviation of 24 mm, as listed in Table 3.2-19, not capturing the overall process behavior.

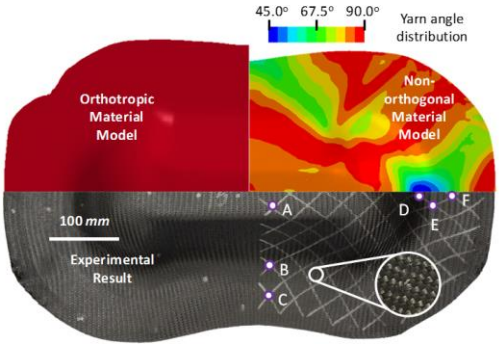

Figure 3.2-88. Simulation and experimental results comparison of deformed geometry and yarn angle distribution for double-dome preformed part of ±45º single layer woven prepreg.

In the non-orthogonal model, yarn angle is defined as an output variable, while MAT_002 does not have the capability for direct visualization. For clarity, Table 3.2-19 compares the resulting shear angles at various locations obtained from the experiment and simulations. Again, it shows that the current model has improved the prediction accuracy. The fiber orientation (yarn angle) prediction errors at only half of the locations reach the proposed 5%, which is unsatisfactory.

Table 3.2-19. Draw-in distance and yarn angle comparison between simulation and experiment: simulation results are from the experiment-based non-orthogonal material model and the conventional orthotropic material model (MAT_002).

Comparison	Draw-in	A	B	C	D	E	F
Non-orthogonal	40.22mm	89º	89º	71º	40º	45º	65º
Orthotropic	25.00mm	70º	85º	86º	47º	59º	77º
Experiment	49.02mm	80º	88º	71º	49º	56º	66º

The reason for the unsatisfactory fiber orientation prediction accuracy is that this non-orthogonal material model only utilizes experimental data from uniaxial tension (pure tension) and bias-extension (pure shear) tests. The coupling between tension and shear is neglected. For real prepregs, an increase of tension along the yarns will increase the contact force and friction force between warp and weft yarns, resulting in a shear resistance increase. This kind of mechanism is not simulated by the experiment-based non-orthogonal model. It is, however, captured by the multiscale preforming simulation method, where virtual material characterization is performed by experimentally calibrated mesoscopic RVE models that can be deformed to arbitrary strain. To demonstrate the improvement from multiscale modeling, its simulation result is compared against the one obtained from the previous non-orthogonal material model. Final prepreg geometry and yarn angle distribution results are demonstrated in Figure 3.2-89 (a) together with the real preformed part. The draw-in distance and the yarn angle at the sampling locations from the simulation and the experiment are listed in Table 3.2-20. The comparison indicates that this multiscale method with tension-shear coupling fulfils the proposed 5% error of fiber orientation (yarn angle) prediction at 5 out of 6 sampling points, and prediction errors at all sampling points are less than 8%.

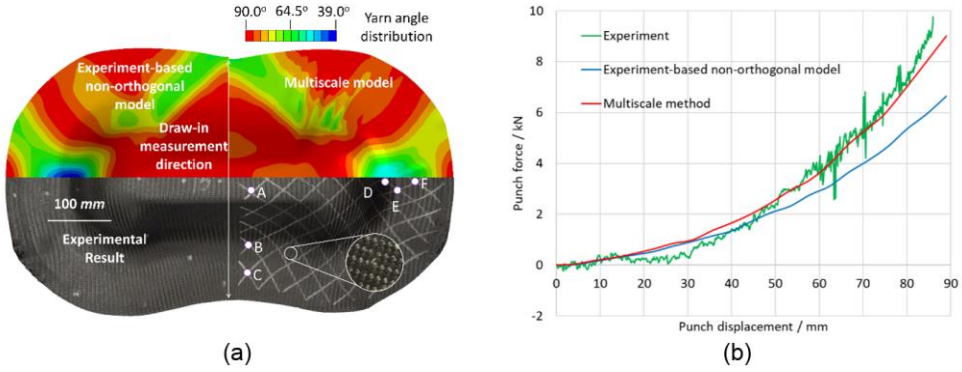

Figure 3.2-89. Preforming simulation: (a) final part shapes and yarn angle distributions, and (b) punch force comparison. In (a), A-E points indicate yarn angle measuring positions.

Table 3.2-20. Draw-in distance and yarn angle comparison between the simulation and the experiment: The simulation results are from the new multiscale material model and the tension-shear decoupled material model.

Comparison	Draw-in	A	B	C	D	E	F
Multiscale	42.25 mm	86º	88º	73º	54º	57º	67º
Non-orthogonal	40.22 mm	89º	89º	71º	40º	45º	65º
Experiment	49.02 mm	80º	88º	71º	49º	56º	66º

The punch force-displacement curves from the two simulation cases and the experiments are compared in Figure 3.2-89 (b). The plots demonstrate that the multiscale preforming simulation method predicts the punch force nearly the same as the experimental one compared to the simulation using the experiment-based non-orthogonal material model, which underestimates the experimental punch force by around 26%. The small discrepancy between the forces from the new simulation method and the experiment when the punch displacement reaches to over 70 mm may be caused by the negligence of the prepreg thickness variation by the shell elements in the simulation. The small force discrepancy when the punch displacement ranges from 20 to 50 mm, however, may result from the fact that the temperature at some locations of the prepreg has not completely reached 23 ºC at the initial stage of the preforming, leading to softer material behavior compared to the one for the simulation. As a summary, this multiscale preforming simulation method with tension-shear coupling can predict the draw-in distance and the yarn angle variation on the preformed prepreg. More importantly, it also predicts the punch force history with high accuracy. This multiscale method, therefore, has stronger predictive capability than the experiment-based non-orthogonal mode does, and can serve as a powerful tool for part performance prediction, process parameters optimization, material design, and defect analysis for future preforming works.

After single layer preforming validation with a ±45º initial fiber orientation and 6 yarn angle measuring locations, further validation with different measuring locations, different initial fiber orientations, and different numbers of prepreg layers (0º/90º one layer, ±45º one layer, and 0º/90º/±45º two layers) were performed. Because of project time limitations, only the simulation results from the experiment-based non-orthogonal model are compared with the experimental ones. The multiscale simulation method was not applied to these configurations.

Simulation and experiment results with different initial fiber orientations are depicted in Figure 3.2-90. The draw-in distance comparison is listed in Table 3.2-21. It can be seen that most of the draw-in distances predicted by simulation are within the ranges of the experiment results. The two largest deviations happened, however, in the x direction draw-in for -45/+45 initial fiber orientation in both single layer and double layers cases. It is also worth noting that for single layer -45/+45 setup, in experiments, specimen size in the x direction actually became larger (negative draw-in distance) after preforming, which is different from not only the simulation, but also common forming processes.

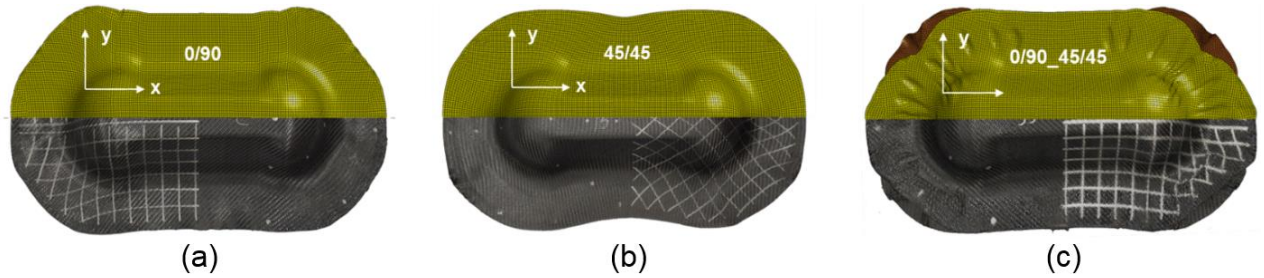

Figure 3.2-90. Double-dome comparison with different initial prepreg layer orientations: (a) 0/90, (b) -45/+45, and (c) 0/90/-45/+45. The simulation results are shown in the top half while the experimental ones are in the bottom half. The silver lines on the experimental results indicate the directions of the warp and weft yarns.

Table 3.2-21. Double-dome draw-in distance comparison.

Initial orientation	exp x draw-in / inch	sim x draw-in / inch	exp x draw-in / inch	exp x draw-in / inch
0/90	0.70 ~ 1.34	1.50	1.27 ~ 1.71	1.73
-45/+45	-0.60 ~ -0.15	0.10	1.43 ~ 1.95	1.70
0/90 in 0/90/-45/+45	1.00 ~ 1.38	1.00	1.53 ~ 1.61	1.46
-45/+45 in 0/90/-45/+45	0.25 ~ 0.32	1.45	0.99 ~ 1.19	1.62

For warp and weft yarn angle distribution, results are shown in Figure 3.2-91. It can be seen that for the single layer cases, the simulation agrees well with the experiment. At nearly all measuring locations simulation results are within experimental deviation and achieve the proposed 5% prediction error compared to the averaged experimental results. For the double layer, however, the discrepancy is larger. The most possible reason for this discrepancy is that the rapid drop of prepreg temperature, as shown in Figure 3.2-92, results in resin melting and re-solidify between two prepreg layers, which causes very tacky or even disappeared prepreg interface, leading to much larger interaction strength and makes relative sliding between prepregs a lot more difficult compared to simulation. Actually from an experimental aspect, the supplied prepreg in this project has the best preforming temperature at 50 to 80 ºC when the resin is molten but not cured. When the temperature drops down to around 23 ºC, the resin will be hard and very sticky, leading to undesired features such as edge breakage, discontinuous deformation, and out-of-plane deformation or even folding, as shown in Figure 3.2-92. In the future not only the temperature-dependent prepreg surface interaction should be taken into account in preforming simulation, but also it might be necessary to adjust the temperature of the tools by warming the coolant to the desired temperature. The purpose for this operation is not simply to reduce simulation and experiment discrepancies, but more importantly, it can improve the quality of the final parts.

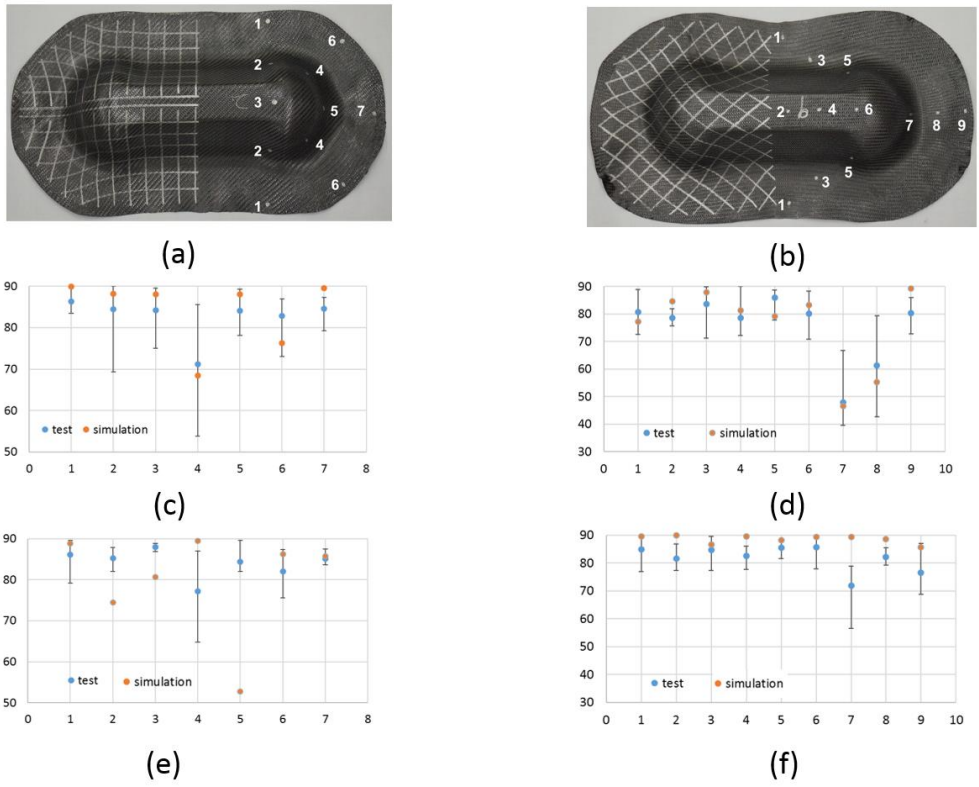

Figure 3.2-91. Double-dome warp-weft yarn angle distribution results: (a) sampling points on the 0/90 prepreg layer, (b) sampling points on the -45/+45 sampling points, (c) angle comparison for the single layer 0/90 fiber orientation preforming, (d) angle comparison for the single layer -45/+45 fiber orientation preforming, (e) angle comparison for the 0/90 fiber orientation layer in the 0/90/-45/+45 double layer preforming, and (f) angle comparison for the -45/+45 fiber orientation layer in the 0/90/-45/+45 double layer preforming.

Figure 3.2-92. Folding of the prepreg after low temperature preforming especially at the edge.

The double-dome preforming benchmark test established can introduce complex double curvature features at the size of common automobile parts. Combined with the corresponding quantitative measurement of local prepreg temperature history, draw-in distance, local yarn angle, and forming force also developed in this ICME project, it serves as an effective experimental approach to validate the preforming simulation methods developed in this project. Validation results indicate that the developed models can reach the proposed fiber orientation prediction error of less than 5% most of the time, guaranteeing the models' application potential.

In addition to model calibration in this project, this double-dome benchmark test can also serve as validation for preforming simulation models developed in the future or from other researchers due to the fact that it considers most of the process parameters and provides the most important criteria for the final parts' performance. As a result, this approach enables researchers in both academic and industrial fields to test their preforming models in a reliable way, so it motivates the invention of accurate preforming simulation models that can help increase production and broaden application of advanced CFRPs, while benefiting environmental emission and fossil fuel control.

Moreover, the double-dome preforming tests performed in this project provide important information about the production of high-quality parts. Temperature control in not only the heated oven but also with forming tools is essential for the resin to fully melt and cause small prepreg deformation resistance and small prepreg surface interaction, which are the keys to smooth and defect-free final parts.

3.2.7.2 Chopped CF SMC plaque compression molding

The objective of this work is to validate the accuracy and effectiveness of the improved compression molding simulation module by Autodesk Moldflow in press force, filling pattern and fiber orientation prediction for chopped carbon fiber SMC composites.

1) Fabrication of SMC initial charge

The raw material of the SMC compression molding is the initial charge. SMC initial charges were made with uncured resin, curing agent and chopped carbon fiber chips. The average cross- section of the chips in the initial charge is approximately 3 mm x 0.1mm and the average length of the chips is 25.4mm. To form the initial charge, chips were chopped from carbon fiber tows with resin and cured agent already dipped on, and then randomly spread to the uncured resin mat and compressed to plaques with planar dimension of 304.8 mm x 304.8 mm and thickness of roughly 2mm covered with plastic film. The initial charges were stored in refrigerator to prevent curing before molding.

2) Compression molding of SMC plaques

The compression molding of the SMC plaques was carried out in lab-scale molding facility. The dimension of the plaques and the shape and position of the SMC initial charge in the mold is shown in Figure 3.2-93.

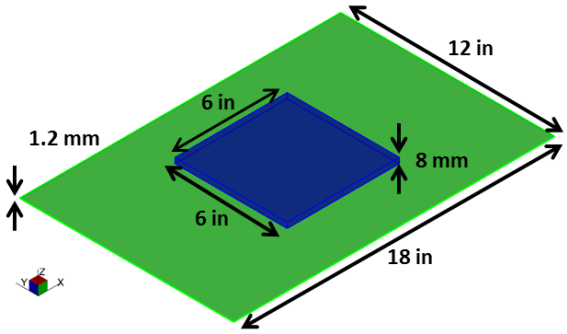

Figure 3.2-93. Dimension of the part (green) and initial charge (blue)

The initial charges were cut from 304.8mm x 304.8mm plaques into 152.4 mm x 152.4 mm quadrants. 4 pieces (8 pieces in the case that the thickness of the plaque is designed to be 2.4 mm) of such quadrants were piled up together and placed at the center location of the 304.8 mm x 457.2 mm cavity. If fully filled, the expected plaque thickness is 1.2mm. To ensure the fiber orientations in the initial charge piles

were as close to 2D random as possible, the 4 quadrants were cut from the same larger plaque and rotated by 0/90/180/270° when placed into the mold so that any anisotropy of fiber orientation during the fabrication of the initial charge can be minimized.

The maximum press force of the machine is 2250kN. Press speed profiles, press force, in-mold temperature and switch criteria from speed to force control are programmed in the user interface of the molding machine. Different press speed and force conditions were tested while molding temperature was kept as 150°C for all the samples. Zero point of molding time, *t*, was defined as the moment when press contacts the initial charge, so that the time recorded by the machine can be well aligned with the time in simulation. With the mold temperature set as 150°C, the crosslinking of the resin happened quickly during the compression molding. Consequently, the viscosity built up which provided resistance for the initial charge to fill in the cavity. If the press speed profile was not fast enough or the press force was not high enough, the initial charge could not fill in the whole cavity and produced the unfilled pattern when curing stage was over. The plaques were then taken out of the cavity and cooled on a steel plate. The actual press force history was recorded in the molding machine, and later extracted to compare with prediction results.

Following the set up described above, two sets of molding trials are performed to obtain in to ~100 fully filled and partially filled plaques for testing and characterization.

i) <u>First molding trial</u>

The processing parameters used in the first molding trial are listed in Table 3.2-22, while the press speed profiles used in the experiments are listed in Table 3.2-23. Only one plaque is molded at the processing condition listed in Table 3.2-22, whereas the #10 processing condition is chosen as the standard processing condition to produce 3 replicate plaques for the validation experiments to compare with the prediction results.

Table 3.2-22 Processing parameters tested in the compression molding experiments. t is the molding time which is defined as 0s when press contacted the top surface of the initial charge.

Experiment #	Press Speed Profile	Press Force at t=0s (kN)	Press Force at t>1s (kN)
1	I	0	0
2	II	0	0
3	II	0	0
4	II	0	250
5	II	0	125
6	II	0	500
7	II	0	1000
8	II	250	1000
9	II	250	500
10*	II	0	1500

Table 3.2-23 Press displacement profile I and II used in the compression molding test.

Step	Press Speed Profile I		Press Speed Profile II	
	Press-Cavity distance (mm)	Press Speed (mm/s)	Press-Cavity distance (mm)	Press Speed (mm/s)
1	200	75	100	50
2	50	25	50	25
3	25	15	10	10
4	15	5	5	5
5	0	1	0	1

For processing condition #1~5, we observed the unfilled plaques, while for processing condition #6~10, the plaques were all fully filled. The unfilled patterns and an example of fully filled plaque are shown in Figure 3.2-94.

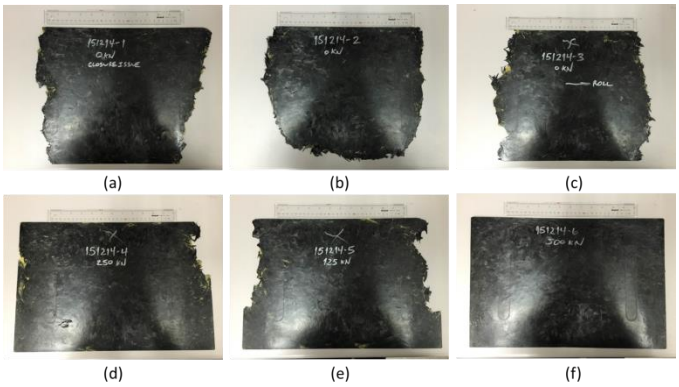

Figure 3.2-94. Examples of plaques obtained from the compression molding experiments. The patterns from experiment #1~6 are shown in (a)~(f) respectively.

ii) Second molding trial

The second molding trial is performed to provide plaques under different processing conditions to provide additional samples for microstructure analysis and mechanical tests. Two different groups of sample plaques are molded in this molding trial. In the first group, the processing parameters are setup to achieve fully filled plaques. The combination of different press force limits and type of press speed profile is listed in Table 3.2-24. Two types of press speed profiles are used in the second molding trial. The "Slow" one corresponds to the profile II in Table 3.2-23, while the Fast one has the press speed 50% higher over the whole filling period than the "Slow" one.

Table 3.2-24 Press displacement profile I and II used in the compression molding test.

Group #	Force Limit	Speed profile	Repeats
1	500kN	Slow	9
2	500kN	Fast	9
3	1500kN	Slow	18
4	1500kN	Fast	9
5	2250kN	Slow	9
6	2250kN	Fast	9
7 (2.4mm)	1500kN	Slow	6

In the second group of the plaques, metal shims with different heights are inserted into the mold to stop the press at selected positions. The curing process is continued after the press reaches the shim and thus the short filled plaques are cured to keep the shape in the mold. The shape of the short filled plaques are then taken out of mold for shape measurement to compare with filling pattern prediction in Moldflow. The processing information and the heights of metal shims are listed in Table 3.2-25. Example of partially filled plaques are shown in Figure 3.2-95. The detailed information regarding the comparison is discussed in the validation sections.

Table 3.2-25 List of processing conditions for short filling plaques.

Group #	Processing	Shims height	Repeats
1	500kN, Slow	4mm	2
2	500kN, Slow	3mm	2
3	500kN, Slow	2mm	2
4	500kN, Slow	1mm	2
5	500kN, Slow	0.5mm	2
6	500kN, Fast	4mm	2
7	500kN, Fast	3mm	2
8	500kN, Fast	2mm	2
9	500kN, Fast	1mm	2
10	500kN, Fast	0.5mm	2

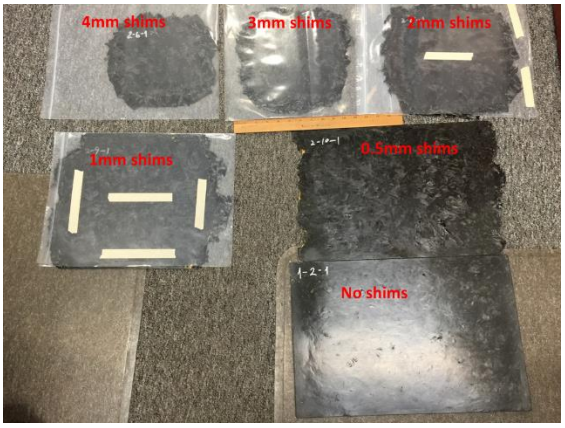

Figure 3.2-95. Intermediate filling patterns of the partially filled plaques. The height of metal shims are labeled in the image. The press force limit is 500kN and the slow speed profile is used to produce these samples.

3) Microstructure characterization on the samples cut from the plaques

Microstructure characterization is performed on selected locations from the plaque, mainly to provide data of fiber orientation tensor measurements. The measurement is conducted on A, B and E locations on the selection plaque. The 1in x 1in sample is cut from the location and then attached to a flat steel plate using hot wax. The plate is then mounted on the autopolisher (Allied High Tech, Multiprep) for polishing. Microscopic images are taken using digital optic microscope (Keyence VHX 2000) and stitched together automatically by the microscope. After the imaging is finished, the mounted sample is polished again using autopolisher to remove certain amount material and reveal the microstructure beneath. The removal thickness can be precisely controlled by the autopolisher and the interval between imaged layers of the sample is set to 100um, with exception at the first layer as additional material needs to be removed to flatten the surface and also at the last layer as wax is not strong enough to hold the sample after a number of repeats. Typically for a sample as thick as 1.2mm, 8-10 polishes can be performed, providing microstructure information at different locations along thickness direction.

The image analysis is then performed on the images. A MATLAB script is developed to align the images and perform the measurement of local direction of fiber pixels. A computer vision algorithm previously developed for fingerprints analysis is adapted to measure the tangential directions of fiber pixels. With the summarized direction distribution, average fiber orientation tensor of the imaged 1in x 1in area can be obtained. The schematic of the autopolishing process and the example images with visualization of computed local fiber directions are shown in Figure 3.2-96.

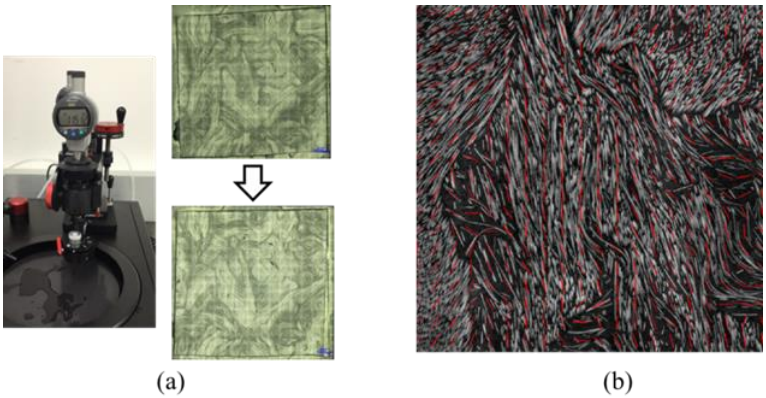

Figure 3.2-96. Schematic and example images for fiber orientation tensor measurement.

4) Validation of predicted manufacturing information

The comparison of the press force from experiment and Moldflow simulation was shown in Figure 3.2-97. Only the comparison with the first 10s of the molding process was shown since the press force remained constant at preset peak force value for both simulations and experiments. For both processing conditions applied in the Moldflow simulation, i.e., experiment #6 (Figure 3.2-97a) and experiment #10 in first molding trial (Figure 3.2-97b), the predicted press force is generally well matched with experimental results. Nevertheless, at the beginning of the process, the experimentally measured press force by the molding machine ramped up more quickly than in Moldflow prediction, root cause of which requires further study.

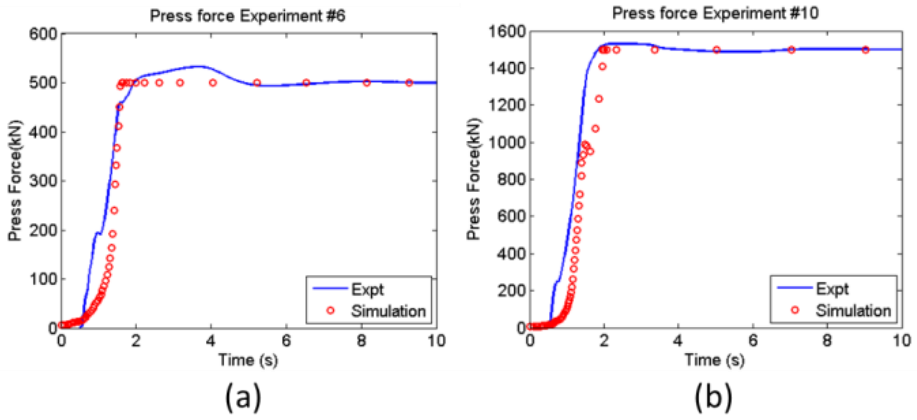

Figure 3.2-97. Comparison between press force experiment and prediction in Moldflow for (a) experiment #6 and (b) experiment #10.

The validation of filling pattern in Moldflow is shown in Figure 3.2-98. The partially filled plaques obtained from the second molding trial are imaged and analyzed in MATLAB. The predicted filling pattern under corresponding processing conditions from Moldflow are also imported into MATLAB for comparison. Generally good match (<10%) difference in filled area is observed throughout the filling stage.

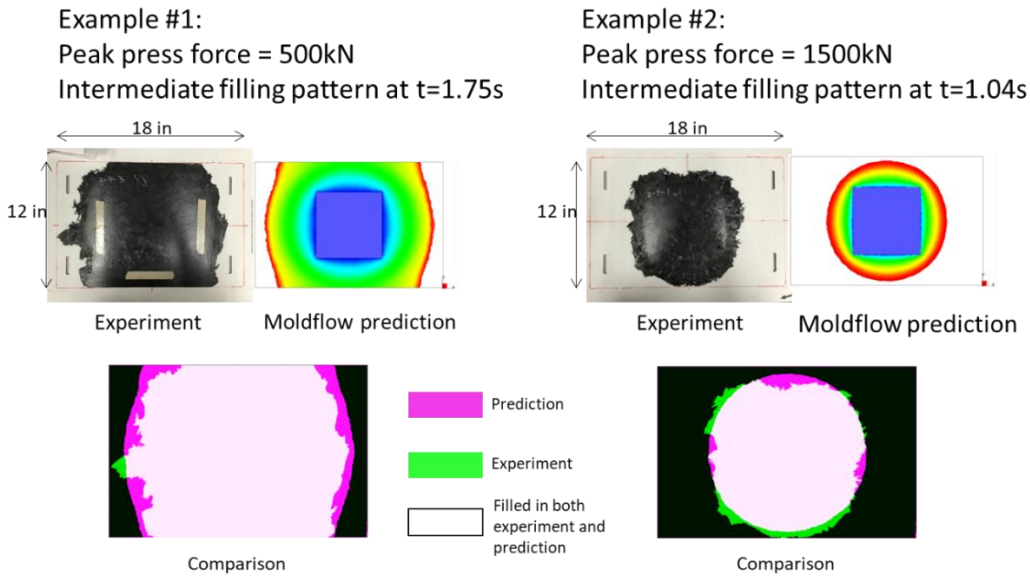

Figure 3.2-98. The examples of validation of filling pattern prediction in Moldflow.

Another quantitative comparison is made between the measured and predicted filling time in order to validate the Moldflow simulation under different processing conditions. The manufacturing data in molding trial 2 are processed to obtain the time at which flow front reaches one of the pressure sensors. The location of the sensor is shown in Figure 3.2-99 (a). The predicted flow front time in the Moldflow models with corresponding processing conditions are obtained from the probe node with the same coordinates as the pressure sensor. The comparison is shown in Figure 3.2-99 (b). The error of prediction ranges from 3.1~11.5% across the #1~#6 processing conditions in the second molding trial.

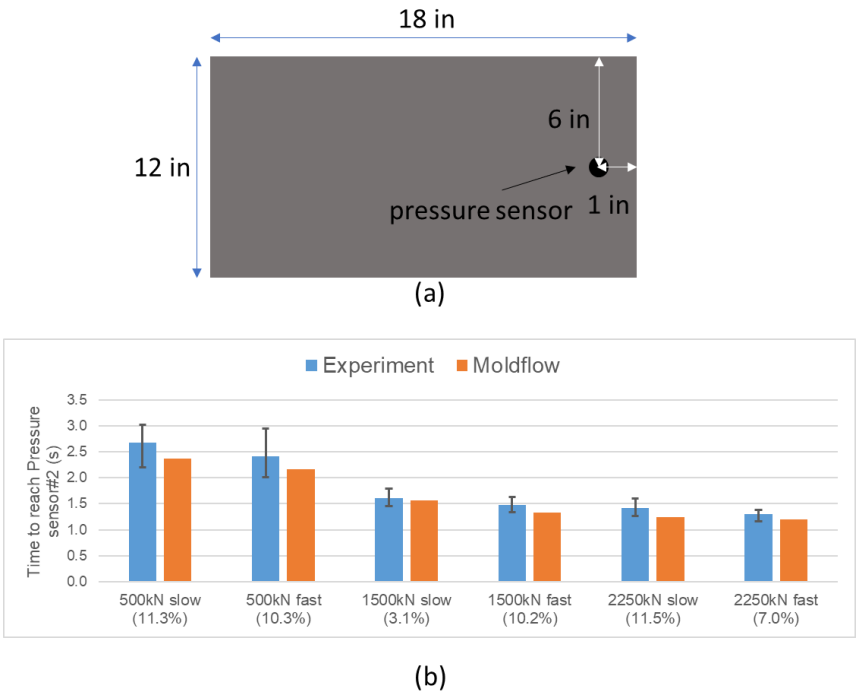

Figure 3.2-99. Comparison of measured and predicted time at which flow front reaches pressure sensor. The location of the sensor on the press is shown in (a). Measured and predicted data are shown in (b). Error bar in (b) represents the max and min value. Prediction error is labeled under the processing condition.

5) Validation of fiber orientation tensor measurement

Two fiber orientation models in Moldflow are used, i.e. Reduced Strain Closure (RSC) and Moldflow Rotational Diffusion (MRD). The validation is performed based on #10 experiment in first molding trial. The experimental measured fiber orientation tensor component, A_{11}, at A, B and E locations are compared with the corresponding prediction obtained from Moldflow. The parameters in the both RSC and MRD models are calibrated using the averaged A_{11} through all points along thickness direction at Position E. It is found that for RSC model, the best parameter is Ci = 0.08 and RSC =0.975, whereas in MRD model, Ci = 0.08 and D1 to D3 set as Moldflow default value, i.e., 1.0, 0.8 and 0.15 gives best match. As shown in Figure 3.2-100, the both models show good prediction of the in-plane fiber orientation component, A_{11}, at the selection locations. The errors of the average A_{11} through thickness at different locations are summarized in Table 3.2-26. However, it is further found that the RSC model tends to over-predict the out-of-plane fiber orientation tensor component, A_{33}, as the constraint of the fiber direction due to part thickness cannot be considered in RSC model. In the case of SMC compression molding, the length of in-plane chopped fiber tow is much larger than part thickness, which restricts out-of-plane components of fiber orientation tensor. This issue is fixed by the anisotropic diffusion terms in MRD model. Therefore, local material properties predicted by using the fiber orientation tensor from MRD model match better with tensile modulus measurement.

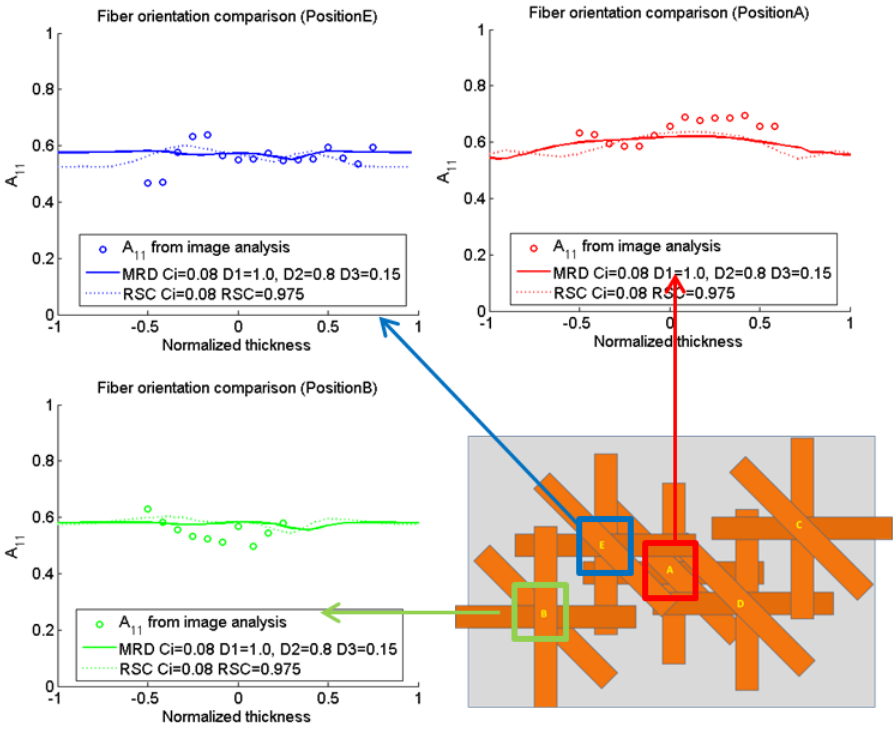

Figure 3.2-100. The comparison between predicted and measured fiber orientation tensor component A11. The prediction from Moldflow is obtained using RSC and MRD model.

Table 3.2-26. Error of predicted A11 at different positions of the plaque.

	Error at Position A	Error at Position B	Error Position E*
RSC	-5.7%	-5.3%	-4.3%
MRD	3.9%	4.6%	0.0%*

*: calibration data set

3.2.7.3 Crash simulation validation on hat sections molded with continuous CF composites

The method developed for CFRP crashing analysis in Section 3.2.4 is further validated with axial crash and dynamic 3-point bending test at different layups and velocities for both UD and woven composites.

1) Experiment work

Different crash experiments are performed at various conditions for the model validations. In this work, CFRP hat section samples are molded with A42 carbon fibers and thermoset epoxy resin. The nominal fiber volume fraction is 50%. The hat section sample was deformed in hot compress and hold for about 5 minutes for curing. Two types of CFRP composite, i.e. UD and Woven fabric (2x2 twill) with different layups are tested for comparison purpose, as listed in Table 3.2-27. Fiber orientations of 0^o are parallel to the length of the hat section and fiber orientations of 90^o are perpendicular to the length direction.

Table 3.2-27 Summary of hat section sample information.

Type	Layup	Test
UD	$[0/90/90/0/0/0]_s$	Axial crash/3-point bending
	$[0/60/-60/0/60/-60]_s$	Axial crash/3-point bending
Woven	$[0]_{4s}$	Axial crash/3-point bending
	$[45]_{4s}$	Axial crash/3-point bending

Hereafter, UD $[0/90/90/0/0/0]_s$ is noted as UD 0-90, UD $[0/60/-60/0/60/-60]_s$ as UD 0-60, Woven $[0]_{4s}$ as Woven 0-90, Woven $[45]_{4s}$ as Woven 45-45.

The geometry of CFRP hat section is shown in Figure 3.2-101 (a). The nominal thickness is 2.4 mm. The UD hat section sample has 12 layers with about 0.2 mm thickness of each layer, while woven hat section has 4 layers with about 0.6 mm thickness of each layer. In order to perform the dynamic 3-point bending test successfully, a back plate of same layup and thickness is glued to the bottom of the hat section sample with Betamate 4601 glue (Dow), as shown in Figure 3.2-101 (b). For axial crashing test, the hat section is cut into two pieces from the center and glued together with Betamate 4601 glue. In order to introduce a progressive crashing mode, a 45 degree cutting on the flange part is applied as a trigger, as shown in Figure 3.2-101 (c).

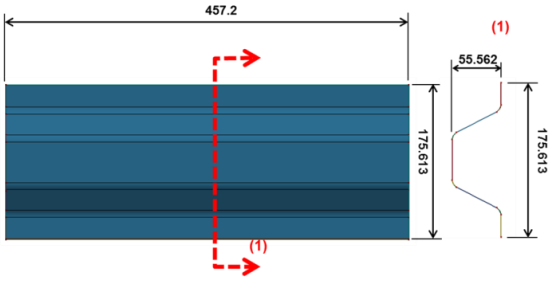

(a)

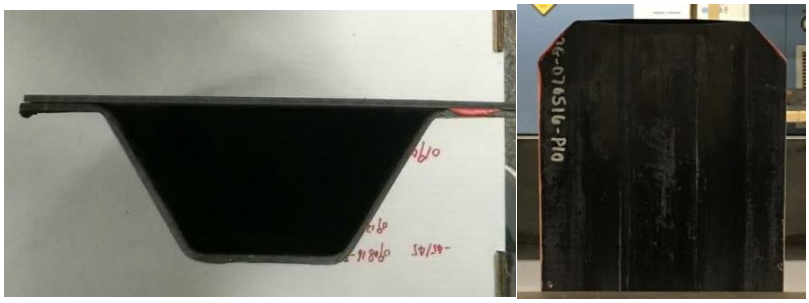

(b) (c)

Figure 3.2-101. Hat section samples: (a) geometry, (b) dynamic 3-point bending test sample, (c) axial crash sample

The set-up of the crash tests is shown in Figure 3.2-102. In dynamic 3-point bending test, an impactor with 25kg mass and 65 mm outer diameter impacts the hat section with different initial impact velocities. The acceleration history of impactor is recorded to evaluate the performance of the hat section. High-

speed camera is applied to record the impact process. In axial crash test, the sample is crashed by a free dropping impactor, as shown in Figure 3.2-102 (b). The total falling mass is 795 kg and two initial impactor velocities (4.4 m/s and 2.2 m/s) are achieved by adjusting the dropping height. The load history is recorded to evaluate the energy absorption. It should be noted that the sample is not crashed to the end but only the loading from initial impact to that of 22ms is recorded.

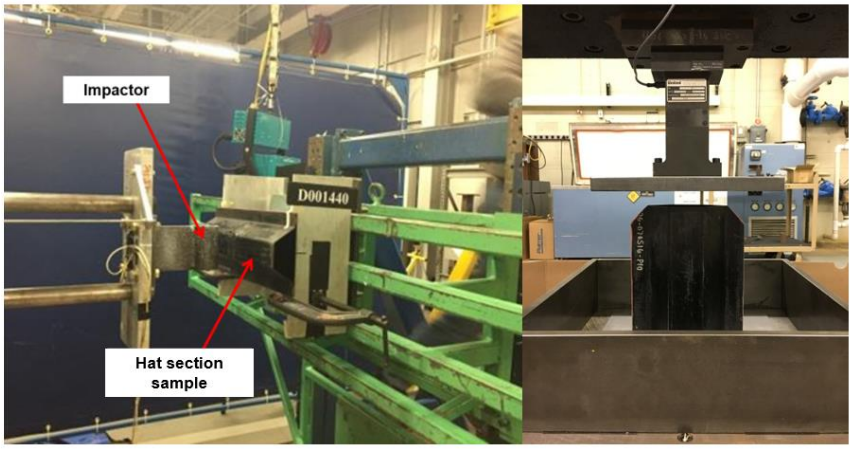

(a) Dynamic 3-point bending (b) Axial crash

Figure 3.2-102. Experimental set-up

2) Experiment results

i) Dynamic 3-point bending test

Figure 3.2-103 shows the acceleration history of the impactors for UD and woven composites with different layups. The acceleration first increases linearly to reach the peak. After that, it drops significantly to a certain value. Then it keeps decreasing gradually to the end of impact. All the curves follow the similar trends. The major difference is that the peak values of UD composites is higher than those of woven composites.

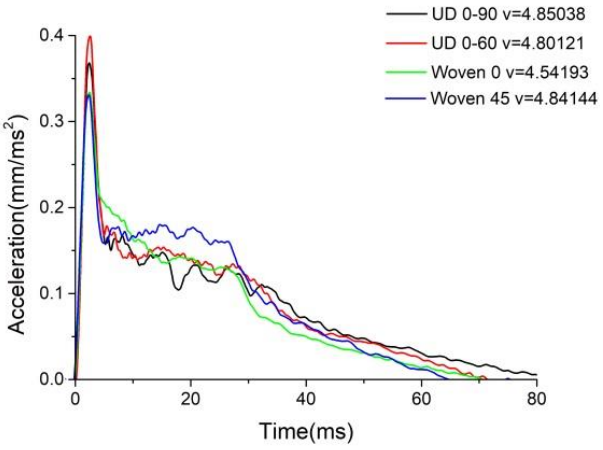

Figure 3.2-103. Acceleration history of impactor for UD and woven composites with different layups.

In dynamic 3-point bending test, the peak load and its corresponding displacement are the two most important parameters. Table 3.2-28 lists the comparison of these two values for various layups. Hat

section of UD 0-60 has the best performance, while the woven at 45 direction has the weakest performance.

Table 3.2-28 Comparison of peak loading and its corresponding distance for different layups.

Layup	Peak load (N)	Diff(%)	Dis (mm)	Diff(%)
UD 0-60	10063.10	-	11.74	-
UD 0-90	9048.24	-10.1	11.45	-2.5
Woven 0	8375.90	-12.4.5	10.88	-7.4
Woven 45	8058.36	-19.9	14.52	23.7

High-speed camera during the test and ultrasonic scan after are applied to analyze the failure modes. As shown in Figure 3.2-104, significant delamination on the side wall can be observed. Ultrasonic scan images show clear delamination in both top and sidewall part. These indicate the delamination plays an important role in bending deformation.

(a) High speed camera images for UD 0-90

(a) (b) High speed camera images for woven 0-90

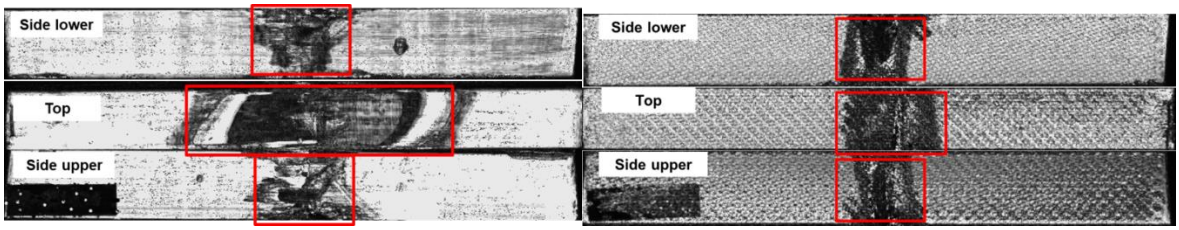

(c) Ultrasonic scan images for UD 0-90 (d) Ultrasonic scan images for woven 0-90

Figure 3.2-104. High speed camera images and ultrasonic scan images of delamination

ii) Axial crash

Figure 3.2-105 plots the load history in axial crash with different layups for both UD and woven composites. All of curves exhibit similar characteristics that the loads increase to a relative high peak at

the moment of contact, after that the loads show significant vibration and reach steady levels gradually. However, the steady load levels are different. UD 0-60 and woven 0 have a very similar load history, while woven 45-45 has the lowest steady value.

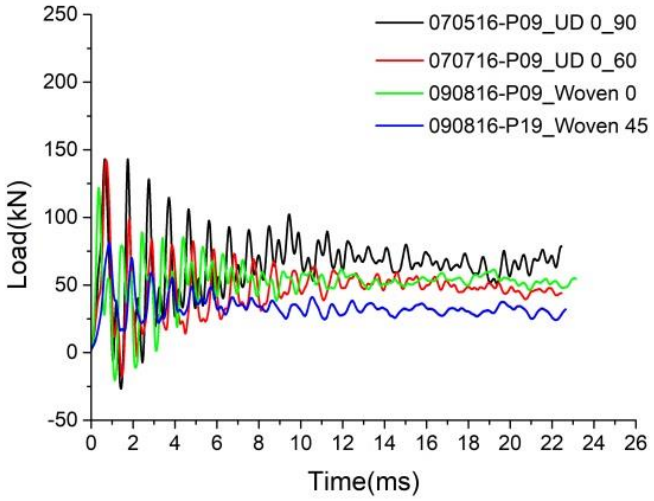

Figure 3.2-105. Comparison of loading histories with different layup.

Table 3.2-29 lists the energy absorption at 50mm crash distance for four different layups. The UD 0-90 hat section shows the highest energy absorption and stable load level. The UD 0-60 and woven 0 show similar performance, but are slightly worse than woven 0-90. Woven 45-45 has the lowest energy absorption and stable load level among all four testing cases.

Table 3.2-29 Comparison of energy absorption and stable loading for different layups.

Layup	Energy absorption (J)	Diff(%)	Stable load (kN)	Diff(%)
UD 0-90	3392.29	-	76.11	-
UD 0-60	2274.08	-33.0	52.27	-31.3
Woven 0	2633.07	-22.4	53.44	-29.8
Woven 45	1747.83	-48.5	28.13	-63.0

Figure 3.2-106 shows the failure pattern of UD and woven samples with initial impact velocity of 4.4m/s. All samples exhibit the characteristic of stable, progressive damage. However, the failure patterns are different. In UD 0-90 samples, a brittle failure mode is observed with a large amount of fiber kinking or breakage. Woven 45-45 shows a tearing failure mode. The fiber tows only break at the corners, while delamination is observed at the rest part of the locations. The failure in woven 0-90 is relative complex. The sample is teared into several pieces, but the pieces are also severely deformed and bent.

The ability of energy absorption is directly reflected from the failure modes. In woven 45-45 samples, only the corner parts would take effect in the energy absorption, while the fragmentation failure mode in UD 0-90 samples cause a large amount of energy absorption during the crash.

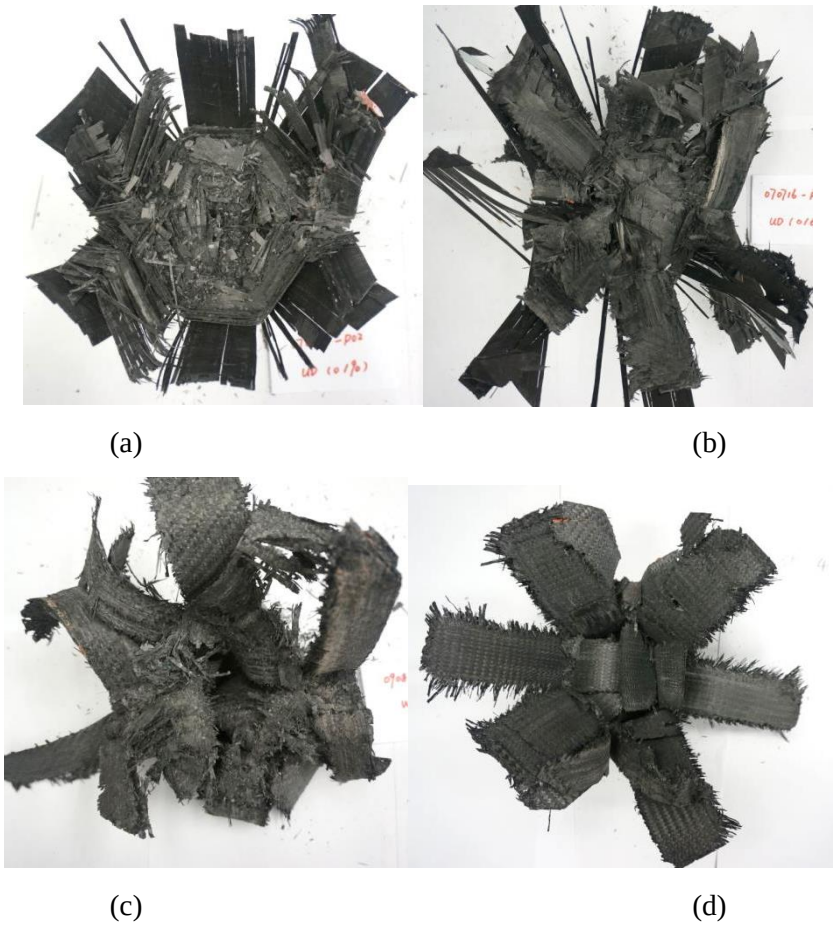

(a) (b)

(c) (d)

Figure 3.2-106. Typical post-crushing morphologies for hat sections with different layups: (a) UD 0-90 layup, (b) UD 0-60 layup, (c) Woven 0-90 layup, (d) Woven 45-45 layup.

3) Crash model validation

Crash simulation on both axial crash and dynamic 3-point bending test with different materials and layups are conducted. The same crash model as developed in Section 3.2.4 is applied. Table 3.2-30 summarizes the comparison between simulation and experiment results

Table 3.2-30 Comparison between simulation and experiment results

UD 0-60		Exp	Sim	error
Axial crushing (v=2.2m/s	Energy(J)	2274.08	2380	4.7%
	Load(KN)	52.27	53.8	2.8%
	Peak L(N)	10300	10057	16%

Dynamic 3-point bending (v=4.10m/s)	Dis(mm)	10.8	11.6	7.3%
UD 0-90		Exp	Sim	error
Axial crushing (v=4.4m/s)	Energy(J)	3392.3	2150	36.7%
	Load(KN)	76.11	42.5	44.2%
Dynamic 3-point bending (v=4.85m/s)	Peak L(N)	9048.24	8690	3.9%
	Dis(mm)	11.45	12.4	8.3%
Woven 0-90		Exp	Sim	error
Axial crushing (v=2.2m/s)	Energy(J)	1478.7	1360.2	8.0%
	Load(KN)	62.5	55.4	11.4%
Dynamic 3 point bending (v=5.20m/s)	Peak L(N)	8111.8	8043	0.85%
	Dis(mm)	12.0	11.1	7.5%
Woven 45-45		Exp	Sim	error
Axial crushing (v=4.4m/s)	Energy(J)	1747.83	1624.60	7%
	Load(KN)	28.13	32.69	16.2%
Dynamic 3-point bending (v=5.68m/s)	Peak L(N)	8058.36	8761.6	8.72%
	Dis(mm)	14.52	11.71	19.4%

Note:

1) The energy absorption in axial crash is calculation for 50mm crash distance (v=4.4m/s) and 35mm (v=2.2m/s), respectively. The reason is that the maximum crash distance at v=2.2m/s is much less than 50mm.

2) The experimental results in UD 0-90 axial crash (v=4.4m/s) shows very large scatter, 14.24% for energy absorption and 22.3% for stable load.

3.2.7.4 UD laminate fatigue life prediction

The objective of this work is to validate the use of the fatigue data from UD composites to predict the fatigue lives of UD laminates.

Uniaxial fatigue experiments on UD and cross-ply laminates

Figure 3.2-107 illustrates the UD laminate sample prepared for fatigue test. The test frequency is 7Hz under stress ratio R=0.1. Figure 3.2-108 shows the S-N curves obtained from fatigue tests.

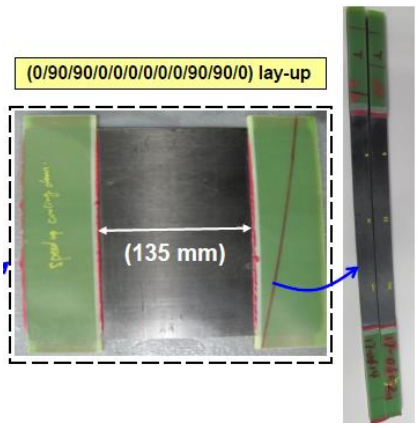

Figure 3.2-107 UD laminate fatigue sample.

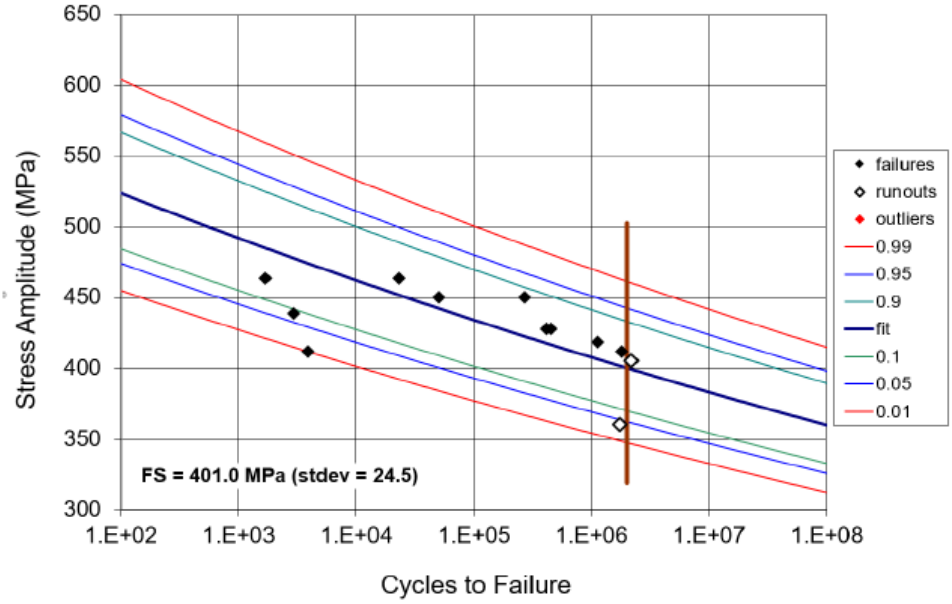

Figure 3.2-108 UD laminate S-N curve at stress ratio R=0.1.

Figure 3.2-109 compares the experimental results for UD and the laminates under the same stress ratio R=0.1. The experimental fatigue lives of the laminated samples are plotted based on the average cross-section area of the 0 degree layer. The cross-section area of the 0 degree layer accounts for 67% of the total cross-section area of the cross-ply laminate samples. Because of the much higher stiffness of 0-degree layer (130 GPa) compared to that of the 90 degree layer (7 GPa) in the loading direction, it is reasonable to assume that the applied stresses or strains are endured by the 0 degree ply alone.

The theoretical predictions shown in Figure 3.2-109 are based on the assumption that the total fatigue life of the laminate is dictated by the life of the 0 degree layer alone. This assumption is valid because as the sample is continually fatigued, the 90 degree ply fails first. The remaining number of fatigue life cycles are then endured by 0 degree alone as validated by optical microscopy observations as shown in Figure 3.2-110. In summary, the total fatigue life of the laminate is equal to the life of the last ply to fail (the 0-degree layers in this case). Two theoretical prediction curves are presented based on the two well-known criteria (i) maximum stress criteria and (ii) maximum strain criteria. Although both criteria are found to give reasonable agreement with the experimental values, it is found that maximum strain criteria

is a better choice than the maximum stress criteria in the current case. This is because the maximum strain criteria considers the stresses both parallel and perpendicular to the loading direction. On the other hand, the maximum stress criteria considers the stresses only in the direction of the applied load.

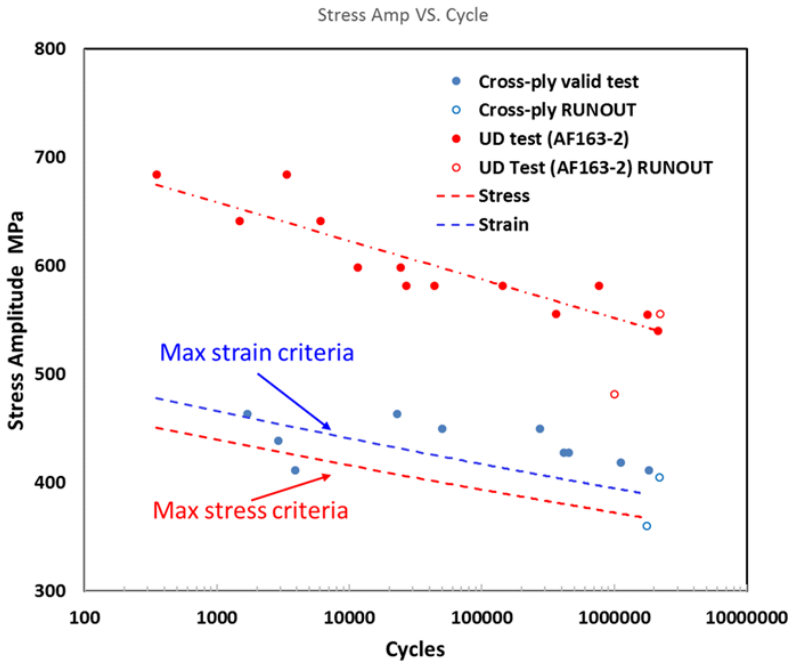

Figure 3.2-109. S-N curve for UD and UD laminates at R=0.1. The theoretical predictions for cross-ply laminates are derived based on UD composites.

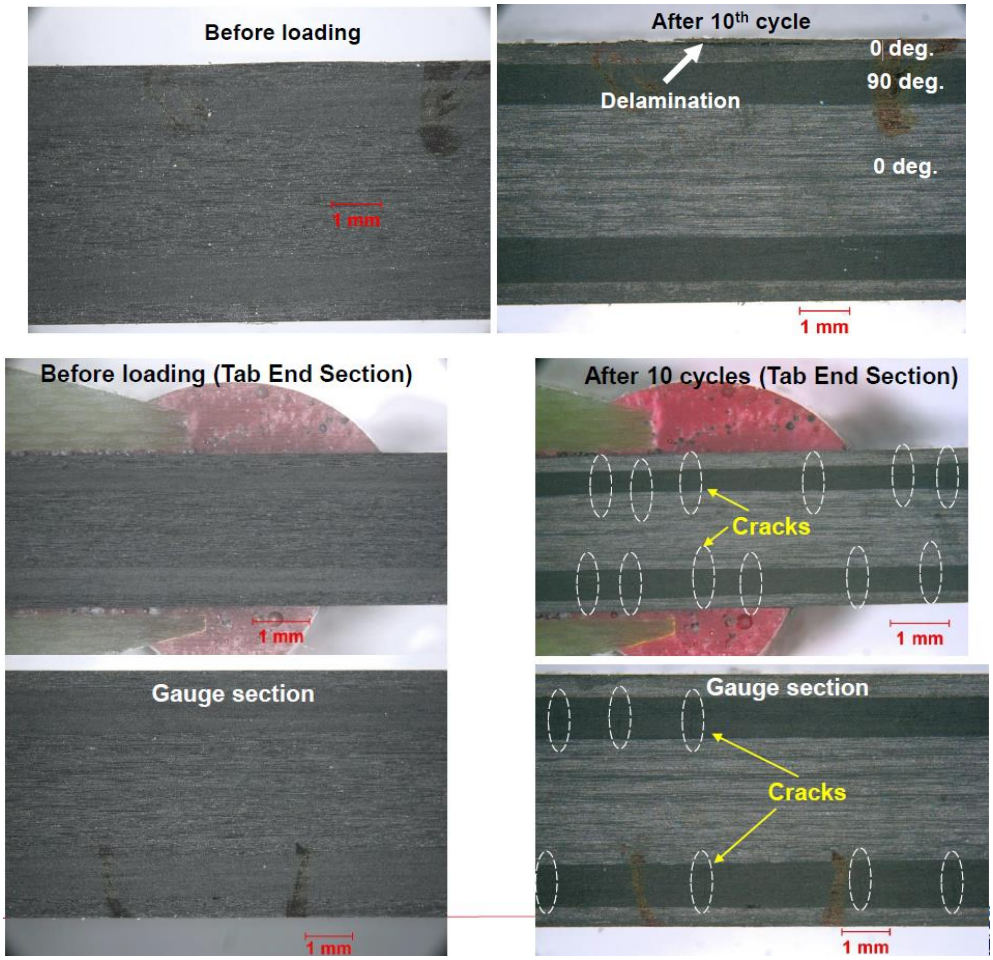

(a) (b)

Figure 3.2-110. (a) Sample surface before loading at different regions of the gauge length (b) Sample surface after 10 fatigue cycles at R=0.1. Cracks are visible.

It is important to note that the experimental fatigue strength of the laminate is 401 MPa at 2 million cycles while the fatigue strength based on the maximum stress and strain criteria are 368 MPa and 388 MPa respectively. The predicted fatigue strengths based on both criteria are within 8% of the experimental value.

It is also important to emphasize that in the current correlation methodology, we do not consider stress redistribution due to failed 90-degree layer in the cross-ply laminate. This may be an important consideration; nonetheless, the predicted results agree well with the experimental results within 10%.

3.3 Task 3: ICME Model Integration and Validation

Task 3 in this project integrates models developed in Task 2 in commercial software. A Common Data Structure is established to facilitate data flow from process simulation to performance simulation. An assembly-level test is conducted with surrogate parts to validate the integrated model at system level. The major developments are

1) The integration of the ICME models is achieved in modeFRONTIER by connecting different modules within the optimization platform.
2) Interfaces of ICME simulation models are developed in modeFRONTIER using multiple types of scripting languages to enable fully automatic optimization runs on Ford's High performance Computing (HPC) system.
3) The efficiency of the ICME workflow is analyzed by evaluating the turnaround time of an example design point.
4) The complete ICME optimization workflow is performed on a top hat assembly for test and validation. Simulation of a design point with the same configuration as the samples used in experiments is performed. The prediction from ICME workflow is close to the experimental result.
5) Based on the lessons learned from the optimization of top hat design, improvements on the optimization scheme are developed.
6) The potential improvements on the optimization algorithm together with uncertainty quantification in the design are proposed.

The carbon fiber composites have the anisotropic properties, heterogeneous multiscale microstructure, and large variations in the material properties induced by the compression molding process. There are three types of epoxy-based thermoset carbon fiber composites investigated in this project: short fiber composites (e.g. Sheet Molding Compound, SMC), unidirectional (UD) long fiber composites, and woven fiber composites. Processing, microstructure and component structure parameters are considered as the design variables (Figure 3.3-1). The end goal is to optimize the processing parameters, material microstructure features, and structure design variables simultaneously to achieve the optimum system performances. Based on the simulation modules developed in each subtask of this project, integrated workflows automate the computational process-structure-properties-performance analysis. These workflows provide the infrastructure for Design-of-Experiments (DOE) study, design optimization, and uncertainty quantification study of the carbon fiber composites.

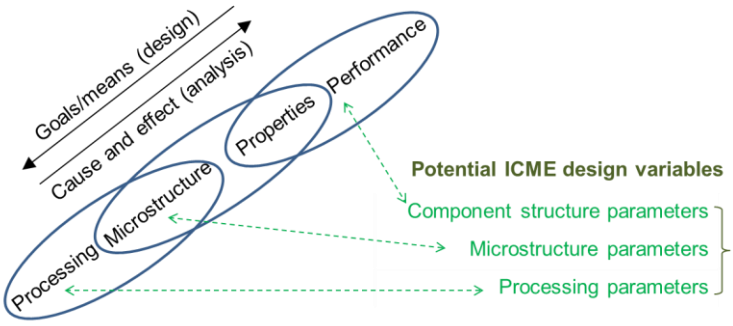

Figure 3.3-1. Chain rule of computational design of materials: Process-Microstructure-Properties-Performance (P-S-P-P). Bottom-up: analysis process; top-down: design process. Design variables can be identified from all levels in the chain rule.

The goals of the development of ICME workflow is to realize the key features shown in Figure 3.3-2, CAD/CAE process automation, DOE, optimization and metamodeling, and data visualization and analysis:

1) CAD/CAE process automation. A variety of CAD and CAE models will be connected under the ICME framework. Therefore, this tool should be able to automate the process of modifying the CAD/CAE models based on the design variables' values, to submit the job to HPC, to postprocess the simulation results, and to transfer the data from one model to another model. The process integration tool should be compatible with different kinds of CAD/CAE software, as well as different operation systems (e.g. Windows, LINUX, etc.) In addition, the process integration tool should provide full control of the entire analysis process, such as the start/stop/pause of each simulation module.

2) Optimization capability. The end goal of process integration is to provide a computational tool for ICME optimization of the manufacturing process, structure design, and composite material design simultaneously. Therefore, the tool should have optimization capabilities, such as optimization search algorithm, Design of Experiments (DOE) methods, and metamodeling.

3) Data visualization and analysis. After DOE or optimization runs, the engineers will collect all the simulation data. To facilitate decision-making or discovering knowledge from the data, the tool should provide data visualization and data mining capabilities.

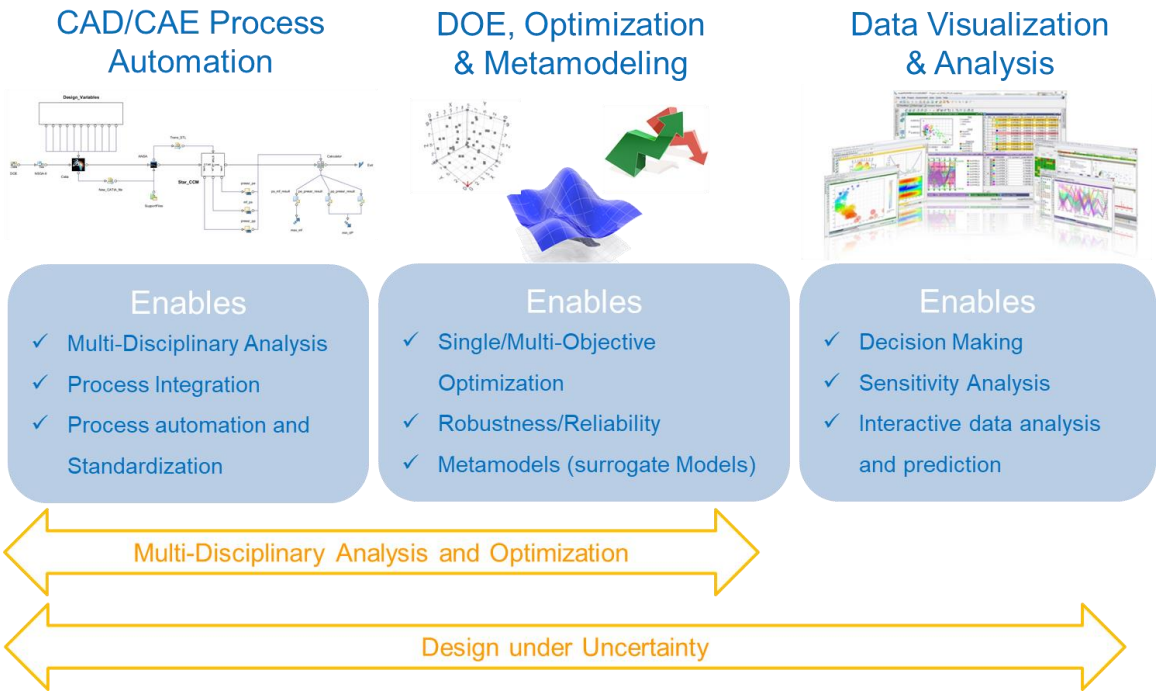

Figure 3.3-2. Three key features of the process integration tool for ICME.

3.3.1 Model Integration in Commercial Software

An ICME workflow is established that integrates all the simulation modules developed in this project. The integrated workflow illustrated in Figure 3.3-3 serves as the infrastructure for computational design optimization of manufacturing process, material microstructure, and structure design.

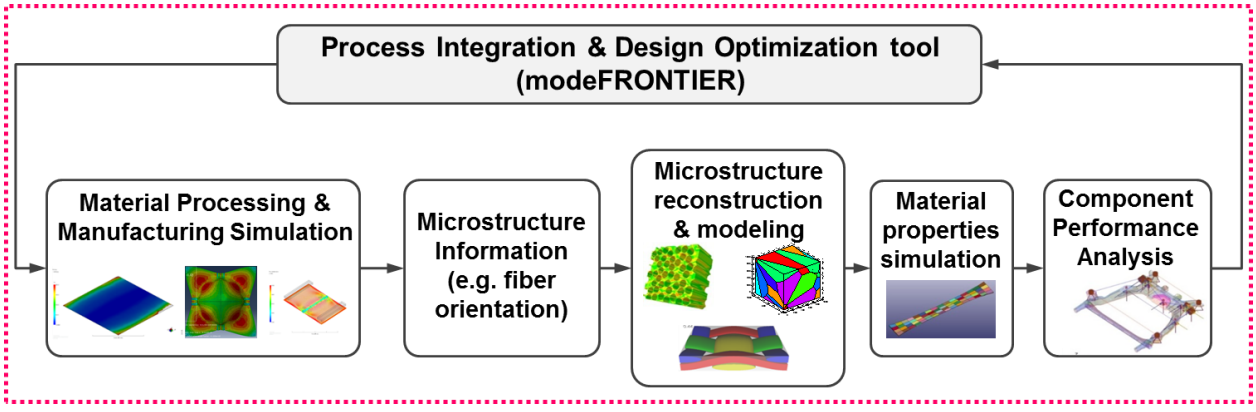

Figure 3.3-3. Three key features of the process integration tool for ICME

There are several commercial tools available, such as modeFRONTIER from ESTECO, iSight from Dassault Systèmes, HEEDS from SIEMENS, and LS-OPT from LSTC. In this work, we present our

integrated workflows in modeFRONTIER. A process integration and optimization software, modeFRONTIER from ESTECO, is selected as the tool for this task.

For ICME analysis and design of carbon fiber composite structures, the following key modules should be included in the integrated workflow (Figure 3.3-4):

1) Optimization and process control module. It provides optimization/DOE algorithm, and parallel computing options.

2) Parametric geometry design module. The geometry of the composite structure is modeled as a parametric CAD model. Structure morphing parameters, material selection of each component, selection of component joint methods and composite layup parameters (number of plies and the orientation of each ply) are considered as design variables. In the work, we establish the parametric CAD model in SFE CONCEPT. The output of SFE CONCEPT CAD module is the mesh of the new structure design.

3) Manufacturing process simulation module. The mesh of the new structure design is passed to this module as the input information. Compression molding simulation is operated to predict the local fiber orientation on the structure (fiber orientation of each element).

4) Multiscale material modeling module. The local material properties are predicted using microstructure Representative Volume Element (RVE) models based on the local microstructure features. The key enabler of multiscale material modeling is stochastic microstructure reconstruction. The input of stochastic reconstruction is the material microstructure statistics (e.g. fiber orientation tensor) obtained from the previous step, manufacturing process simulation (e.g. compression molding simulation). The outputs of stochastic microstructure reconstruction are random but statistically equivalent 3D microstructure models, which provide the mesh information for the FEA prediction of material properties. As each element in the structure model has its own microstructure features, the local material properties of each element need to be predicted. With infinite computational resources, one could establish microstructure model for each element in the structure. However, it is not a realistic solution for engineering applications. To relieve the heavy computational burden of microstructure simulation, one way is to establish metamodels of the relation between microstructure characteristics and the resultant material properties. The metamodels are established based on the training data collected by Design of Experiments (DOE). For each DOE point in the space of microstructure characteristics, the correspondent microstructure RVE model is reconstructed. Material properties of the DOE samples are obtained by FEA. The process of establishing the microstructure characteristic – property metamodel is considered as an “offline” preparation step; and the process of using the trained metamodel to predict the local material properties of each element in the structure is considered as an “online” prediction step.

5) Attribute simulations. After assigning local material properties to each element of the structure model, attribute simulations are conducted to predict the performances of the structural design. The attribute simulations include: stiffness analysis (MSC Nastran), fatigue analysis (MSC Nastran + nCode), strength analysis (Abaqus), and crash analysis (LS-DYNA). The simulation results are taken as the responses of the structural designs.

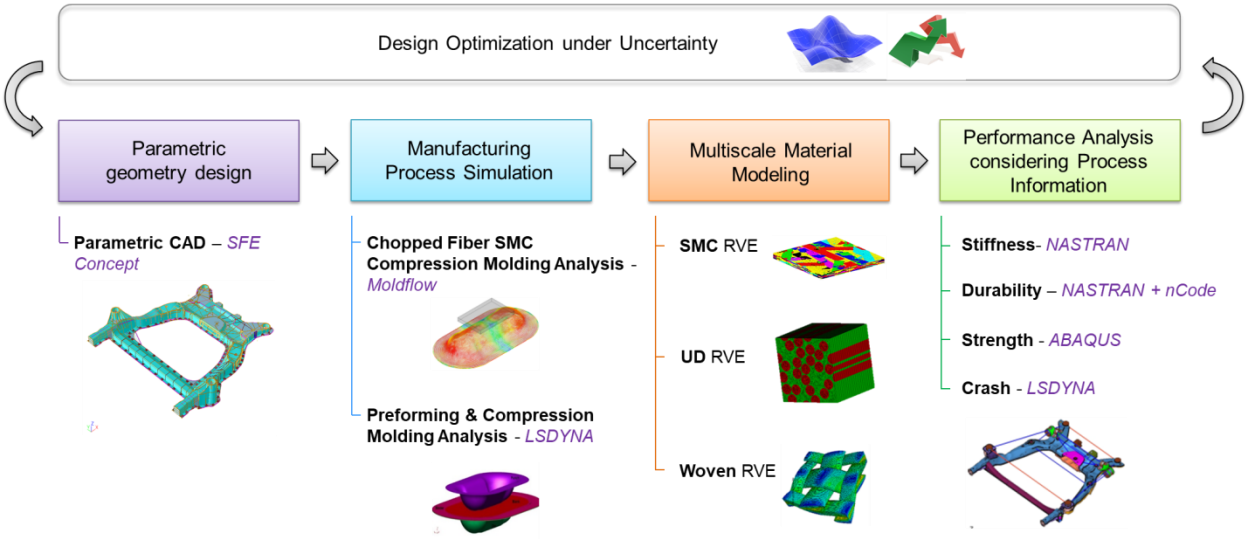

Figure 3.3-4. General framework of ICME process integration for carbon fiber composites

A full ICME workflow has been developed to integrate all computational modules for the analysis and optimization of carbon fiber composite structures. The blue blocks in Figure 3.3-5 represent the design variables, which are defined as input parameters in modeFRONTIER; the yellow blocks represent the computational model; the purple blocks represent the files generated by or passed to each model. The key linkages between different modules that is developed in this project are numbered in Figure 3.3-5. The detailed information regarding the development of linkages are discussed in Section 3.3.2. This workflow contains three major modules:

1) Geometry and composite layup design. Design variables are defined to parametrize the structural geometry (e.g. height, width, cross-section shape, etc.) and the composite layup of the laminate components (e.g. number of layers and the fiber orientation angle of each layer). SFE CONCEPT is utilized to generate mesh of the geometry based on the geometry parameters. We also developed Jython scripts to translate the composite layup variables into the part information in the FEA input solver decks. The output of this module are FEA meshes and section/part definitions that will be used in the CAE models in the following two modules.

2) Manufacturing simulation. The structure information is reformatted (by Hypermesh Tcl scripts) and input into processing simulations. For SMC, Moldflow is employed to predicted the local fiber orientation on each integration point after compression molding; for UD and woven composites, LS-DYNA model is developed to predict the changes in local fiber orientation/woven angle in preforming. The simulation results are mapped to the final structural mesh that is used for performance simulations. It is to be noted that the mesh used in structure performance simulations is different from the mesh for manufacturing simulation. The material properties of each element in the final mesh is assigned based on the pre-train metamodels of the fiber orientation-property relation. The training data of the metamodels are generated by the material microstructure Representative Volume Element (RVE) models. The output of this module is the local material properties that assigned to each element in the CAE model. One part/section is defined for each element.

3) Performance simulation. The simulation input decks are assembled and submitted to HPC. Six attributes of the design are evaluated:

- **Stiffness**: MSC Nastran is selected as the solver, and Jython scripts are developed for postprocessing.
- **Fatigue:** MSC Nastran is employed to obtain the stress distribution in the structure, and then nCode is employed to predict the fatigue life. The simulation results are postprocessed by a Jython script.
- **Strength:** Abaqus is selected as the solver. Permanent deformation is obtained for metal components, and Tsai-Wu criteria value is obtained for composite components. Jython scripts are developed for postprocessing.
- **Impact:** peak force and energy absorption are obtained from LS-DYNA model.
- **Cost:** a Jython script is developed to estimate the total cost of the design based on the weight of each type of materials used in the design.
- **Mass:** the mass of the structure is obtained from the simulation result file of the MSC Nastran model.

Execution of the three modules, data I/O, and handshaking between different modules are managed by modeFRONTIER. modeFRONTIER provides the capability of generating new design points, sends the design variable values into each simulation model, submits the simulation and post processing jobs to HPC following the predefined sequence, reads the quantities of interest from the simulation results, and activates the optimization algorithm to generate new designs based on the existing design points.

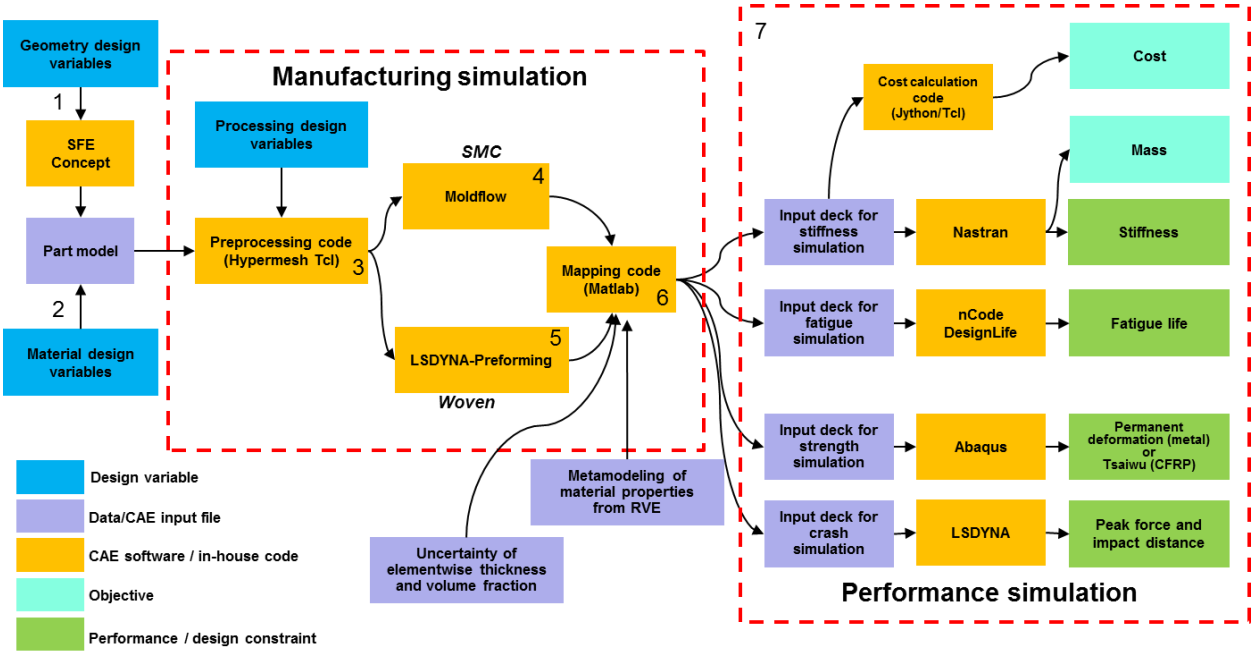

Figure 3.3-5. Full ICME workflow developed in this project

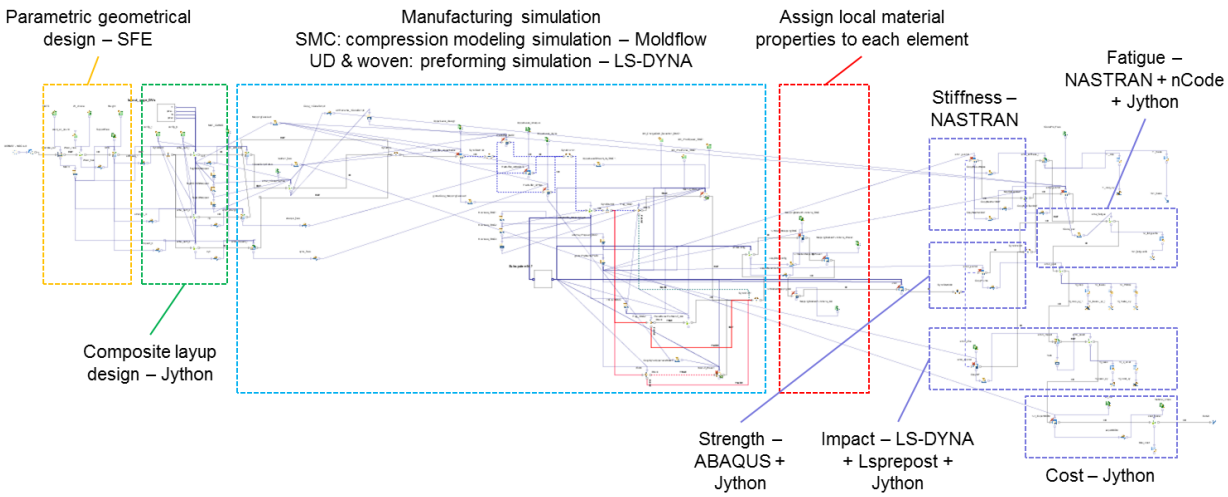

Figure 3.3-6. Implementation of the full ICME integrated workflow in modeFRONITER.

A DOE study is conducted to demonstrate the capability of the workflow, illustrated in Figure 3.3-6, with the top hat assembly as the exemplar part. The formulation of the design problem and the results are discussed in details in Section 3.3.4.

3.3.2 Software Interface Development

While the modeFRONTIER provides an outstanding platform for model integration, there still exists some significant challenges when implementing the details in this platform. Moreover, while most of the models are developed on local workstations by different users, usually with the Windows operating system, the whole workflow has to reside and run on Ford's HPC system using Linux (distribution: SLES 12). This transplantation from Windows to Linux system provides additional challenges in implanting some of the linkages in the workflow.

As shown in Figure 3.3-5, the numbered items represent the key interfaces and/or linkages between different integrated modeling tools. Even though implementation of the developed ICME models are mostly done in the corresponding commercial software, there are no existing solutions for linkages in modeFRONTIER. The requirement that massive optimization runs must be in batch mode with no user interference provides an additional challenge for the linkages. Therefore, a huge amount of the scripting is developed internally at Ford to provide interfaces using different scripting languages. Depending on the designed functions and type of models being connected, the interfacing scripts in different linkages are coded using different languages. The scripting tools involved in the workflow include the following categories:

1) API (application programing interface) scripts for CAE: e.g., Abaqus Python, LS-PrePost cfile, HyperMesh Tcl.
2) General purpose coding tools that directly operates on files with ASCII texts or for calculation: modeFRONTIER Jython, Java, MATLAB
3) Flow control scripts for simulations on Ford HPC: Linux Shell

Detailed information of the developed interfacing scripts for some of the key linkages in the ICME workflow are listed in Table 3.3-1:

Table 3.3-1. Information of developed interfacing scripts for key linkages between models for ICME workflow in modeFRONTIER

Linkage number in Figure 3.3-5	Function description	Scripting language	Input	Output
1	Send the geometric design variables for SFE CONCEPT	modeFRONTIER Jython, SFE CONCEPT Scripts	Design variables	SFE CONCEPT model (.mac) CAE input decks for mesh and load
2	Send material selection design variables to SFE CONCEPT model	modeFRONTIER Jython	Design variables	Overall material definition in CAE input decks
3	Generate manufacturing simulation models from designed geometry	modeFRONTIER Jython, HyperMesh Tcl, Moldflow studymod	Process design variables, CAE input decks for SMC components from SFE CONCEPT	Moldflow mesh (.udm) and model (.sdy) LS-DYNA preforming model (.k) with one-step forming control card
4	Obtain predicted fiber orientation tensor from Moldflow simulation for SMC compression molding	Moldflow studyrlt, modeFRONTIER Jython	Completed Moldflow simulation	Fiber orientation tensor on Moldflow mesh
5	Retrieve fiber yarn direction from LS-DYNA woven preforming simulation	modeFRONTIER Jython	Completed LSDyna woven preforming simulation	Fiber yarn direction in for Woven components (.dynain)
6	Map predicted microstructure prediction to obtain local material properties	MATLAB	Microstructure prediction (fiber orientation tensor / yarn direction)	CAE decks with predicted local material properties
7	Run performance simulations and check constraints	modeFRONTIER Jython, Linux Shell Script, APIs for different CAE tools	Generated CAE decks from mapping	Predicted part performance

Two of the most challenging procedures which may be of great value to the future development in this field, i.e., the linkage #3 and #6 are described in details below, along with the visualized intermediate results:

1) Linkage #3: Automatic preprocessing to obtain manufacturing simulation models

One of the most challenging links in the ICME optimization workflow is to complete the setup of the Moldflow simulation model completely in batch mode. While the user interface has already been well developed in Moldflow on Windows platform, the scripting capability is relatively limited compared to mainstream commercial CAE software, for example, ABAQUS. A typical procedure to set up a Moldflow simulation model for SMC compression molding includes: importing geometry for part and initial charge, defining material properties and processing conditions, meshing and providing initial fiber orientation states in the initial charge elements. User operations is usually required for all these links, since the CAD of the top hat model keeps changing during optimization since parametric geometry design is implemented by using SFE CONCEPT. The meshes in Moldflow needs to change from design to design, for both the part and the initial charge of the composite material.

Solutions using Moldflow APIs to automate part of this modeling procedure are available only on Windows platform but not the Ford's HPC platform that uses Linux. Besides, not all of the necessary modeling functions for developing a compression molding simulation model can be realized. Therefore, effort is spent to find an alternative solution for this procedure. The solution we come up with combines the usage of HyperMesh automated via Tcl script, XML scripts for Moldflow utility studymod, and modeFRONTIER Jython scripts to assemble input decks. As a demonstrative example, the flat top surface and neighboring chamfers in the top hat are considered as a SMC part that's formed through compression molding. The automatic preprocessing procedure we implement is used to generate the corresponding Moldflow simulation model for this component. The intermediate results at different stages of the procedure are shown in Figure 3.3-7.

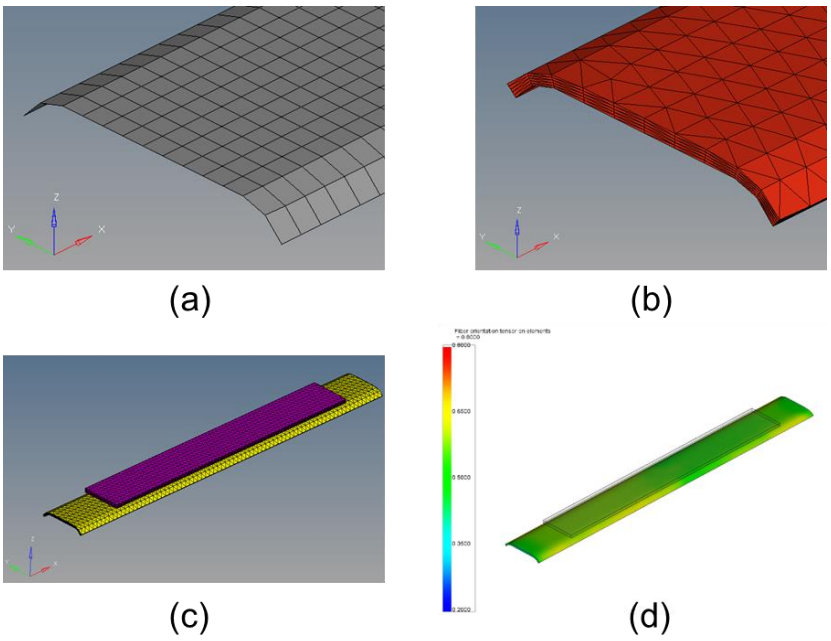

Figure 3.3-7. Intermediate results when exercising the developed automatic procedure to generate a Moldflow simulation model from 2D shell mesh obtained from parametric CAD design via SFE CONCEPT.

At the beginning of the design, parametric CAD design based on design variables in modeFRONTIER is generated by SFE CONCEPT (Linkage #1 in Figure 3.3-5 and Table 3.3-1), and then meshed with 2D quad elements. A zoom-in image of the mesh is shown in Figure 3.3-7a. To convert this 2D mesh into a

3D mesh that can be used in Moldflow, the 2D quad mesh is first transformed to tria using 2D automesh function in HyperMesh and then extruded to wedge elements based on the target thickness, which is also a design variable passed from modeFRONTIER. A split function is followed to divide the wedge elements into tetrahedron elements which are compatible in Moldlfow. The zoom-in of the resultant 3D mesh is shown in Figure 3.3-7b. In the next step, the volume of the component is calculated in HyperMesh and an initial charge piece with slightly large volume is modeled and assembled with the meshed part, as depicted in Figure 3.3-7c. The meshed part is exported in the format of MSC Nastran ***.bdf and then imported into Moldflow using an XML script that runs in Moldflow studymod utility and the initial charge mesh was added using a modeFRONTIER Jython script that direct modifies the Moldflow mesh file (***.udm). The material properties, processing conditions and other required inputs for compression molding simulation are also added using XML scripts in Moldflow studymod, which completes a Moldflow model (***.sdy file). One of the results of the simulations (distribution of fiber orientation tensor) is shown in Figure 3.3-7d. The codes run successfully on Linux platform on Ford's HPC. To improve compatibility with the optimization workflow, all the scripts are packaged using a subprocess in modeFRONTIER for seamless exchange of design variables. This subprocess can also run independently with minor modifications in input and output and thus may be restructured as an independent utility for similar applications in case needed.

There are certain limitations in the developed linkage. The core part of the linkage is the conversion between a 2D shell mesh and a 3D tetra mesh. While the methodology works in the top hat geometry thanks to the simplified geometry, this conversion is generally a very challenging problem for models with real-life geometric complexity. The linkage is not expected to work for the subframe part. To our best knowledge, to perform such conversion, a huge amount of manual operations must be provided by the user even if state-of-art meshing software packages are used. This shortcoming is one of the factors that inhibits the massive ICME optimization runs of SMC CFRP subframe.

2) Linkage #6: Mapping of microstructure predictions to obtain CAE decks with local material properties

Another key enabling linkage for the complete ICME workflow is the mapping process in which predicted microstructure information from manufacturing simulation is used to predict the local material properties in a CAE input deck. The microstructural descriptor that affects the local material properties most in the present study is the direction of the fibers. For chopped carbon fiber SMC, the direction of the fibers is usually expressed in the form of fiber orientation tensors, whereas in continuous carbon fiber composites like UD or Woven CFRP, the yarn angles are sufficient to describe the fiber direction.

Due to the nature of the manufacturing process, the fiber directions vary spatially in the composites. The output of the fiber orientation tensor or the yarn angles are generated for elements in the manufacturing simulation model, which is usually meshed differently compared to part performance CAE. The spatial correlation between elements in manufacturing simulation model and those in performance CAE needs to be established so that the fiber orientation tensor in elements in performance CAE decks can be predicted and then the local material properties are then computed as a function of local fiber directions. For the CAE decks in the optimization workflow, the elementwise anisotropic elastic moduli are computed.

The flow chart of the mapping code is shown in Figure 3.3-8. The procedure starts with parsing the input decks from target mesh to be used for performance simulation and the mesh and results from manufacturing simulation. Two point clouds are extracted in this step, i.e., the points in target mesh where local material properties need to be defined and those in source mesh where output is reported.

Specifically, in the problem of our interests, these point clouds refer to integration points in CAE model and element centroids in Moldflow, respectively. To evaluate the spatial correlation between the meshes represented by the point clouds, the coordinates of every point in target mesh are extracted and the sources points in close proximity are located. The correlation of the target point and the source points are evaluated with Reproducible Kernel Particle Method in which fiber orientation tensor on points with smaller distance to the target point have higher weight in determination of the mapped value on target point.

After fiber orientation tensor of all the points are determined for target mesh, the local material properties are computed. Either of the two algorithms can be selected. If the results of offline RVE simulations are available, the elementwise anisotropic elastic modulus are obtained through metamodeling based on the RVE results; otherwise micromechanics theory will be employed for the computation. The obtained properties are then written into corresponding format for material cards in different CAE simulations to replace the original material properties. The resulting input deck, in which material properties are defined on every element, is usually much larger in terms of file size compared to original deck. Finally, the updated CAE decks are submitted on Ford HPC for simulation.

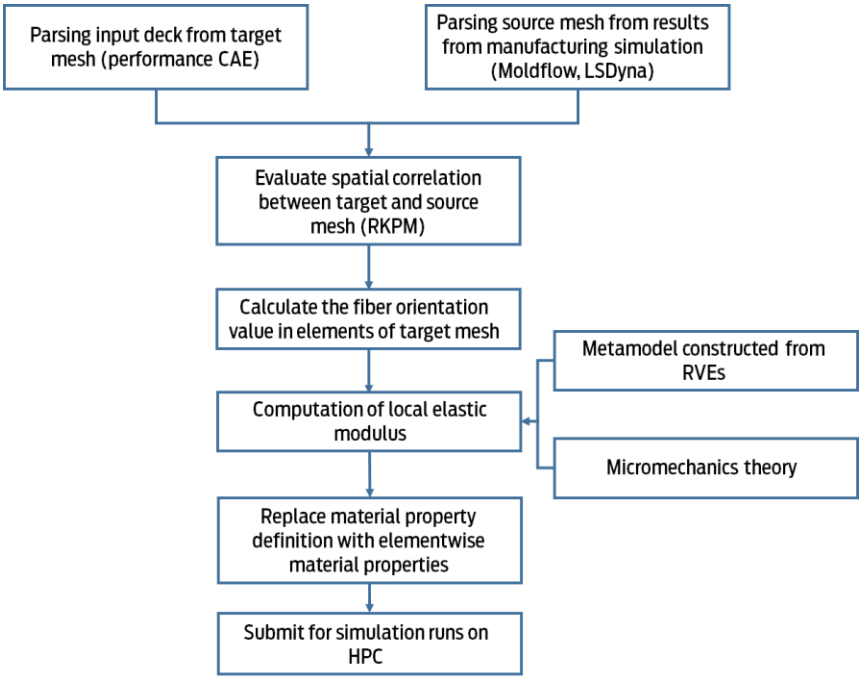

Figure 3.3-8. Flowchart of the mapping code.

To validate the accuracy of mapping for the developed tool, a T-shape geometry is used as a demonstrative example. The source model in Moldflow is composed of ~1 million tetrahedron elements whereas the target mesh has ~25,000 shell elements. A comparison of the A_{11} component in Moldflow and the shell mesh after mapping is shown in Figure 3.3-9. Close match of fiber orientation tensor on the surface of these two different meshes are observed. In terms of prediction of local material properties, the validation is shown in Task 2.

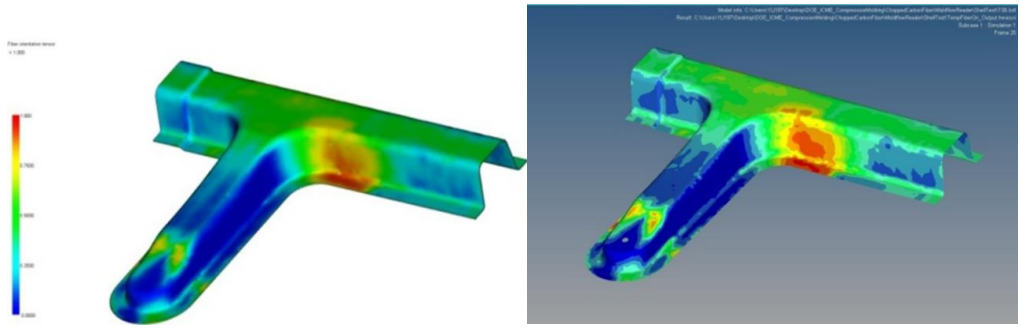

Figure 3.3-9. Comparison of the mapped fiber orientation tensor component (A_{11}) from a T-shape model in Moldflow with 1 million tetra elements to a structural model meshed with 25,000 shell elements in MSC Nastran. Color scale is set as the same in both contours.

3.3.3 Model Reliability, Robustness and Efficiency

The efficiency of the integrated ICME process is influenced by the following factors:

- Robustness of the simulation models. During the DOE/optimization process, a wide range of values is assigned to the model parameters, such as geometrical variables, material parameters, composite layup parameters, etc. The simulation models may encounter convergence issues if improper parameters are assigned to the model.
- Turnaround time of the simulation models. As the performance simulations (stiffness, strength, fatigue, and impact) are parallelized, the total turnaround time of the performance simulations is determined by the model that takes the longest time.
- Limited software licenses. Although a large number of jobs can be submitted to HPC simultaneously, the number of running jobs are constraint by the number of available licenses.
- Limitations in the number of available CPUs. Long queueing time on HPC is one of the major hurdles of improving the efficiency of ICME optimization.
- Material selection for the hat section design. If metals are selected for all structural components, the manufacturing simulation module and local property mapping will be skipped. The performance simulations also take much less time compared to the composite structures.
- The failure rate and turnaround of the analysis of each DOE point are recorded to provide insights into the efficiency and robustness. Less than 8% of the designs end up with failures in simulations (no result is obtained). In general, this ICME workflow demonstrates a good robustness.

For the ICME analysis of a composite top hat section design, the turnaround time is approximately 115 minutes. In the DOE study, the longest turnaround time for one top hat design is over 19 hours due to the queueing time on HPC. By breaking down the total turnaround time into each simulation model (Figure 3.3-10), it is identified that impact simulation in LS-DYNA, mapping local material properties to each element, and manufacturing simulation requires the most time. Stiffness analysis, strength analysis, fatigue analysis and impact analysis are operated in parallel, so the turnaround time is determined by the impact analysis that takes the longest time.

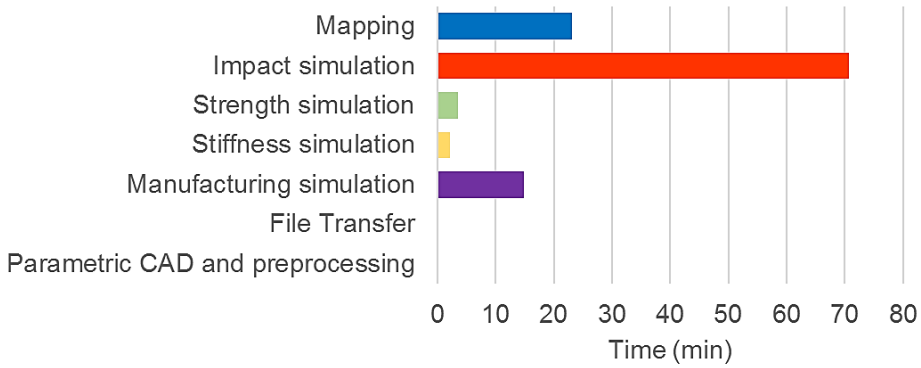

Figure 3.3-10. Turnaround time of the major steps in the ICME workflow – top hat design example

3.3.4 Assembly-Level Testing and Model Validation

An assembly-level design problem tests and validates the developed ICME workflow before it is applied to the design of CFRP subframe with considerable geometric and performance complexity. The "Top Hat" part, as shown in Figure 3.3-11, is selected for optimization based on several considerations. First, the structure of the top hat is a representative geometry in composites part. The side member and cross member of the subframe are designed with similar structure, i.e., a convex upper thin plate closed out with a flat back-plate. It is thus expected that the experience and conclusions working with this geometry would benefit the development of the subframe workflow in Task 4 of this project. Second, the design variables in the top hat, listed in Table 3.3-2, have the same categories as the subframe part: geometry design variables, processing condition variables and material selection variables. Therefore, all the developed and integrated models in the ICME workflow can be utilized and examined in this reduced scale problem.

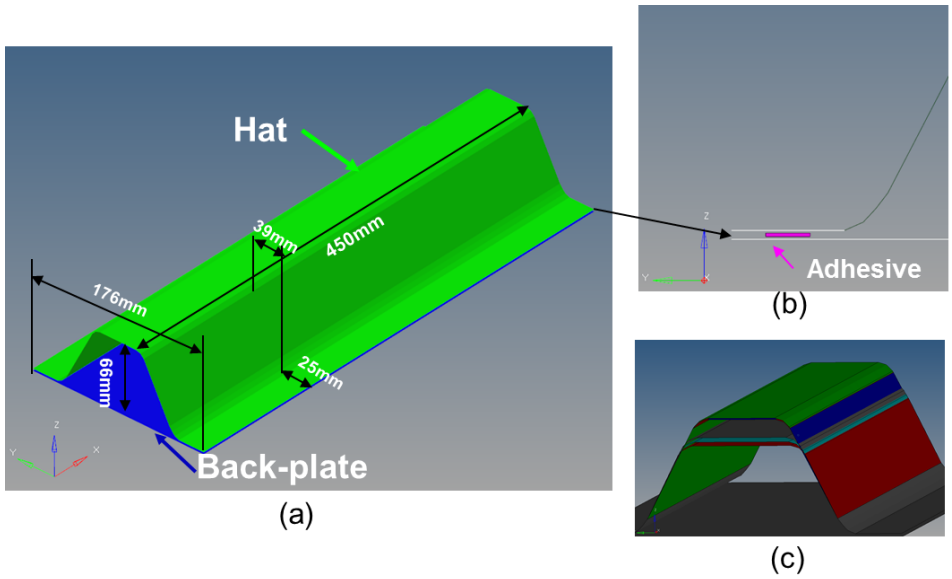

Figure 3.3-11. Geometry of the top hat. The overall geometry of the hat and back-plate (baseline design) is shown in (a). The adhesive elements joining the two parts are shown in the zoom-in view

in (b). Assembly geometry with different height values of the hat generated from SFE CONCPET are overlaid in (c).

Table 3.3-2. List of the design variables in top hat optimization

	Type	Levels/range
Material selection	Categorical	6
Layup-angle	Discrete	12
Half-thickness of hat	Continuous	[0.5mm, 4mm]
Half-thickness of back-plate	Continuous	[0.5mm, 4mm]
Height of hat part	Continuous	[-1, 1]
Initial charge geometry	Categorical	2
Press force/speed for SMC	Discrete	6

The full ICME workflow is implemented in modeFRONTIER to demonstrate its capability on the example of hat section analysis and design. The performance simulations are summarized in Figure 3.3-12. There are two components in the assembly: top hat and the bottom plate. Five candidate materials can be selected for each component: steel, aluminum, UD, woven, and SMC. When UD and woven are selected, the composite layup design variables (total number of layers, and fiber orientation of each layer) are activated. Otherwise, the continuous thickness variable is activated for this component. A geometric design variable (height) is defined for the top hat. In addition, we also defined several processing related design variables. For SMC, compression speed (two levels) and compression force (three levels) are defined as discrete design variables; for UD and woven, binder force and temperature and selected as the processing design variable.

The objective of the optimization is to achieve the largest weight saving compared to the baseline part, where both the hat and the back-plate are manufactured with 1.5 mm of steel. The constraints of the design ensure that the performance of the top hat is no worse than the performance of the baseline steel assembly. Three different groups of constraints are considered as detailed in Figure 3.3-12. The stiffness of the assembly is evaluated by r1_disp, which is the Z displacement of the node located at the center of the back-plate part (node #100) under 4-point bending condition with unit load. The strength constraints include three descriptors: r3_peeq and r3_tsaiwu characterizes the integrity of the material, whereas the r3_disp evaluates the permanent deformation of the assembly, all evaluated under 4-point bending condition with 100N force. The crashworthiness performance of the par is evaluated under side impact loading condition. The maximum value of the peak force, r4_peak, and the displacement of the top surface center from initial contact to the time that impact force reaches maximum, r4_peak, are used as descriptors. The detailed threshold values for the constraints are listed in Table 3.3-3.

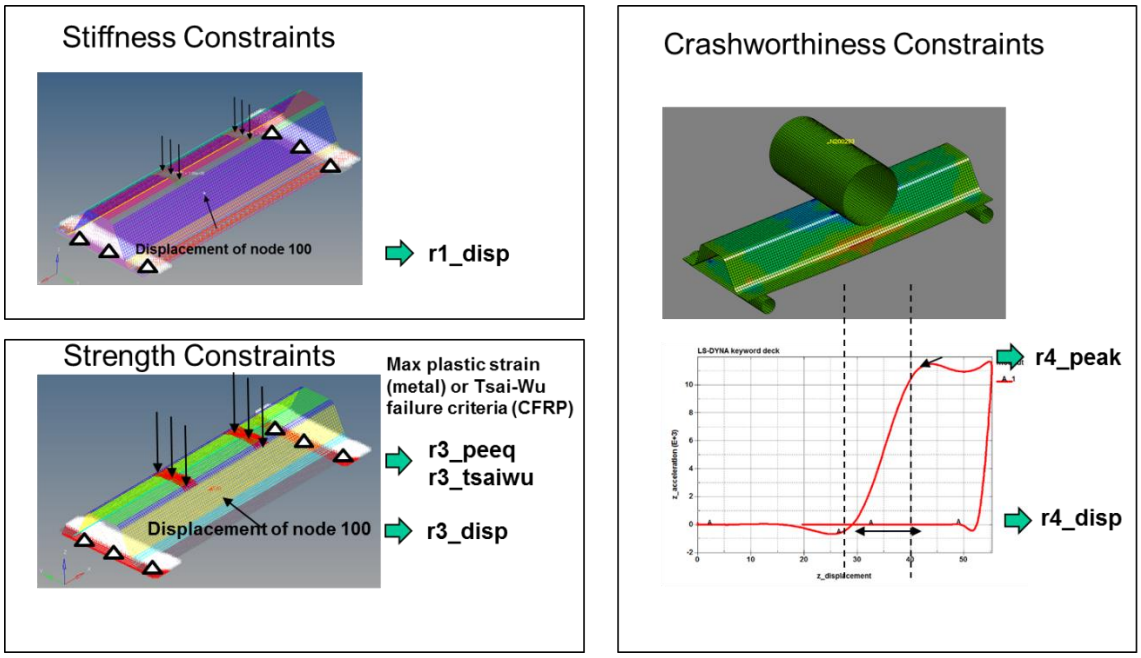

Figure 3.3-12. List of design constraints for the top hat optimization.

Table 3.3-3. List of the constraint value for the design

Constraints	direction	Threshold
r1_disp	≤	1.13e-4 (mm)
r3_peeq	≤	0.1%
r3_tsaiwu	≤	1.0
r3_disp	≤	1.0 (mm)
r4_peak	≤	31.4 (kN)
r4_disp	≤	13.51 (mm)

One essential consideration in this workflow is to enable the consideration of the local material properties due to the spatially varying microstructure predicted by the manufacturing simulation. One example from a design point with SMC selected for the top hat is shown in Figure 3.3-13 to demonstrate the heterogeneity of the material properties. It's observed that by incorporating the fiber orientation tensor prediction from Moldflow to obtain the elastic properties in the performance CAE model, the Young's modulus of the elements in the model shows clear spatial variation. The flange part at the bottom has modulus approximately 45 GPa, which is 50% higher than the value if the chips are assumed to be randomly oriented in the plane (Ex = 30 GPa in this case).

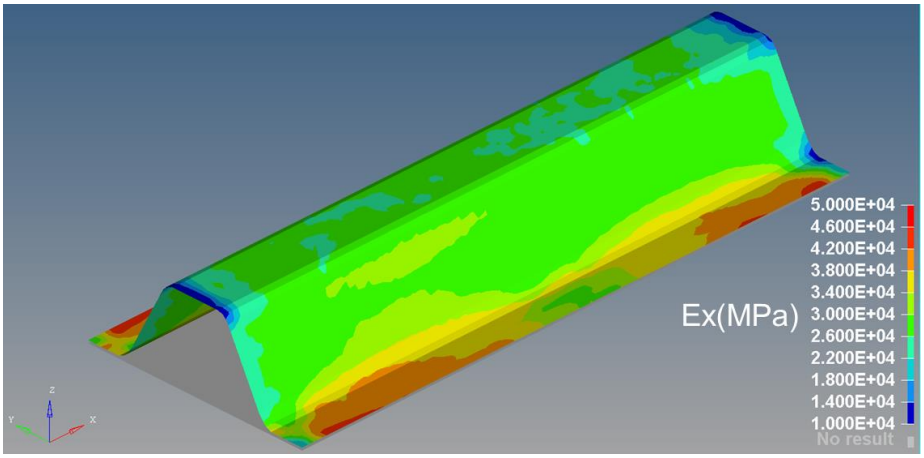

Figure 3.3-13. Spatial distribution of elementwise Young's modulus along X direction.

Another test run to validate the ICME workflow for top hat assembly is performed on a design of which experimental results from side impact test are available. The tested top hat is assembled with a UD hat and a UD back-plate, joined by adhesive. Both of the components are with the thickness as 2.4 mm and the layup as [0/60/-60/0/60/-60]s. The comparison of the results from side impact simulation and experiments is shown in Table 3.3-4. The error of r4_disp and r4_peak from the workflow is -1.8% and 8.8%, respectively, which satisfy the accuracy requirement.

Table 3.3-4. Validation of ICME workflow for top hat assembly. A design point that is the same as one of the hat section samples used in side impact experiment is generated. The predicted performance indicators r4_disp and r4_peak are compared to the experimental results.

	Experiment	**ICME workflow**	**Error**
r4_disp	10.73 (mm)	10.54 (mm)	-1.8%
r4_peak	10.33 (kN)	9.42 (kN)	8.8%

Optimizations runs using the ICME workflow Different sampling algorithms are attempted to generate the design points, including random DOE, Latin Hypercube and a responsive surface model ("Fast" algorithm in modeFRONTIER). There are 599 design points in total, among which 27 unique designs are found to meet all the constraints. The designs that with mass lower than the mass of the baseline top hat are listed in Table 3.3-5.

Table 3.3-5. List of feasible designs that have mass less than baseline steel top hat while meet all design requirement

Height of the hat	Hat Material	Back-plate Material	Hat Half Thickness	Back-plate Half Thickness	Mass (kg)
0.84	WOVEN	UD	1.8	1.8	1.06
-0.37	UD	WOVEN	2.4	1.2	1.08
-0.64	UD	WOVEN	1.8	3.6	1.40
-0.37	UD	UD	4.2	0.8	1.42
-0.44	SMC	UD	3.2	1.8	1.42
-0.53	WOVEN	WOVEN	3.9	1.2	1.46
-0.27	SMC	SMC	1.8	3.6	1.48
-0.87	WOVEN	WOVEN	2.4	3.6	1.64
0.12	WOVEN	WOVEN	3.6	1.8	1.64
0.97	WOVEN	WOVEN	4.2	1.2	1.65
0.64	SMC	WOVEN	2.0	4.2	1.66
0.12	SMC	WOVEN	3.8	1.8	1.64
-0.43	SMC	WOVEN	3.6	2.4	1.70
-0.50	SMC	WOVEN	4.0	1.8	1.89
-0.26	SMC	UD	3.6	3.2	1.90
0.06	UD	SMC	4.0	2.8	1.91
-0.19	UD	UD	3.8	3.0	1.93
-0.40	SMC	UD	4.1	3.0	1.96

The best design is given by the combination of 3.6 mm-thick Woven Hat, with lay-up as [-45/45 45/-45 90/-90]s, and 3.6 mm-thick UD Back-plate, with lay-up [90/90/45/90/90/-45/45/90/45]s, respectively. The mass of this design is 1.06 kg, which is 47% lower than baseline steel assembly (2.0 kg). However, it should be noted that due to the vast design space to explore and the limited computational resources, further optimization of the design is possible, which is beyond the scope of this demonstrative ICME workflow.

Based on the lessons learned in the top hat design problem, one major challenge of implementing the ICME approach for composite design is that the design space is notably enlarged by including design variables from multiple domains. Second, the composite design problem is often mixed-variable type, i.e., the design variables are a mixture of continuous (e.g., part thickness and height, fiber volume fraction),

discrete (e.g., fiber rotation angle, levels of speed and force in preforming), or categorical variables (e.g., type of materials), posing challenge to optimization search due to the combinatorial nature.

To address this challenge, we first develop a latent variable Gaussian process (LVGP) modeling approach that can create a metamodel with both continuous and categorical (or discrete) variables.[1] This approach offers a new way of constructing a covariance function in two steps. In the first step, each categorical variable is mapped to a two-dimensional continuous latent variable. Then the latent variables and continuous variables are mapped to the covariance values. Through benchmarking problems, the approach has been proved to be more efficient and accurate compared to other existing techniques for mixed-variable GP modeling.

Bayesian optimization (BO) is an efficient global optimization method that utilizes the uncertainty information provided by a metamodel to guide the search of the optimum. Like the regular Gaussian process modeling approach, LVGP offers uncertainty predictions at un-sampled points. Therefore, LVGP can be integrated with Bayesian optimization to effectively search a large and irregular design space with mixed variables. Compared to other gradient-based methods or heuristics, BO tends to use fewer function evaluations and is less prone to being trapped at a local optimum, thus making it well-suited for composite design optimization. As the original BO strategy is only developed for unconstrained optimization problems, a constrained BO algorithm [2] based on the LVGP model is developed in this project, where LVGP models are built for the constraints and a feasibility indicator function is applied to the improvement function compared to the current best design. Hence, the acquisition function becomes the product of expected improvement and probability of failure to prevent sampling (search) in the infeasible domain. A preliminary study of BO (Figure 3.3-14), using a LVGP metamodel in replacing the ICME workflow for simulations, shows that BO is capable of iteratively optimizing the top hat design under constraints.

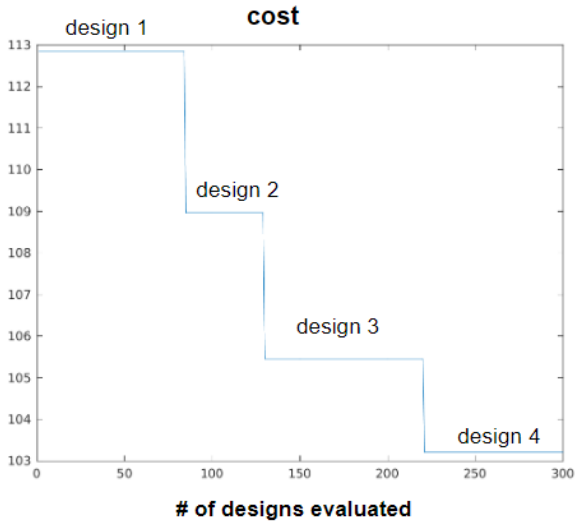

ID	hat mat	bp mat	hat t	bp t	hgt
1	UD	steel	1.37	1.36	0.45
2	Al	SMC	2.95	0.12	-0.47
3	Al	UD	2.23	0.04	0.95
4	Al	Al	1.55	0.56	0.97

From left to right: design ID, hat material, backplate material, hat thickness, backplate thickness, height.

infeasible design

feasible design

Figure 3.3-14. Preliminary results of BO of top hat cost under constraints

Uncertainty in part level variables exhibits both within-sample (spatial) and among-sample (part-to-part) variations. For example, the top hat thickness data not only differs from sample to sample, but varies at different locations in a single sample. An additive Gaussian process (AGP) modeling approach [3] is applied to model such type of data. The AGP method uses two separate GPs to capture the within-sample and among-sample variations. The resulting models are both predictive and generative, in the sense that it can both predict the response with no measurements by interpolation, and sample random realizations

from the underlying Gaussian processes. Some sample realizations from the thickness model are shown in Figure 3.3-15.

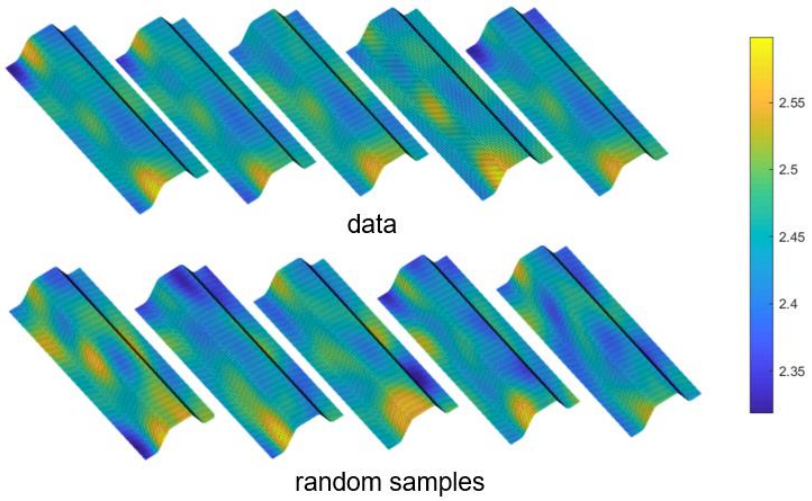

Figure 3.3-15. Random realizations of thickness profile of top hats from the AGP model

Given all the methods mentioned above, some potential future work includes (1) developing a multi-objective LVGP-based constrained BO framework (currently the multi-objective optimization problems are handled by integrating the objectives via weight sum) (2) conducting a complete UQ study at the part level by considering various sources of uncertainty (Figure 3.3-16) and investigate their impact on the performance, and (3) developing a concurrent process and product design optimization framework under uncertainty combining findings from (1) and (2).

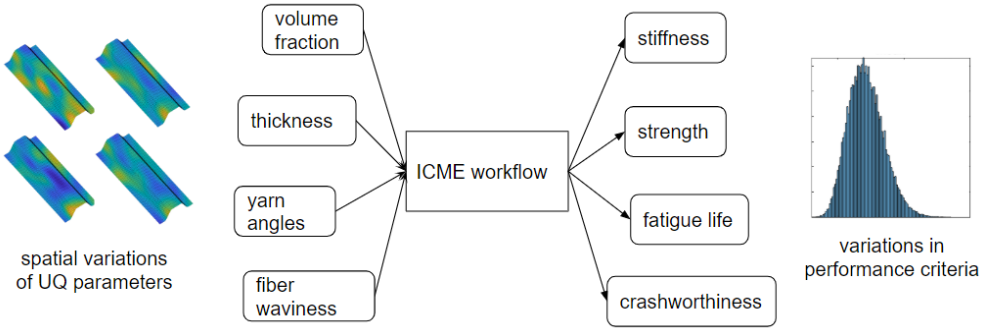

Figure 3.3-16. Proposed UQ study

Accomplishments of Task 3 are:

- Established an integrated workflow to automate the entire ICME analysis process (processing-microstructure-property-performance). This ICME workflow serves as the platform for ICME analysis, design optimization and uncertainty quantification. It is demonstrated on the two-component hat section example.
- Developed new design optimization methods to improve the efficiency of composite layup optimization.

- Key linkages between modeling modules in the ICME workflow are developed to enable a fully automatic optimization for the demonstrative top hat assembly. They are also used in the optimization workflow for the subframe design.
- A design with 47% weight-saving compared to the baseline top hat assembly is found by using the optimization workflow.

Lessons learned and potential next steps:

To shrink the vast design space and improve the efficiency of the design optimization, the range of each design variable needs to be determined by a "pre-optimization" step, in which topology optimization algorithm is employed to determine the thickness of each component solely based on stiffness performances. This step provides a better starting point for the full optimization search.

The existing solutions in the commercial software for model integration need to be improved to handle the developed models in the ICME workflow, as the linkages of different modules requires information of spatially-varying and anisotropic material properties as a characteristic for CFRP.

Despite the effort to improve the efficiency in the models involved in the ICME workflow, computational cost is still too high for a massive run of optimization, even for the simplified top hat assembly. Future work on improving the efficiency by finding a better optimization algorithm and/or increasing the simulation speed for individual manufacturing simulation and CAE models will be helpful.

References

[1] Yichi Zhang, Siyu Tao, Wei Chen, and Daniel Apley, "A Latent Variable Approach to Gaussian Process Modeling with Qualitative and Quantitative Factors", *Technometrics*, submitted May 2018.

[2] Jacob Gardner, Matt Kusner, Zhixiang Xu, Kilian Weinberger, and John Cunningham. "Bayesian Optimization with Inequality Constraints." In *ICML*, pp. 937-945. 2014.

[3] Linmiao Zhang, Kaibo Wang, and Nan Chen. "Monitoring wafers' geometric quality using an additive Gaussian process model." *IIE Transactions* 48, no. 1 (2016): 1-15.

3.4 Task 4: ICME-Based Design and Optimization

This task, ICME-Based Design and Optimization, applies the newly developed Integrated Computational Materials Engineering tools to the design and optimization of a front subframe, connecting structural performance to the local material properties that depend on the manufacturing process. The multi-disciplinary subframe design utilizes the optimization scheme developed in Task 3 using modeFRONTIER to couple the subframe geometry and materials to the performance evaluation and variable cost estimation. These Design of Experiments investigations produce five interesting designs, one of which meets the 25% weight save target and also meets the $4.27 additional variable cost per pound saved target.

This task accomplishes:

1) Demonstration of an ICME-based design for a complex part including geometry, material and composite layup in a batch process on an industrial high performance computing platform;
2) Evaluating four performance attributes concurrently; and
3) Estimating weight and cost from the design variables for each subframe candidate design.

The ICME procedure developed within this project demonstrates that a mix of geometry and material variables can be concurrently considered to produce a design that meets stiffness, strength, durability, safety and cost targets. For the first time these diverse design variables are concurrently investigated in an automated procedure processed in batch mode on a high performance computing platform for a design to meet multiple engineering performance metrics and variable cost. This exercise produces a multi material design of a complex automotive component, the front perimeter subframe.

The design that meets both the weight save and cost target is primarily steel with carbon fiber composite stiffeners and reinforcements. The design includes both chopped carbon fiber sheet molding compound (SMC) and carbon fiber unidirectional non-crimped fabric patches. The initial design is a 30% weight reduction at an additional variable cost of four dollars per pound of weight saved. The design utilizes steel, 79% by weight, with reinforcements of chopped carbon fiber SMC, 16% by weight, and selected patches of unidirectional carbon fiber composite, 5% by weight.

The key lesson learned for accelerating the ICME methods in carbon fiber composite design highlights the need for improvements in the geometry and architecture morphing to the computer aided engineering (CAE) models for manufacturing simulation and performance predictions.

From the Statement of Project Objectives (SOPO) Task 4 attacks four areas:

Task 4.1 – Subframe Concept Development and Topology Optimization

Create an optimized subframe topology assuming that material response is monotonic.

Task 4.2 - ICME-Based Design Optimization

Incorporation of ICME tools in the framework of a Multi-level, Multi-disciplinary Design Optimization with the consideration of material property change as a result of constituent, fiber architecture and manufacturing processes and with consideration of uncertainties in the system.

Task 4.3 - Performance Analysis and Model Demonstration

Examine the design against performance criteria stiffness, strength, durability and crash.

Task 4.4 - Weight and Cost Analysis

Compare the weight and cost of the CFRP subframe to the baseline steel design.

Table 3.4-1 summarizes the results from Task 4 compared to the SOPO requirements.

Table 3.4-1. Task 4 SOPO Milestones with description and final status

Milestone	Type	Description	Final Status
ICME Model Reliability, Robustness and Efficiency Assessed	Technical	An assessment of the reliability, robustness and efficiency of the integrated ICME model completed	Each model **<15%** error Robust process, Long Run times for Moldflow
Subframe Design Concept Developed	Technical	A design concept for the CFRP subframe is developed	Build from two design concepts / architectures
Design Optimization Completed; Performance, Weight and Cost	Technical	The weight and cost analysis CFRP subframe to the baseline steel design demonstrated	Completed **~ 10,000** Design evaluations to find Optimum
CFRP Subframe Concept Meets Design Targets	Technical	CFRP subframe chassis system satisfies weight savings and variable cost increase FOA targets	**One Design achieves Weight and Cost Targets** Four other interesting designs identified.

This task concurrently investigates and optimizes the geometry, material, grade, gauge and layup for a multi material component including steel, aluminum and three forms of thermoset carbon fiber composite, chopped carbon fiber SMC, unidirectional carbon fiber non-crimped fabric and woven continuous carbon fiber fabric. This is an industry first. Task 4 exercises the ICME Multi-level, Multi-disciplinary Design Optimization to develop initial designs for a perimeter front subframe. This complex automotive component must meet stiffness, strength, durability and crash safety performance targets at an affordable cost. The comparison for the performance, weight and cost is the high volume, stamped steel, metal inert gas welded perimeter front subframe.

The ICME-based Multi-level, Multi-disciplinary Design Optimization effort addresses certain key performance metrics to produce an initial design. A complete final design would need to be confirmed for many additional engineering performance metrics including corrosion protection, bolted connection capacity, manufacturability, installation and repair requirements. This ICME-based design optimization produces an initial design meeting key requirements.

The front subframe attaches to the body structure in a unibody vehicle typically with four isolators. The subframe provides the foundation for the powertrain roll restrictor, stabilizer bar, steering system, lower control arm (LCA) that holds the front wheels, and the exhaust system. Figure 3.4-1 shows a representation of the front subframe with the list of the attached components.

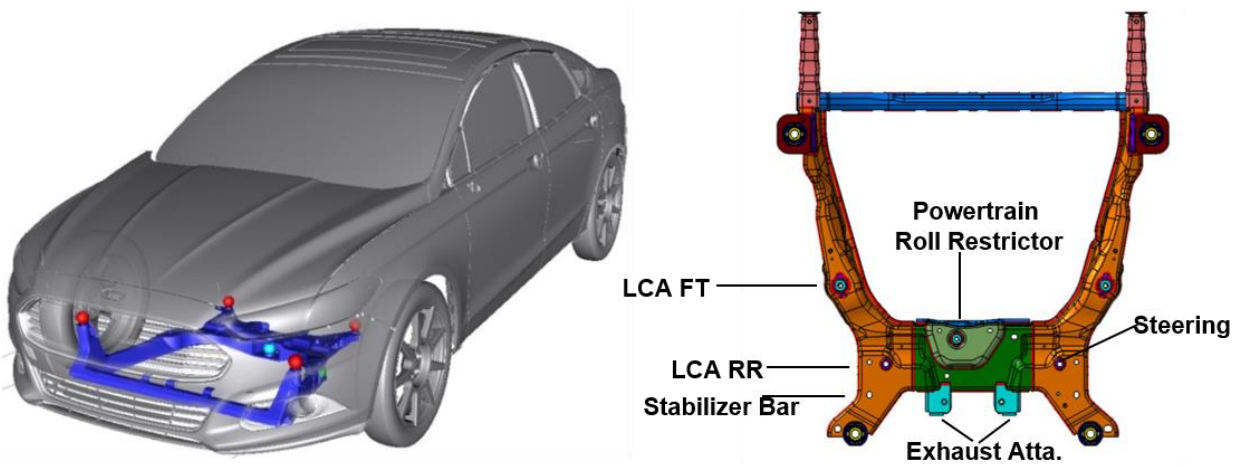

Figure 3.4-1. Perimeter front subframe in a unibody vehicle.

3.4.1 Subframe Concept Development and Topology Optimization

The project started by developing the topology results for the stiffness and strength performance requirements for the front perimeter subframe. This gave the locations and general forms of where material needed to be placed to meet requirements. The topology optimization began with the allowable design space block for the front perimeter subframe. The topology study included the stiffness and strength performance requirements and used isotropic material properties for each of the candidate materials.

The topology results clearly showed that the most efficient design included closed box sections for the wide rear area and tubular sections for the longitudinal members from the lower control arm attachments to the front body mounts. This architecture matches typical subframe design experience.

Initially three concepts were developed for the subframe based on the topology results. These three concepts were: (1) clam shell design, (2) tubular design, and (3) multiple piece design. These three seed designs were developed using isotropic material properties. The designs met the twenty-seven stiffness requirements and the strength requirements. These designs were then modeled in SFE CONCEPT Modeler that morphs the design using geometry design variables such as section height and width, thickness of ribs and shells, and material and produces shell meshes for performance simulations.

Two designs, the clam shell and tubular designs, were successfully modeled in SFE CONCEPT Modeler for batch processing of geometry design variables. The third concept, the multiple piece design, was not easily modeled in SFE CONCEPT Modeler due to the large number of parts and connections. Only minimum geometry variations could be included in batch processing. The details of the connections between the parts, especially at corners where more than two parts came together, often failed to produce an acceptable mesh for engineering performance evaluations. Therefore, this architecture was dropped from the full ICME multi-disciplinary optimization. Figure 3.4-2 depicts these three initial architectures developed from topology optimization.

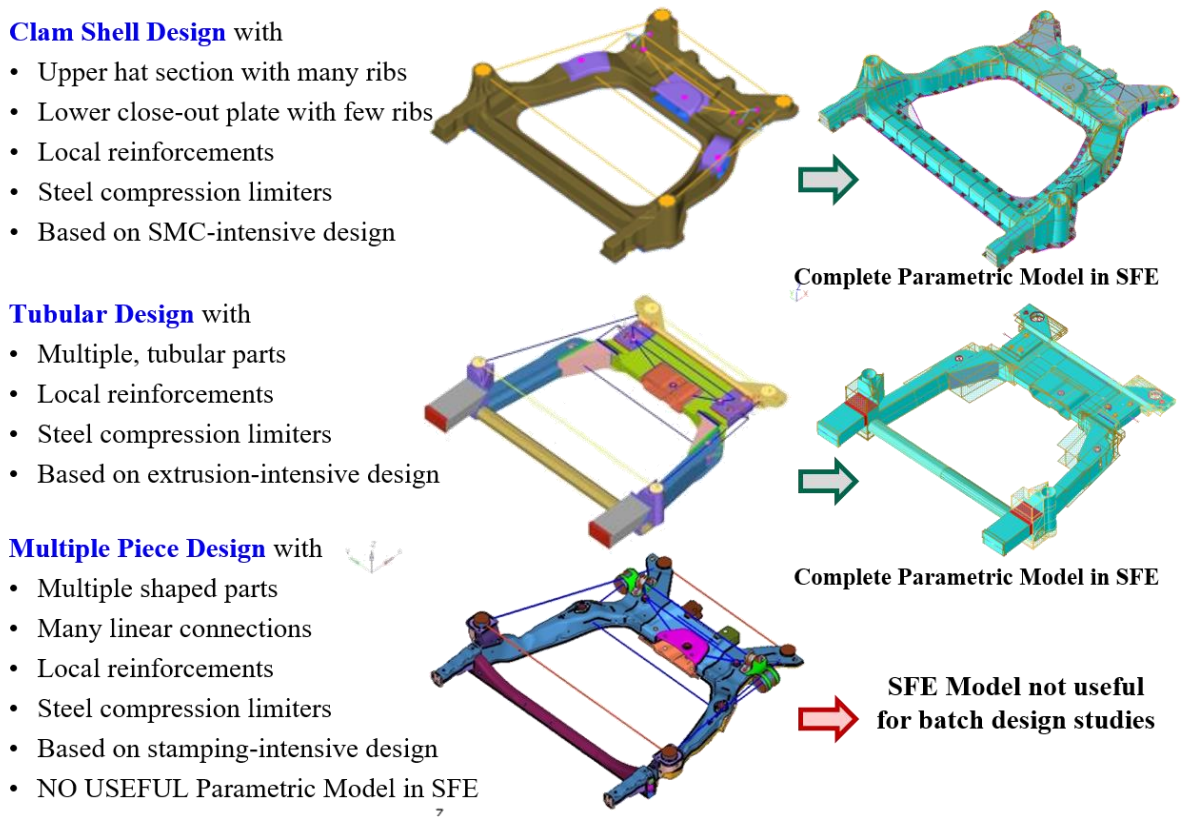

Figure 3.4-2. Initial design concept architectures.

The two SFE CONCEPT models were incorporated by the Task 3 team into a Multi-level, Multi-disciplinary Design Optimization using modeFRONTIER. The Task 3 team created a modeFRONTIER workflow similar to the workflow used for the ICME-based optimization of the top hat assembly previously described in Task 3. Linkages equivalent to those described in Figure 3.3-5 and Table 3.3-1 linkages #1 and #2 for the hat section assembly were generated for the modeFRONTIER workflow for this subframe investigation. These linkages passed the geometric design variables into SFE CONCEPT to modify the subframe geometry and sent material selection design variables to the SFE CONCEPT model to specify the material at each portion of the subframe.

While the complete workflow for the subframe was being developed, the most time consuming analysis proved to be the Moldflow simulation for the compression molding of the carbon fiber composite for the full subframe. The Moldflow simulation took approximately 90 hours of CPU time for the upper clam shell of the subframe. The lower clam shell Moldflow simulation took approximately 50 hours to complete. Due to the license structure of Moldflow within the Ford High Performance Computing platform minimal parallelization was available to reduce the clock time for this analysis.

Also, SFE CONCEPT produced shell mesh for the subframe that worked well for engineering performance simulation but could not be used for Moldflow compression molding simulation. The team was unable to create a batch mode process to automatically convert the subframe shell mesh into the high quality three dimensional tetrahedron mesh required by Moldflow for compression molding analysis. This increased the difficulty in connecting Moldflow for compression molding simulation into the modeFRONTIER workflow for optimizing the subframe,

Several key performance metrics were identified to develop the initial design for the subframe. Key stiffness, strength, durability and safety metrics usually determine the majority of the design for a subframe. While not the complete list of all design requirements for a production subframe, meeting these critical requirements produces an initial design that can be slightly modified to meet the full set of all requirements, usually with only modest changes to weight and cost. Table 3.4-2 lists the performance metrics included in the ICME-based Multi-level, Multi-disciplinary Design Optimization incorporated into the modeFRONTIER workflow.

Table 3.4-2. Performance metrics for subframe

TOTAL SUBFRAME								
Weight	Saved from Steel Design			(lb)	**43.6**			
Percentage	Weight Save			(%)	**25%**			
	Weight Buy - Additional Variable Cost per Pound Saved			($/lb)	**4.27**			
STIFFNESS				**DURABILITY High Cycle Fatigue**				
FLCA Front Left	(kN/mm)	12.6		Design meets Expected Vehicle Life in CAE (NASTRAN + nCode)			(min life)	**1.0**
FLCA Front Left	(kN/mm)	10.1						
FLCA Front Left	(kN/mm)	3.2						
FLCA Front Right	(kN/mm)	12.5		**STRENGTH Overload single event**				
FLCA Front Right	(kN/mm)	10.4		**Cases**				
FLCA Front Right	(kN/mm)	3.2		**Level 1**				
FLCA Rear Left	(kN/mm)	9.7		**AFT-L1**	Disp after unloading (Loading Location)		(mm)	**1.0**
FLCA Rear Left	(kN/mm)	29.4			CFRP Tsai-Wu			**0.7**
FLCA Rear Left	(kN/mm)	2.9						
FLCA Rear Right	(kN/mm)	9.5		**LAT-L1**	Disp after unloading (Loading Location)		(mm)	**1.0**
FLCA Rear Right	(kN/mm)	29.6			CFRP: Tsai-Wu			**0.7**
FLCA Rear Right	(kN/mm)	2.9						
Steering Gear Left	(kN/mm)	11.4		**STABBAR**	Disp after unloading (Loading Location)		(mm)	**1.0**
Steering Gear Left	(kN/mm)	19.0			CFRP: Tsai-Wu			**0.7**
Steering Gear Left	(kN/mm)	3.7						
Steering Gear Right	(kN/mm)	11.7		**Level 2**	**Severe Loading "Limp Home"**			
Steering Gear Right	(kN/mm)	19.2		**AFT-L2**	Metal: Max. Plastic Strain ≤ 50% of ultimate Strain		(%)	**22%**
Steering Gear Right	(kN/mm)	3.7			CFRP: Tsai-Wu			**0.7**
Roll Restrictor	(kN/mm)	16.0						
Roll Restrictor	(kN/mm)	15.9		**LAT-L2**	Metal: Max. Plastic Strain ≤ 50% of ultimate Strain		(%)	**22%**
Roll Restrictor	(kN/mm)	2.1			CFRP: Tsai-Wu			**0.7**
Stabar Left	(kN/mm)	8.7						
Stabar Left	(kN/mm)	16.0						
Stabar Left	(kN/mm)	4.4		**SAFETY 10 mph 1500 pound impactor**				
Stabar Right	(kN/mm)	8.9			Peak Load in Subframe		(kN)	**100**
Stabar Right	(kN/mm)	16.0			Energy Absorption at 150 mm		(J)	
Stabar Right	(kN/mm)	4.4						

3.4.2 ICME-Based Design Optimization

Design optimization of the subframe requires the evaluation of a large number of design points in the design space. The long turnaround time of manufacturing processing simulation limits the application of full integration ICME workflow on the subframe design. With the limited time constraints, the fully integrated workflow can only explore a handful of design points, which provide few information for the search of global optimum. To resolve this issue, a bi-level optimization strategy has been proposed for the ICME of carbon fiber composite structures (Figure 3.4-3). On the upper level, subframe structural optimization is conducted based on attribute simulations (stiffness, durability, strength, impact, weight and cost). The following design variables are considered:

1) Geometry of each part in the structure

2) Material selection for each part,

3) Connection method (adhesive or welding)

4) Gage (thickness) of the part, if SMC or metal material is selected

5) composites layout (number of layers and the orientation angle of each layer) of the part, if continuous fiber composites (UD or woven) are selected

Deterministic material properties are used in the top level optimization. The purpose is to find the optimal values of the above mentioned parameters to minimize the total weight and cost, while satisfying all the design constraints on stiffness, durability, strength and impact (without considering the spatial variations in local material properties). The critical parts (e.g. parts that are close to, or on the boundary of the design constraints) are identified for the bottom level optimization.

On the bottom level, the manufacturing simulation module is applied on the "optimized" structure design generated by the upper level optimization. The local material properties in each element of the "optimized" structure model is obtained based on the material processing, microstructure RVE simulation and multiscale analysis, such that the spatial variations in material properties can be captured. The part geometry and the composites layout are not changed. On the bottom level, the manufacturing process parameters and part thickness are optimized to achieve the best properties/performances.

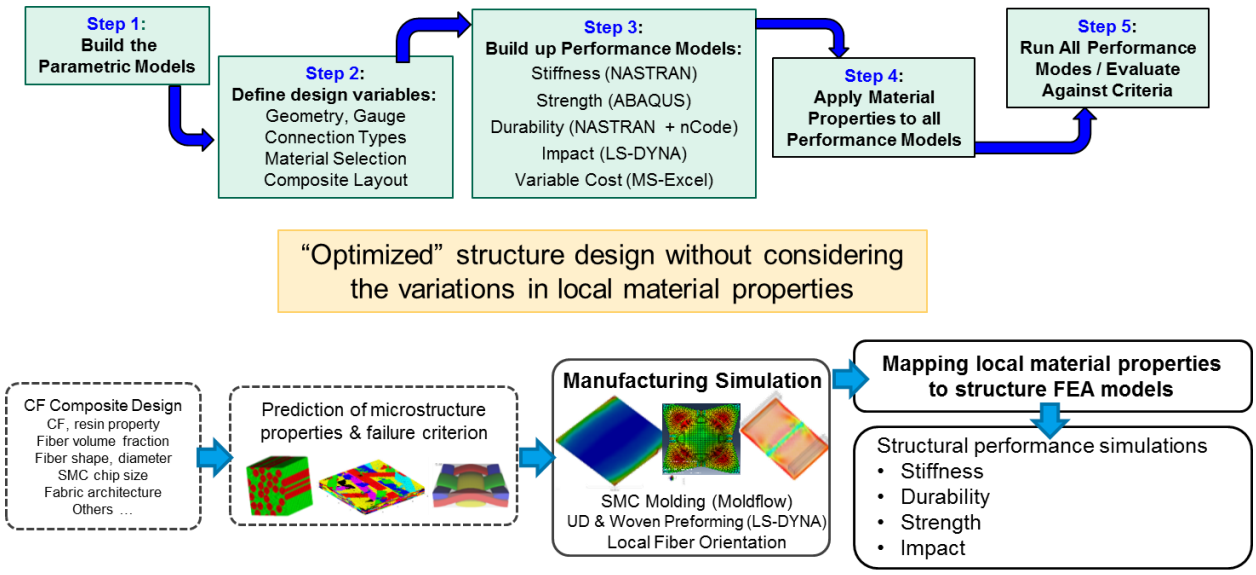

Figure 3.4-3. Bi-level strategy for vehicle subframe analysis and design. Upper level: subframe structural optimization; lower level: manufacturing process and gage thickness optimization. Source: Ford Motor Company

The upper level workflow for SMC subframe design is shown in Figure 3.4-4. The average performances of all simulation codes are listed as follows:

SFE CONCEPT (parametric CAD) has limited licenses. It requires around 10 minutes to finish one run. However, the current SFE CONCEPT model fails when the gage thickness is larger than seven millimeters.

MSC Nastran (stiffness and the first step of durability analysis) takes around 30 minutes to finish one run. Only 5% of the DOE runs fails due to numerical, queueing, or network connection issues.

nCode (the second step of durability analysis) takes around 1.5 hours to finish one run. It is also constrained by the limited number of licenses. In this project, a new development is accomplished in nCode to improve the efficiency of the fatigue analysis. Instead of screening all elements from the stress analysis by MSC Nastran, only the key elements in the high stress region is considered in fatigue analysis. By reducing the number of elements in fatigue analysis, the turnaround time of nCode model is reduced significantly.

Abaqus (strength) requires around 45 minutes to finish one run. ~30% of the DOE runs fails.

LS-DYNA (impact) requires around 3.5 hours to finish one run. ~40% of the DOE runs fails.

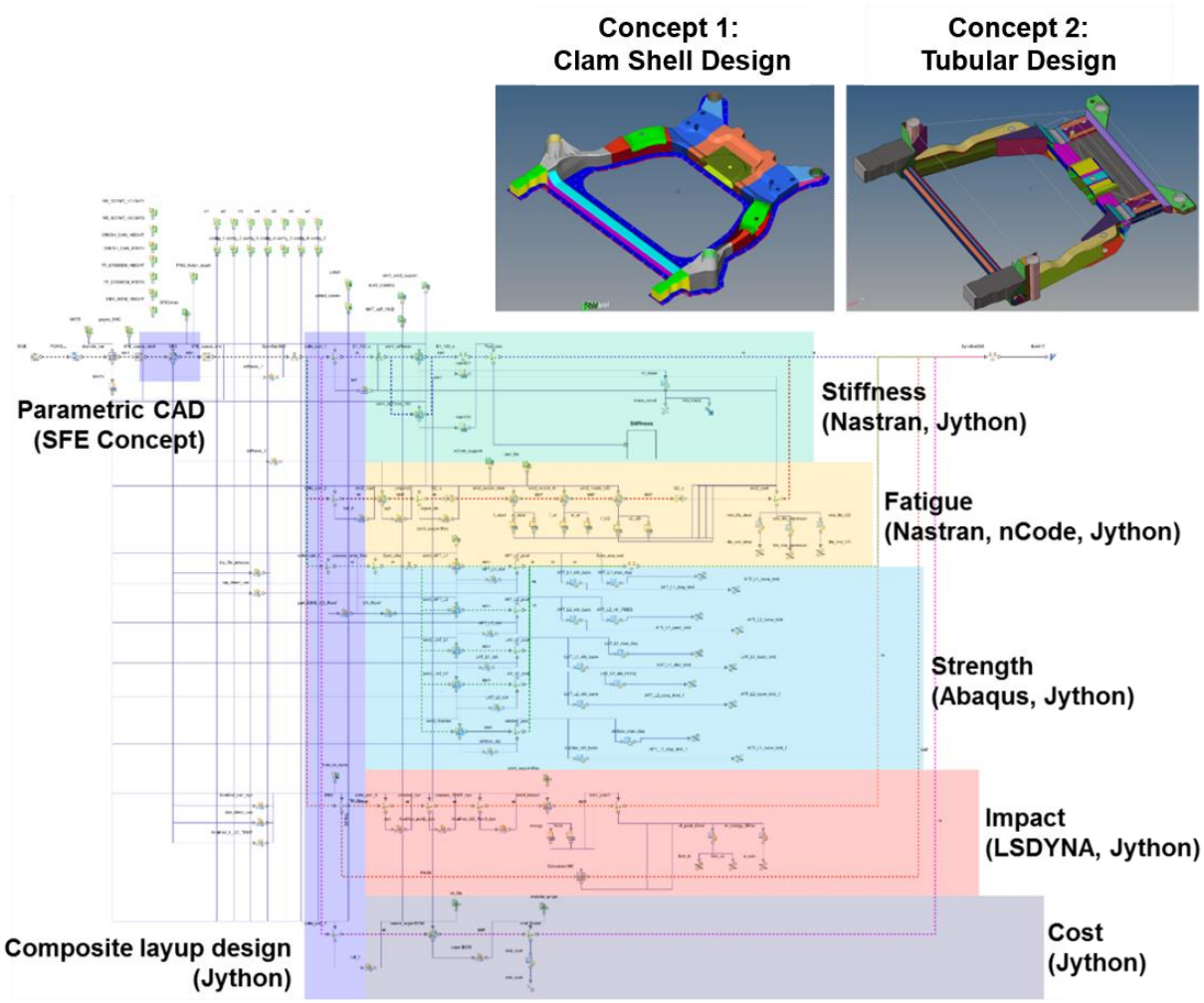

Figure 3.4-4. Upper level workflow for the subframe structural optimization.

Even though the optimization problem is broken into two levels, we are still facing a large-scale design problem with over 200 design variables and 39 constraints on the upper level optimization. Most of the design variables are related to thickness for different parts of the subframe. Apart from the numerical optimization challenges for such a large search space, there are additional challenges such has

large run times for simulations, license limitations and computational infrastructure. For example, one simulation of impact in LS-DYNA would take approximately four hours. Some software licenses were limited to one and henceforth, were not parallelizable.

A hybrid approach is adopted for the subframe structure optimization. First, topology optimization determines the thicknesses of all components such that the stiffness constraints are satisfied. This process has relatively low computational costs for two reasons:

1) Only the component thicknesses are considered.

2) Only linear elastic stiffness analysis is involved.

The preliminary design from topology optimization is used as the starting point for the full optimization search, which includes all the design variables and all nonlinear attribute analyses.

To accelerate the full optimization search, two sets of sensitivity analysis are performed to have a better understanding of the problem.

(1) The contribution of each design variable to the cost and weight targets are quantified using Random Forest technique. Only a few variables are identified as critical design variables, while others could be kept constant during optimization search to reduce the dimension of the problem.

(2) Sensitivity analysis is also employed to understand which constraints were hard to meet relative to each other.

The sensitivity analyses allow the team to focus on key design variables that impact the critical constraints. The range of values of some design variables are also narrowed according to the results of sensitivity analysis. To further improve the efficiency of searching, the material selection is constrained to a number of promising combinations, as the "seed designs". With the aforementioned acceleration strategies on the optimization search the team accomplished approximately 100 to 150 design investigations each day by reviewing the previous design iterations each morning then proposing an updated starting design and updated variables with updated limits each afternoon.

In the first round of searching, all the jobs for optimization of "seed designs" obtained designs that satisfied the required performance criteria. However, none of the optimized designs met the cost target, which indicated that the material selection of the seed designs might not be most wisely chosen. A new seed design needed to be proposed. To obtain a seed that was more promising in terms of meeting cost target while avoiding the necessity of running expensive integrated MDO process, we analyzed our time-wise inexpensive cost model in details to suggest the new combination of materials. Figure 3.4-5 shows the variation in cost penalty with SMC fraction by weight. The black starred line indicates the cost target. All the other curves are iso-weight curves i.e., for a given weight how does the cost penalty change with carbon fiber composite fraction. Based on the numerical analysis on the cost model, the new seed design should be fabricated with approximately 18-22 wt% of CFRP and 78-82 wt% of structural steel.

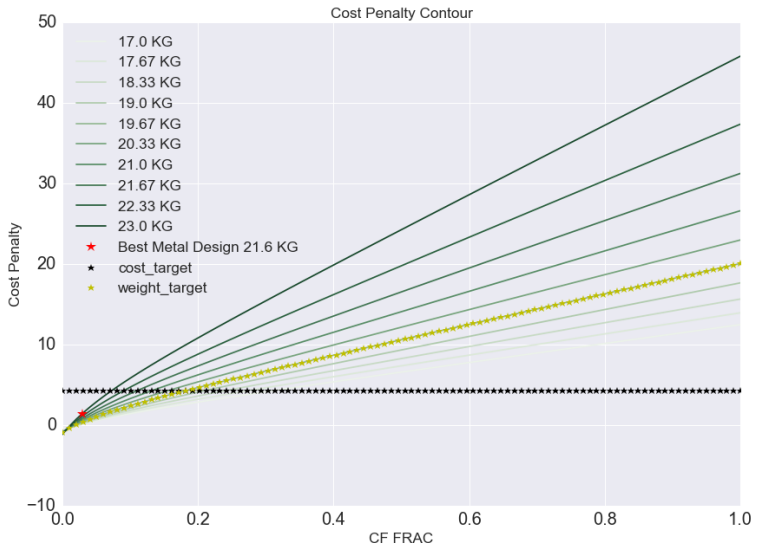

Figure 3.4-5. The relation between cost penalty and the weight percentage of SMC in the structure.

The next step in the strategy before initiating the MDO process on the seed is to determine the material selection for different local regions in the subframe design. Intuitively enough, the local regions that bear high loads should be assigned with either continuous fiber patches or structural steel. Replacing these loading bearing regions with SMC would result in a much thicker gage and thus the efficiency of weight saving was low. A quick evaluation of the weight saving efficiency of different local regions, we examined the already those already optimized seed designs that were assigned with different material selection and found to meet all performance requirements. The weight difference when switching from steel to SMC was calculated for the local regions. It turned out that at some of the local regions, replacing SMC with steel could not save weight at all, while significant weight-saving was observed in others. According to these analyses, we came up with a new seed design, assigning SMCs at those regions with high weight-saving potential and structure steel in the rest. After running the MDO process with ICME models for this seed design, we obtained a design that weighs 40.69 pounds, a 30% weight savings, and costs an additional $4.01 per pound saved, while meeting all the performance requirement. This multi material 79% steel, 16% carbon fiber SMC and 5% carbon fiber unidirectional patches design meets both the weight savings and addition cost per pound of weight saved targets. The schematic of this “staggered” searching strategy was summarized in Figure 3.4-6.

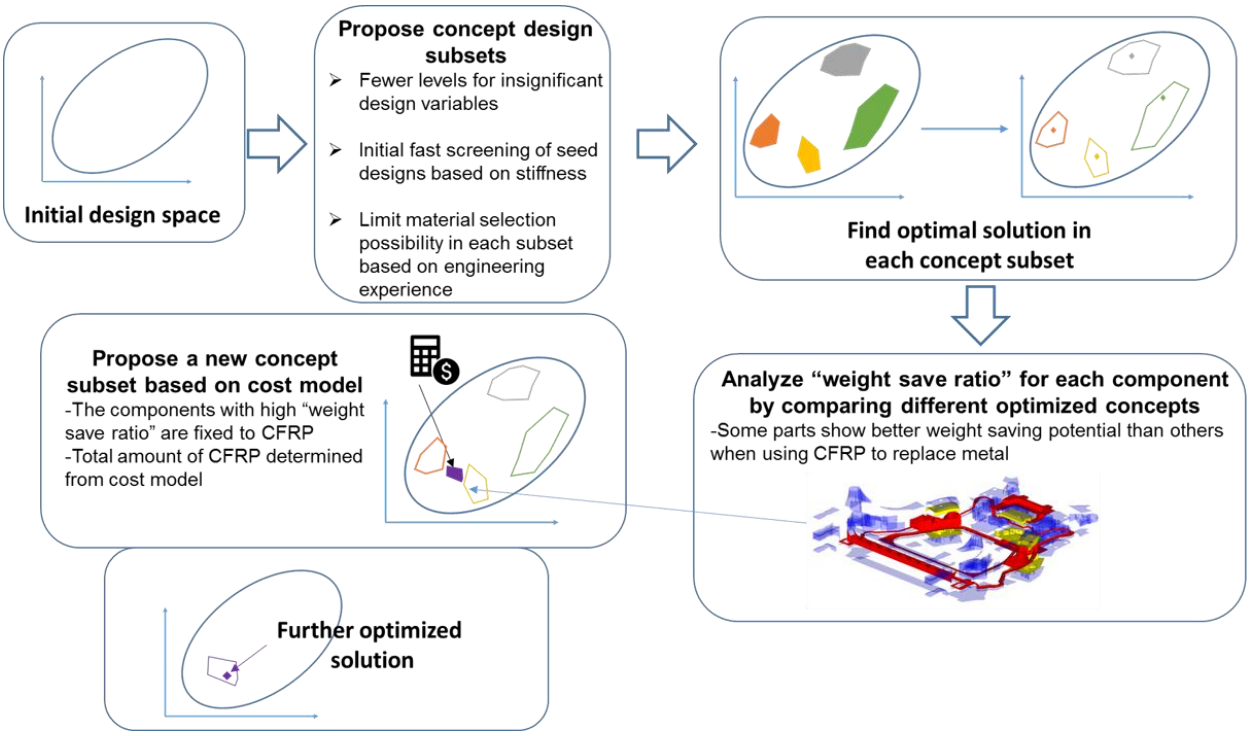

Figure 3.4-6. Staggered design optimization process.

In total, ~10,000 runs were performed, before we ended up with the final design that met all the targets. With aforementioned acceleration strategies, the team accomplished approximately 100 to 150 design investigations each day. Weekly meetings were held to review the status of the MDO runs and propose updated search directions. This final design may be further improved in a MDO scheme with no limits on values of design variables, yet the computational cost to search the vast design space could be too much compared to the resources that we can access.

3.4.3 Performance Analysis and Model Demonstration

The engineering performance metrics listed in Table 3.4-2 are critical minimum requirements that typically define the subframe design. These are a small subset of the full list of engineering requirements for a production subframe. Also, a final design addresses manufacturing, service, corrosion, and repair requirements for a high-volume production automotive subframe. The results from this exercise produces an initial design that could be used as a starting point for the more detailed final design. Experience shows that moving from a strong initial design to a final design typically results in small changes to weight and variable cost.

The twenty-seven stiffness requirements in Table 3.4-2 controls the attachment point stiffness for all the chassis parts that rely on the subframe for a foundation. The front lower control arm (FLCA) attaches the wheel to the subframe. The steering gear delivers steering inputs to the wheels. The roll restrictor controls powertrain fore-aft roll during acceleration and deceleration and limits powertrain vibration inputs to the passenger compartment. The stabar is the front cross-car stabilizer bar that is also called an anti-sway or anti-roll bar that reacts the overturning moment during sharp turns. The attachment stiffness at the connection of these components to the subframe typically determine the overall subframe design for stiffness.

The durability requirement ensures that the subframe survives aggressive customer use for 15 years or 150,000 miles. The performance metric is expressed as multiples of vehicle lives (15 years or 150,000 miles of aggressive use). When all portions of the subframe meet or exceed the requirement of unity, then the subframe is expected to provide 15 years or 150,000 miles of service without fatigue damage.

The strength requirements force the subframe to perform acceptably during single extreme loading events such as curb impacts, deep potholes or rough railroad tracks. The subframe must endure the level 1 loads without any degradation to the function of the subframe. For metals this means less than one millimeter of plastic deformation. For composites this means no cracking. All chassis systems such as steering, and braking will perform robustly even if the connection points move by one millimeter.

The subframe must withstand the level 2 loads without catastrophic failure. No part of the subframe can separate. For metals this means staying below half of the allowable plastic strain of the material. For composites this means no cracking. These design requirements give the subframe robustness so that the drive can maneuver the vehicle to a safe position such as onto the shoulder or into a parking lot.

The safety requirement ensures that the subframe will perform adequately in a frontal crash. This requirement is a component level cascade from typical full vehicle requirements. The requirement of the subframe withstanding 100 kN load enable the rest of the passive safety systems in the vehicle to perform as designed to keep our customers safe in the event of a frontal crash.

The modeFONTIER workflow orchestrated all these analyses for each candidate design of the subframe. In all, over 10,000 designs were investigated.

3.4.4 Weight and Cost Analysis

After exercising the modeFRONTIER workflow, a number of interesting designs emerged. One of these designs met both the weight target of at least 25% weight reduction and the cost target of adding less variable cost than $4.27 per pound of weight saved.

The weight calculation resulted directly from the design. Knowing the geometry and thickness of each part plus the density of each material in the design determined the weight. The weight calculation is straightforward from the design information.

The variable cost estimating module in the modeFRONTIER workflow also relied on the design information. The model estimated the subframe variable cost based on the weight of the materials in each design. The estimate used ratios of the materials coupled with internal Ford material and manufacturing costs for stamped steel, aluminum and carbon fiber composite subframes as the reference points. Incorporating this material weight based variable cost estimate into the modeFRONTIER workflow allowed the optimization scheme to include variable cost as a response to be minimized.

The variable cost estimate assumes that the carbon fiber cost matches the DOE target cost of $5.00 per pound for the carbon fiber on a keel. The variable cost then estimates the cost of the carbon fiber composite as the cost of the carbon fiber plus the cost of the resin plus the processing cost to produce the SMC, UD non-crimped fabric composite or the woven composite, plus typical markup. The cost estimate also includes manufacturing costs for the parts, assembly costs for the subframe assuming typical labor, burden and markup rates.

While far from exact, this initial cost estimate added valuable texture to the optimization process. Certainly, as design information improves, such as number of parts, number of point connections such as rivets, number and length of continuous connections such as adhesive bond lines or metal inert gas (MIG) welding, etc. The variable cost estimate can be improved. This effort did not address tooling costs.

One design met both the weight and cost targets. A 79% steel, 16% chopped carbon fiber SMC and 5% carbon fiber unidirectional composite material (weight percentages) design met both the weight and cost target. This design saves 30% weight (target: 25%) and costs and additional $4.01 per pound of weight saved (target: $4.27). The lightest weight design includes 83% CF SMC with 12% steel and 5% CF unidirectional material. This lightest weight design saves 41% weight and costs an additional $8.90 per pound saved. Figure 3.4-7 shows five interesting designs on the percentage weight saved versus additional variable cost per pound saved plot. All five of these designs met the few critical performance metrics included in the multidisciplinary optimization, as shown in Table 3.4-2.

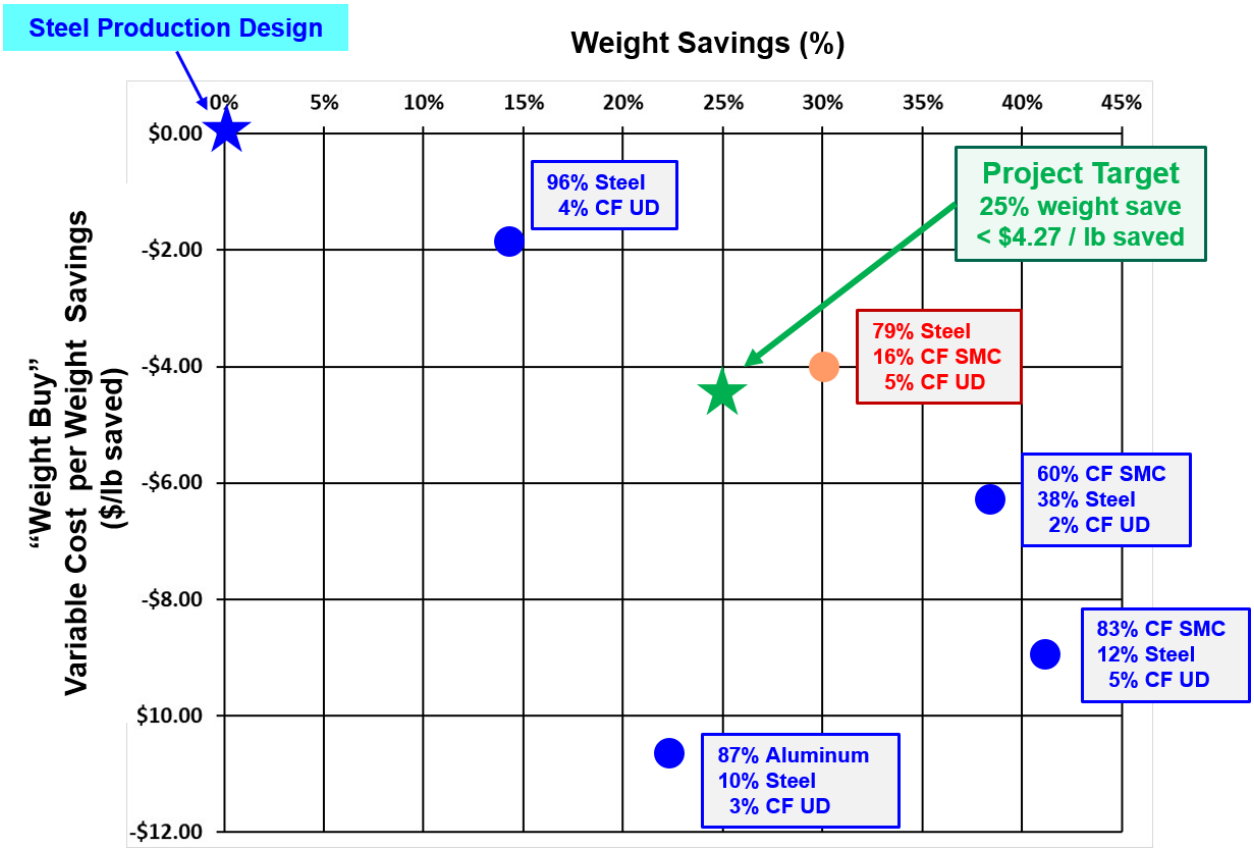

Figure 3.4-7. Five interesting designs plotted on percentage weight saved versus additional variable cost per pound saved graph.

The steel intensive design, the orange dot and the red box in Figure 3.4-7, that meets both the weight and cost targets is primarily stamped steel, 79% by weight. The random chopped carbon fiber sheet molding compound, 16% by weight, stiffens the steel shell. The unidirectional carbon fiber non-crimped fabric patches (5% by weight) reinforce the high load attachment points at the roll restrictor and the front attachment of the front lower control arm. Figure 3.4-8 shows the design and the exploded view of the three materials.

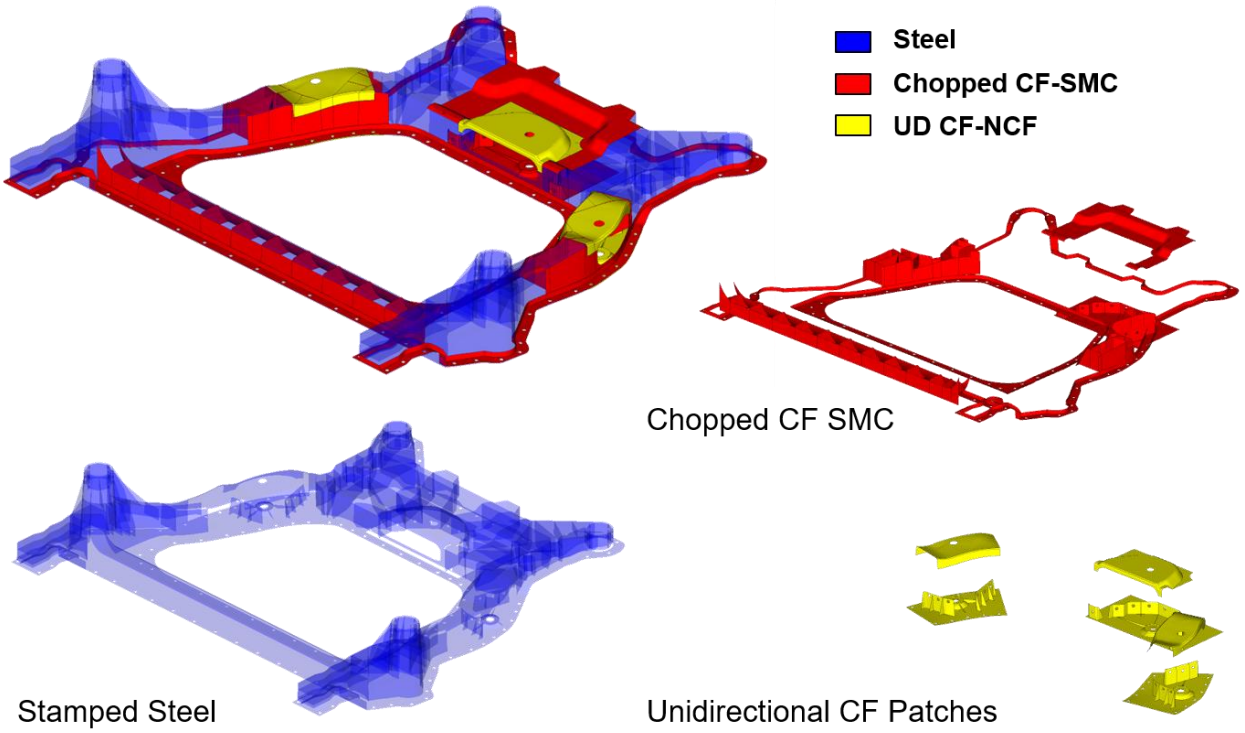

Figure 3.4-8. Steel intensive design at 30% weight save and additional cost of $4.01 per pound saved material distribution.

While this design certainly has manufacturing challenges, it meets the critical engineering performance requirements from Table 3.4-2. This initial design could be further developed into a final design for a production vehicle subframe.

Overall, this exercise shows that the modeFRONTIER multidisciplinary design process can be used to develop initial designs with the ICME-based tools. The most successful search method includes experience based starting points and direction for the design of experiments iteration modifications. All the designs include multiple materials to produce improved, cost effective designs.

Accomplishments of Task 4 are:

Task 4 accomplished its goals of exercising the full suite of ICME tools to demonstrate how an ICME-based multidisciplinary optimization workflow can be applied to a complex automotive component, the front subframe. The modeFRONTIER workflow simultaneously considered a wide range of design variables, evaluated design of experiments generated candidate designs for stiffness, durability, strength, and safety performance criteria and calculated the weight and variable cost of each candidate design. Through the multidisciplinary optimization workflow, a multi material design was found that meets the identified engineering performance requirements, exceeds the weight save target at an additional variable cost below the target.

The design that met the performance requirements plus both the weight save and additional variable cost per pound of weight save cost targets was a steel intensive design with carbon fiber reinforcements. The design includes 79% steel, 16% chopped carbon fiber SMC and 5% unidirectional carbon fiber non-crimped fabric composite. While the initial design identified through the multidisciplinary design process has manufacturing challenges, it is a solid starting point for a detailed final design.

This task demonstrates that the modeFRONTIER workflow can accommodate a wide range of design variables from geometry, material, gauge and composite laminate layup, evaluate candidate designs for multiple engineering performance requirements and provide an estimated weight and variable cost for each candidate design. This process can run in a batch process on a high performance computing system to accelerate design for carbon fiber composite components.

Lessons learned and potential next steps:

The key lesson learned from this task is that the ICME-based multidisciplinary design process requires robust Computer Aided Engineering (CAE) models. This task highlighted the need for improvements in the geometry and architecture morphing to produce high quality CAE models for manufacturing and engineering performance simulations. The different mesh requirements for the preforming, molding, stiffness, durability, strength and safety simulations presents the most difficult challenge in using these tools in an automated batch process. Particularly the Moldflow requirement for tetrahedral mesh in a continuous closed volume is so different from the shell mesh that is most appropriate for the durability and safety simulations that an automated process to produce both these meshes proved elusive within this project.

The highest value next step is to make improvements in going from parameterized geometry of a complex part to various high-quality finite element meshes of different elements (tetrahedrons and shells) to reduce the barriers to an automated process.

The next improvements are needed in the accessibility of design information beyond geometry and material for improved manufacturing and variable cost estimates. Improved design information would include the number of parts in a design, the number of point connections such as spot welds, rivets or other fasteners, the number and length of continuous connections such as adhesive bond lines or metal inert gas (MIG) welding. This deeper design information could be used to improve the manufacturing assessment and variable cost estimate.

Another lesson learned from Task 4 provides insight into the value and potential business case for carbon fiber composite components for automotive structures. The cost model uses five dollars per pound for the cost of carbon fiber based on the Department of Energy targets. Even at this better than market carbon fiber price, the carbon fiber composite intensive subframe designs fall short of the cost target for the project. The high manufacturing costs associated with the carbon fiber composite subframe force the costs for the fully completed subframe above the $4.27 per pound of weight saved project target. Certainly, the costs of carbon fiber must reach or be lower than the $5.00 per pound target. Also, the costs of the full manufacturing system: the epoxy, the compounding, the molding, the machining, the joining, the final machining, and the processing costs of any inserts or added parts must all be lower to make a carbon fiber composite intensive subframe economically attractive.

4. FINAL CONCLUSIONS AND REMAINING GAPS

After four years of serious efforts, the project extends and complements the knowledge of CFRP epoxy materials with woven carbon fiber, unidirectional carbon fiber and chopped carbon fiber SMC used in compression molding of structural parts. The project creates an industry first ICME-based multi-disciplinary optimization modeFRONTIER workflow that combines part geometry, material, and carbon fiber composite layup design variables with compression molding simulation to generate local material properties feeding into engineering performance simulations for stiffness, overload strength, high cycle fatigue durability and crash safety while tracking component weight and estimating variable cost. The workflow demonstrates the full ICME process on a small part, the top hat section. A similar workflow investigates the design of a large, complex automotive structural component, the front subframe. This optimization workflow finds an initial design that exceeds the project targets for $\geq$25% weight save at a variable cost $\leq$\$4.27 additional variable cost per pound of weight saved. The initial subframe design includes 79 wt% steel, 16 wt% chopped carbon fiber SMC and 5 wt% unidirectional carbon fiber epoxy composite. This initial design saves 30% weight at an additional variable cost of \$4.01 per pound of weight saved compared to the production stamped steel subframe.

The material characterization task performed over 700 specimen material characterization tests for mechanical properties. All the test conditions and results are now included in the NIST CFRP composite material database for the benefit of future researchers and engineers. The largest gap in this testing arena is the definition of a robust fatigue testing protocol for the variety of CFRP composites that are under development. This project makes substantial strides forward on fatigue testing but much more work remains to be done.

The material modeling task developed and improved local material models and engineering performance material models. The largest gap appears to be the fatigue modeling. The fatigue modeling future improvements include further understanding of multi-axial fatigue properties of CFRP composites and development of a multiaxial fatigue failure criterion. The modeling task made good progress on these models, but further work remains.

The ICME modeling integration efforts successfully integrated numerous models into a full multi-disciplinary workflow. The largest gaps in this area are still the special scripts that must be developed to pass information between the various simulation codes. Also, the multitude of potential design variables make the full ICME-based optimization problem challenging even for Ford's High Performance Computing platform.

The design effort successfully found an attractive initial design meeting all the requirements and objectives. The largest gap in the overall design effort is the different modeling requirements for the different simulation software codes. The connection between geometry changes and robust models for the simulations is tenuous and needs improvements.

The industry first ICME-based multi-disciplinary optimization scheme highlights and includes all the successes from this large carbon fiber composite project. The accomplishments of the project teams advance the state-of-the-art and the knowledge base for epoxy thermoset carbon fiber composites in three forms, unidirectional non-crimped fabric, woven fabric and random chopped sheet molding compound.

5. SOFTWARE DEVELOPED UNDER THIS AWARD

LSTC model implementation in LS-DYNA

New Material Models:

MAT_293_COMPRF

for carbon fiber prepreg forming simulation, released 2nd quarter 2017.

MAT_278_CF_MICROMECHANICS

for carbon fiber prepreg forming simulation, released 1st quarter 2017.

Material Model Improvements:

MAT_277 ADHESIVE_CURING_VISCOELASTIC

material model for resin curing processing, released 2nd quarter 2016.

MAT_054 ENHANCED_COMPOSITE_DAMAGE

material model for carbon fiber crash simulation, released 1st quarter 2018.

New Features:

Mapping interface program for fiber orientation mapping

user interface to utilize molding simulation result from Moldflow and Moldex3D for crash simulation, released in LS-PrePost in 1st quarter 2018.

*New LS-DYNA keyword *DEFINE_LAYER*

for automating the prepreg forming model setup, released in 4th quarter 2017

Moldflow (software from Autodesk)

SMC Compression Molding Improvements in 2019 Moldflow version

Flexible charge placement; Improved solution stability for complex part designs; New switch over to press force controlled filling

nCode (software from HBM Prenscia)

Composite fatigue prediction module for continuous carbon fiber composites

6. PUBLICATIONS UNDER THIS AWARD

1. N. Vu-Bac, M. A. Bessa, T. Rabczuk, and W. K. Liu. "A multiscale model for the quasi-static thermo-plastic behavior of highly cross-linked glassy polymers." *Macromolecules* 48, no. 18 (2015): 6713-6723.
2. X. Bai, M. A. Bessa, A.R. Melro, P.P. Camanho, L. Guo, and W. K. Liu. "High-fidelity micro-scale modeling of the thermo-visco-plastic behavior of carbon fiber polymer matrix composites." *Composite Structures* 134 (2015): 132-141.
3. I. M. Daniel, "Yield and failure criteria for composite materials under static and dynamic loading." *Progress in Aerospace Sciences* 81 (2016): 18-25.
4. Y. Li, W. Chen, H. Xu, and X. Jin. "3D Representative Volume Element Reconstruction of Fiber Composites via Orientation Tensor and Substructure Features." Proceedings of the American Society for Composites: 31st Technical Conference, 2016, Williamsburg, VA.
5. W. Zhang, H. Ren, J. Lu, Z. Zhang, L. Su, Q. J. Wang, D. Zeng, X. Su, and J. Cao. "Experimental methods to characterize the woven composite prepreg behavior during the preforming process." *Proceedings of the American Society for Composites: 31st Technical Conference*, 2016, Williamsburg, VA.
6. Y. Li, Q. Zhao, M. Mirdamadi, D. Zeng, and X. Su. "Finite element simulation of compression molding of woven fabric carbon fiber/epoxy composites: Part I material model development." *SAE International Journal of Materials and Manufacturing* 9, no. 3 (2016): 729-736.
7. Z. Liu, M. A. Bessa, and W. K. Liu. "Self-consistent clustering analysis: an efficient multi-scale scheme for inelastic heterogeneous materials." *Computer Methods in Applied Mechanics and Engineering* 306 (2016): 319-341.
8. W. Zhang, H. Ren, Z. Wang, W. K. Liu, W. Chen, D. Zeng, X. Su, and J. Cao. "An integrated computational materials engineering method for woven carbon fiber composites preforming process." *AIP Conference Proceedings*, 1769, no. 1 (2016): 170036.
9. Z. Meng, M. A. Bessa, W. Xia, W. K. Liu, and S. Keten. "Predicting the macroscopic fracture energy of epoxy resins from atomistic molecular simulations." *Macromolecules* 49, no. 24 (2016): 9474-9483.
10. J. Gao, B. Liang, W. Zhang, Z. Liu, P. Cheng, R. Bostanabad, J. Cao, W. Chen, W. K. Liu, X. Su, D. Zeng, and Q. Zhao. "Multiscale modeling of carbon fiber reinforced polymer (CFRP) for integrated computational materials engineering process." *Proceedings of the American Society for Composites: 32nd Technical Conference*, 2017, West Lafayette, IN.
11. W. Zhang, H. Ren, Biao Liang, D. Zeng, X. Su, J. Dahl, M. Mirdamadi, Q. Zhao, and J. Cao. "A non-orthogonal material model of woven composites in the preforming process." *CIRP Annals* 66, no. 1 (2017): 257-260.
12. W. Zhang, Z. Zhang, J. Lu, Q.J. Wang, X. Su, D. Zeng, M. Mirdamadi, and J. Cao, "Experimental Characterization Of The Interaction Between Carbon Fiber Composite Prepregs During The Preforming Process." *Proceedings of the ASME 2017 12th International Manufacturing Science and Engineering Conference*, 2017, Los Angeles, CA.

13. L. A. Powell, W. Luecke, M. Merzkirch, K. Avery, and T. Foecke, 'High Strain Rate Mechanical Characterization of Carbon Fiber Reinforced Polymer Composites using Digital Image Correlations', *SAE International Journal of Materials and Manufacturing* 10 no.2 (2017): 138-146.
14. H. Cheng, J. Gao, O. L. Kafka, K. Zhang, B. Luo, and W. K. Liu. "A micro-scale cutting model for UD CFRP composites with thermo-mechanical coupling." *Composites Science and Technology* 153 (2017): 18-31.
15. I.M. Daniel, J. S. Fenner and B. T. Werner, "Characterization and Modeling of Composite Sandwich Core Foam under Static and Dynamic Loading," *Proceedings of the 2016 Annual Conference on Experimental and Applied Mechanics*, 2016, Orlando, FL.
16. J.S. Fenner and I.M. Daniel, 'Mixed Mode and Mode II Fatigue Crack Growth in Woven Composites', *Proceedings of the 2016 Annual Conference on Experimental and Applied Mechanics*, 2016, Orlando, FL.
17. I. M. Daniel, S. M. Daniel, and J. S. Fenner. "A new yield and failure theory for composite materials under static and dynamic loading." *International Journal of Solids and Structures* 148 (2018): 79-93.
18. S. Lin, Y. Chen, D. Zeng and X. Su, "Meso-modeling of Carbon Fiber Composite for Crash Safety Analysis", *SAE World Congress Experience*, 2017, Detroit, MI.
19. H. Xu, J. Yang, C. H. Chuang, and Z. Zhan. "Study of the Design Representation Methods for the Optimization of Multi-Layer Composite Structures." *ASME 2017 International Design Engineering Technical Conferences and Computers and Information in Engineering Conference*, 2017.
20. Z. Chen, Y. Li, Y. Shao, T. Huang, H. Xu, Y. Li, W. Chen, D. Zeng, K. Avery, H. Kang, and X. Su. "A Comparative Study of Two RVE Modelling Methods for Chopped Carbon Fiber SMC." *SAE Technical Paper* 2017-01-0224, 2017.
21. H. Xu, Y. Li, and D. Zeng. "Process Integration and Optimization of ICME Carbon Fiber Composites for Vehicle Lightweighting: A Preliminary Development." *SAE International Journal of Materials and Manufacturing* 10, no. 3 (2017): 274-281.
22. Y. Li, Z. Chen, H. Xu, J. Dahl, D. Zeng, M. Mirdamadi, and X. Su. "Modeling and simulation of compression molding process for sheet molding compound (SMC) of chopped carbon fiber composites." *SAE International Journal of Materials and Manufacturing* 10, no. 2 (2017): 130-137.
23. M. Matthias, L.A. Powell, and T. Foecke. "Measurements of Mode I Interlaminar Properties of Carbon Fiber Reinforced Polymers Using Digital Image Correlation." *Key Engineering Materials*, 742(2017): 652-659.
24. Z. Chen, T. Huang, Y. Shao, Y. Li, H. Xu, K. Avery, D. Zeng, W. Chen, and X. Su. "Multiscale finite element modeling of sheet molding compound (SMC) composite structure based on stochastic mesostructure reconstruction." *Composite Structures* 188 (2018): 25-38.
25. R. Bostanabad, B. Liang, J. Gao, W. K. Liu, J. Cao, D. Zeng, X. Su, H. Xu, Y. Li, and W. Chen. "Uncertainty quantification in multiscale simulation of woven fiber composites." *Computer Methods in Applied Mechanics and Engineering* 338 (2018): 506-532.
26. H. Tang, Z. Chen, G. Zhou, Y. Li, K. Avery, H. Guo, H. Kang, D. Zeng, and X. Su. "Correlation between failure and local material property in chopped carbon fiber chip-reinforced sheet molding compound composites under tensile load." *Polymer Composites* (2018).
27. Q. Sun, D. Zeng, D. Li, and X. Su. "Experiment and Simulation Study on Unidirectional Carbon Fiber Composite Component under Dynamic Three-Point Bending Loading." *SAE International Journal of Materials and Manufacturing* 11 (2018): 499-504.

28. J. S. Fenner, and I. M. Daniel. "Testing the 2-3 Shear Strength of Unidirectional Composite." *Mechanics of Composite, Hybrid and Multifunctional Materials*, 5 (2019): 77-84.
29. W. Zhang, R. Bostanabad, B. Liang, X. Su, D. Zeng, M. A. Bessa, Y. Wang, W. Chen, and J. Cao. "A numerical Bayesian-calibrated characterization method for multiscale prepreg preforming simulations with tension-shear coupling." *Composites Science and Technology* 170 (2019): 15-24.
30. Y. Li, Z. Chen, L. Su, W. Chen, X. Jin, and H. Xu. "Stochastic reconstruction and microstructure modeling of SMC chopped fiber composites." *Composite Structures* 200 (2018): 153-164.
31. A. Ojha, Z. Li, H. Liu, C. C. Engler-Pinto, X. Su, "Fatigue modeling of Carbon/epoxy Woven Composites: Theory and Experiments", submitted to *International Journal of Fatigue*, 2018.
32. Q. Sun, Z. Meng, G. Zhou, S. P. Lin, H. Kang, S. Keten, H. Guo, and X. Su. "Multi-scale computational analysis of unidirectional carbon fiber reinforced polymer composites under various loading conditions." *Composite Structures* 196 (2018): 30-43.
33. Q. Sun, H. Guo, G. Zhou, Z. Meng, Z. Chen, H. Kang, S. Keten, and X. Su. "Experimental and computational analysis of failure mechanisms in unidirectional carbon fiber reinforced polymer laminates under longitudinal compression loading." *Composite Structures* 203 (2018): 335-348.
34. B. Liang, W. Zhang, J.S. Fenner, J. Gao, Y. Shi, D. Zeng, X. Su, W.K Liu, and J. Cao. "Multi-scale modeling of mechanical behavior of cured woven composites accounting for the influence of yarn angle variation." submitted to *Composites Part A: Applied Science and Manufacturing*, 2018.
35. H. Liu, A. Ojha, Z. Li, C. C. Engler-Pinto, X. Su, Q. Sun, H. Kang, W. Wen, and H. Cui. "Fatigue modeling for carbon/epoxy unidirectional composites under various stress ratios considering size effects." *International Journal of Fatigue* 120 (2019): 184-200.
36. Q. Sun, G. Zhou, Z. Meng, H. Guo, Z. Chen, H. Liu, H. Kang, S. Keten, and X. Su. "Failure criteria of unidirectional carbon fiber reinforced polymer composites informed by a computational micromechanics model." *Composites Science and Technology* 172 (2019): 81-95.
37. Q. Sun, H. Guo, G. Zhou, Z. Meng, Z. Chen, H. Kang, S. Keten, and X. Su. "Experimental and computational analysis of failure mechanisms in unidirectional carbon fiber reinforced polymer laminates under longitudinal compression loading." *Composite Structures* 203 (2018): 335-348.
38. H. Tang, G. Zhou, Z. Chen, L. Huang, K. Avery, Y. Li, H. Liu, H. Guo, H. Kang, D. Zeng, C. C. Engler-Pinto, and X. Su. "Fatigue Behavior Analysis and Multi-Scale Modelling of Chopped Carbon Fiber Chip-Reinforced Composites under Tension-Tension Loading Condition." *Composite Structures* 215 (2019): 85-97.
39. R. Bostanabad, B. Liang, J. Gao, W.K. Liu, J. Cao, D. Zeng, X. Su, H. Xu, Y. Li and W. Chen, 'Multiscale Simulation of Fiber Composites with Spatially-Varying Uncertainties', *Uncertainty Quantification in Multiscale Materials Modeling*, ed. Y. Wang and D. McDowell, Elsevier S&T, 2018.
40. Z. Chen, H. Tang, Y.Shao, Q. Sun, G. Zhou, Y. Li, H. Xu, D. Zeng, and X. Su. "Failure of chopped carbon fiber Sheet Molding Compound (SMC) composites under uniaxial tensile loading: Computational prediction and experimental analysis." *Composites Part A: Applied Science and Manufacturing* 118 (2019): 117-130.
41. H. Tang, Z. Chen, G. Zhou, X. Sun, Y. Li, L. Huang, H. Guo, H. Kang, D. Zeng, C. C. Engler-Pinto, and X. Su. "Effect of Fiber Orientation Distribution on Constant Fatigue Life Diagram of Chopped Carbon Fiber Chip-Reinforced Sheet Molding Compound (SMC) Composite." submitted to *International Journal of Fatigue*, 2019.